

Gyrotron physics from linear to chaotic regimes: experiment and numerical modeling

THÈSE N° 6959 (2016)

PRÉSENTÉE LE 20 MAI 2016
À LA FACULTÉ DES SCIENCES DE BASE
CRPP - PHYSIQUE DU TOKAMAK TCV
PROGRAMME DOCTORAL EN PHYSIQUE

ÉCOLE POLYTECHNIQUE FÉDÉRALE DE LAUSANNE

POUR L'OBTENTION DU GRADE DE DOCTEUR ÈS SCIENCES

PAR

Falk Hans BRAUNMÜLLER

acceptée sur proposition du jury:

Prof. V. Savona, président du jury
Dr S. Alberti, Dr J.-Ph. Hogge, directeurs de thèse
Prof. J. Jelonnek, rapporteur
Dr M. Blank, rapporteuse
Dr T.-M. Tran, rapporteur



ÉCOLE POLYTECHNIQUE
FÉDÉRALE DE LAUSANNE

Suisse
2016

Abstract

Gyrotrons belong to the family of high-power coherent radiation sources known as Electron Cyclotron Masers (ECMs) and are based on the physical mechanism of the ECM-instability, converting electron rotational kinetic energy into coherent electromagnetic radiation. The worldwide gyrotron R&D is mainly driven by the application in heating a magnetically confined fusion plasma, which requires coherent radiation sources with MW power-level in the sub-THz frequency range. In the last two decades, an application for gyrotrons emerged in the field of Nuclear Magnetic Resonance (NMR) spectroscopy, where a dramatic enhancement in sensitivity can be achieved via Dynamic Nuclear Polarization (DNP), requiring a low-power ($\sim 1-10$ W), sub-THz frequency ($\sim 100-600$ GHz) coherent radiation.

The subject of this thesis is a gyrotron prototype developed at SPC/EPFL for the DNP-application. It is designed for continuous mode (CW)-operation on the $TE_{7,2}$ -mode and has a maximum radio-frequency (RF)-power of $P_{RF}=150$ W at a frequency of $f_{RF}=260.5$ GHz.

The DNP-gyrotron has demonstrated to be an ideal test-bench for fundamental research on the highly non-linear beam-wave interaction process. The weakly overmoded gyrotron cavity is such that transverse mode competition can be neglected and the studied dynamical regimes concentrate on the 1D-longitudinal dynamics. The main topic of this work concentrates on the experimental measurements and numerical modeling of novel non-stationary regimes, characterized by a multi-frequency spectrum and a modulated RF-power.

These experimental results have shown that the very fast dynamics (nanosecond time-scale) observed in non-stationary regimes is such that the usual assumption, in which the cavity electromagnetic field is not varying during the electron time of flight, is no more valid. To overcome this assumption a new model based on a Particle-In-Cell (PIC) approach has been developed and a new code TWANG-PIC has been written and successfully exploited. Also, the linear regime has been revisited from the theoretical point of view by developing a new moment-based model. Based on this model a new code TWANGLIN has been written and used for a detailed analysis of the experimentally measured threshold conditions (starting current) covering operating points from forward to backward-wave gyrotron regimes.

Among a large variety of non-stationary regimes, that are described and analyzed, a novel specific nanosecond-pulsed regime was studied, in which the multi-frequency spectrum consists of frequency-equidistant, phase-locked sidebands. This novel regime may open up new applications for gyrotrons.

For the first time it has also been possible to experimentally investigate, and model via numer-

ical simulations, the dynamical properties from the linear regime up to chaotic regimes. The numerical simulations with TWANG-PIC are in good qualitative agreement with the experimental results and showed that the observed non-stationary regimes are associated to non-linear axial mode-competition.

Another important task was to configure the gyrotron for the DNP-NMR spectroscopy application. Several state-of-the-art features have been included, such as a continuous frequency-tuning over 1.2GHz by varying several control parameters simultaneously, a fast ($\lesssim 15$ kHz) frequency-modulation over ~ 100 MHz and a feedback-controller for stabilizing RF-parameters. Currently the gyrotron is routinely and successfully operated on a 400MHz DNP-NMR experiment.

keywords: gyrotron, beam-wave interaction, DNP-NMR spectroscopy, frequency-tuning, non-stationary oscillations, sidebands, gyrotron modeling, chaotic radiation

Kurzzusammenfassung

Gyrotrons gehören zur Familie der Elektron-Zyklotron-Maser (ECM) und basieren auf dem physikalischen Mechanismus der ECM-Instabilität, die die kinetische Rotationsenergie in kohärente elektromagnetische Strahlung umwandelt. Die weltweite Gyrotron-R&D wird hauptsächlich angetrieben von der Anwendung zur Heizung eines magnetisch eingeschlossenen Fusionsplasmas, welches nach kohärenten Strahlungsquellen mit MW-Leistungsniveau im sub-THz Frequenzbereich verlangt. In den letzten zwei Jahrzehnten entwickelte sich eine Anwendung für Gyrotrons im Bereich der Kernspinresonanz (NMR)-Spektroskopie, wo extreme Sensitivitätsverstärkung durch Dynamisch-Nukleare Polarisierung (DNP) erreicht wird, was kohärente Strahlung (RF) mit niedrigerer Leistung ($\sim 1-10\text{W}$) und sub-THz-Frequenz ($\sim 100 - 600\text{GHz}$) erfordert. Das Thema dieser Dissertation ist ein Gyrotronprototyp, der am SPC/EPFL für die DNP-Anwendung entwickelt wurde. Er wurde entworfen für Dauerbetrieb in der $TE_{7,2}$ -Mode und hat eine Maximal-Strahlungsleistung von $P_{\text{RF}}=150\text{W}$ bei einer Frequenz von $f_{\text{RF}}=260.5\text{GHz}$.

Das DNP-Gyrotron erwies sich als ideales Versuchsobjekt für die Erforschung der Strahl-Wellen-Wechselwirkung. Der schwach übermodierte Resonator erlaubt es, die transversale Modenkonzurrenz zu vernachlässigen und die untersuchten dynamischen Regime konzentrieren sich auf die 1D longitudinale Dynamik. Das Hauptthema dieser Arbeit konzentriert sich auf experimentelle Messungen und numerische Modellierung eines neuartigen nicht-stationären Regimes, das sich durch ein Mehrfrequenzspektrum und modulierte RF-Leistung auszeichnet.

Diese experimentellen Ergebnisse zeigen, dass durch die beobachtete sehr schnelle Dynamik (Nanosekunden-Zeitskala) in den nicht-stationären Regimes die gebräuchliche Annahme, dass das elektromagnetische Feldprofil invariant ist während der Elektronendurchflugszeit, ausser Kraft gesetzt wird. Um diese Annahme zu beseitigen wurde ein neues, auf einen Particle-In-Cell (PIC)-Ansatz basierendes Modell entwickelt und ein neuer Code TWANG-PIC wurde geschrieben und erfolgreich angewandt. Ebenso wurde die Theorie des linearen Regimes neu aufgegriffen durch die Neuentwicklung eines momentenbezogenen Modells. Basiert auf dieses Modell wurde ein neuer Code TWANGLIN geschrieben und verwendet für die Analyse der experimentell gemessenen Schwellenbedingungen (Startstrom) verteilt über Arbeitspunkte vom Rückwärts- bis Vorwärtswellen-Regime.

Unter der grossen Vielfalt an nicht-stationären Regimen, die beschrieben und analysiert wird, ergibt sich ein neuartiges Regime mit Nanosekundenpulsen, in welchem das Mehrfrequenzspektrum aus äquidistanten, phasengekoppelten Seitenbändern besteht. Dieses neuartige Regime könnte neue Anwendungsbereiche für Gyrotrons eröffnen.

Erstmals war es auch möglich, die dynamischen Eigenschaften vom linearen Regime bis hin zum chaotischen Regime experimentell zu erkunden und mithilfe von numerischen Simulationen zu modellieren. Die numerischen Simulationen mit TWANG-PIC sind in guter qualitativer Übereinstimmung mit experimentellen Ergebnissen und zeigten, dass die nicht-stationären Regimes mit axialer Modenkonzurrenz assoziiert sind.

Eine weitere wichtige Aufgabe dieser Dissertation bestand aus Vorkehrungen des Gyrotrons für die DNP-NMR Spectroskopie-Anwendung. Mehrere hochmoderne Funktionen wurden eingebunden, wie z.B. eine kontinuierliche Frequenzanpassung über 1,2GHz durch Variation mehrerer Kontrollparameter, eine Frequenzmodulation über ~100MHz und ein Feedback-Kontrollsystem zur Stabilisierung von RF-Parametern. Aktuell wird das Gyrotron routinemässig und erfolgreich an einem 400MHz DNP-NMR-Experiment betrieben.

Schlagwörter: Gyrotron, Strahl-Wellen-Wechselwirkung, DNP-NMR Spectroskopie, Frequenzverstimmung, nicht-stationäre Schwingungen, Seitenbänder, Gyrotron Modellisierung, chaotische Strahlung

Contents

1	Introduction	1
1.1	Background and Motivation	1
1.2	Magnetic fusion research	2
1.2.1	Electron Cyclotron Resonance Heating	4
1.3	Applications for low-power, high-frequency gyrotrons	5
1.3.1	Dynamic Nuclear Polarization - Nuclear Magnetic Resonance spectroscopy	5
1.4	Principle of gyrotrons and related devices	7
1.5	Gyrotron setup	8
1.5.1	Electromagnetic properties of the cavity	9
1.6	The beam-wave interaction	11
1.7	Challenges in modern gyrotron development	15
1.7.1	High-power gyrotrons for plasma heating	15
1.7.2	Frequency-tunability	15
1.7.3	Non-stationary oscillation in gyrotrons	16
1.8	Goal of the thesis	16
1.9	Outline of the thesis	17
2	Experimental Setup	19
2.1	Design and setup of the DNP-NMR gyrotron	19
2.1.1	Cavity geometry and RF-properties	23
2.1.2	Operating parameters	24
2.1.3	Normalized parameters	26
2.2	Setup in LPMN-laboratory	29
2.3	Gyrotron control system	29
2.3.1	Labview control system	30
2.3.2	Beam-current stabilization	34
2.4	The RF-beam profile	35
2.5	Diagnostics	37
2.6	Data Analysis Tools	41

3 Gyrotron Modeling	43
3.0.1 Electron-optics simulation: DAPHNE	44
3.1 Cold-cavity calculations	45
3.2 Non-linear self-consistent beam-wave interaction	46
3.3 Trajectory-approach: The TWANG-model	48
3.3.1 Numerical Approach and applications	53
3.4 1D-Particle-In-Cell approach: TWANG-PIC	54
3.4.1 TWANG-PIC model	55
3.4.2 Numerical Approach and Applications	56
3.4.3 Calculation of RF-parameters	58
3.4.4 Benchmarking and confirmation of necessity for PIC-model	58
3.5 Linear model and starting current calculations	64
3.5.1 TWANGLIN-model	65
3.5.2 TWANGLIN-benchmarking	69
3.6 Summary of modeling	70
4 The Stationary Gyrotron Operation Regime	73
4.1 Linear analysis	74
4.1.1 Starting current analysis	75
4.2 Behavior close to starting current	77
4.2.1 Linear versus non-linear phase of interaction in forward-regime	77
4.2.2 Behavior in backward-region: regime with low RF-power	81
4.3 RF-Frequency and RF-power for DNP	83
4.3.1 Frequency - tuning and RF-power: experimental results	83
4.3.2 Frequency - tuning and RF-power: experiment-theory comparison	85
4.3.3 Frequency-modulation for DNP-spectroscopy	87
4.4 Influence of pitch-angle	89
4.4.1 Pitch-angle variation from Anode-voltage fluctuation	90
4.5 Pulsed operation	92
4.6 Frequency and power stabilization	93
4.7 Summary of characterization of stationary operating regime	94
5 Analysis of the non-stationary regime	97
5.1 The non-stationary regime: Operational domain	98
5.2 Categorization of non-stationary oscillations	99
5.2.1 Sideband category	99
5.2.2 Period doubling category	99
5.2.3 Period tripling category	100

CONTENTS

5.2.4	Chaotic category	101
5.2.5	Broad sideband category	102
5.3	Simulation of non-stationary oscillations	102
5.3.1	Experiment-theory comparison of non-stationary regime categories	105
5.4	Dependency of rf-characteristics on operating parameters	109
5.5	Temporal variation of spectra induced by anode voltage fluctuations	112
5.6	Analysis of chaotic regime and the route towards chaos	115
5.6.1	Routes to Chaos	115
5.6.2	Calculation of the Lyapunov-exponent	120
5.7	Analysis of the sideband-regime	125
5.7.1	Nanosecond power pulses in non-stationary oscillation	126
5.7.2	Analysis of phase relation between sidebands	131
5.7.3	Dependence of sideband frequency separation on operating parameters	133
5.7.4	The axial profiles of sideband-modes	140
5.8	Non-stationary oscillations in high-power gyrotrons	143
5.9	Interpretation of non-stationary oscillations with simulations	145
5.9.1	Possible interpretations from literature	145
5.9.2	Interpretation of observed non-stationary oscillation	147
5.10	Summary and conclusions of non-stationary oscillations	150
6	Summary and Conclusions	151
A	Numerical Implementation of TWANG	153
A.1	Numerical discretization	153
A.1.1	Space discretization using Finite Elements	153
A.1.2	Time integration	155
A.1.3	Implementation of equations of motion with 4th order Runge-Kutta method	155
B	Symbol List	157
	List of Figures	161
	List of Tables	175
	Glossary	177
	Acronyms	179
	Bibliography	183

Chapter 1

Introduction

1.1 Background and Motivation

The development of gyrotrons is closely related to the history of magnetic fusion research, where a hot ionized gas, a plasma, is magnetically confined. The goal of this research is the development of a new sustainable primary energy source, based on nuclear fusion. In a nuclear fusion reaction, the nuclei of two lighter atoms fuse to a heavier nucleus, releasing a large amount of energy. In order to create nuclear fusion reactions with a positive overall energy balance, the plasma has to be heated to temperatures of ~ 100 million $^{\circ}\text{C}$. An essential heating method for this application is based on the heating of electrons in the plasma via Electron Cyclotron Resonant Heating (ECRH). This is performed by injection of high-power (0.1-2 MW) electromagnetic radiation with a frequency in the range 28-170 GHz.

The only source capable of producing such electromagnetic radiation is the gyrotron, a device producing coherent electromagnetic radiation based on the stimulated excitation of radiation from a magnetized electron beam in a cavity-resonator. Therefore, the research and development of gyrotrons was triggered and motivated by their application in plasma heating of magnetically confined plasmas.

Later it was realized, that gyrotrons are capable of producing electromagnetic radiation also at higher frequencies of several hundred GHz with a power ranging from Watts to kiloWatts. This capability is unique for radiation sources and opens new fields of application. One of them is an application in Nuclear Magnetic Resonance (NMR)-spectroscopy, where organic compounds and matter are studied by analyzing the spectra of magnetized nuclear spins excited by a low-frequency (<1 GHz) radio-frequency (RF) wave. In Dynamic Nuclear Polarization (DNP), the high-frequency radiation generated by the gyrotron (0.1-1 THz) interacts with the magnetized electron spins, which, via a quantum-mechanical coupling to the nuclear spins, significantly enhances the NMR-signal. The gyrotron that is the subject of this thesis has been developed as a radiation-source for the DNP-application.

In this thesis, a full description and characterization of the gyrotron will be presented. In particular, it will be described, how the gyrotron was configured and characterized for an optimization in view of its application in DNP-spectroscopy, including the implementation of several state-of-the-art features, that have already proven their benefits in DNP-experiments.

It was found, that the radiation characteristics observed with the DNP-gyrotron significantly extend the current understanding of beam-wave interaction in gyrotrons.

For correctly modeling the threshold of radiation excitation in the DNP-gyrotron, a new model for the linear beam-wave interaction was developed, based on the linearized model of the non-linear equations considered in the code TWANG, based on a novel moment-based approach. This model, implemented in the code TWANGLIN, takes into account the change of the self-consistent field properties due to the coupling to the electrons, so that the code can be applied also in regimes, where other models are not valid, within particular gyro-backward wave regimes. In the characterization of the DNP-gyrotron, the phenomenon of non-stationary oscillation with a transition to chaotic radiation was observed. This phenomenon, which is characterized by radiation parameters varying self-consistently on the time-scale of nanoseconds, is not yet entirely understood and has been described only superficially in other gyrotron-experiments. It is a very relevant topic for gyrotrons of the same class as the one described here, where the frequency is tuned continuously over a range of the order of 1 GHz.

It was found, that commonly used beam-wave interaction models and simulation codes are not appropriate for describing the non-stationary oscillations observed in the DNP-gyrotron. This triggered the development of a novel model, which is based upon the model of the TWANG-code, and which is implemented into the new simulation code TWANG-PIC. In the model of TWANG-PIC, a separation between the time-scales of field-variation and electron transit-time in the interaction region is removed, extending the validity of the model to regimes with rapidly varying (\sim ns) radiation parameters.

In this thesis, the non-stationary regime is for the first time completely characterized experimentally. This includes a detailed categorization of the types of non-stationary oscillations observed on different operating points, characterizing the appearance of chaotic radiation in experiment, and a detailed analysis of a regime that is characterized by the appearance of sidebands in the radiation spectrum.

With the help of the code TWANG-PIC, the detailed experimental results can also for the first time be directly compared to simulations based on an appropriate modeling. Finally, the simulations can be used to interpret the non-stationary phenomena observed in experimental measurements.

1.2 Magnetic fusion research

In this section, the research of magnetic fusion will be briefly described, which is the driving force in gyrotron development.

The increasing global energy demand makes the world community search for new energy resources, that are safe, sustainable and compatible with the environment. All currently available energy sources have disadvantages of one kind or the other, be it global warming for fossil fuels, the risk of a major nuclear accident for nuclear fission or a lack of predictability for solar- and wind energy. One potential clean, reliable and flexible source of energy is nuclear fusion, which is also the energy resource of the sun.

The principle of fusion is a nuclear reaction, in which two light atoms (e.g. Deuterium, ^2H , with Tritium, ^3H) fuse to a heavier nucleus, while releasing a large amount of energy in this reac-

1.2. MAGNETIC FUSION RESEARCH

tion. In order to induce a nuclear fusion reaction, the electrostatic repulsion between the two positively charged nuclei must be overcome, requiring high particle kinetic energies. At temperatures, where such energies occur frequently enough, the hydrogenic atoms are fully ionized, i.e. in a plasma state.

A plasma has to be confined with a sufficient density, temperature and confinement time in order to achieve a positive energy-balance for nuclear fusion. Since charged particles are influenced by electromagnetic fields, a possible method of confining this plasma is by using magnetic fields. Therefore, in the most developed concept of magnetic fusion the confinement is provided by closed magnetic field lines helically wound in a toroidally shaped plasma.

An example of an experimental device for magnetic fusion research is displayed in Fig. 1.1,

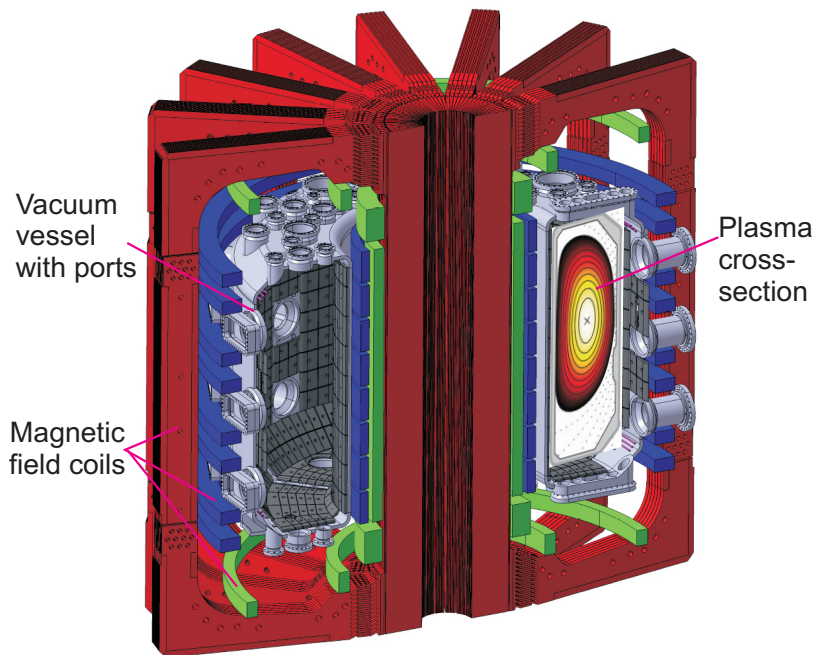


Figure 1.1: Schematic view of half-torus of TCV with plasma-cross-section. Height of vacuum vessel: 1.54m.

showing a schematic half-torus of the TCV-experiment (Tokamak à Configuration Variable) at Swiss Plasma Center (SPC). The plasma has to be heated to very high temperatures $T_{\text{plasma}} \sim 1 - 10 \text{ keV}$ in fusion-relevant experiments, for which the most advanced auxiliary heating system is the injection of high-power RF (electromagnetic radiation) into the plasma, where it is resonantly absorbed by the magnetized ions or electrons. Considering the magnetized light electrons, the wave-particle interaction in the plasma transferring energy to the electrons (heating) occurs via the Electron Cyclotron Resonant Heating (ECRH).

Through their application in this heating method, gyrotrons play an important role for the progress in magnetic fusion research. In particular, for a possible future fusion reactor producing energy, the delivered RF-power and the efficiency for converting electrical power to RF-power have to be as high as possible. Without such high-efficiency heating methods, the goal of achiev-

ing a positive overall energy balance in a fusion reactor would be extremely difficult. Therefore, the development of reliable gyrotrons with a possible further increase in efficiency is an important factor for reaching the goal of commercially available fusion energy.

1.2.1 Electron Cyclotron Resonance Heating

As mentioned above, the most advanced heating concept for magnetic fusion experiments is ECRH with the help of gyrotrons [1]. As illustrated in Fig. 1.2, for this concept, an RF-beam is in-

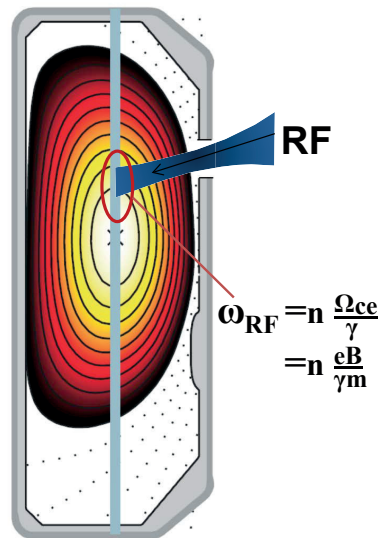


Figure 1.2: Concept of ECRH on resonant layer in plasma.

jected into the plasma from a port in the vacuum-vessel. It penetrates the plasma until it reaches a resonant layer, where the radially changing magnetic field is such, that the RF-frequency equals the (relativistic) electron cyclotron frequency

$$\frac{\Omega_c}{\gamma} = \frac{eB_0}{\gamma m_e} \quad (1.1)$$

or its harmonics (with magnetic field B_0 and electron charge, mass and relativistic factor e , m_e and γ). At this position, the wave is absorbed in the plasma. However, depending on the plasma density and the magnetic field-value, the injected RF-beam may first encounter a cutoff-layer and be reflected, before encountering the resonant layer. Then, higher frequencies have to be used, situated at higher harmonics of the cyclotron-frequency. Such is the case for the plasma in the Tokamak à Configuration Variable (TCV)-experiment, where the second and third harmonics are used for electron heating in X-mode, characterized by a nearly perpendicular injection of the RF-wave with respect to the confining magnetic field, \mathbf{B}_0 , and an RF-electric field perpendicular to \mathbf{B}_0 .

Using ECRH, the efficiency for locally absorbing the RF-power at the desired location in the plasma is generally very high, although decreasing for higher cyclotron harmonics [2]. Therefore,

ECRH with gyrotrons can be used to heat very locally, which is necessary for the suppression and control of certain instabilities in the plasma [3]. At the same time, the wave can drive a localized current in the plasma via Electron Cyclotron Current Drive (ECCD) [1].

1.3 Applications for low-power, high-frequency gyrotrons

In addition to the application of plasma-heating, gyrotrons are used as microwave-sources for many other applications in the range of $\sim 100\text{ GHz} - 1\text{ THz}$, where often only a power of several Watts is needed. Here, gyrotrons manage to partly bridge the so-called Terahertz power-gap, which describes the lack of radiation-sources with sufficient power ($\gtrsim 1\text{ W}$) in the frequency range $0.1 - 10\text{ THz}$. A full summary of possible applications of such gyrotrons can be found in [4, 5]. The most wide-spread application is the DNP-NMR spectroscopy, which is also the main purpose of the gyrotron described in this manuscript.

Other possible applications of sub-THz gyrotrons include Electron Spin Resonance (ESR) spectroscopy [6, 7], direct spectroscopy of positronium [8, 9], material processing [10], detection of radioactive material [5], plasma diagnostics [11], characterization of semiconductor superlattices [4] and several others.

In low-power high-frequency gyrotrons, as the ones used in DNP-NMR spectroscopy, Ohmic losses in the wall of the cavity resonator play only a small role in gyrotron design, compared to high-power gyrotrons, even though they can be comparable to the radiated power. At the same time, in such devices a continuous frequency-tuning over $\gtrsim 1\text{ GHz}$ bandwidth can be achieved.

1.3.1 Dynamic Nuclear Polarization - Nuclear Magnetic Resonance spectroscopy

In Nuclear Magnetic Resonance (NMR) spectroscopy [12, 13], the energy-levels of the hyperfine-structure of molecules and atoms are measured in a strong magnetic field, which corresponds to the splitting of atomic energy levels for nuclear spins aligned and antiparallel to the magnetic field. A precise measurement of the energy-splitting gives information on the detailed chemical structure in a material, where generally the details of the hydrogen energy-levels are used for analyzing the details of organic compounds and organic matter [13].

In NMR-spectroscopy, the energy-levels are measured through an effect of the bulk-magnetization, which is the magnetization due to the fact that more nuclear spins are aligned in the direction of the magnetic field than antiparallel. Because the magnetic moment of the nuclear spins is very small, also the energy-difference between aligned and antiparallel spins is small, which reflects in an only weakly predominating alignment of the spins. Therefore, also the bulk-magnetization is generally very small and difficult to measure.

Generally, the method for measuring the NMR-signal is to flip the vector of the bulk-magnetization by 90° (initially aligned with magnetic field). Being perpendicular to the field-direction, the magnetization vector rotates in a Larmor-precession. This precessing magnetization can then be detected as an oscillating magnetic field signal, which represents the NMR-spectroscopy signal.

In Dynamic Nuclear Polarization (DNP)-enhanced NMR-spectroscopy, the NMR-signal can be strongly increased. This technique makes use of the magnetization of the electron spins in the

magnetic field. The electron magnetic moment, as well as its bulk-magnetization, is by a factor ~ 660 larger than the proton magnetic moment. The small nuclear magnetization can be coupled to this large electron magnetization by irradiating with a frequency, that is resonant with the energy levels for changing the orientation of both nuclear spin and electron spin simultaneously. This is illustrated in Fig. 1.3, showing the resonant RF-irradiation from the gyrotron on the energy-levels of the proton.

Because the gyrotron RF continuously induces transitions with a change of both spin-orientation,

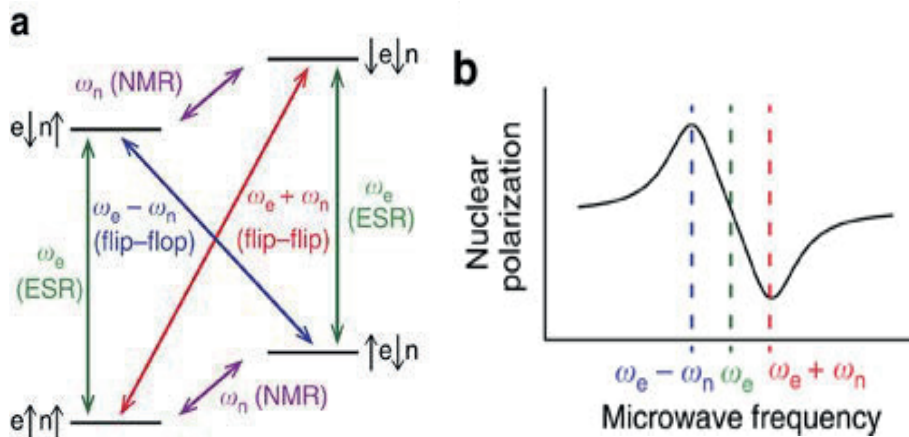


Figure 1.3: a) Transitions between energy-levels of the proton, induced by gyrotron RF (red and blue). The radiation changes the orientation of electron spin and nuclear spin simultaneously. b) Dependence of enhancement on tuning of the gyrotron frequency, through change between the different transitions. The frequencies are ω_n : resonance for nuclear spin-flip, ω_e : resonance for electron spin-flip, and the two combinations of simultaneous spin-flips correspond to the DNP-frequencies. From [14].

it effectively couples the orientation of the nuclear spin to that of the electron spin. This way, the number of aligned nuclear spins effectively corresponds to the alignment of spins with the magnetic moment of the electrons. Thus, a nuclear magnetization as high as the electron magnetization can be reached.

Resulting from this much larger nuclear magnetization, also the NMR-signal experiences a large enhancement, ϵ , which could theoretically be as large as $\epsilon = 660$ (for protons), while in real DNP-NMR-experiments, enhancements of $\epsilon > 100$ are generally reached [15]. An example of such a result is presented in Fig. 1.4, where the original signal is compared to the enhanced signal due to gyrotron radiation and the DNP-effect. The figure shows the enhancement both from [16], and in comparison the enhancement that has already been obtained in the DNP-gyrotron studied here [17], including an effect of frequency-modulation that will be explained later.

The effect of DNP has reached a widespread significance since the pioneering paper from MIT [18], describing the first DNP-NMR experiment with the use of a 140 GHz gyrotron. In later experiments, it has been shown, that the continuous frequency-tunability of sub-THz gyrotrons is

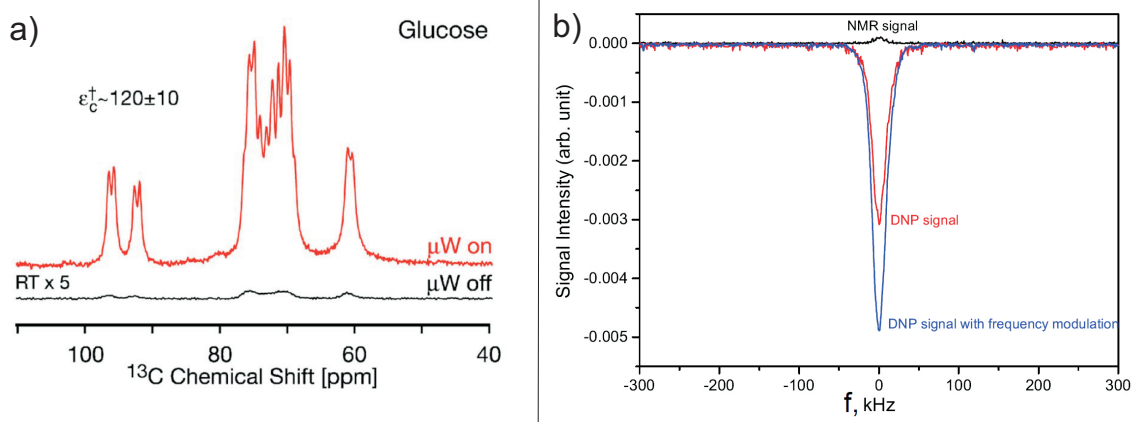


Figure 1.4: Enhancement of the NMR-signal due to the irradiation with RF and the DNP-effect. a) Black: signal without RF from gyrotron. Red: signal with gyrotron. From [16]. b) Black: signal without RF from gyrotron. Red: signal with gyrotron. Blue: Enhancement increased via frequency-modulation of gyrotron-RF. Maximum enhancement $\epsilon \approx 80$. From [17].

of great use in this application [19, 4]. This feature is important for localizing the DNP-resonance frequency without tuning the magnetic field in the NMR-magnet, as well as for characterizing the frequency-dependence of the enhancement inside the DNP-NMR resonance (right inlet in Fig. 1.3).

1.4 Principle of gyrotrons and related devices

Gyrotrons are a class of sources of coherent electromagnetic radiation with a power of $\sim 0.1\text{ W} - 2\text{ MW}$ and a frequency in the range of few GHz to 1 THz, spanning approximately the microwave-range and belonging to the category of vacuum-electronics microwave sources.

Vacuum-electronics microwave sources are based on the emission of coherent radiation by an electron beam, situated inside a vacuum tube. The concept of the emission is a synchronism between electromagnetic radiation and electron motion, meaning that the electrons move in some way synchronously with the wave. The beam-wave interaction leads to a bunching of electrons, creating an AC current density in the electron beam [20]. This bunching then generates a collective stimulated emission of radiation.

For creating the synchronism between the electrons and the electromagnetic radiation, gyrotrons exploit the orbital electron motion of gyrating electrons in an external magnetic field, meaning that a transverse field oscillates with a frequency close to the electron cyclotron frequency. Then, the synchronism condition requires

$$\omega_{\text{RF}} - k_{\parallel} v_z \approx \frac{\Omega_c}{\gamma} \quad (1.2)$$

with the angular RF-frequency ω_{RF} and axial wavenumber k_{\parallel} of the electromagnetic radiation and the electron axial velocity v_z , non-relativistic electron cyclotron frequency Ω_c and electron

relativistic factor γ .

Due to this synchronism, a bunching of the electrons in orbital motion can be created through the Electron Cyclotron Maser (ECM) instability, a relativistic effect involving the dependency of the electron cyclotron frequency on the electron energy. Due to this instability, which under some conditions will be explained later on, the orbital motion of the electrons is, on average, decelerated and the orbital kinetic energy is transferred to the wave energy.

In a gyrotron, the electromagnetic wave is supported by a smooth-wall cylindrical cavity with adiabatically changing wall-radius. In this cavity, the electrons interact with a given transverse eigenmode supported by the cylindrical wall structure. The transverse size of this cavity and the operating transverse mode determine the RF-frequency of the gyrotron.

The ECM-instability has been discovered theoretically almost simultaneously by Twiss [21], Schneider [22] and Gaponov [23, 24] in 1958/59. The first Electron Cyclotron Maser (ECM) experiment was then presented in 1964 [25] and the first gyrotrons with a setup close to modern devices have been developed in Russia in the late 1960s [26, 27]. Textbook literature describing gyrotrons and their applications can be found in [28, 29, 30].

The wave-particle interaction in a gyrotron, occurring close to the cutoff frequency of a given transverse mode, is such that the phase velocity of the excited wave is higher than the speed of light, hence, a gyrotron is often classified as a fast-wave device. This is in contrast to the class of vacuum electron devices called slow-wave devices in which the phase velocity is lower than the speed of light. In the slow-wave microwave sources, the phase-velocity of the wave is slowed down in a cavity with a periodic wall-structures. The best-known members of the slow-wave devices include magnetrons, klystrons and Traveling-Wave Tubes (TWTs). Creating the slow-wave field necessitates wall structures smaller than the wavelength and an electron beam, that passes very close to this structure. Due to the decrease of wavelength with increasing frequency, this condition strongly limits the employment of slow-wave devices for frequencies of tens of GHz and higher .

1.5 Gyrotron setup

The general setup of a gyrotron is shown in the sketch of Fig. 1.5. Inside a vacuum tube, a hollow electron beam is created by a cathode with an annular emitter. Because the cathode is located in a region with a strong magnetic field and a transverse electric field, the action of the electric field is to both impart an initial transverse velocity to the electron, but also to accelerate them along the magnetic field lines. At the same time the vacuum tube is inserted inside a magnet with a field strength of $B_0 \sim 1 - 10$ T, which forces the electrons to follow the magnetic field lines, while also gyrating in the magnetic field. Because of the adiabatically increasing magnetic field, the electrons experience magnetic compression, where their perpendicular (orbital) momentum is increased according to the conservation of the magnetic moment $p_{\perp}^2 / B_0 = \text{const}$ [29] (p_{\perp} is the perpendicular electron momentum, B_0 the magnetic field strength). The cavity resonator is located around the maximum of the magnetic field profile along the magnetic axis.

The excited electromagnetic field supported by the cavity has the transverse structure of a $\text{TE}_{m,p}$ -eigenmode.

This electromagnetic radiation exits the cavity in the same direction as the electrons. In the

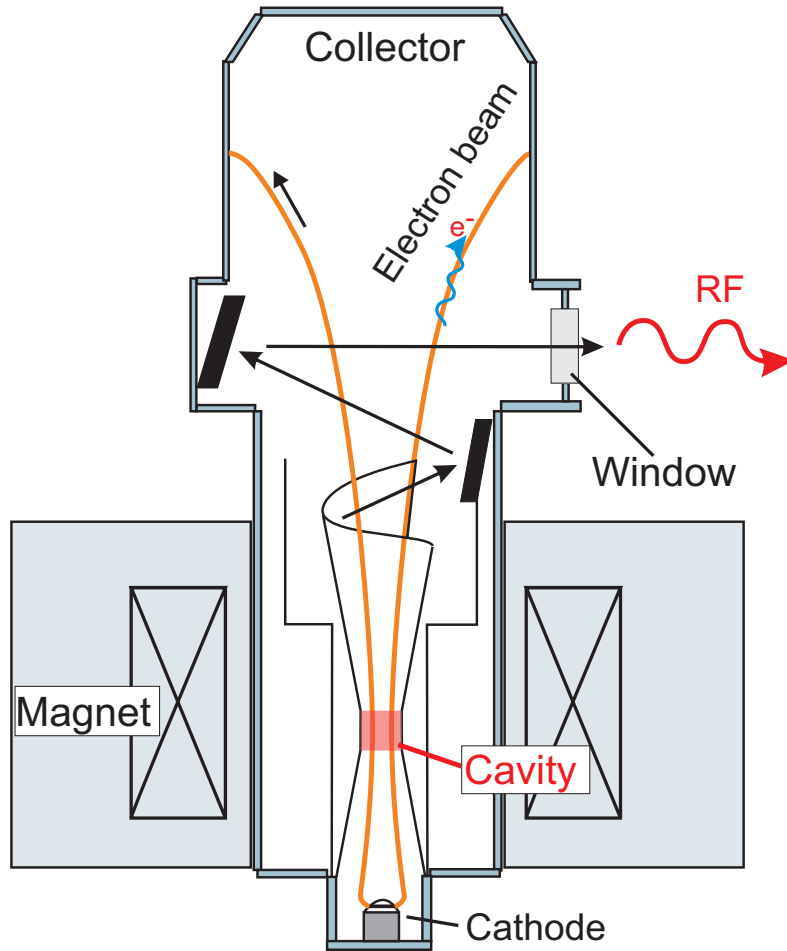


Figure 1.5: Schematic view of a gyrotron. The RF-radiation is excited in the cavity resonator shaded in red and is directed out of the window (black arrows). The circular cross-section beam of gyrating electrons from cathode to collector is shown in orange.

following cylindrical waveguide antenna, the so-called launcher, the transverse mode, which is excited in the cavity, is converted into a Gaussian-like RF-beam propagating in free space. The launcher radiates in the transverse direction (black arrow in Fig. 1.5) towards a series of mirrors, which correct the beam-shape and re-direct the microwave beam towards a low-loss vacuum window, where the RF-beam exits the device. The spent electron beam follows the field lines and is absorbed on a collector.

1.5.1 Electromagnetic properties of the cavity

The metallic-wall cavity has a circular cross-section, which imposes $TE_{m,p}$ - or $TM_{m,p}$ -transverse eigenmodes, having a field pattern with m periods in azimuthal direction and p extrema in radial

direction. In a gyrotron, the interaction of the electron beam with $TE_{m,p}$ -eigenmodes is used.

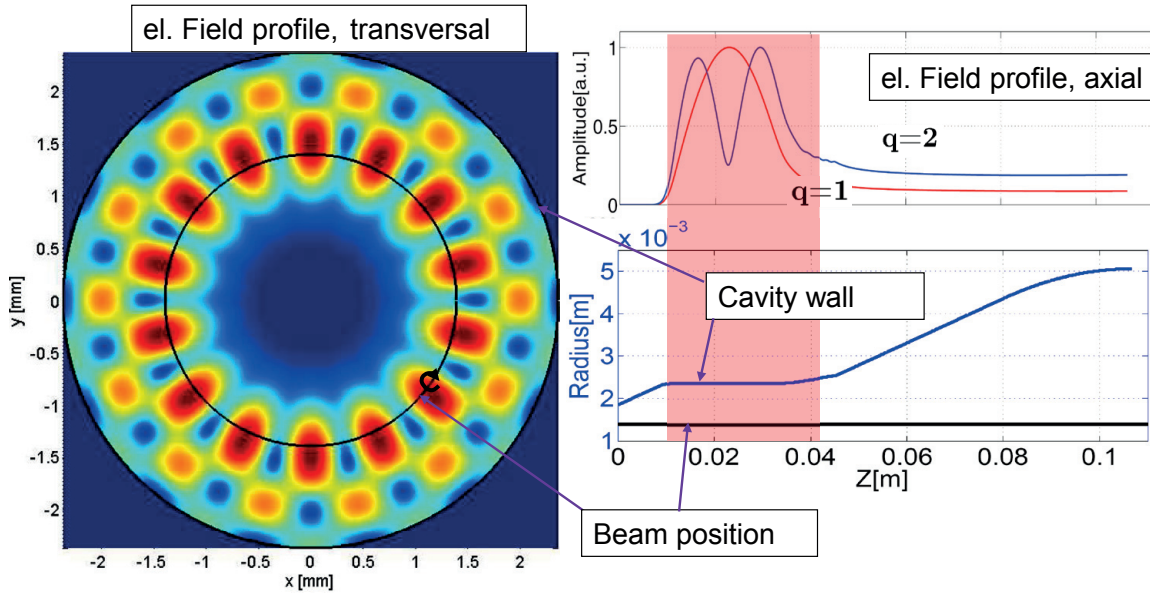


Figure 1.6: Amplitude profile of RF-electric field for $TE_{7,2,q}$ -eigenmode inside cavity structure in transverse cross-section (left) and axial direction (right, two different axial modes). In the transverse profile, the direction-independent amplitude of the field is shown as color-coding, whereas on the right, the represented field amplitude at each axial position corresponds to the maximum value of the transverse field profile at the electron guiding center radius. In the axial view, the interaction with the electron beam takes place in the cavity-region shaded in red around the region of constant wall-radius (compare setup in Fig. 1.5). The position of the electron beam is indicated in both views.

An example of the field amplitude profile of a $TE_{m,p}$ -eigenmode in the cavity-structure is presented in Fig. 1.6, showing both the transverse field structure in a cross-section and the axial profile for a cold-cavity cavity eigenmode (i.e. without electron beam). The transverse field structure (left) includes both the radial and the azimuthal RF-electric field component. The electron beam is positioned approximately at the radial position of the maximum RF-field for a most efficient interaction and has a width of a few Larmor-radii. In the axial profile of the RF-field, the shown amplitude represents the maximum amplitude at the radial position of the electron beam. For a given transverse mode $TE_{m,p}$, different axial modes exist (mode number q), of which on the right half of Fig. 1.6 the axial profiles of the two lowest-order axial modes are shown.

The transverse modes in the cavity are distinguished in positive or negative azimuthal index, which specifies the direction of rotation of the transverse mode. Referring to the electron-cyclotron motion, the modes are labeled co-rotating and counter-rotating modes (positive / negative m).

While the transverse field profile is assumed to be unchanged by the presence of the electrons

[28], the axial profile can be strongly influenced by the interaction with the electron beam.

1.6 The beam-wave interaction

In this section, the general concept of the beam-wave interaction in a gyrotron cavity is introduced.

As mentioned in section 1.4, the interaction between an annular cross-section electron beam and a self-consistently created RF-field in the cavity arises from the ECM-instability. This instability, also called 'negative mass instability', is manifested by a bunching of the electrons in their gyro-phase, which is the azimuthal phase of their cyclotron motion. The mechanism of this bunching and the resulting conversion of orbital kinetic energy to wave energy will be explained in the following.

The bunching effect is illustrated in Fig. 1.7, showing the rotating electron orbital velocity and

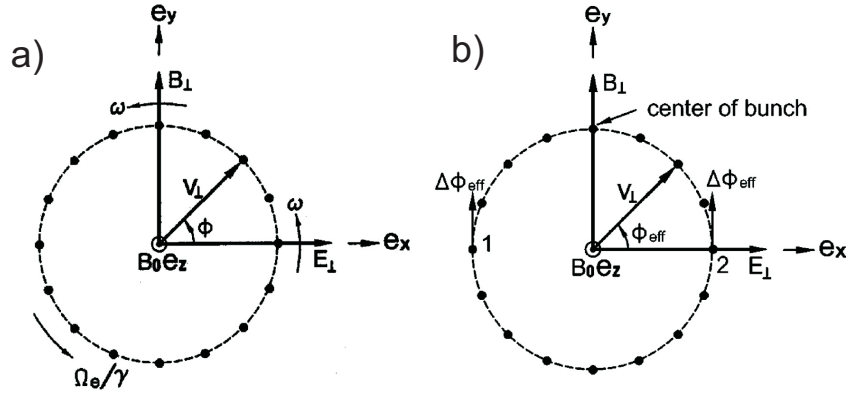


Figure 1.7: a) Snapshot of electrons and RF-field in electron velocity-space. The electron velocity rotates with approximately the same angular frequency as the oscillation of the RF-electric field vector (ω for field at electron position, Ω_c/γ for electrons). b) Concept of snapshots at integer multiple of field period. In this view, the field direction stays fixed and the bunch forms at the top of the graph. From: [20].

the oscillating RF-electric field. The graph shows the field experienced by the electrons, which oscillates at an angular frequency $\omega = \omega_{\text{RF}} - k_{\parallel} v_z$.

If the orbital velocity of the electrons is resonant with the RF-field, $\frac{\Omega_c}{\gamma} = \omega$, the electric field is for half of the electrons always in the same direction as the velocity, while for the other half it is always opposed to the motion. This means that half of the electrons are decelerated and the other half accelerated.

For a better view of the gyro-phase with respect to the field of the electric field phase, Fig. 1.7b) introduces the concept of snapshots taken at integer multiples of the field period. Here, the electric field always stays in the same direction and the electron gyro-phase Φ has been replaced by the slow effective phase, which is the phase-difference between electrons and field. Here, the electrons which are accelerated are on the left half and those decelerated on the right.

The accelerated electrons increase in their relativistic factor and thus decrease in electron cyclotron frequency, $\frac{\Omega_c}{\gamma}$, whereas the frequency of the decelerated electrons increases. This leads to a slower gyration in the left half of Fig. 1.7b) and a faster rotation in the right half, so that both in the left half and in the right half, electrons move towards the positive \mathbf{e}_y -axis. This leads to a bunching of the electrons at this position.

With an exact resonance, $\frac{\Omega_c}{\gamma} = \omega$, the bunching process itself does not yet effectively extract energy from the electrons, since half of the electrons gain energy, while the other half loses energy. Additionally, the RF-frequency is required to be slightly larger than the electron cyclotron frequency. This way, the bunch dephases with respect to the electric field and moves as a whole into the decelerating phase (right half in Fig. 1.7b)). Because then the majority of the electrons are gathered for some time in the gyro-phase where they lose energy, a large fraction of the electron orbital kinetic energy is converted into RF-field energy.

The entire bunching mechanism, including the non-linear phase of the interaction, is illus-

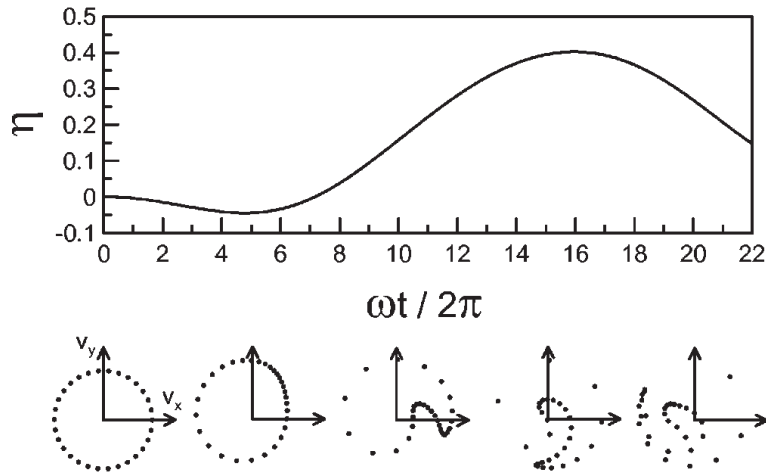


Figure 1.8: Typical interaction efficiency and snapshots of the bunching process as a function of the field phase ωt , following the electrons along their trajectory. The snapshots are taken at integer multiples of the field phase, so that the field direction is always in \mathbf{e}_x -direction. A detuning between field frequency and gyration-frequency makes the bunch gather in the decelerating phase. From: [20].

trated in Fig. 1.8. The figure shows the interaction efficiency (fraction of orbital kinetic energy converted to RF-energy) and velocity-space snapshots (as in Fig. 1.7b)) for electrons along the interaction region. In the second snapshot of the electron phase space, it is observed, how the electrons bunch towards the v_y -axis, but a detuning between wave frequency and gyro-motion makes the bunch move to the decelerating phase (to positive v_x).

The resulting energy extraction continues, until a significant fraction of the bunch moves back into accelerating phase section, which happens in the fourth snapshot. At this point, the efficiency is at its maximum and generally gyrotron cavities are designed in such a way, that at this point the interaction is interrupted, because the advancing electrons reach the uptaper-region. Here, the parallel wavenumber k_{\parallel} changes due to the changing wall radius, so that the (approx-

imate) resonance between field and electron-gyration is lost ($\omega_{\text{RF}} - k_{\parallel} v_z \neq \frac{\Omega_c}{\gamma}$). If however the interaction continues as in Fig. 1.8, a so-called overbunching occurs, in which a large fraction of the electrons move back to the accelerating phase section, where they gain back a part of the previously lost energy. This then leads to a decreased interaction efficiency, as it is observed in the top-half of Fig. 1.8.

The most fundamental equations that describe the interaction are the electron equations of motion with the Lorentz-force together with the wave-equation, derived from Maxwell's equations and including a source term:

$$\text{Eqs. of motion:} \quad \frac{d\mathbf{p}_j}{dt} = -e(\mathbf{E} + \mathbf{v}_j \times (\mathbf{B}_0 + \mathbf{B})) \quad (1.3a)$$

$$\text{Wave equation:} \quad \frac{1}{c^2} \frac{\partial^2 \mathbf{E}}{\partial t^2} - \nabla^2 \mathbf{E} = -\mu_0 \frac{\partial \mathbf{J}}{\partial t} - \frac{1}{\epsilon_0} \nabla \rho_e. \quad (1.3b)$$

Here, \mathbf{p}_j , \mathbf{v}_j and e are the momentum, velocity and charge of an individual electron, \mathbf{E} and \mathbf{B} are the wave electric and magnetic field, \mathbf{B}_0 the external magnetic field and c , μ_0 and ϵ_0 are the vacuum speed of light, permeability and permittivity respectively. The current density \mathbf{J} and charge density ρ_e are defined as:

$$\mathbf{J} = \sum_j -e \cdot \mathbf{v}_j \cdot \delta(\mathbf{r} - \mathbf{r}_j) \quad (1.4a)$$

$$\rho_e = \sum_j -e \cdot \delta(\mathbf{r} - \mathbf{r}_j). \quad (1.4b)$$

The RF-electric and magnetic fields in Eqs. (1.3) act as a force on the electron motion in the right hand side (r.h.s.) of the equations of motion. The electrons for their part act on the fields via the source term (r.h.s.) in the wave equation.

The profile, frequency and power of the RF-field are determined by Eqs. (1.3)-(1.4), subject to the appropriate boundary conditions of the field in the interaction region. An example of the eigenmodes, that result from the transverse and axial boundary-conditions in the wave-equation was shown in Fig. 1.6, where no coupling to the electron beam was included.

In the description above, it was mentioned that an efficient bunching of the electrons in the decelerating phase requires an RF-frequency which is very close to resonance with the cyclotron frequency. This resonance can be illustrated with the uncoupled dispersion relations of the electron beam-mode and of the RF-field in a circular cross-section waveguide, shown on an example in Fig. 1.9. Here the uncoupled dispersion relations of the beam and circular cross-section waveguide are described by [28]

$$\omega_{\text{beam}} = \frac{\Omega_c}{\gamma} + v_z k_{\parallel} \quad (1.5a)$$

$$\omega_{\text{cavity}} = \sqrt{\omega_{\text{co}}^2 + (c k_{\parallel})^2}, \quad (1.5b)$$

where ω_{co} is the cutoff angular frequency of the waveguide for the considered $\text{TE}_{m,p}$ -mode for the mode of interest.

In this representation, an intersection of the two dispersion relations shows, that the electron

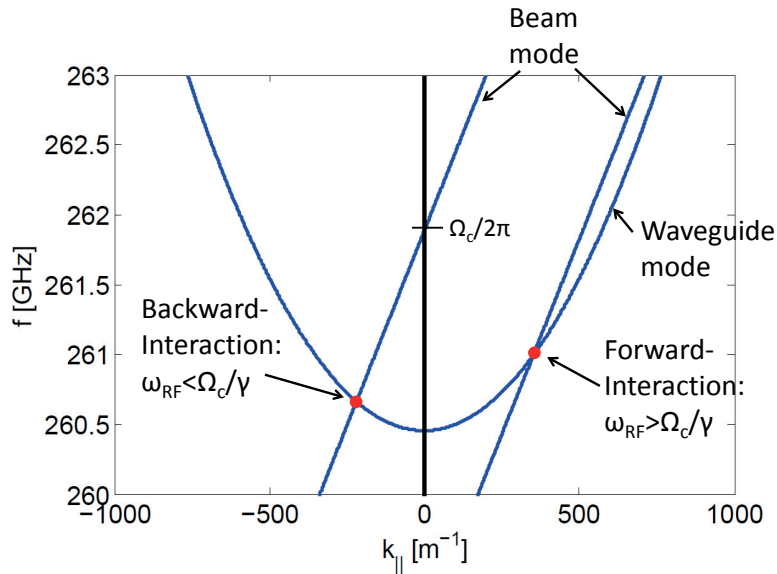


Figure 1.9: Uncoupled dispersion relations (frequency versus parallel wavenumber) for electron beam (two examples with different cyclotron frequencies) and of cylindrical waveguide TE-mode. An intersection of the dispersion relations (red points) shows a synchronism between wave and particle with possible interaction. An interaction with an intersection at positive wavenumbers is called forward-interaction and occurs for $\omega_{\text{RF}} > \Omega_c/\gamma$ while backward interaction means $k_{\parallel} < 0$ and $\omega_{\text{RF}} < \Omega_c/\gamma$.

gyration is in synchronism with the cavity-eigenmode and that thus a resonant interaction can lead to an instability.

If the interaction occurs with the RF-frequency exceeding the cyclotron frequency, i.e. $\omega_{\text{RF}} > \Omega_c/\gamma$, the intersection occurs at positive wavenumbers and the interaction occurs mainly with the forward-component of the RF-field [31], so that this is called the forward-regime. In the backward-regime, with $\omega_{\text{RF}} < \Omega_c/\gamma$, the electrons interact mainly with the backward-propagating component of the RF-field. As it will be described in the following chapters, the behavior between the forward- and backward regime is fundamentally different. The highest power and the operating points of high-power gyrotrons are located in the forward-region, whilst a large frequency-tuning is obtained in the backward-region [29]. The backward-interaction interaction is exploited in gyro-Backward-Wave Oscillators (BWOs), where the radiated RF is usually extracted in the direction towards the cathode.

If the condition of beam-wave synchronism is fulfilled, one does not necessarily observe an instability with emitted RF-power. For a given interaction structure and operating parameters, the power provided by the electron beam for RF-excitation has to exceed a certain threshold for achieving the excitation of the operating mode with RF-emission [20]. This threshold is expressed in the form of a minimum current, the starting current.

The starting current can be calculated using a linear theory, which treats the beam-wave interaction in the limit of small RF-field amplitude and which describes the initial start-up phase of

the interaction. In the general case however, the interaction is strongly non-linear and the gyrotron operates in a saturated interaction. For complete picture of this non-linear self-consistent interaction, numerical modeling is necessary.

1.7 Challenges in modern gyrotron development

1.7.1 High-power gyrotrons for plasma heating

Because the gyrotron development since its beginning is mainly aimed at producing gyrotrons with high power and efficiencies for plasma-heating, it is necessary to introduce in this section shortly the challenges and developments of this type of gyrotrons.

When achieving the high RF-powers and efficiencies required in plasma-heating, one has to take measures to keep the density of Ohmic losses dissipated in the cavity wall at an acceptable level for the available cooling techniques, which is typically $< 2 \text{ kW/cm}^2$ [32]. The reduction of the density of Ohmic losses is achieved by the use of large oversized cavities with high-order transverse operating modes. This is made possible by a precise mode-selection through cavity design and gyrotron control [27].

An implication of the higher and higher transverse mode numbers is a more and more complicated suppression of unwanted transverse modes [33, 34, 35], because the number of possible competing modes is strongly increased. At the same time, also the development of mode converters [36] and of the high-power handling, e.g. in the collector becomes more complicated. Presently, Megawatt-power levels $P_{\text{RF}} \geq 1 \text{ MW}$ in pulses of seconds to continuous wave (CW)-operation have been achieved in a series of gyrotrons [37, 38, 39, 40, 41]. The highest power to date $P_{\text{RF}} = 2.3 \text{ MW}$ [42] has been achieved in short pulses in a coaxial gyrotron developed by the European Gyrotron Consortium (EGYC).

To achieve the operation with highest possible efficiency, high-power gyrotrons can be operated in the hard-excitation region, an operating region in the forward-regime, where due to a hysteresis-effect the oscillation can only be sustained, if it is accessed already with a sufficient power.

The gyrotron efficiency could be increased to $\gtrsim 50\%$ by the use of a depressed collector, which reduces the remaining energy after the interaction in a voltage depression [43, 42, 44, 38]. Additionally, for obtaining a higher flexibility for plasma heating, the state-of-the-art development are multi-frequency gyrotrons, that can operate at several operating transverse modes for achieving high power at several ECRH-relevant frequencies [43, 45, 46].

1.7.2 Frequency-tunability

In gyrotrons, two kinds of frequency-tunability exist, step-wise and continuous frequency-tunability. Step-wise frequency tunability is achieved by changing the operating transverse mode in the cavity. This way, the frequency changes in discrete steps of the order of several GHz between the transverse modes. This step-tunability can achieve a very wide range, of $> 100 \text{ GHz}$ [46, 47]. For continuous frequency-tuning however, the frequency is tuned while remaining on the same operating mode by changing the operating parameters. This kind of frequency-tuning is nec-

essary for an application of the gyrotron in spectroscopy, as it is the case for the DNP-gyrotron in this thesis, because there a certain frequency-range is scanned for identifying generally narrow resonances. The tuning in a single transverse mode requires a relatively low-order transverse mode for having less/no competing transverse modes, and allows a change of the frequency over $\sim 1 - 2$ GHz.

For both methods of frequency-tuning, the cavity magnetic field, the electron energy or the electron pitch-angle (ratio of perpendicular to parallel velocity) can be adjusted [48].

1.7.3 Non-stationary oscillation in gyrotrons

In the common gyrotron interaction, the beam-wave interaction occurs in a saturated state, for which the radiated power is constant in time and the RF-spectrum is mono-frequency. However, it was found, that for certain operating parameters, the interaction changes from this stationary operating regime to a non-stationary regime, characterized by a multi-frequency or broadband RF-spectrum with a bandwidth of typically less than 3 GHz and a power which fluctuates in time. The typical dominant timescale of this fluctuation is of the order of nanoseconds. As it will be explained in chapter 5, such a non-stationary regime has been observed in the DNP-gyrotron described here.

Non-stationary oscillations in gyrotrons have been described for the first time in detail in the late 1980's [49, 50, 51]. Since then, this phenomenon has been the subject of many publications [29, 20], both in gyrotrons and in devices with a similar interaction mechanism. It has been observed, that the non-stationary regime includes both a self-modulation regime, where additional discrete frequencies appear in the RF-spectrum, and a chaotic regime where the spectrum obtains a broadband-component.

Experimental studies of the non-stationary regime in ordinary gyrotrons are few and little detailed (e.g. [52]), whereas a larger number of simulation studies was performed. It will be shown in this thesis, that many of these studies used a model with a questionable validity.

In many of the simulation studies, also an attempt was presented for explaining the basic mechanism of non-stationary interaction. However, no agreement could be found to date for the reason of the excitation of non-stationary oscillations.

This lack of general understanding of non-stationary oscillations was the motivation for a detailed study of this phenomenon in this thesis.

A better understanding of non-stationary oscillations would be of importance especially for the development and operation of continuously frequency-tunable gyrotrons. In these devices, avoiding non-stationary oscillations can be a limiting factor for the tunability [53]. Furthermore, the non-stationary oscillation might also have applications on its own. One possibility would be the use of RF-pulses with a well-defined pulse width, repetition rate and frequency for ESR-spectroscopy [6].

1.8 Goal of the thesis

The goal of this thesis is to increase the understanding of the gyrotron beam-wave interaction on a single transverse mode. For this, the operation of the DNP-gyrotron is characterized and

attempted to be explained, covering all the appearing operating regimes. This is achieved by comparing the results of a detailed experimental characterization with modeling. In order to achieve this, new modeling tools had to be developed within the frame of this thesis.

The most important aspect of beam-wave interaction that is investigated in this thesis is the non-stationary oscillation. The lack of understanding of this phenomenon, combined with its importance e.g. for achieving frequency-tunability within a single transverse mode, was the motivation to pursue a detailed analysis of this regime.

The ultimate goal of this investigation would be to obtain a complete understanding of all aspects of non-stationary oscillation, which would allow to predict the operating parameters where it appears for any gyrotron and which would possibly allow to tune the non-stationary oscillation such as to make the RF compatible with possible applications.

The first step in this direction, which is presented in this thesis, is to for the first time characterize all the details of the non-stationary regime. A second step, which is also attempted in this thesis, is explaining the mechanism and origin of the details of non-stationary oscillation, that have been described in the characterization. This is performed with theory and modeling.

With these two steps being for the first presented in this thesis, an important step towards a complete understanding of non-stationary oscillations is presented in this thesis.

1.9 Outline of the thesis

A brief introduction to gyrotrons with their background, concept and applications was presented. The scientific background and technological challenges, which are relevant for the DNP-gyrotron, were discussed.

- In chapter 2, the experimental setup of the DNP-gyrotron is presented. The design parameters and the composition of the gyrotron is presented with its sub-components and operating parameters. Its present integration and configuration for DNP-experiments are described, as well as the RF-diagnostics.
- Chapter 3 introduces the relevant models and simulation codes. In the course of this thesis, a significant progress has been accomplished in the modelling of the gyrotron beam-wave interaction. These advancements are based on the code TWANG and its basic model, which will be described first. Thereafter, the newly developed model and code TWANG-PIC is introduced, that allows an appropriate modeling of non-stationary oscillations. Furthermore, the new linear self-consistent model of TWANGLIN is described, which includes most of the spatial inhomogeneities of a real experiment and therefore allows direct interpretation of experimental data.
- Chapter 4 characterizes the behavior of the DNP-gyrotron in the stationary regime. It is described, how this regime has been optimized for the DNP-application. The experimental characterization of the starting current, a fast and slow RF-frequency tuning and the achievable RF-power are shown, as well as their analysis with simulations. Furthermore, the stability of RF-parameters and a pulsed operation are presented in view of the DNP-application.

- In chapter 5 the non-stationary operating regime is introduced and characterized in detail, including many novelties. The observed types of non-stationary oscillations sorted into major categories, of which the chaotic regime and the sideband regime are analyzed in depth. It will be shown, that simulations with the new code, that is appropriate to non-stationary oscillations, can reproduce the main dependencies and results and especially that they allow an interpretation and explanation for important characteristics of the non-stationary regime. The source of the non-stationary oscillations will be shown to be closely related to a competition between different modes with different axial profiles of the RF-field.
- Finally, chapter 6 summarizes the main results and conclusions of the document.

The variables are generally introduced, where they appear first in the document, but a summary of all the symbols for quantities, parameters and constants can also be found in Appendix B.

Chapter 2

Experimental Setup

2.1 Design and setup of the DNP-NMR gyrotron

The gyrotron prototype used in the frame of this thesis was designed at SPC whereas its manufacturing was carried out by the French company Thales Electron Devices. The purpose of the gyrotron - DNP-enhanced NMR spectroscopy - defined its design parameters.

An important feature of the gyrotron design is its modular concept, allowing an exchange of certain sub-elements, simplified by the use of high temperature bakable vacuum CF-flanges. For instance, an exchange of the cavity and mode-converter would allow the adaption of the tube frequency for a use on other NMR spectrometers.

In its present configuration, it was designed to be integrated into an existing 400 MHz NMR-spectrometer operated at Laboratoire de Physique des Matériaux Nanostructurés (LPMN) at École Polytechnique Fédérale de Lausanne (EPFL). This task led to the design specification of the RF-parameters listed in table 2.1 [54].

A 3D-cut of the gyrotron inserted in the superconducting magnet is shown in Fig. 2.1, and its

Nominal frequency	263.64 GHz
Frequency tuning	> 800 MHz
Line width	< 1 MHz
Long term stability	< 20 MHz / 8 h
Output power	> 10 W
Output power stability	< 0.5 %
Operation type	CW
Output mode	Gaussian
RF-output	lateral

Table 2.1: Design specifications of the DNP-gyrotron.

sub-assemblies will be described in the following (see also [55, 56]).

The gyrotron tube is inserted into a 10T liquid Helium-free **superconducting magnet** with a warm-bore diameter of 75mm, manufactured by Cryogenic Ltd. (London,UK). It consists of a liquid He-free cryostat [57] with a nominal operating temperature of the NbTi superconducting

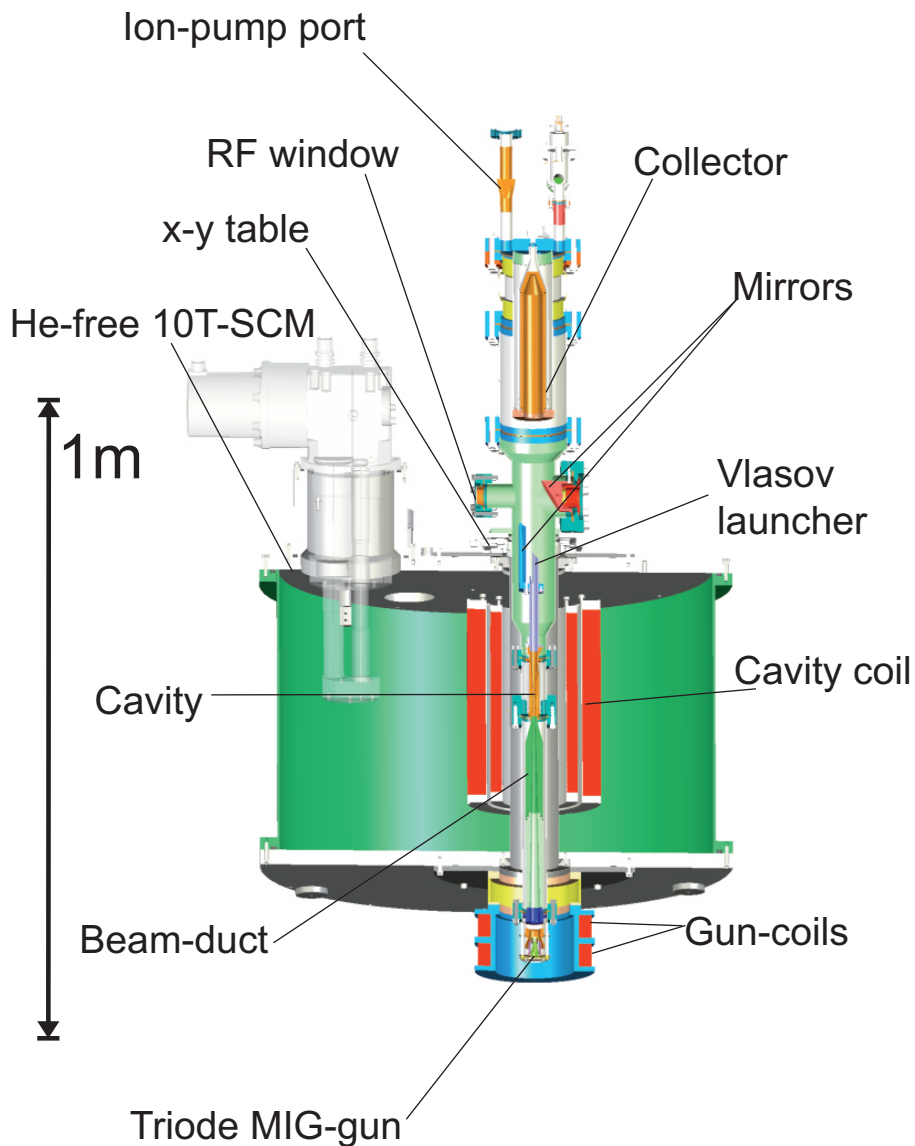


Figure 2.1: Schematic view of gyrotron setup with the main components. The approximate size is shown by the scale on the left.

solenoid at 3.7 K. In the region of the cathode, an additional control of the magnetic field and its derivative along the gyrotron axis is made possible by two uncooled copper **gun coils**. Inside the warm-bore of the magnet, the gyrotron position can be optimized by moving the entire gyrotron tube with the help of an **x-y alignment table**, on which the tube is mounted. The position in both directions can be adjusted precisely with the help of micrometer-screws. The initial setup of the tube was greatly eased by this design feature, which allowed a simple opti-

2.1. DESIGN AND SETUP OF THE DNP-NMR GYROTRON

mization of gyrotron power by fine tuning the x - y position.

The choice of the operating mode, made possible by the relatively low RF-power requirements, was driven by the fact that a single $TE_{m,p}$ -mode should be excited over the entire frequency tuning range 800MHz, to avoid frequency jumps. Therefore, the density of transverse modes in frequency has to be small enough, such to avoid transverse mode competition with neighboring modes when the required frequency-tuning is obtained via a magnetic field tuning. Thus, the relatively **low-order transverse mode** $TE_{7,2}$ is used. The resulting density of TE-modes in frequency is shown in Fig. 2.2. One observes, that the next mode with a higher frequency, that might interfere in the frequency-tuning, is the counter-rotating mode $TE_{-2,4}$ (field azimuthally counter-rotating w.r.t. electron gyration) at 265.4GHz.

A direct consequence of the combined high-frequency and low-order mode of operation is that

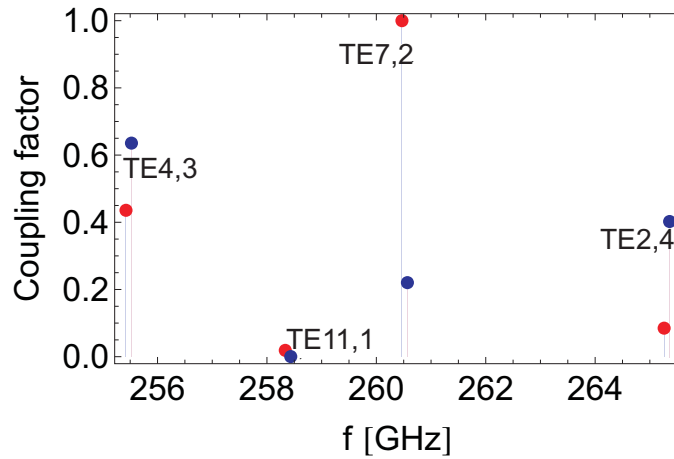


Figure 2.2: Density of transverse modes in frequency and their coupling factors for the DNP-gyrotron. The red and blue dots correspond to co- and counter-rotating modes respectively, which are separated only for clarity.

the fraction of Ohmic losses in the cavity to the output power is large (of the order of 1) [55]. This is however not a concern since the tube efficiency is not an issue and the total amount of Ohmic losses to be dissipated remains small (<200 W), while their density on the wall is below 100 W/cm².

The gyrotron design includes a **triode-magnetron injection gun (MIG)**, shown in the schematic of Fig. 2.3 with the corresponding reference voltages and an example of the beam propagation. In a triode configuration (as opposed to a diode configuration widely used in gyrotrons), the electric field at the cathode emitter-surface can be changed by an independent voltage-control of both anode and cathode, both referenced to ground. The control of the anode-voltage allows an independent adjustment of the electron pitch-angle over a wide range, as well as a fast frequency-tuning and a pulsed operation. The independently controlled anode also allows a precise determination of the threshold for appearance of reflected electrons. Furthermore, the triode MIG gun design gives also sufficient flexibility for a possible operation at the second harmonic instead of the fundamental of the cyclotron frequency.

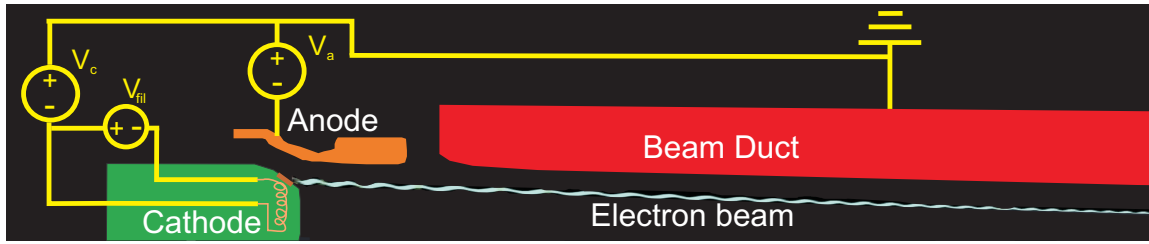


Figure 2.3: Schematic view of the triode-Magnetron Injection Gun (MIG) with an example of beam propagation and the applied voltages. V_{fil} defines the voltage driving the filament current I_{fil} for heating the cathode emitter, V_c is the cathode voltage and V_a the anode-voltage.

The used **emitter** is of an S-type [55] with an average radius of 8 mm, 1 mm thickness and an angle (with respect to the z -axis) of 25° . The cathode is operated in the so-called temperature-limited regime. A heater filament, embedded below the emitter surface, is used to reach the working temperature. The voltage of the cathode is set using a TECHNIX **High-Voltage Power Supply (HVPS)** (Model: SR-20-F-3000, 0 - 20kV / 0 - 150mA) whereas for the anode voltage a TREK High-Voltage amplifier has been used (Model: 20/20C-H-CE-EX ± 20 kV, ± 20 mA, slew-rate > 350 V/ μ s).

The **beam-duct** (i.e. the drift region between the cathode and the cavity) is made of stainless steel. In order to minimize the possible growth of unwanted oscillation that could be detrimental to the operation of the tube, the last section before the cavity entrance is machined on its internal surface such to obtain a random surface with an equivalent surface roughness of approximately $\lambda/8$ where λ is the free-space wavelength at 260 GHz.

The **cavity** and adjacent uptapers have been manufactured with a technique based on electro-deposition of copper on an aluminum mandrel. The copper conductivity considered in the numerical simulations is 1/2 of the ideal copper conductivity $\sigma_{Cu} = 5.8 \cdot 10^7$ S/m, to account for the surface roughness and temperature effects. An active water cooling coaxial jacket surrounds the cavity with a nominal flow of 5 l/min.

During the gyrotron characterization, a frequency of $f_{RF} = 260.5$ GHz was measured at the optimum operating point. The 3.1 GHz difference with respect to the design frequency of 263.6 GHz is attributed to a $30 \mu\text{m}$ deviation in cavity wall radius during the manufacturing process.

The **Vlasov launcher** and the two following **mirrors** are made of Oxygen-Free High thermal conductivity Copper (OFHC). The Vlasov launcher has been designed for the nominal operating $TE_{7,2}$ co-rotating mode. The neighboring possible TE-modes have significantly different caustic radii and therefore exhibit a poor coupling to the $TEM_{0,0}$ free-space Gaussian mode [58].

The **sapphire window** was designed to have minimum losses at the frequency of 263.5 GHz and has a thickness of $4\lambda/2 = 0.74$ mm, where λ is the wavelength in the sapphire at this frequency (Relative permittivity $\epsilon_r = 9.394$, loss tangent $\tan \delta = 4.5 \cdot 10^{-4}$) [55]. At the measured frequency of 260.5 GHz, the power reflection and absorption coefficients are 3.7% and 1%, respectively. For minimizing the possible reflection back to the cavity, the window has been mounted with a 1.5° tilt with respect to the CF-flange-normal on which the window is brazed.

The **collector** is electrically isolated via an insulation ceramic at the connecting flange and is water cooled with a nominal flow of 10 l/min. The electrical isolation permits to have a mea-

surement of the collector current, which is very useful for verifying the full transmission of the electron beam from cathode to collector. Moreover, the isolated collector could allow the gyrotron to be operated in a depressed collector configuration. A 2l/min **ion vacuum pump** is connected to the gyrotron tube at the collector and allows a monitoring of the gyrotron vacuum.

2.1.1 Cavity geometry and RF-properties

The wall profile of the interaction structure (cylindrical cavity resonator and subsequent uptaper) of the gyrotron is shown in Fig. 2.4, together with a profile of the external magnetic field.

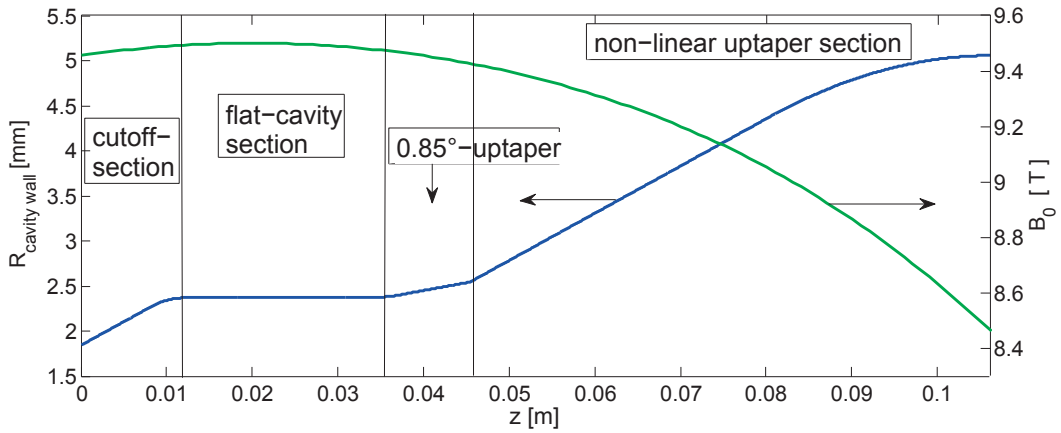


Figure 2.4: Axial profile of cavity wall radius (blue) and of magnetic field B_0 (green).

The constant-radius section has a length of $L = 22$ mm. This represents a relatively long cavity-length, since it leads to a normalized interaction length $\hat{\mu} = 22$ (discussed in section 2.1.3) and a Fresnel-parameter $C_F = 19$, following the descriptions in [59, 60] and [61] respectively, which is higher than the typical values for high-power gyrotrons mentioned therein. Including the above-mentioned $30 \mu\text{m}$ -deviation of the cavity-wall radius, the cavity wall radius in the constant-radius section is $R_w = 2.3691$ mm. This leads to a cutoff frequency for the $\text{TE}_{7,2}$ mode in the constant-radius section of $f_{co} = 260.45$ GHz.

The after-cavity uptaper starts with a 10 mm section having a small uptaper-angle of 0.85° , followed by a non-linear uptaper section which ends in an output waveguide radius $R_w = 5$ mm.

For this cavity profile, the cold-cavity eigenfrequencies for the first three axial modes are listed in table 2.2 together with their diffractive and total quality factors (in cold-cavity approximation: $Q_{\text{tot}} = \frac{\omega_{\text{cold}}}{2\omega_i}$ and $Q_{\text{tot}} = \frac{1}{Q_{\text{diff}}^{-1} + Q_{\text{ohm}}^{-1}}$, where $Q_{\text{ohm}} = \frac{R_w}{\delta_{\text{sk}}} \left(1 - \frac{m^2}{v_{mp}^2}\right)$, ω_{cold} and ω_i the real and imaginary part of the cold-cavity angular frequency, R_w the flat-section wall radius, δ_{sk} the skin depth, m the azimuthal mode number, v_{mp} the p^{th} zero of Bessel-derivative $J'_m(x)$). The quality factors underline the fact, that for the operating mode $\text{TE}_{7,2}$, the Ohmic losses in the $q=1$ -axial mode are equivalent to the diffractive output. For the higher order axial modes, the ratio of Ohmic losses to the diffraction output is much smaller.

$TE_{7,2,q}$	f_{cold} [GHz]: $\sigma = \infty / \sigma = 2.9 \cdot 10^7 \text{ S/m}$	$Q_{\text{diff}}/Q_{\text{tot}}$
1	260.521 / 260.507	11860 / 5160
2	260.713 / 260.699	2950 / 2230
3	261.034 / 261.020	1310 / 1150

Table 2.2: Cold cavity frequencies and quality factors of the first 3 axial modes ($q=1-3$) of the nominal transverse mode $TE_{7,2}$ both with and without Ohmic losses. A copper conductivity, $\sigma = \sigma_{\text{Cu}}/2 = 2.9 \cdot 10^7 \text{ S/m}$ corresponding to half of the ideal conductivity has been considered for calculating the Ohmic losses.

2.1.2 Operating parameters

The attainable region of operating points where the $TE_{7,2}$ -mode is excited is determined by the above-described cavity-design and by the limitations of the auxiliaries. A summary of this region of operating points is shown in table 2.3, giving the typical range of operating parameters used in experiment.

A change of the RF-characteristics is performed by tuning these parameters, where the beam-

Transverse mode	$TE_{7,2}$	co-rotating
Magnetic field	B_0	9.49 – 9.70 T
Beam current	I_b	< 120 mA
Cathode voltage	V_c	15.5 kV
Anode voltage	V_a	7.8 – 11 kV
Electron pitch-angle	α	1 – 2.5
Guiding center radius	R_g	1.394 mm

Table 2.3: Experimental operating parameters in the usual operating region of the DNP-gyrotron. R_g and α are derived quantities, that are controlled mainly by the anode-voltage and the current in the gun coils.

current is controlled indirectly via the cathode heating current. Here, V_c and V_a are in fact negative voltages referred to ground, but throughout this manuscript they will be defined by their absolute value.

When comparing experimental results with simulations, the best fit is obtained, when a systematic shift in the magnetic field of $\Delta B_0 = 0.05 \text{ T}$ is considered ($B_{0,\text{sim}} = B_{0,\text{exp}} + \Delta B_0$) between the value in simulations, $B_{0,\text{sim}}$, and the one in experiment, $B_{0,\text{exp}}$. Since this shift is observed consistently for all simulations, it is concluded that the true magnetic field corresponds to $B_{0,\text{sim}}$, so that the offset $\Delta B_0 = 0.05 \text{ T}$ has been added to the experimental magnetic field value in all experimental results throughout this document.

In table 2.3, the pitch-angle and guiding center radius are mainly controlled by the anode-voltage and the two gun coil currents. The values of these quantities at the entrance of the interaction region are necessary input parameters for simulations of the beam-wave interaction and are calculated using the electron-optics code DAPHNE [62].

The pitch-angle and its spread (root mean square (RMS) of individual pitch-angles) from these

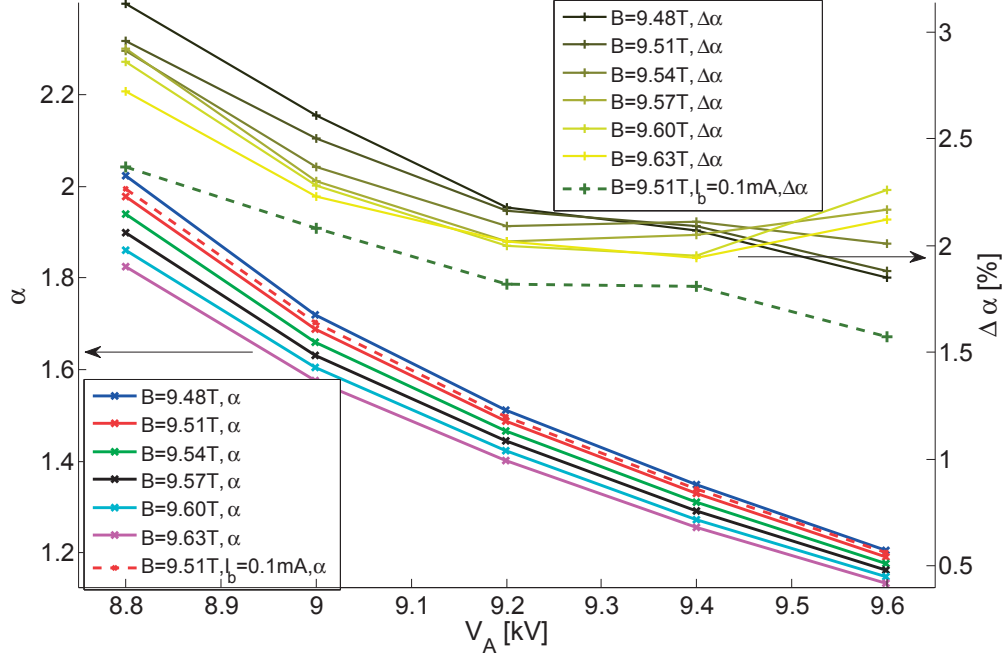


Figure 2.5: Average pitch-angle α and relative spread $\Delta\alpha$ versus the anode voltage V_a for different cavity magnetic field values, cold-cavity values from DAPHNE. Note that α is decreased by increasing V_a . Beam-current $I_b = 100$ mA (unless indicated differently), for other parameters see table 2.3. Here, the gun-coil currents $I_{gc,top} = -1$ A for the top coil and $I_{gc,bot} = -2$ A for the bottom coil were used.

simulations are shown in Fig. 2.5, using the operating parameters of table 2.3. Here it should be mentioned that in the DAPHNE-results shown in [55] a mistake in the gun-coil currents was identified and corrected in the results shown in Fig. 2.5. The results show that the pitch-angle is essentially controlled by the anode voltage with a weak dependence on the cavity magnetic field. Furthermore, it shows, that the operating pitch-angle in this DNP-gyrotron can be high in comparison with common values in fusion gyrotrons (typically $\alpha = 1.0 - 1.5$), but also compared to other low-power gyrotrons.

Also the additional magnetic field of the gun coils has a strong influence on the pitch-angle. This is illustrated in Fig. 2.6, which shows the average pitch-angle and its spread as a function of the gun coil current. In all results shown in this manuscript, the gun coil currents were chosen as $I_{gc,top} = -1$ A and $I_{gc,bot} = -2$ A.

In addition to the pitch-angle, the DAPHNE-simulations also determine the electron guiding center radius in the cavity R_g (see table 2.3) and the relativistic factor of the electrons at the cavity entry γ_0 . This value can be different from the value obtained from the cathode-voltage because of space-charge effects. In this gyrotron however, this influence is negligible, so that the cathode-voltage can be directly used as beam-voltage $V_b \approx V_c$.

The operating parameters that have to be used in experiment are also strongly determined by

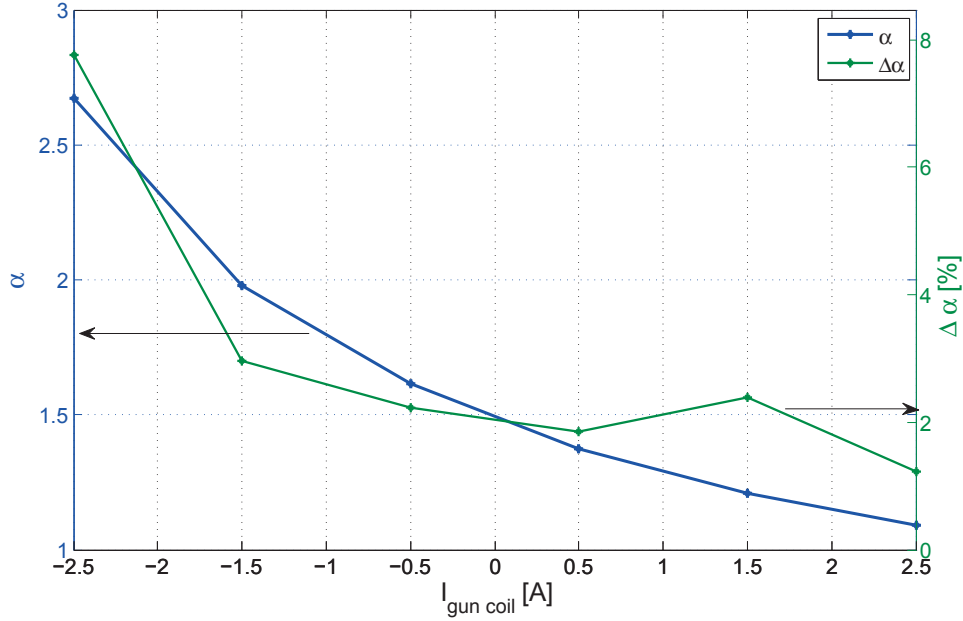


Figure 2.6: Average pitch-angle α (blue) and relative spread (green) versus gun coil currents. $I_{\text{gun coil}}$ in the x -axis shows the average of the two gun coils for a fixed difference $I_{\text{gc,top}} - I_{\text{gc,bot}} = 1A$, cold-cavity values from DAPHNE. Generally, in this document the operating point with the average value $I_{\text{gc}} = -1.5A$ was used. $V_a = 8.8 kV$, $B_0 = 9.51 T$, $I_b = 100 mA$, for other parameters see table 2.3.

the starting current of the operating mode. During the design phase, the starting current curves have been calculated using a non-self consistent model based on a fixed-field profile [28], which gives a rough idea of the available operating region. Results of this non-self-consistent calculation are presented in Fig. 2.7, showing the starting current of different axial modes, determined using their cold-cavity field profiles. Here, the top x -axis shows the normalized detuning Δ_0 between the cold-cavity frequency and the electron-cyclotron frequency, whereas the right y -axis shows the normalized current \hat{I} , which both will be introduced in the next subsection 2.1.3. It shows, that by changing the magnetic field, the gyrotron can operate either in the forward regime with positive detuning (gyro-TWT-like regime) or in the backward regime with negative detuning (gyro-BWO-like regime). The limit between these regimes, the point with $\Delta_0 = 0$, is located at the magnetic field $B_0 = 9.589 T$.

It is observed, that the minimum starting current is only of the order of several milli-Ampère and that different axial modes can be excited when tuning the magnetic field.

2.1.3 Normalized parameters

In this document, generally physical quantities are used instead of the normalized quantities, that are common in gyrotron literature [59, 29, 28]. These normalized quantities include the normalized detuning $\hat{\Delta}$, the normalized current \hat{I} and the normalized interaction length $\hat{\mu}$. In

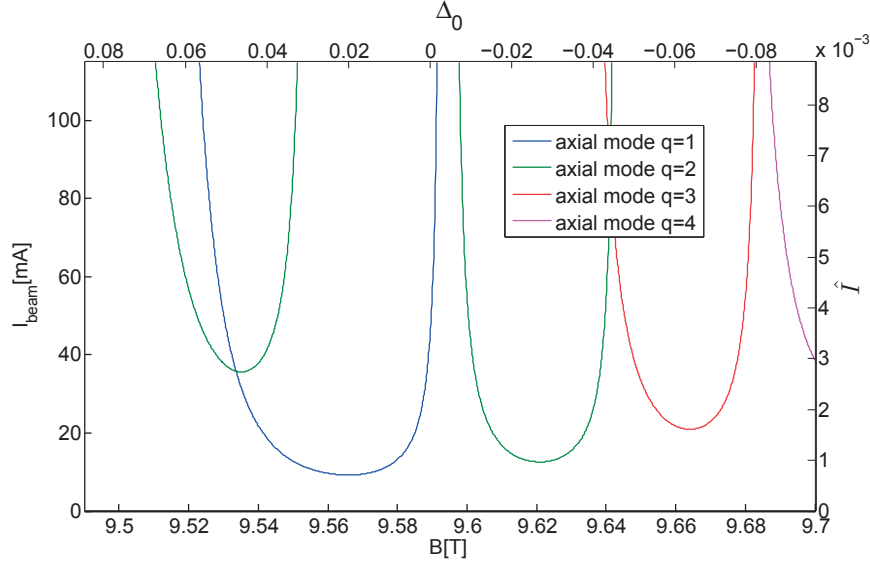


Figure 2.7: Starting currents as a function of the magnetic field, calculated with Eq. (5.40) in [28], using the fixed field profiles of the cold-cavity eigenmodes with axial mode number $q=1$ to $q=4$. The normalized detuning Δ_0 and the normalized beam-current \hat{I} are shown as top-axis and right vertical axis. Zero-detuning at $B_0 = 9.589$ T. Pitch-angle: $\alpha = 1.7$.

order to allow a comparison to gyrotron literature, here the definitions for these quantities will be presented, as well as their magnitude for the DNP-gyrotron.

The normalized detuning, which is included in several graphs in this document, is the one from the model used in the TWANG-code package, calculated at the entrance of the cavity. It is defined as

$$\Delta_0 = \frac{\gamma_0 - s \frac{\Omega_c}{\omega_0}}{\hat{p}_{z,0}}, \quad (2.1)$$

where γ_0 is the electron relativistic factor, s is the cyclotron harmonic number and $\hat{p}_{z,0} = \frac{p_{z,0}}{m_e c}$ the normalized parallel momentum (with parallel electron momentum $p_{z,0}$, electron mass m_e and speed of light c) at the cavity input, Ω_c is the non-relativistic cyclotron angular frequency and ω_0 is a reference angular frequency, for which the cold-cavity angular frequency of the $q=1$ -axial mode is used.

This expression should be compared to the expression of the normalized detuning, that is used e.g. in [63, 59, 29, 28, 64]

$$\hat{\Delta} = \frac{2}{\beta_{\perp,0}^2} \left(1 - \frac{s \Omega_c}{\gamma_0 \omega_0} \right), \quad (2.2)$$

where $\beta_{\perp,0} = v_{\perp,0}/c$ is the normalized perpendicular electron velocity at the cavity input. Because this frequency changes self-consistently, it is set to the cold-cavity frequency ($\omega_{RF} = \omega_0$) as in equation 2.1. The magnitude of both expressions of the detuning is presented for typical operating parameters of the DNP-gyrotron in Fig. 2.8.

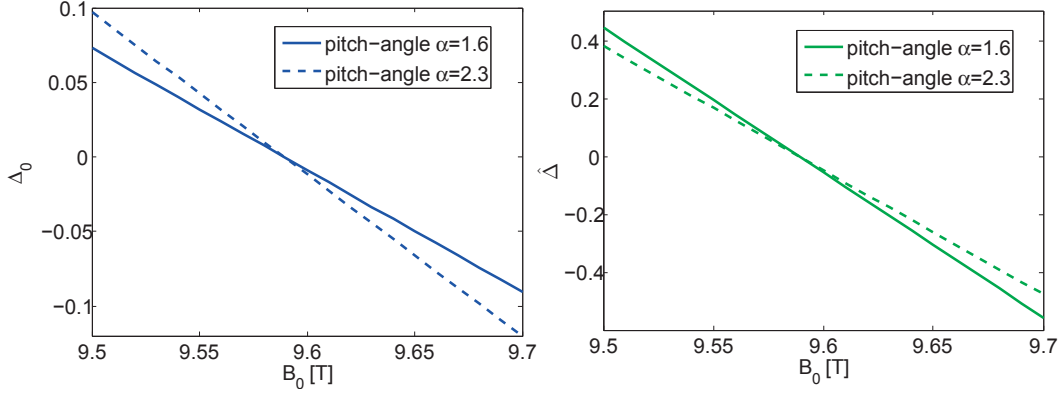


Figure 2.8: Normalized detuning Δ_0 as in Eq. (2.1) and $\hat{\Delta}$ as in Eq. (2.2) for typical values of magnetic field and pitch-angle for the DNP-gyrotron. Beam voltage: $V_b = 15.5$ kV.

For the normalized beam current of a $TE_{m,p}$ -mode, different expressions are used in literature. Here we will show the expression given in [63, 64, 55] for non-fixed field profiles:

$$\hat{I} = \frac{16e}{\pi\epsilon_0 m_e c^3} \frac{I_b \beta_{\parallel,0} \beta_{\perp,0}^{2(s-4)}}{\gamma_0} \left(\frac{s^s}{2^s s!} \right)^2 \frac{J_{m\pm s}^2(k_{\perp} R_g)}{(\nu_{mp}^2 - m^2) J_m^2(\nu_{mp})}, \quad (2.3)$$

where e and ϵ_0 are the electron charge and vacuum permittivity, respectively. The normalized parallel velocity at the cavity entrance is given by $\beta_{\parallel,0}$ and the electron beam radius is R_g . The constant ν_{mp} is the p^{th} zero of the derivative of the Bessel-function $J'_m(x)$ and the perpendicular wave vector is k_{\perp} . For modes co-rotating with the electrons, the Bessel-function J_{m-s} is used in Eq. (2.3), and for counter-rotating modes J_{m+s} . Equation (2.3) shows, that the normalized current depends linearly on the beam current and strongly non-linearly on the perpendicular velocity. This dependence is presented in Fig. 2.9a), showing the normalized current of the DNP-gyrotron as a function of the pitch-angle. An example of the typical range of the normalized parameters is equally shown in Fig. 2.7, where the normalized detuning Δ_0 , is shown on the top x -axis and the normalized current \hat{I} on the right y -axis.

The normalized interaction length is given by [63]

$$\hat{\mu} = \frac{\beta_{\perp,0}^2 \omega_0}{2\beta_{\parallel,0} c} L_{\text{eff}}, \quad (2.4)$$

where L_{eff} is the effective interaction length, which is well defined for a fixed profile such as a gaussian profile [59, 29]. In this document, the effective interaction length has been determined on the $q=1$ -axial mode cold-cavity profile shown in Fig. 1.6 as the width of an equivalent gaussian profile, giving $L_{\text{eff}} = 20$ mm. The normalized interaction length determined with this value and its dependency on the pitch-angle α is shown in Fig. 2.9b).

2.2. SETUP IN LPMN-LABORATORY

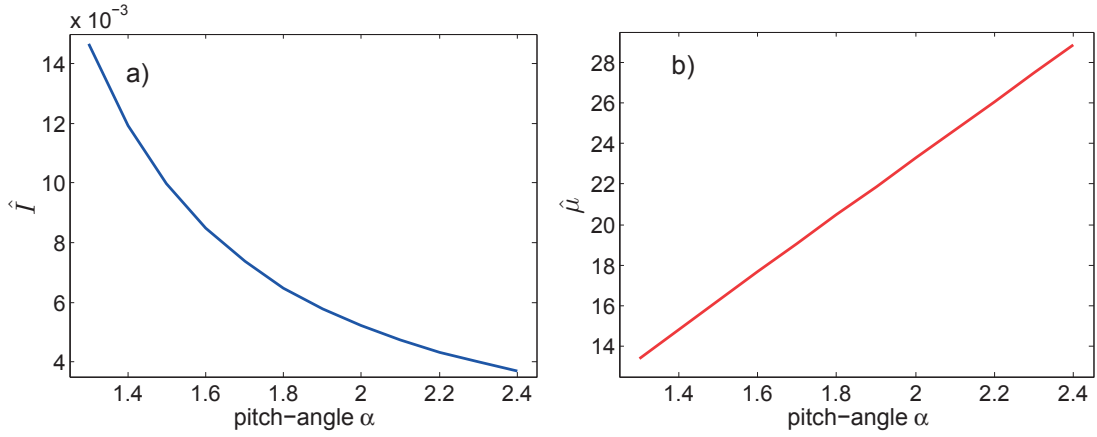


Figure 2.9: Dependence of a) normalized beam current \hat{I} and b) normalized interaction length $\hat{\mu}$ on the pitch-angle for DNP-gyrotron with parameters as described in subsection 2.1.2. In part a), a beam current of $I_b = 100$ mA was used and in b) an effective length $L_{\text{eff}} = 20$ mm was used.

2.2 Setup in LPMN-laboratory

After manufacturing, a first characterization of the DNP-gyrotron was performed at SPC, after which the gyrotron was moved to the LPMN laboratory, where it is presently used for its designated application of DNP-NMR spectroscopy.

Its present integration in the NMR-experiment is shown in Fig. 2.10. The gyrotron (on right side of the image) is placed inside its superconducting magnet, which is fixed by a support-structure. The emitted RF-output from the RF-window is coupled into the waveguide by the matching optics unit (MOU), composed of a plane mirror, a polarizer mirror with $\lambda/4$ -corrugations, a focusing mirror, and a $\lambda/8$ polarizer mirror, which are designed for maximizing the coupling of the RF-beam from the gyrotron into the $HE_{1,1}$ mode of the corrugated waveguide [65, 17]. The two corrugated polarizer mirrors in the MOU allow a transformation of the linearly polarized gyrotron output to a circular or elliptical polarization.

The low-loss waveguide was developed by the SPC-spin-off company Swissto12 [66]. Inside the NMR-spectrometer, the RF is coupled into the NMR-sample using a DNP-NMR-probe, composed of an open corrugated waveguide and radiating into a sample placed inside an NMR resonator circuit [17].

The rack, which accomodates the entire gyrotron control and protection system as well as all the auxiliary power supplies is shown in Fig. 2.11.

2.3 Gyrotron control system

The gyrotron control and protection system was designed and developed at EPFL and is based on a National Instruments Field-Programmable Gate Array (FPGA) (NI CompactRIO) with a Labview (National Instruments Inc.) interface.

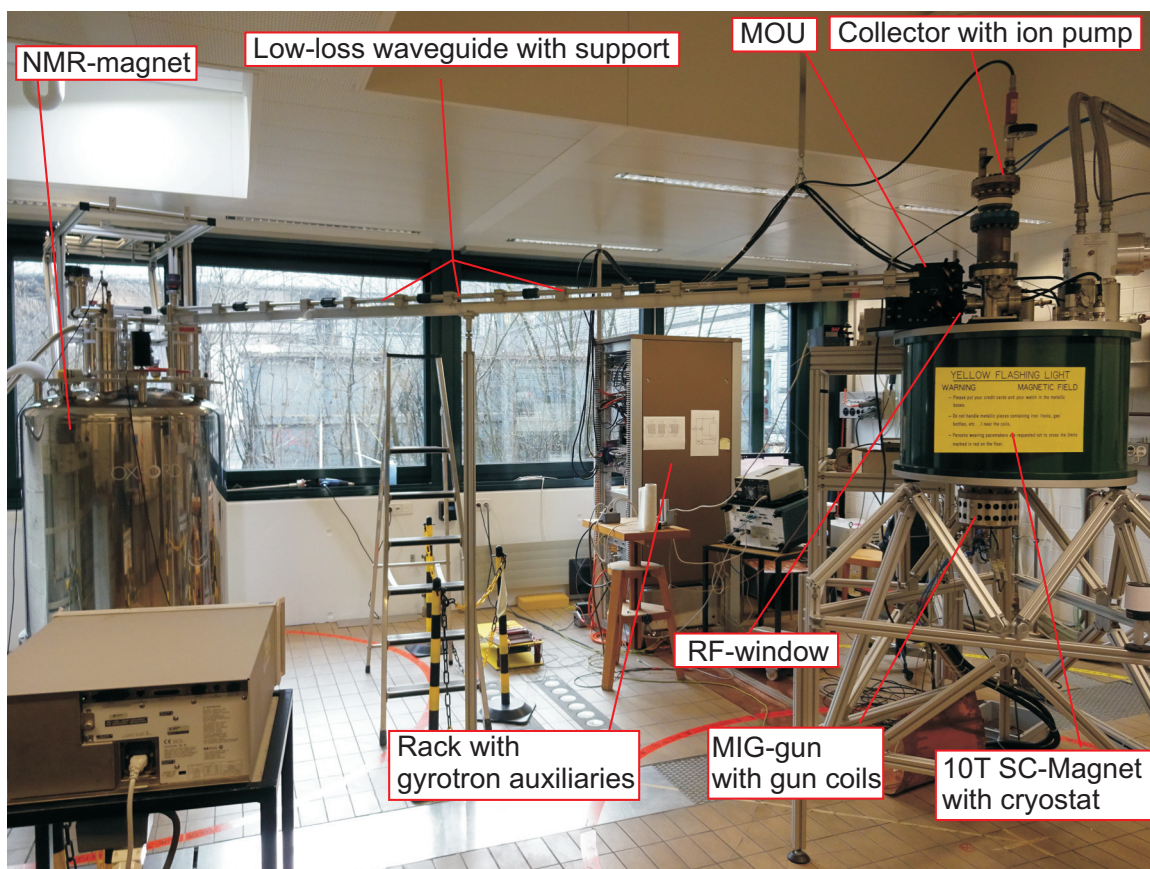


Figure 2.10: Integration of DNP-gyrotron (on the right) in its present environment for use in DNP-NMR experiments.

Both FPGA and the controlling computer are included into the rack shown in Fig. 2.11. All interlock signals acting on the different power supplies are handled by the control and protection system, that is described in the following.

2.3.1 Labview control system

The control and protection system has been designed such as to guarantee human and hardware protection, but also to allow a non-gyrotron specialist to take advantage of the wide operational flexibility of this gyrotron needed for advanced DNP-experiments.

The interface of the gyrotron control is implemented in a Labview-program, from where all the main parameters can be adjusted and monitored. Two different versions of the program have been developed: One 'gyrotron experts' and one 'DNP-experts' interface.

In the first, the user has basically the complete freedom of operating the gyrotron and the control over all the independant parameters. A screenshot of the user interface of this Labview-program ('gyrotron experts' mode) is shown in Fig. 2.12. On the right half of the window, the control-

2.3. GYROTRON CONTROL SYSTEM

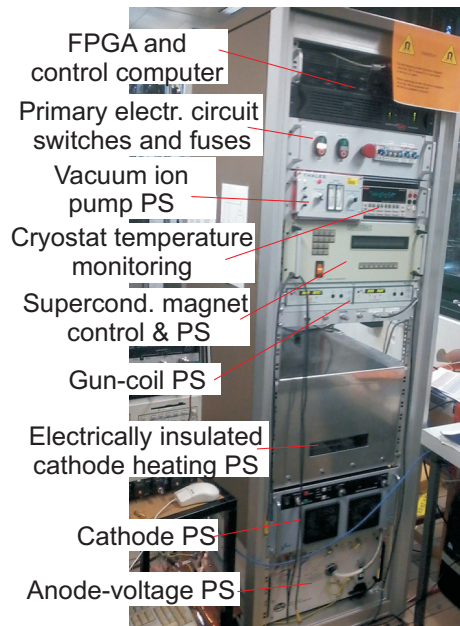


Figure 2.11: Rack with power supplies (PSs) and other auxiliaries for gyrotron operation.

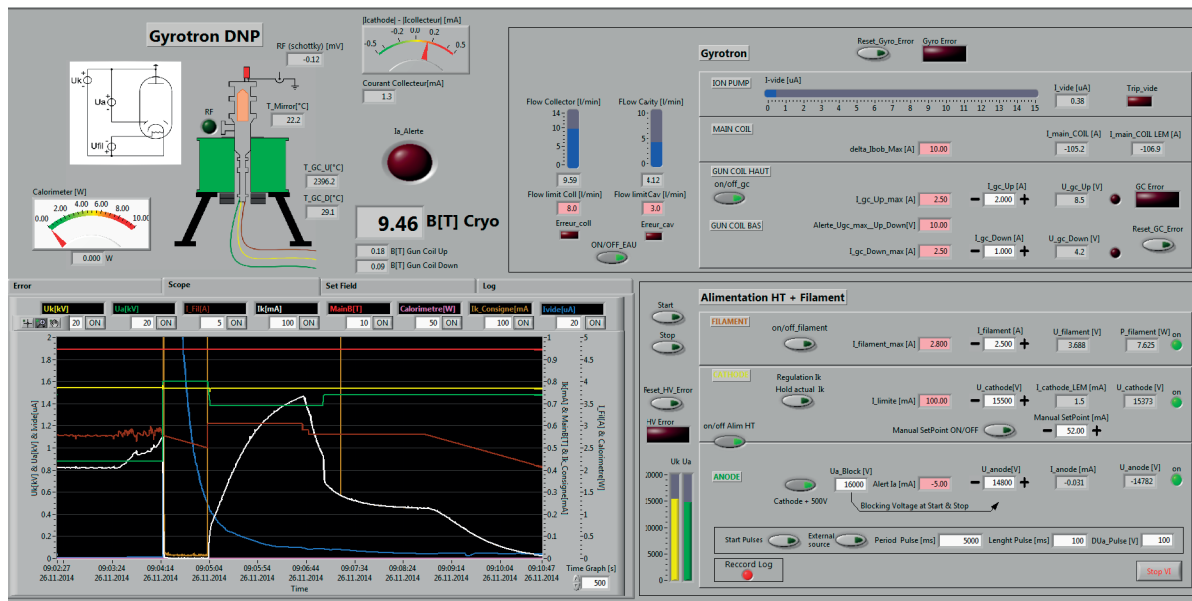


Figure 2.12: Interface in Labview-program for gyrotron control, screenshot of version for gyrotron experts. The white (active) number fields on the right show the control parameters, whereas the grey fields show indications and the red fields show limitations. The main parameters are monitored as time-traces on the window on the left.

parameters are: the super-conducting magnet magnetic field, the cathode voltage, the anode-voltage, the cathode heating filament current and the current in both gun coils. At the same time, the program monitors many parameters, namely all the mentioned control parameters, the cathode current and the collector current, the cooling water flow through cavity and collector, the current in the ion pump (proportional to the vacuum pressure), the current from the anode and temperatures at gun coils and internal mirror. Additionally, the power-measurement from the calorimeter and from a Schottky-diode can be monitored as well.

An arbitrary selection of these parameters can be observed in continuously updated time-traces included in the interface (see Fig. 2.12). This is extremely helpful for operating the gyrotron, especially in the case of unexpected events which can then be inspected as time-traces after the event. Another important feature of the Labview-control is that all important system parameters are automatically acquired and written in a text-file to keep a record of the entire operation. The acquisition-rate for this log-file can be set in the program and is typically 1 s. This feature is equally useful for debugging the system.

For many of the control parameters there are limitations set by the program which however can be changed manually in case of need. If one of these limitations is exceeded, the control program automatically stops the gyrotron operation. In several default cases, only the electron beam is switched off via the anode voltage by a fast setting of its value to a voltage 500 V more negative than the cathode voltage. For major errors however, the operation is stopped entirely by decreasing both cathode and anode-voltage immediately to zero.

The main protection strategy of the gyrotron is associated with the vacuum level inside the gyrotron (slow interlock) and possible arcing events. The arc-detection is included into the cathode HVPS and into the FPGA, by identifying a sudden increase in cathode current or anode-current. Furthermore, an interlock has been implemented which shuts down the electron beam whenever a possible electron beam interception is detected by a significant difference between the cathode and collector current.

For the start of the gyrotron operation, a time sequence (which is included in the time-traces in Fig. 2.13) has been implemented which rises first the anode-voltage and then the cathode-voltage, where the cathode-voltage is set to its nominal value and the anode-voltage 500 V higher in order not to extract any beam-current. For stopping operation, the anode-voltage is first increased above the cathode-voltage to block the beam, after which the two voltages are decreased simultaneously keeping the beam blocked.

The Labview-control also includes the possibility of applying pulses on the anode-voltage for creating RF-pulses, which will be shown in section 4.5.

In summary, with the presented version of the Labview-program the user has complete freedom in changing all possible control-parameters. Even though the gyrotron system is well protected, in the 'gyrotron-expert' mode, it is possible to operate the gyrotron in a strange situation. This was the motivation for creating the mode 'DNP-expert' of the control-program for the gyrotron's use in DNP-NMR. There, the utilization has been strongly facilitated, but also restricted, so that any user who is not familiar with the details of gyrotron control or gyrotron physics can operate the gyrotron with this interface.

The Labview-interface of this version is presented in Fig. 2.13. Here, it can be seen that the amount of adjustable parameters is strongly decreased, because practically the entire gyrotron

2.3. GYROTRON CONTROL SYSTEM

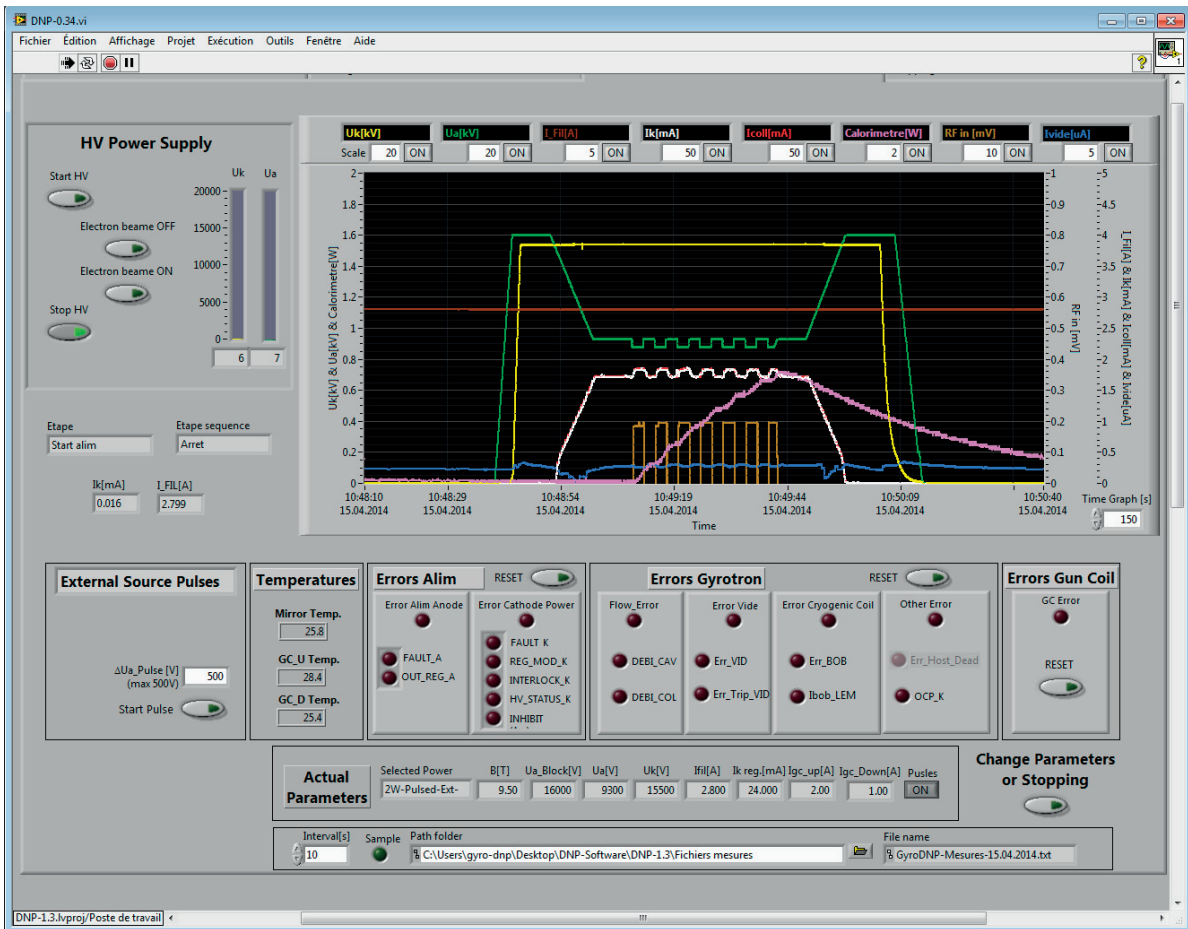


Figure 2.13: Interface of Labview-program for gyrotron control, version for application in DNP-spectroscopy. The gyrotron is essentially controlled by the buttons, which trigger a sequence for gyrotron start or stopping, together with external triggering.

control is automatized. In this operational mode, the user can choose between a list of operating points with pre-determined RF-power and frequency. These operating points usually allow external triggering of RF, but can also be assigned for CW-operation or with predefined pulses. After choosing the operating point, as soon as the system has arrived at the the nominal magnetic field and filament current, the interface of Fig. 2.13 appears. As shown in the time-trace on the chart, the start-up of voltages, which is triggered just by the button 'Start HV', follows the same sequence as described above. Then, via the button 'Electron beam ON', the anode-voltage is decreased close to the excitation limit. From there, the RF is triggered by the button 'Start pulse' and by applying an external trigger. For stopping the operation, it suffices to press 'Stop HV', which initiates the reversed sequence automatically.

Some operating points have also been assigned for including a fast frequency-sweep via an anode-sweep, that will be described later on.

In the 'DNP-expert' configuration, the gyrotron is currently operated since 2014 on a daily basis by students and scientists performing DNP-experiments. The overall system behaves very reliably and has demonstrated a high level of flexibility for testing advanced DNP experiment scenarios.

2.3.2 Beam-current stabilization

Originally, the beam-current is controlled indirectly via the heating-filament current in the cathode-emitter. This filament current controls the emitter-temperature, which in turn determines the electron beam current via the Richardson-Dushman equation for thermionic emission. Via the Schottky-effect, the beam current is also influenced by the field at the emitter-surface, determined by the difference between the anode and the cathode voltage.

With identical operating parameters, the beam current can drift over time due to long- and short-term heat equilibration processes of the emitter with surrounding gyrotron components. Another reason for an I_b -drift can be the conditioning of the cathode surface, where the surface can degrade from long-term operation (or non-operation) or also improve emission due to a cleaning effect of the emitter surface, resulting in change of the emitter work function. An exam-

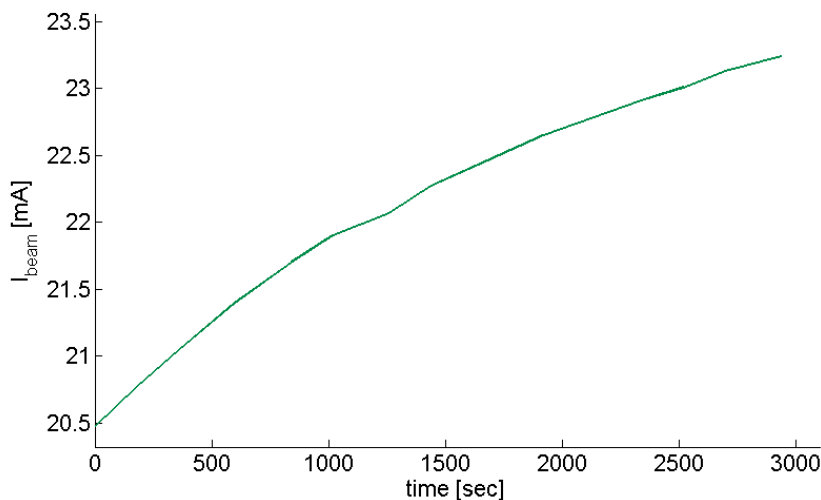


Figure 2.14: Long-term drift of beam current with a fixed operating parameters (fixed filament heating current). This shows, that a feedback control for the current is necessary.

ple of such a beam-current drift with fixed operating parameters is shown in Fig. 2.14, where the beam current changes over $\sim 14\%$ while the gyrotron is left operating for nearly one hour.

For preventing such drifts in beam-current, a feedback-control was implemented in the gyrotron control system on the FPGA. This feedback-controller sets the beam-current to a chosen value by acting on the filament heating current. For this, a Proportional-Integral (PI)-controller was chosen, for which Fig. 2.15 shows the reaction of the feedback-controller to steps of the I_b set-value. With the implemented parameters of the controller, it is observed, that even for relatively

large steps the beam-current arrives at the set-value within a few seconds with only a small overshoot. In the time where the set value is unchanged, the beam current remains very close to this set value, which can be sustained over an arbitrary time.

Because pulsed operation with oscillations in anode-voltage can lead to an instability of the

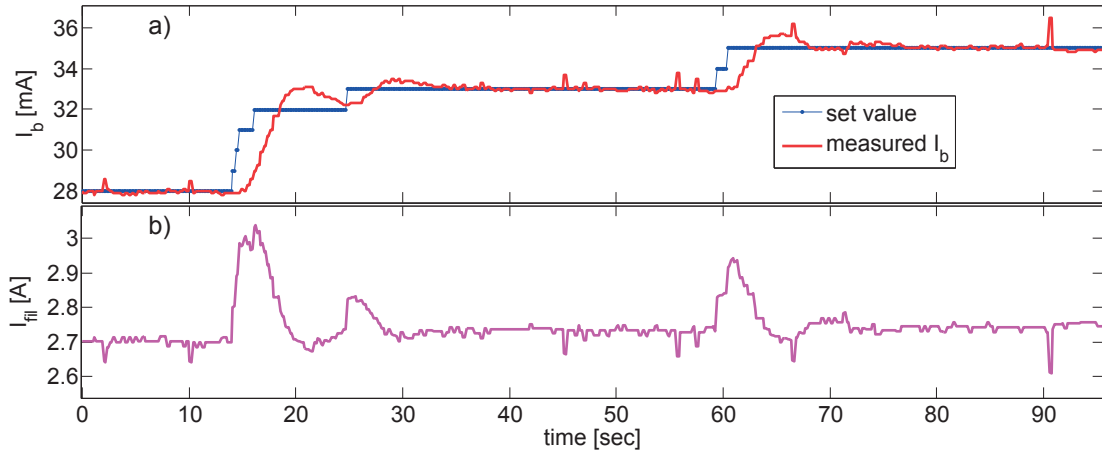


Figure 2.15: Reaction of feedback-controller on application of steps of I_b set-value. a) Measured I_b (red) compared to set value (blue). b) Filament heating current, adapted by feedback-controller to act on beam-current.

feedback-controller, in operation with RF-pulses the current-controller acts only during the off-time.

Similar feedback-controller have been described in other experiments for power-stabilization and/or frequency-stabilization [67, 19, 68]. In section 4.6, it will be illustrated that also in the case of the DNP-gyrotron this feedback-control of the beam-current was necessary for a stabilization of the RF-characteristics.

2.4 The RF-beam profile

The RF-beam pattern of the DNP-gyrotron was analysed in a detailed measurement series based on an inverse method [69] in which the phase information is recovered from amplitude profile measurements taken at predetermined distances along the RF-wave propagation axis. The amplitude profile measurements have been taken using a dielectric target placed in the beam path and measuring the temperature profile with an InfraRed (IR) camera due to dielectric absorption.

At this point we only present the major results of the analysis, which are also included in [70, 71].

An example for measured beam profiles is shown in Fig. 2.16, which has been acquired at a distance of $z = 90$ mm from the window plane and post-processed. In this logarithmic power-scaling, small deviations from a gaussian beam become apparent. In particular, an astigmatism is visible, corresponding to a different waist of the gaussian profile in x - and y -direction. In an estimation by a fit of a Gaussian to the beam-profile, the content of the fundamental (astigmatic)

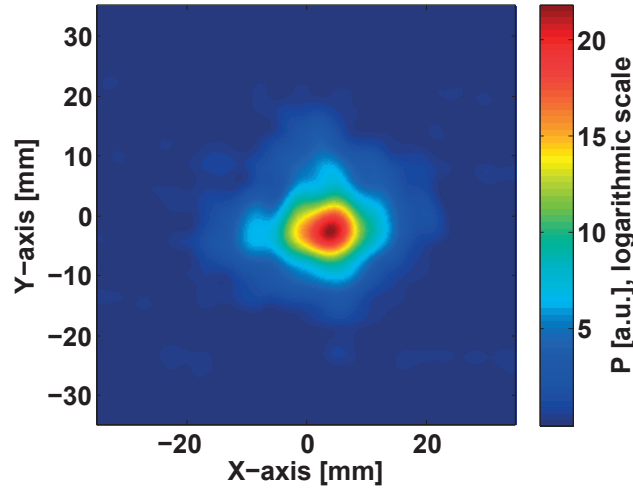


Figure 2.16: Beam profile at a distance $z = 90$ mm from window, from perspective-corrected, centered and filtered temperature-profile measurement with the help of an IR-camera. Methods described in [69].

Gaussian mode in the beam was evaluated to be of the order of $\geq 85.5\%$.

Three such beam-profiles from different distances were used for reconstructing the field phase

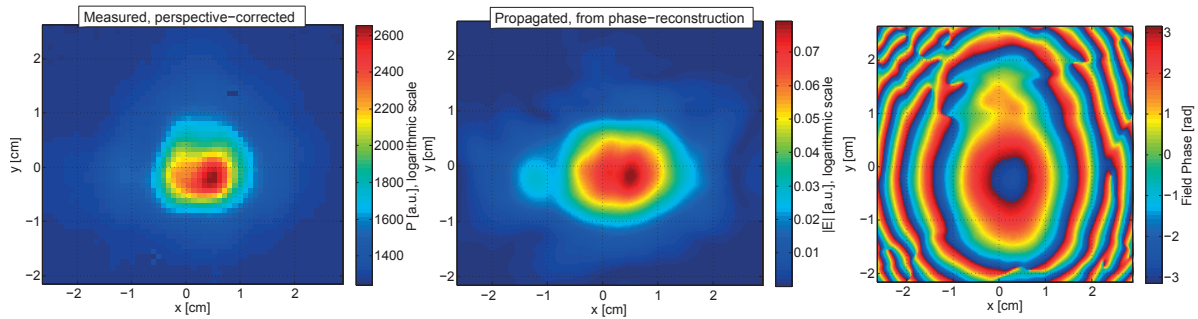


Figure 2.17: Measured (perspective-corrected) beam amplitude profile (left, at $z = 120$ mm), compared to beam amplitude and phase profile from phase-reconstruction, propagated to a distance $z = 120$ mm from window. Methods described in [69].

profile on these planes. With the help of this beam reconstruction, the beam electric field profile can be propagated to any distance from the window. This is illustrated in the amplitude and phase profile in Fig. 2.17, where the beam has been numerically propagated to a distance $z = 120$ mm from the window plane (middle and right inlet). The amplitude from the reconstruction can be compared to the measured beam profile (left inlet).

In addition to the beam shape, also its position and direction had to be determined. This information was used for designing the quadratic optics in the MOU [65], in order to maximize the

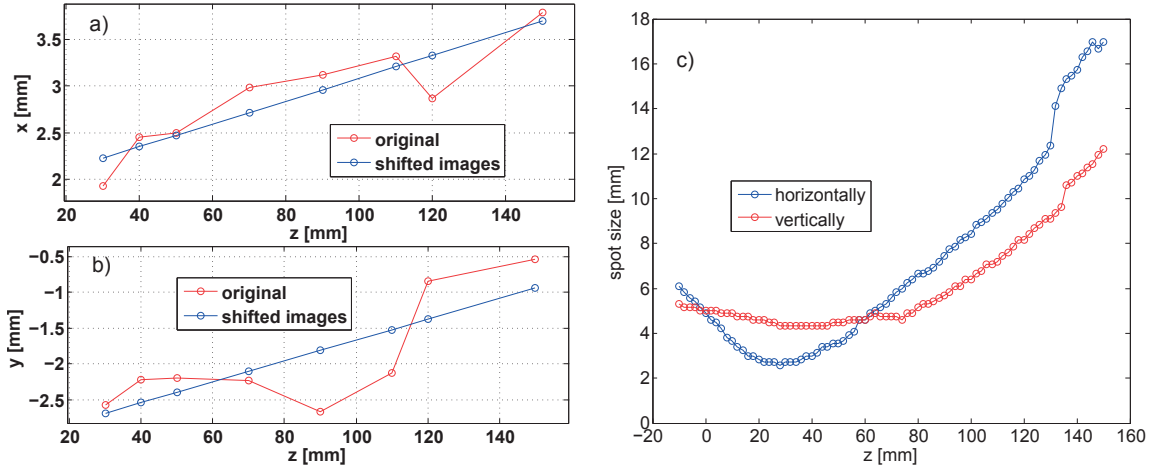


Figure 2.18: a) Displacement of center of gravity of the RF-beam as a function of the distance from the window, x -direction (positive=right, looking onto window): original (red) from unshifted IR-camera images and after alignment of images onto straight line (blue). b) center of gravity, y -direction (positive=up). c) Evolution of spot size in x - and y -direction as function of distance from window.

coupling of the RF-beam into the $HE_{1,1}$ mode of the corrugated waveguide towards the NMR-spectrometer.

For this, Figs. 2.18 a) and b) show the position of the beam center of gravity for all the measured planes along the z -axis in the perspective corrected images, together with a fit that is used to align these images. The beam is (looking onto the window) located on the lower right side of the window axis, moving up and to the right. Part c) shows the beam waist in the two directions, plotted against the propagated distance from the window. This shows again, that the beam is astigmatic, with a smaller waist in horizontal direction. The waists from this analysis are $w_{0,x} = 2.6$ mm at $z = 28$ mm and $w_{0,y} = 4.3$ mm at $z = 36$ mm.

The Vlasov converter together with the internal optical system ensures the high gaussian mode content shown above of the RF-beam at the RF-window. These components are however designed for the radiation of the $TE_{7,2}$ -mode and an operation at 263 GHz, so that the field profile and emission direction can be different for the neighboring TE-modes. This is illustrated in Fig. 2.19, which shows the beam-pattern directly after the window-plane for the mode $TE_{2,4}$, for a magnetic field of $B_0 = 9.75$ T and a frequency of 265 GHz. It is observed, that the strongly astigmatic beam exits the gyrotron close to the edge of the RF-window.

2.5 Diagnostics

A picture of the diagnostic setup generally used to measure the RF-characteristics (frequency spectrum and power) of the gyrotron is presented on Fig. 2.20, and the corresponding schematic view on Fig. 2.21.

By using either a polarizing wire-grid or a rotatable mirror in front of the gyrotron window,

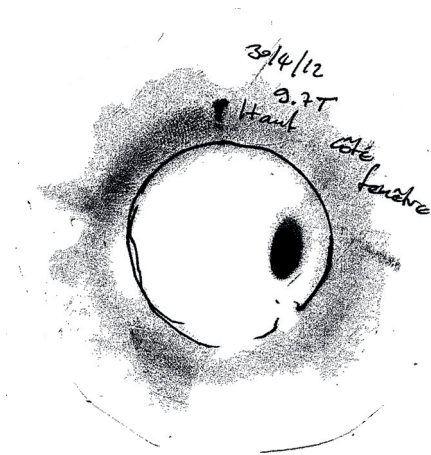


Figure 2.19: Beam pattern (blackened spot) of $TE_{2,4}$ -mode, captured with temperature-sensitive paper directly in front of the window. The window circumference is indicated by a line. Operating point at $B_0 = 9.75$ T.

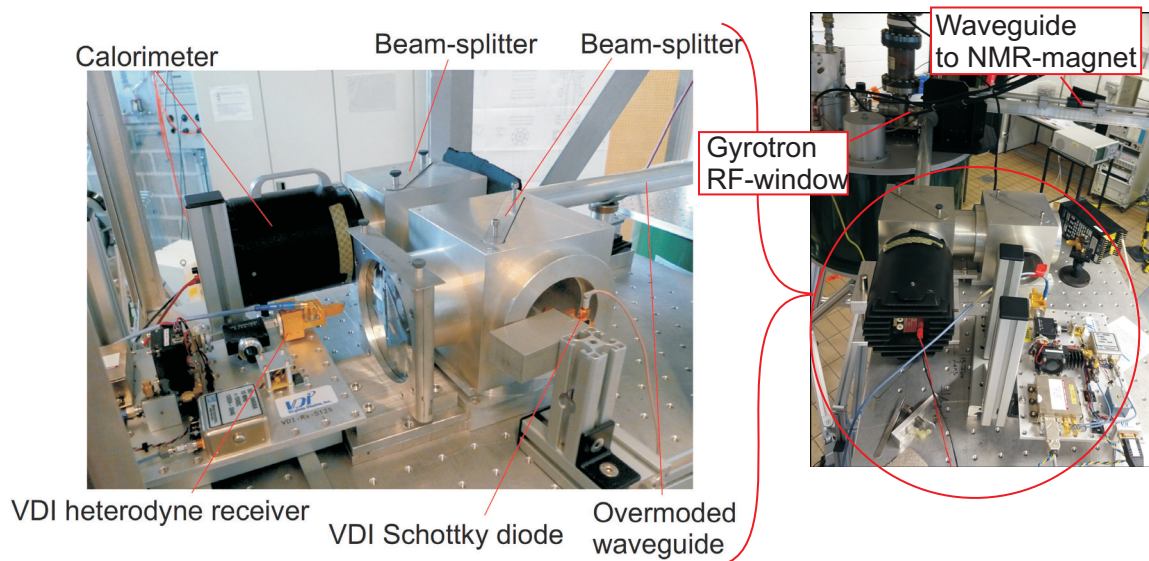


Figure 2.20: Diagnostic setup (left) and its context in LPMN-laboratory (right, compare Fig. 2.10). The RF is directed into the overmoded waveguide and from there distributed to the diagnostics by the beam splitters.

the RF-beam (or a part of it) can be directed into the overmoded waveguide connected to the detection setup. As shown in the sketch in Fig. 2.21, two beam-splitters divide the signal into three measurement branches, where usually most of the power is transmitted straight from the waveguide into the calorimeter for an absolute power measurement, and smaller fractions of the power are directed towards both a heterodyne receiver and a Schottky-diode. The beam-

2.5. DIAGNOSTICS

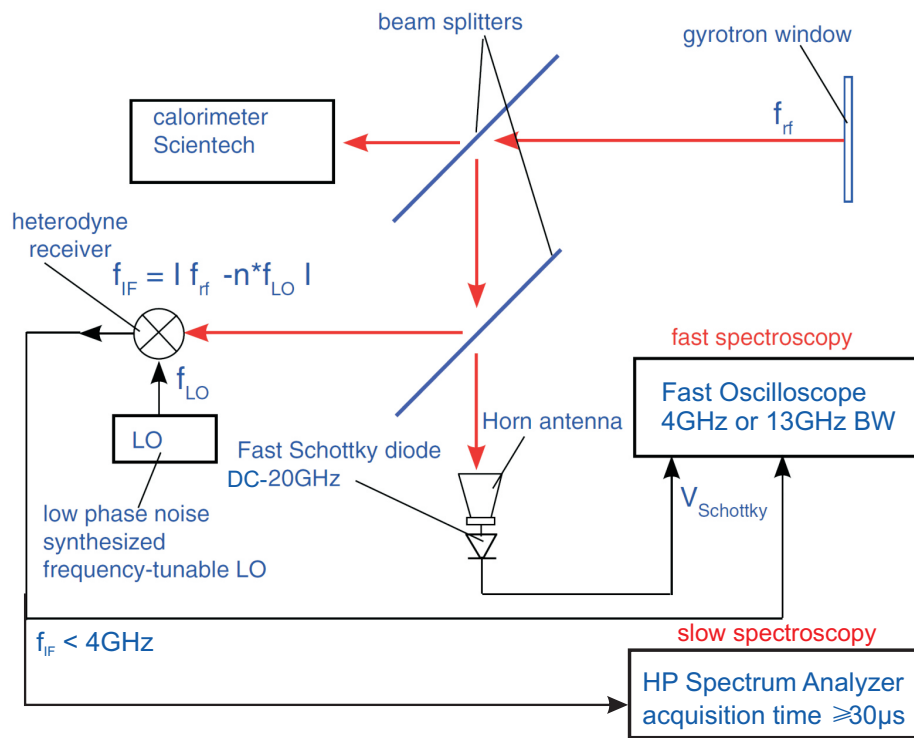


Figure 2.21: Schematic view of diagnostic setup, shown as a photograph in Fig. 2.20.

splitter transmission and reflection were adapted to the needs by using different beam-splitter foil materials (Mylar/PET, sometimes metallized).

The essential diagnostic for measuring the RF-frequency consists in a heterodyne receiver from Virginia Diodes Inc. (VDI), shown in Fig. 2.22. This device creates an Intermediate Frequency

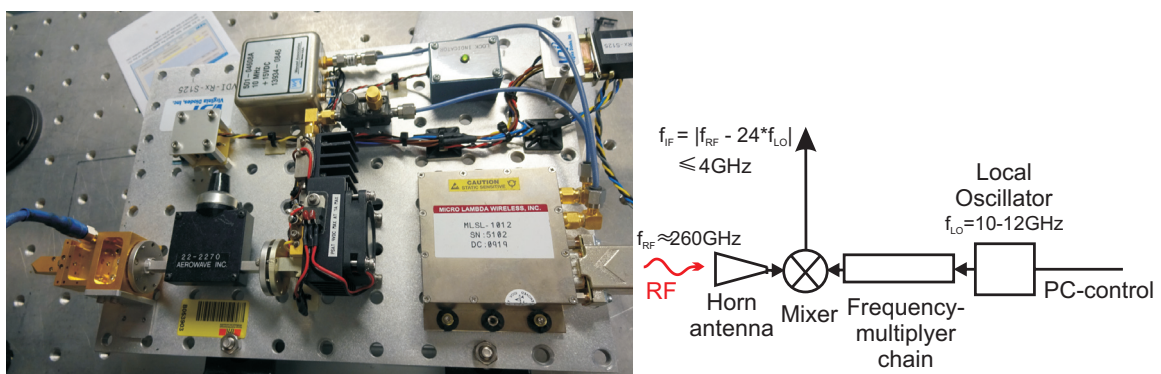


Figure 2.22: VDI-heterodyne receiver: photograph and schematic.

(IF)-signal, which contains all the information of the RF-signal, but which is moved to a lower frequency.

The heterodyne receiver works as illustrated in the schematic view in Fig. 2.22: A phase-locked Local Oscillator (LO) creates a signal with a well-defined frequency f_{LO} in the range 10 – 12 GHz. It consists in a step-tunable synthesizer (step size: 500 kHz, phase noise: -110 dBc/Hz at 100 kHz offset) with a digital frequency-control. It is then frequency-multiplied in a frequency-multiplier chain and subsequently mixed in a (second-harmonic) mixer with the RF-signal, creating the IF-signal (nominal conversion loss < 6 dB). In the mixer, the $n = 24^{\text{th}}$ harmonic is used as a reference signal, which results in an IF-signal at the frequency

$$f_{IF} = |f_{RF} - 24 \cdot f_{LO}|. \quad (2.5)$$

By setting the reference frequency $f_{ref} = 24 \cdot f_{LO}$ close to the RF-frequency, the IF-signal can be adjusted to be in the range of e.g. DC-4 GHz. The situations of $f_{RF} > f_{ref}$ or $f_{RF} < f_{ref}$ can be discriminated by analysing the dependency $f_{IF}(f_{LO})$ for a given f_{RF} (same for possibly appearing IF-signal of other LO-harmonics).

The nominal bandwidth of the heterodyne receiver is $f_{RF} = 255 - 270$ GHz for the RF-signal and $f_{IF} = 0 - 21$ GHz for the IF-signal. Generally, the mixer was operated with $f_{LO} = 10.65 - 10.8$ GHz.

The IF-signal is then acquired with a fast oscilloscope or with a spectrum analyzer (see schematic Fig. 2.21), with a large-enough bandwidth (BW) for directly analyzing the IF-signal.

During the gyrotron characterization, the IF-signal was analyzed with a spectrum analyzer, that consists of a modular analogue system of the Hewlett-Packard (HP) 71000 series. This system acquires the spectra by measuring the spectral amplitude in a scan over the frequency-span. The minimum acquisition time of a spectrum with this system is of the order of 30 ms, which makes it a slow measurement. A full description of this system can be found in [72], Appendix C.

Alternatively, the IF-signal of the heterodyne receiver was analysed with a fast oscilloscope. Here, for most measurements, a 4 GHz-bandwidth Tektronix oscilloscope was used (model TDS7404), with a sampling rate of $f_{sample} \leq 20$ GHz in single-channel operation and an input impedance of 50Ω .

For some measurements, a higher bandwidth was desired. In this case, a 13 GHz analogue bandwidth oscilloscope from Teledyne LeCroy (model WaveMaster 813Zi-A) was used. On this device, the maximum sampling frequency reaches $f_{sample} = 40$ GHz.

The absolute measurement of RF-power relied on a Scientech Laser Calorimeter (Model 360401, 100 mm diameter, $P_{RF} < 100$ W). Its absorbing plate is covered with a 3M Nextel coating for maximizing the RF-absorption, resulting in a power-absorption of $\sim 97\%$ at the relevant frequencies (from measurements with a Vector Network-Analyzer (VNA)). The time constant of this calorimeter is of the order of 50 s, so that it could be used for a slow, integrated power-measurement. The signal from the calorimeter is acquired with a NI-DAQ board (National Instruments Data Acquisition) and is included in the monitoring of the Labview-control program. The instantaneous RF-power level was monitored using one of two available Schottky diodes from VDI (Model: WR-3.4 Zero-Bias Detector, 220-325 GHz). One of these Schottky diodes has been specifically developed by VDI and has a bandwidth of DC–20 GHz, so that the instantaneous power of fast power pulses can be measured. This signal was acquired by one of the fast oscilloscopes (4 GHz or 13 GHz analogue BW) in order to register fast power-variations.

The signal of the Schottky-diode with the slower reaction time was either acquired with the NI-DAQ board and included in the monitoring of the Labview-control program, or acquired by a

350 MHz-bandwidth oscilloscope (Keysight, model DSO-X 3034A).

As described above in section 2.3.1, for further diagnostics simultaneously to this measurement of RF-power and frequency, all the important system parameters are acquired automatically in a log-file of the Labview-control program.

2.6 Data Analysis Tools

For evaluating the RF spectral characteristics, a time-resolved spectral analysis is performed by producing spectrograms, which show a color-coded spectral amplitude in the parameter-plane of frequency and time. This is illustrated in the example of Fig. 2.23, which shows the change of RF-frequency during an RF-startup of the DNP-gyrotron. Here, each column of color-coded

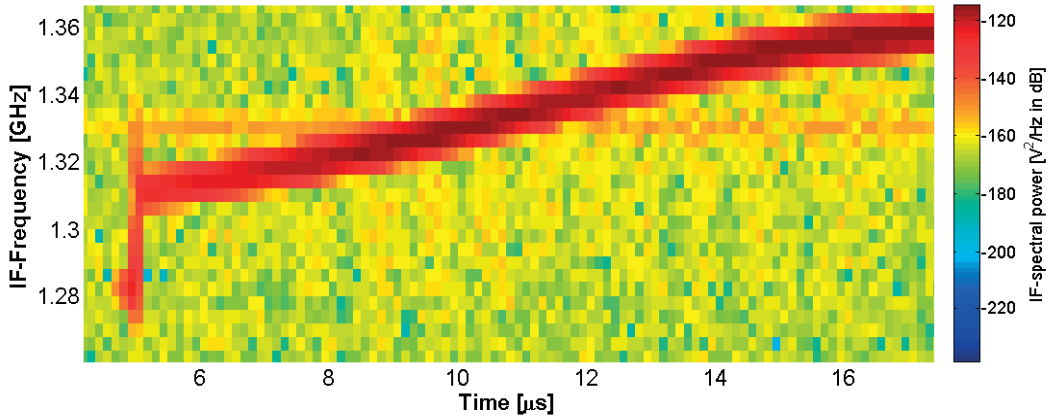


Figure 2.23: Example for spectrogram, showing the change of frequency during an RF-startup in the DNP-gyrotron. Here, the IF-signal amplitude on the oscilloscope was approximately $3.5 \text{ mV}_{\text{RMS}}$.

pixels in the spectrogram corresponds to a spectrum from an Fast Fourier Transform (FFT) of the IF-signal over a time-window of $2.5 \mu\text{s}$. In a spectrogram the basic temporal and frequency-resolution are connected as $\Delta f = \frac{1}{\Delta t}$, leading to a resolution of $\Delta f = 4 \text{ MHz}$ in the shown spectrogram. The temporal resolution is however increased by choosing an overlap between neighboring FFT-windows, where for all the shown spectrograms an overlap of $\Delta t/2$ with the neighboring windows is chosen, which effectively doubles the temporal resolution.

The color-coding of the spectrogram corresponds to the power spectral density ($[\text{V}^2/\text{Hz}]$), with a logarithmic scale ([dB]). Because the importance is usually given to the frequency-position of the RF and not to its absolute amplitude, the colorbar is generally omitted. For the FFT, a Hammersley-windowing is used. Finally, instead of showing the intermediate frequency, generally the RF-frequency is calculated as $f_{\text{RF}} = 24 \cdot f_{\text{LO}} + f_{\text{IF}}$ and shown on the frequency axis.

Chapter 3

Gyrotron Modeling

The complexity of modern gyrotrons makes it indispensable to perform numerical simulations for in gyrotron design prior to construction, as well as for understanding and interpreting experimental observations, that may be caused by complex dynamics.

In this chapter, we will introduce the most important models used for studying the physics of gyrotrons.

Besides the modeling of the beam-wave interaction through the ECM-instability, gyrotron modeling includes several other important fields of research, that treat different subcomponents and functionalities based on separate models, numerically implemented in simulation codes. A summary of the most important models include:

- 'Cold-cavity' models, solving a Helmholtz-equation for calculating the field profile and quality factors of the resonator eigenmodes without any influence from an electron beam (no source term in the wave-equation). In this calculation, the axial profile for a given TE-eigenmode is purely determined by the adiabatically varying cavity wall-profile and the corresponding boundary conditions.
- Models describing the radiation generation from the self-consistent beam-wave interaction through the ECM-instability, transferring the gyration energy of the electrons towards the RF-field. This includes:
 - Linear models for finding the excitation conditions for both the desired cavity-mode and for possible 'parasitic' modes, that can be excited in the central cavity region, in the preceding beam-duct or in the following uptaper and launcher sections.
 - Non-linear models in order to determine the detailed characteristics of the radiation generation in and around the cavity interaction region, where a reduced version of Eq. (1.3) has to be solved. For this, a large variety of approaches exists, spanning from very restrictive non-self-consistent simulations with a fixed field profile all the way to full-wave full-PIC models.
- Electron-optics models, determining the electron beam properties in the static electric and magnetic fields from the cathode up to the collector. These simulations also determine the electron beam properties at the cavity entrance.

- In order to design the radiation extraction following the interaction region, field propagation simulations are essential. The models that are implemented for this task use a variety of approaches, based on different approximations of the wave equation such as the Huygens-Fresnel principle or ray-tracing methods. They are employed for designing the launcher - including its mode converter - and the following mirrors for coupling the created RF-radiation out of the cavity waveguide structure and out of the gyrotron window.
- Thermo-mechanical models for determining stress and deformation on different components as well as the heat transport and deposition.

The following sections describe in detail the domains of validity and application of the simulation codes as they are used at SPC, the covering the first three bullets of the above-mentioned simulation tasks. Because this chapter is focused on the modeling of beam-wave interaction in the cavity, the electron-optics modeling is only described very briefly in subsection 3.0.1. Section 3.1 will introduce the cold-cavity models on the example of the model implemented in the code-package `CAVITY`.

The modeling of the *non-linear* beam-wave interaction will then be introduced in section 3.2, which gives an overview of the different approaches that exist to describe the non-linear interaction. At SPC, two different non-linear models are implemented in simulation codes, into the codes `TWANG` and `TWANG-PIC`. The first, `TWANG`, will be introduced in section 3.3, where also a detailed description of the model is included. `TWANG-PIC` and its model are then described in the following section 3.4.

Also for the less-demanding linear simulations, several different simulation codes are available at SPC, which will be described in section 3.5. The relatively basic code `SC` calculates the linear starting-current based on a model with a fixed RF-field profile. The self-consistent linear codes `TWANGLIN` and `TWANGLIN-SPEC`, on the other hand self-consistently find the correct RF-field profiles as part of the simulations, as it will be described in these sections.

3.0.1 Electron-optics simulation: DAPHNE

For electron-optics modeling, the code `DAPHNE` is used at SPC, of which details can be found in a publication [62]. It calculates the electron trajectories in the external electric and magnetic fields from the cathode to the cavity region and determines their properties at the cavity entrance. This is performed by solving the two-dimensional (2D) cylindrical Poisson-equation in a predefined electrostatic and magnetic field, including the space charge. Other codes for this purpose elsewhere are e.g. the `EGUN`-code [73] and the more advanced code `ARIADNE` [74] at Karlsruhe Institut für Technologie (KIT). The main output parameters of such simulations are the electron beam radius R_g , the pitch-angle α , the beam-energy and their respective spreads in the cavity region, that are then used as initial conditions for the beam-wave interaction simulation.

3.1 Cold-cavity calculations

The basic electromagnetic properties of the cavity resonator are described by the so-called cold-cavity eigenmodes, i.e. without an electron beam. In general, the properties of the eigenmodes have to be determined as a first step of gyrotron modeling. They are defined by the realistic three-dimensional (3D)-boundary conditions of the cavity resonator.

The smoothly varying wall radius causes internal reflections along the cavity profile so that the eigenmodes are provided with a standing wave field profile with a decay time, that is related to the diffractive quality-factor Q_{diff} of the cavity as $\tau_{\text{decay}} = \frac{2Q_{\text{diff}}}{\omega_{\text{RF}}}$ (ω_{RF} being the mode's angular frequency).

The most basic equation describing the cold-cavity RF-field is the electromagnetic wave equation in vacuum, corresponding to the wave-equation in Eq. (1.3) without the source term:

$$\frac{1}{c^2} \frac{\partial^2 \mathbf{E}}{\partial t^2} - \nabla^2 \mathbf{E} = 0. \quad (3.1)$$

The axial direction and the transverse direction can be decoupled, if for the field a separation ansatz is chosen as the following:

$$\mathbf{E} = \text{Re} \left(\sum_{m,p} \hat{F}(z) \hat{\mathbf{e}}_{mp} e^{-i\omega_{\text{cold}} t} \right). \quad (3.2)$$

Here, the transverse field is developed into different transverse eigenmodes with the azimuthal and radial indices m and p and with an angular eigenfrequency ω_{cold} , an axial profile of the field amplitude $\hat{F}(z)$ and a transverse profile of the field vector $\hat{\mathbf{e}}_{mp}$.

As mentioned earlier, the transverse eigenmode of a uniform cylindrical waveguide corresponds to $\text{TE}_{m,p}$ and $\text{TM}_{m,p}$ -modes, where in a gyrotron the electron beam interacts with a $\text{TE}_{m,p}$ -mode. As described e.g. in [75, 28], if the cavity wall radius varies adiabatically, these transverse modes can be regarded as uncoupled. The axial component of the wave equation can thus be solved for a single transverse mode $\text{TE}_{m,p}$, which results in the following Helmholtz-equation [75, 28]:

$$\frac{\partial^2}{\partial z^2} F - k_{\parallel}^2 F = 0, \quad (3.3)$$

where the normalization for the RF-field

$$F(z) = \frac{e}{m_e c^2} \frac{s^s}{2^s s!} \frac{\hat{F}}{k_{\perp}}, \quad (3.4)$$

is introduced, that is used in the model of the code *CAVITY*. The parallel wavenumber is given by $k_{\parallel}^2 = k^2 - k_{\perp}^2 = \left(\frac{\omega_{\text{cold}}}{c}\right)^2 - \left(\frac{\omega_{\text{co}}}{c}\right)^2$, with $k_{\perp} = \frac{\omega_{\text{co}}}{c} = \frac{\nu_{mp}}{R_w}$ being the perpendicular wavenumber (R_w is the radius of the cavity wall and ν_{mp} is the p^{th} root of the Bessel-derivative $J'_m(x) = 0$) of the $\text{TE}_{m,p}$ -mode, $\omega_{\text{co}} = \omega_{\perp}$ being its cut-off angular frequency, and s is the cyclotron harmonics number. In this equation the normalization factor of the field profile can be chosen arbitrarily.

In the axial direction, the open cavity has to be described with an outgoing-wave boundary condition at the two ends of the interaction structure, as:

$$\left. \frac{\partial F}{\partial z} \right|_{z_{\text{in/out}}} = \pm i \sqrt{\frac{\omega_{\text{cold}}^2 - \omega_{\text{co}}^2}{c^2}} F(z_{\text{in/out}}). \quad (3.5)$$

with ω_{co} being the cutoff-frequency of the TE-eigenmode and where the signs '+' and '-' correspond to the cavity entrance and exit correspondingly.

The equation Eq. (3.3) together with the boundary condition Eq. (3.5) can be expressed as an eigenvalue problem with ω_{cold} being the eigenvalue and the field profile $F(z)$ being the eigenvector, the solutions of the problem. At SPC, the equations are solved by the package *CAVITY* with its two functions *COLD* and *EIGM*.

Ohmic losses in the cavity wall are included self-consistently by replacing the parallel wavenumber in Eq. (3.3) with a modified parallel wave-vector, which has been described in [76] and which is expressed as:

$$\kappa_{\parallel 0}^2 = 1 - \frac{k_{\perp}^2}{k^2} \left[1 - (1 + i) \left(1 + \frac{m^2}{v_{mp}^2 - m^2} \frac{k^2}{k_{\perp}^2} \right) \frac{\delta_{sk}}{R_w} \right], \quad (3.6)$$

where $\delta_{sk} = \sqrt{\frac{2}{\omega_{cold} \mu_0 \sigma}}$ is the skin depth (μ_0 being the vacuum permeability, σ the wall conductivity).

Because the boundary conditions (3.5) depend on the eigenvalue (eigenfrequency), *CAVITY* solves the matrix, which expresses Eq. (3.3) and 3.5, iteratively. This is performed by calculating a first approximate eigenfrequency with a scan in frequencies in the program *COLD* and refining this result towards the true value in the program *EIGM* by using Müller's method [77].

Solving Eq. (3.3), the code determines the eigenvector, which corresponds to the axial profile of the complex RF-field, and the complex eigenvalue, which comprises the cold-cavity RF-frequency and the decay rate of the mode.

The typical resulting field profiles of different axial modes are shown in Fig. 3.1. For this calculation, the cavity profile corresponds to the one from the DNP-gyrotron. The frequencies and quality-factors for these modes were listed in table 2.2.

The properties of these cold-cavity longitudinal eigenmodes, are of interest both in cavity design studies and as a starting point for further gyrotron simulations. There, the resulting field profile is used for calculating gyrotron radiation properties with the fixed-field approach or as the initial condition of the field profile (i.e. $F(z, t = 0) = F_{cold}(z)$) for fully self-consistent codes as *TWANG*, *TWANGLIN* or *TWANG-PIC*, while the cold-cavity RF-frequency is usually used as reference frequency in those codes.

3.2 Non-linear self-consistent beam-wave interaction

Self-consistent non-linear modeling is necessary to determine the transient and asymptotic properties of the generated RF-field in realistic conditions. As described earlier, this is described by the physics of the interaction between a ring-shaped beam of gyrating electrons and the self-consistently created field profile inside the cavity. The most fundamental equations describing this situation is the intricate set of Eqs. (1.3), consisting of the relativistic equations of motion of electrons undergoing the Lorentz force and the electromagnetic wave equation with a source term, derived from Maxwell's equations.

Solving this set of equations leads to numerically extremely heavy simulations, since both the timescales, outlined in Fig. 3.2, and the spatial scales that have to be resolved span many orders of magnitude. Here, the smallest time- and spatial scale is that of the electron gyro-motion,

3.2. NON-LINEAR SELF-CONSISTENT BEAM-WAVE INTERACTION

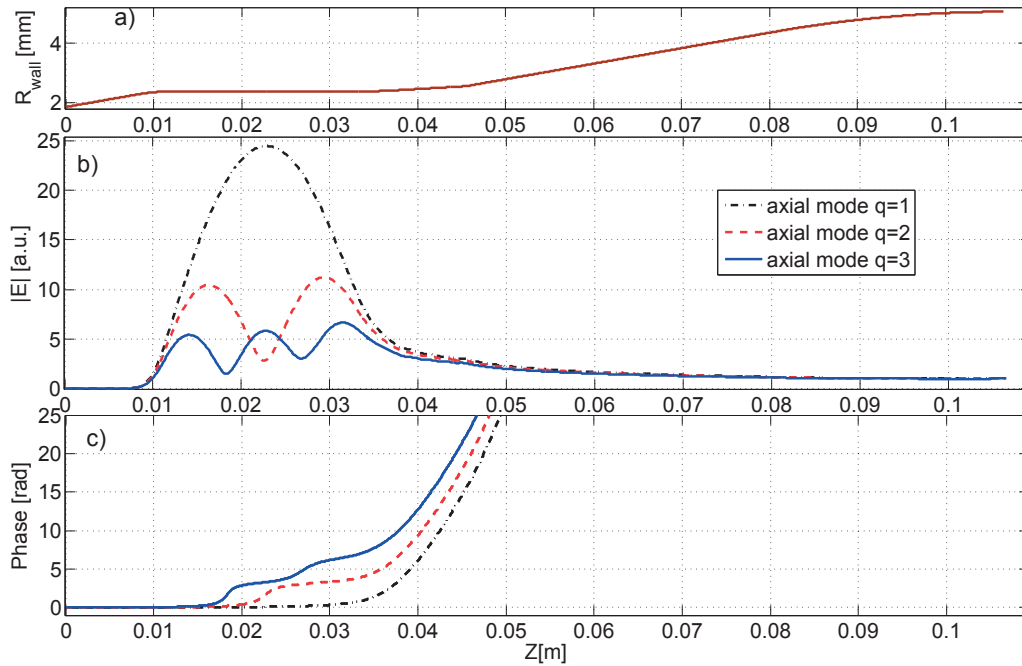


Figure 3.1: Cold-cavity axial eigenmodes for the $\text{TE}_{7,2}$ -mode in the DNP-gyrotron: a) Cavity wall-profile. b) Cold-cavity field amplitude profile for different axial modes (for colors and line-styles see legend) from code package CAVITY, normalized to output value. c) Cold-cavity field phase profiles. Frequencies and quality-factors: see table 2.2. Here, for the Ohmic losses, a wall conductivity of $\sigma = \sigma_{\text{Cu}}/2 = 2.9 \cdot 10^7 \text{ S/m}$ was used.

while the largest spatial scale is the entire volume of an overmoded cavity and uptaper and the largest temporal scale is that of the development of a non-linearly saturated or asymptotic state of interaction.

Nonetheless, this type of first principle simulations are sometimes employed for gyrotron beam-

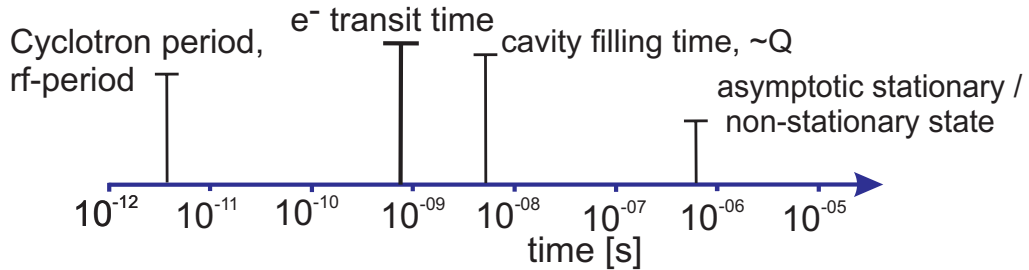


Figure 3.2: Sketch of the relevant time-scales in gyrotron interaction and in gyrotron modeling. The positions of the different time-scales apply to the here-described DNP-gyrotron and are different in other gyrotrons.

wave interaction calculations. This is possible with so-called full-PIC / full-wave codes, that usu-

ally include a 2.5-dimensional (e.g. 3-D velocity, 2-D spatial) or 3-D description of the particle motion and a full-wave approach for the RF-field. Members of this group include the commercial software packages CST Microwave Studio [78] and MAGIC [79] as well as several other codes [51, 80, 81, 82]. Because of the very demanding computational resources, they are mostly used only for verification of results or in some cases for gaining a better understanding of certain phenomena [80, 83, 84, 85]. Even in this case, sometimes a down-scaled version of the real cavity and eigenmode have to be used for preventing inhibitingly large computation times [86].

Because of these drawbacks, reduced models are developed, in which the equations of motion and the wave-equation have been simplified by applying several well-chosen restrictions and approximations [87].

The introduced modifications consist in an averaging of the fast time scales describe only the global evolution of the beam-wave interaction, so that the necessary time-step is increased by a large factor. At the same time the spatial description can be reduced to one spatial coordinate. The resulting model can be implemented in numerically very fast codes, which are suitable for large simulation studies covering many operating points in parameter scans. These models include multimode-models, describing the interaction with several transverse modes, and monomode models, describing the interaction with a single transverse mode.

A commonly used model is implemented into the SPC-code TWANG and will be introduced in more detail in section 3.3. It describes the time-dependent self-consistent wave-particle interaction equations for a given transverse cavity eigenmode $TE_{m,p}$ and is based on the slow-timescale formulation (i.e. averaged description). The approach assumes that changes of the RF-field profile occur on a time scale significantly longer than the electron transit time, i.e. the electron time of flight through the interaction region.

This assumption generally restricts the fastest variation of the field profile to ~ 10 ns (see Fig. 3.2), which means that the approximation can fail in the case of fast field variations due to non-stationary oscillations.

Therefore, a novel simulation model and code has been developed, in which the restriction of a time-scale separation between field and electron transit is relaxed. For this development, described in section 3.4, the model of the TWANG-code was adapted from a trajectory-like approach towards a gyro-averaged 1D PIC approach (spatially 1D).

3.3 Trajectory-approach: The TWANG-model

The kind of model, which is implemented into the code TWANG, was first introduced by Fliflet et al. [88], but also described in detail e.g. by S. Kern [89], E. Borie [75], K.R. Chu et al. [76] and A.R. Choudhury [90]. At SPC, such a model is implemented into the self-consistent, time-dependent code TWANG, but similar models are implemented in most gyrotron simulation codes, such as for example in the KIT-codes SELFT [89] and EURIDICE [91], the code MAGY [92] or the codes at the Institute of Applied Physics (Nizhny Novgorod) [93]. For a complete description of the derivation, the reader can refer to one of these publications.

In the following, it will be briefly summarized, which are the approximations and restrictions included in the model, and when / why they are justified. The approximations will be described, that are used for deriving the reduced model from the original equations of motion and the wave

3.3. TRAJECTORY-APPROACH: THE TWANG-MODEL

equation (as in Eqs. (1.3)).

AC-space charge effects can be neglected [82] for the beam-wave interaction in gyrotrons, because no influence of space charge instabilities is expected, if the beam density stays below a certain threshold, and because the interaction mechanism intrinsically does not include density fluctuations. The non-negligible DC-effect of space charge voltage depression [94, 95] can be taken into account à posteriori by adapting the beam energy.

Another simplification that is justified in most cases consists in neglecting the coupling between transverse modes, reducing the field description to a single $\text{TE}_{m,p}$ -mode [28].

Similarly to the cold-cavity description of section 3.1, the electric field is described by an ansatz with a fixed transverse profile and a z -dependent amplitude. The temporal evolution is separated into a fast reference oscillation (close to RF-frequency) and a (in comparison) slowly varying field amplitude::

$$\mathbf{E} = \text{Re} \left(\hat{F}(z, t) \hat{\mathbf{e}}_{mp}(r, \varphi) e^{-i\omega_0 t} \right), \quad (3.7)$$

where $\hat{F}(z, t)$ represents the axially varying complex amplitude of the transverse field, and $\hat{\mathbf{e}}_{mp}(r, \varphi)$ is the fixed normalized transverse field profile of the $\text{TE}_{m,p}$ -mode, that is assumed not to be modified by the interaction. By integrating the field contribution over the cylindrical cross section, an average is taken over the transverse field profile, so that the spatial dependence of the field is reduced to the field at the particle position and the field envelope $\hat{F}(z, t)$.

The arbitrary reference frequency ω_0 for the mode $\text{TE}_{m,p}$ is **chosen** close to the actual oscillation frequency, so that the profile $\hat{F}(z, t)$ includes a variation, that is slow compared to ω_0 :

$$\frac{\partial \hat{F} / \partial t}{\hat{F}} \ll \omega_0. \quad (3.8)$$

Therefore, the term with the second order time derivative $\frac{\partial^2 \hat{F}}{\partial t^2}$ that appears in the wave-equation can be neglected and one obtains a parabolic wave equation, with a first-order time derivative and a second-order derivative in the axial variable z .

The transverse field vector is replaced by the radial and azimuthal transverse fields of TE_{mp} -eigenmodes in a cylindrical conducting surface waveguide, which is expressed in Bessel-functions [96]. The evaluation of the interaction term is strongly simplified by moving the origin of the coordinates from cylindrical coordinates with the center on the cavity-axis to an origin at the center of gyro-motion (using Graf's theorem [97]).

In order not to have the electron motion expressed in a Bessel-function, which is more complicated to solve numerically, one uses the approximation of small Larmor-radius $k_{\perp} r_L \ll 1$, which is true for not strongly relativistic electrons ([75]: $V_{\text{beam}} < 250 \text{ kV}$) and which allows the use of a Taylor-development for expressing the motion without temporally varying Bessel-functions.

In the trajectory-approach, the electron equations of motion are not solved in the time-domain, but instead in the spatial domain by replacing the temporal derivative with a spatial derivative as:

$$\frac{d}{dt} \longrightarrow \frac{d}{dz} \frac{dz}{dt} = v_z \frac{d}{dz} = \frac{\hat{p}_z c}{\gamma} \frac{d}{dz} \quad (3.9)$$

This modification is combined with the approximation, that the field profile is practically unchanged during the electron transit through the entire interaction region, which is equivalent

to

$$\Delta\omega_F \sim \frac{1}{|F|} \left| \frac{\partial F}{\partial t} \right| \ll \frac{v_z}{L} \sim \Delta\omega_{\text{ib}}, \quad (3.10)$$

where v_z is the electron axial velocity, the quantity $\Delta\omega_F$ is the characteristic frequency bandwidth of the excited RF-field and $\Delta\omega_{\text{ib}} = \frac{1}{\tau_{\text{el}}}$ is the characteristic instability bandwidth and the inverse of the electron transit time.

This condition, meaning that the electrons interact with a constant field envelope, is satisfied for stationary (single-frequency) regimes or in non-stationary regimes as long as its bandwidth $\Delta\omega_F$ is small enough.

Under the condition of timescale separation in Eq. (3.10), the resulting equations of motion can then be solved along the entire interaction region between each time step of the wave equation, using the full field profile obtained in the wave equation in the previous time step.

All these manipulations and approximations allow obtaining the following model used in TWANG, where the equations of motion ($2 \times N_{\text{inj}}$ Ordinary Differential Equations (ODEs) for N_{inj} macro-electrons) in perpendicular direction are:

$$\frac{d\mathcal{P}}{d\hat{z}} = \left(-i\Delta + \frac{s}{2} \frac{d(\ln B_0)}{d\hat{z}} \right) \mathcal{P} + s(-\gamma F^* + i\hat{p}_z F'^*) C_0 \frac{\hat{p}_\perp^{2s-2}}{\hat{p}_z}. \quad (3.11)$$

The parallel components of the equations of motion are:

$$\frac{d\hat{p}_z}{d\hat{z}} = -\frac{C_0}{\hat{p}_z} \text{Im}(F' \mathcal{P}) - \frac{1}{2} \frac{\hat{p}_\perp^2}{\hat{p}_z} \frac{d(\ln B_0)}{d\hat{z}}. \quad (3.12)$$

The self-consistent model is completed by the time-dependent parabolic wave equation for the wave electric field envelope $F(\hat{z}, t)$:

$$\left(\frac{2i}{\omega_0} \frac{\partial}{\partial t} + \frac{\partial^2}{\partial \hat{z}^2} + \kappa_{\parallel 0}^2 \right) F = i \mathcal{S} \left\langle C_0 \frac{\mathcal{P}^*}{\hat{p}_z} \right\rangle. \quad (3.13)$$

Here, the dynamic variable of the slow-timescale perpendicular electron momentum has been introduced as:

$$\mathcal{P} = \hat{p}_\perp^s e^{-i\Psi}, \quad (3.14)$$

expressed with the slow-timescale electron gyro-phase Ψ and with the perpendicular momentum, which is normalized like the parallel one:

$$\hat{p}_\perp = \frac{p_\perp}{m_e c} \quad \text{and} \quad \hat{p}_z = \frac{p_z}{m_e c}. \quad (3.15)$$

Furthermore, the relativistic factor of the macro-electron γ_j is included and in the equations of motion the index of the macro-electron has been omitted.

The field envelope has been normalized by:

$$F = \frac{e}{m_e c^2} \frac{s^s}{2^s s!} \frac{\hat{F}}{k_\perp}, \quad (3.16)$$

3.3. TRAJECTORY-APPROACH: THE TWANG-MODEL

with the axial derivative of the field as $F' = \frac{\partial F}{\partial z}$, and the axial variable was normalized as:

$$\hat{z} = k_0 z = \frac{\omega_0}{c} z. \quad (3.17)$$

Furthermore, the following normalized, dimensionless quantities have been used:

Detuning:

$$\Delta = \frac{\gamma - s \frac{\Omega_c}{\omega_0}}{\hat{p}_z} \quad (3.18a)$$

Normalized beam current:

$$\mathcal{I} \equiv \frac{e Z_0}{m_e c^2} \frac{I_b}{C_{mp}} \left(\frac{s^s}{2^s s!} \right)^2, \quad (3.18b)$$

Parallel wavenumber with Ohmic losses:

$$\kappa_{\parallel 0}^2 = 1 - \frac{k_{\perp}^2}{k_0^2} \left[1 - (1+i) \left(1 + \frac{m^2}{v_{mp}^2 - m^2} \frac{k_0^2}{k_{\perp}^2} \right) \frac{\delta_{sk}}{R_w} \right], \quad (3.18c)$$

Coupling factor:

$$C_0 \equiv \left(\frac{k_{\perp}}{k_0} \right)^s \left(\frac{s \Omega_c}{\omega_0} \right)^{1-s} J_{m-s}(k_{\perp} R_g), \quad (3.18d)$$

Normalizing constant for $\text{TE}_{m,p}$ -mode:

$$C_{mp} = \frac{\pi}{2} (v_{mp}^2 - m^2) J_m^2(v_{mp}), \quad (3.18e)$$

where, as in the case of the cold-cavity description (section 3.1), the normalized complex axial wavenumber $\kappa_{\parallel 0}$ takes into account the Ohmic wall losses self-consistently [76]. In the wave equation the averaging of the source term has been defined as: $\langle V \rangle = \frac{1}{N_{\text{inj}}} \sum_{j=1}^{N_{\text{inj}}} V_j$ for N_{inj} electrons at a given \hat{z} and t , where V is standing for any phase space quantity. A summary of all the remaining standard variables that have been introduced in Eqs. 3.11-3.13 and Eqs. 3.18 is presented in table 3.1.

In Eqs. 3.11 and 3.14, the condition that the electron motion is represented in the slow-timescale representation with the slow gyro-phase Ψ , imposes that the reference frequency (defined close to RF-frequency) also has to be close to the harmonic of the self-consistently changing cyclotron frequency:

$$\frac{1}{|\mathcal{P}|} \left| \frac{d\mathcal{P}}{dt} \right| \ll 1 \quad \iff \quad \omega_0 \approx s \frac{\Omega_c}{\gamma}. \quad (3.19)$$

In order to clarify the meaning of these equations, the significance of each of the relevant terms in the TWANG-equations (Eqs. (3.11)-(3.13)) will be rapidly introduced at this point.

In the perpendicular equations of motion Eq. (3.11), the detuning Δ between reference frequency and the harmonic of the actual gyro-frequency $s \frac{\Omega_c}{\gamma}$ leads to an oscillatory behavior of the perpendicular momentum \mathcal{P} during the advancing of the electrons. The second term takes into account the conservation of magnetic moment, including a transfer of kinetic energy between parallel and perpendicular motion due to an adiabatically changing guiding magnetic field with

Beam current	I_b		[A]
Magnetic field	B_0		[T]
Azimuthal mode number	m		
Radial mode number	p		
Bessel-function of order m	$J_m(x)$		
Bessel-zero	v_{mp}	p^{th} root of $J'_m(x) = 0$	
Cyclotron harmonic number	s		
Non-relativistic angular cyclotron frequency	Ω_c	$= \frac{eB_0}{m_e}$	[rad/s]
Electron mass	m_e		[kg]
Electron charge	e		[C]
Vacuum impedance	Z_0		[Ω]
Speed of light	c		[m/s]
Reference wavenumber	k_0	$= \frac{\omega_0}{c}$	[1/m]
Perpendicular wavenumber	k_{\perp}	$= \frac{\omega_{ce}}{c}, = \frac{v_{mp}}{R_g}$	[1/m]
Reference parallel wavenumber	$k_{ ,0}$	$k_{ ,0}^2 = k_0^2 - k_{\perp}^2$	[1/m]
Guiding center radius	R_g		[m]
Cavity wall radius	R_w		[m]
Skin depth	δ_{sk}	$= \sqrt{\frac{2}{\mu_0 \omega \sigma}}$	[m]
Cavity wall conductivity	σ		[S/m]
Vacuum permeability	μ_0		[Vs/Am]
No. of electrons	N_{inj}		

Table 3.1: Summary of standard constants and quantities used in this section. Other quantities are defined in the text and can be found in Appendix B.

the normalized gradient $\frac{dB_0/dz}{B_0} = \frac{d}{dz} \ln(B_0)$.

The latter half of the right-hand side of Eq. (3.11) represents the actual action of the RF-field onto the perpendicular momentum, with the term proportional to F^* arising from the RF-electric field and the term with the axial derivative F'^* from the RF-magnetic field.

Equivalently, in the parallel equations of motion Eq. (3.12), the first term on the right-hand side accounts for the action of the RF-magnetic field and the second term arises from the conservation of magnetic moment.

In the wave-equation (Eq. (3.13)), the term with the reference axial wavenumber $\kappa_{||0}^2$ represents the expected RF-field variation at the reference frequency, arising from $k_{||,0}^2 = \frac{\omega_0^2}{c^2} - k_{\perp}^2$ and including a change in field amplitude due to Ohmic losses. Thus, the first and second term on the left-hand side describe the temporal and axial variation of the RF-field, that is not included in the reference axial wavenumber, but in the slow-timescale field envelope. As mentioned earlier, the term on the right-hand side of the wave equation represents the source term of the RF-field, accounting for the action of the electrons onto the field.

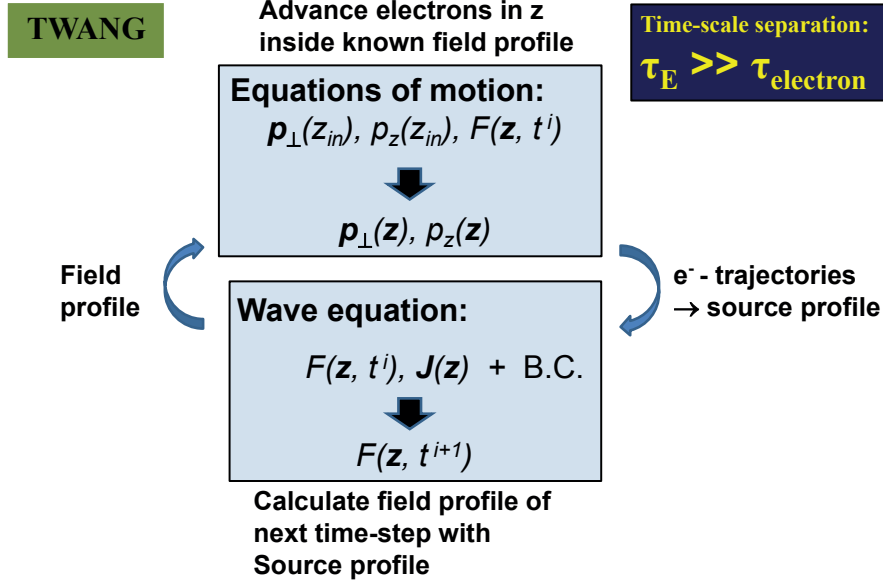


Figure 3.3: Algorithm for solving the system of equations in the code TWANG. The equations of motion are advanced over the entire interaction region using a 4th-order Runge-Kutta method and the field profile is updated in the parabolic wave equation by using a combination of a finite-difference predictor-corrector approach in time-domain with a finite-element approach in spatial domain.

3.3.1 Numerical Approach and applications

The algorithm used in TWANG for solving the system of equations Eqs. (3.11)-(3.13) is shown schematically in Fig. 3.3 and works in the following way. In the equations of motion (ODEs in Eqs. 3.11-3.12), at each time-step the field profile $F(\hat{z}, t_i)$ together with the initial momenta $\mathcal{P}(\hat{z}_{in})$ and $\hat{p}_z(\hat{z}_{in})$ are used to calculate the electron momenta along the entire interaction region. The obtained trajectories $\mathcal{P}(\hat{z})$ and $\hat{p}_z(\hat{z})$ are then used in the source term of the wave equation (right-hand side of Eq. 3.13) in order to advance the field in time, calculating $F(\hat{z}, t_{i+1})$. The equations of motion Eqs. (3.11)-(3.12) for N_{inj} electrons are solved using a 4th order Runge-Kutta method and the time-dependent envelope wave equation, Eq. (3.13), is solved using a finite element method (FEM) scheme based on B-splines of any order in spatial domain as well as a finite difference method with a predictor-corrector method in the time domain. The details of the numerical implementation of the wave-equation have been included in Appendix A. At the boundaries of the interaction space, radiation boundary conditions are considered, which, with the Finite Element Method (FEM) numerical scheme, are natural conditions. The radiation boundary conditions (for any t) are defined as:

$$\left. \frac{\partial F}{\partial \hat{z}}(t) \right|_{\hat{z}_{in/out}} = \pm i \frac{k_{||0}}{k_0} F(\hat{z}_{in/out}, t). \quad (3.20)$$

Here, $k_{||0}^2 = k_0^2 - k_{\perp}^2(\hat{z}_{\text{in/out}}) = \frac{\omega_0^2 - \omega_{co}^2(\hat{z}_{\text{in/out}})}{c^2}$ is the axial wavenumber without the loss term and '+' and '-' correspond, respectively, to the boundary conditions at the beginning ($\hat{z} = \hat{z}_{\text{in}}$) and output ($\hat{z} = \hat{z}_{\text{out}}$) of the considered interaction region. With this boundary condition, exact zero reflection is obtained at the reference frequency ω_0 , which however might be different from the wave frequency. In order to obtain zero reflections for the case of an oscillation with a single-frequency spectrum, the reference frequency ω_0 needs to be iteratively matched to the computed self-consistent oscillation frequency. However, in the case of a multi-frequency or broadband-spectrum, where the reference frequency cannot be matched to a single oscillation frequency, part of the oscillation frequencies might undergo stronger reflections from the boundary conditions. Because of this, instead of the boundary condition Eq. (3.20) an integro-differential type boundary condition [98, 99] can be chosen at the cavity ends, which yields negligible reflections for all implied frequencies.

As initial condition for the field profile, a cold-cavity field profile is used (by default $q=1$ axial mode), that was previously calculated with the code CAVITY (see Fig. 3.1). As an initial condition of the electron variables in the equations of motion, at the cavity entrance normally the quantities are used, that have been obtained by simulations with the code DAPHNE. The N_{inj} electrons, for which the equations of motion are calculated, are distributed uniformly in the initial slow gyrophase at the interaction space entrance and in case of simulations with spread they are additionally distributed uniformly in guiding center radius and/or with a gaussian distribution in pitch-angle and/or relativistic factor γ . For all these distributions, a quiet-start algorithm is used, based on a Hammersley-sequence [100, 101].

The program TWANG is written in the language FORTRAN90 and has been parallelized for solving the equations of motion using MPI (Message Passing Interface) for rapid execution on multiple cores of a cluster or of a single processor [102].

3.4 1D-Particle-In-Cell approach: TWANG-PIC

As it was described in section 3.2, the model described above and implemented in TWANG is well-suited for simulating stationary regimes, in which case the field profile is constant in time after a transient phase of the simulation, or for narrow-bandwidth non-stationary regimes for which Eq. (3.10) is valid. Whenever the self-consistent oscillation in the cavity is non-stationary, the field profile may change during the electron transit, therefore violating the assumption described by Eq. (3.10). One example are the non-stationary oscillation on a single transverse mode, that are observed experimentally on the DNP-gyrotron. As will be described in the following chapter 5, on this gyrotron, nanosecond-pulses were observed [103, 55, 104], that result in a fast variation of the RF-power and therefore also of the cavity field profile. Another situation, in which the model of TWANG is no longer valid is the appearance of dynamic After-Cavity Interaction (ACI) [105, 106, 107], for which it remains unclear, whether it is the cause of experimentally observed parasitic frequencies [108, 109]. In both these examples, the timescale of field profile variation is of the same order as the electron transit time (or faster):

$$\tau_F \sim \tau_{\text{el}}, \quad (3.21)$$

3.4. 1D-PARTICLE-IN-CELL APPROACH: TWANG-PIC

where the timescale of field variation is defined as $\tau_F = \frac{1}{\Delta\omega_F}$ ($\Delta\omega_F$ defined in Eq. (3.10)) and the electron transit time is defined as $\tau_{el} = L/v_z$ (L being the interaction length and).

In order to be able to simulate these situations realistically, one has to relax the time-scale separation (3.10), that was introduced in the model of TWANG with the trajectory-approach.

Therefore, the model and the related numerical algorithm for solving the equations has to be modified in order to reliably simulate a rapid variation of the field profile. Because the field profile is now allowed to vary faster than the electron transit, it is no longer possible to calculate the full electron trajectory at each time step with a fixed field profile. This means that the equations of motion have to include the temporal variation of the field envelope.

For the model of TWANG-PIC, the equations of motion were moved back from spatial domain to the time domain, so that electrons are advanced in temporal and spatial steps, resulting in a 1D/3D-reduced PIC-approach (1D spatially, 3D in velocity space). The details of this model and code have been published in [110] and at conferences [111, 112] and will be described in the following subsections.

3.4.1 TWANG-PIC model

During the introduction of the model of TWANG, it was described how the trajectory approach was included into the model by replacing the temporal derivative by a spatial derivative (in Eq. (3.9)). For allowing a faster variation of the field profile, the main modification is to step back from the replacement of the derivative:

$$\frac{d}{dt} \longleftarrow \frac{d}{dz} \frac{dz}{dt} = v_z \frac{d}{dz} = \frac{\hat{p}_z c}{\gamma} \frac{d}{dz} \quad (3.22)$$

The resulting equations in a PIC-approach, which describe the equations of motion in the temporal domain, are implemented into the code TWANG-PIC in the following form:

$$\begin{aligned} \frac{d\mathcal{P}}{d\tau} &= \left(-i\Delta + \frac{s}{2} \frac{\hat{p}_z}{\gamma} \frac{d(\ln B_0)}{d\hat{z}} \right) \mathcal{P} \\ &\quad + sC_0 p_{\perp}^{2s-2} \left(-F^* + i \frac{\hat{p}_z}{\gamma} F'^* \right) \end{aligned} \quad (3.23a)$$

$$\frac{d\hat{p}_z}{d\tau} = -\frac{C_0}{\gamma} \text{Im}(\mathcal{P}F') - \frac{p_{\perp}^2}{2\gamma} \frac{d(\ln B_0)}{d\hat{z}} \quad (3.23b)$$

$$\frac{d\hat{z}}{d\tau} = \frac{\hat{p}_z}{\gamma} \quad (3.23c)$$

$$\left(2i \frac{\partial}{\partial \tau} + \frac{\partial^2}{\partial \hat{z}^2} + \kappa_{\parallel}^2 \right) F = i\mathcal{S} \frac{1}{N_{inj}} \sum_{j=1}^{N_{inj}} \frac{C_{0j} \mathcal{P}_j^*}{\gamma_j} \Delta\tau \delta(\hat{z} - \hat{z}_j), \quad (3.23d)$$

where, in addition to the dynamic variables, coefficients and normalizations described in the section 3.3, the normalized time $\tau = \omega_0 t$ and the simulation time-step $\Delta\tau$ have been introduced. As a part of moving the equations of motion back to time-space, the source term was modified as:

$$\frac{\Delta t}{\Delta z} = \frac{1}{v_z} = \frac{\gamma}{\hat{p}_z c} \longrightarrow \Delta t \cdot \delta(z - z_j). \quad (3.24)$$

The same motivation also caused the introduction of Eq. (3.23c), coupling the spatial and temporal advance of the electrons.

A similar model has been described e.g. in the code Gyrodyne [113]. Different approaches for including the possibility of a rapidly changing field profile as in relation (3.21) have been described in [114], as well as in [115, 116] and applied e.g. in [117].

3.4.2 Numerical Approach and Applications

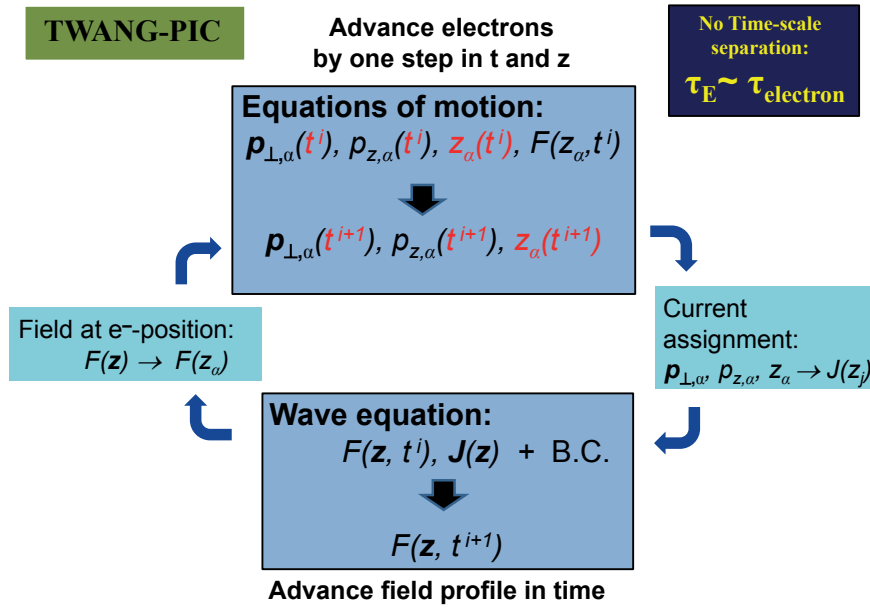


Figure 3.4: PIC-algorithm for solving the system of equations in the code TWANG-PIC. The equations of motion are advanced in time using a 4th-order Runge-Kutta method and the field profile is updated in the parabolic wave equation using a combination of a finite-difference predictor-corrector numerical scheme in time-domain with a finite-element scheme in spatial domain.

In comparison to the description of the numerical approach used in TWANG (section 3.3.1), the equations of motion of TWANG-PIC are solved in the time-domain and the field equation is re-evaluated between each Runge-Kutta step of the electrons.

The algorithm, that is used in TWANG-PIC to solve the system of Eqs. (3.23a-3.23d), and that corresponds to a typical Particle-In-Cell (PIC)-algorithm, is shown schematically in Fig. 3.4. The field experienced by the electrons (which are not necessarily on the grid points any more) is obtained using interpolation [101], while the source term of the wave equation is calculated on the grid points, using a grid deposition scheme [101], both using B-splines of any order. The equations of motion are now solved in time by a 4th order Runge-Kutta method, while for the wave equation a finite difference method in time is combined with a finite element scheme in the spatial domain, as in TWANG.

3.4. 1D-PARTICLE-IN-CELL APPROACH: TWANG-PIC

At the first time-step, the simulation is initiated with a filled cavity, where electrons are distributed in z -direction with initial parameters, that include the effect of the non-uniform magnetic field.

The numerical algorithm for pushing of the electrons has been described in detail in [118] and is done in the following way. At each time step, a set of N_{inj} electrons is injected at the beginning of the interaction region with a set of predefined parameters. In particular, by varying the initial phase of the injected electrons in-between time steps, the effective number of represented particles can be increased, because a larger number of discrete initial gyro-phase values can participate in the interaction. The interacting electrons are then handled in a single array of memory. At the end of the interaction region, the exiting electrons are removed from the storage array and holes in the array are re-filled by injected particles and by compacting the array. Energy, velocity and/or guiding center spreads are simulated by a quiet-start particle loading scheme [101].

In TWANG-PIC, again either the single-frequency boundary condition Eq. (3.20) or the broadband non-reflecting boundary condition [98, 119] can be chosen in the wave equation. The equations of the model described in section 3.4.1 were implemented in FORTRAN into the new code TWANG-PIC.

This code is an intermediate approach between fast codes with reduced physics (such as TWANG) and the numerically very demanding 2.5-D or 3-D PIC-codes, that mostly include the full-wave physics, such as the commercial software packages CST Microwave Studio [78] and MAGIC [79] as well as several other codes [51, 80, 81, 82]. Due to the described approximations included in the TWANG-PIC-model, it is less generally valid, but has the advantage of requiring acceptable computation resources.

The required numerical resources were analyzed and are summarized in table 3.2 for the typical simulation parameters as: Number of points in z : $n_z = 500$, $N_{inj} = 64$ injected particles at each time step, leading to approximately 25000 simultaneously simulated electrons, time step $\Delta t = 4.3$ ps and simulated time span $t_{max} = 100$ ns. The non-perfect speedup with increasing number of cores is mainly caused by global MPI communication.

The required numerical resources represent a significant increase in comparison to the code

Number of cores	Intel Haswell i7-4770 quad-core processor	2 Intel-Sandy Bridge 8-core processors combined, 2.2GHz
1	1650sec	1899sec
2	870sec	985sec
4	510sec	528sec
8		308sec
16		173sec

Table 3.2: TWANG-PIC runtime on two different compute nodes, using a different number of processor-cores. The speedup with increasing number of cores is not perfect because of MPI-communication.

TWANG, where for the same case the typical input parameters $\Delta t = 60$ ps, $N_{inj} = 512$ and $t_{max} = 100$ ns result in a run-time of about 91 seconds on the four cores of the above-mentioned Intel Haswell i7 quad-core processor. Nevertheless, this kind of computational requirements allows

one to use the code for parameter-scans in gyrotron design studies or in experiment interpretation, which is usually not the case for full-PIC simulation codes [80]. Considering the increased regime of validity with respect to the trajectory-codes as TWANG, this shows, that the code has advantages both with respect to these trajectory-based codes and to the full-PIC codes.

The maximum time step in TWANG-PIC is limited by a numerical instability, that appears, if the axial step of the electrons during a time step exceeds the spatial discretization, so if $\Delta z < v_z \Delta t$. This limitation could be slightly relaxed by smoothing short-range spatial fluctuations of the source term in the wave equation at each time step. It might be related to the numerical Cerenkov Instability and the Courant-Friedrich-Levy condition [120, 121].

3.4.3 Calculation of RF-parameters

In this subsection, it will be briefly described how the physical quantities of the RF-parameters are deduced from the simulation parameters.

The RF-power, is calculated as follows:

$$P_{\text{RF}} = \frac{C_{mp}}{Z_0} \frac{1}{k_0} \left| \frac{\hat{F}}{k_{\perp}} \right|^2 \text{Im} \left(\frac{1}{\hat{F}} \frac{\partial \hat{F}}{\partial z} \right) \Big|_{z_{in}}^{z_{out}} \quad (3.25)$$

and the total dissipated power in the cavity wall is calculated as:

$$P_{\text{dissp}} = \frac{C_{mp}}{Z_0} \frac{1}{k_0} \int_{z_{in}}^{z_{out}} dz \frac{\delta_{\text{sk}}}{R_w} \left(1 + \frac{m^2}{v_{mp}^2 - m^2} \right) |\hat{F}|^2, \quad (3.26)$$

The integrated field energy in the interaction region corresponds to:

$$W_{\text{RF}} = \frac{C_{mp}}{Z_0} \frac{k}{\omega_0} \int_{z_{in}}^{z_{out}} dz \left| \frac{\hat{F}}{k_{\perp}} \right|^2. \quad (3.27)$$

The electron efficiency is deduced from the powers, assuming numerical energy conservation:

$$\eta_{\text{el}} = (P_{\text{RF}} + P_{\text{diss}} + dW_{\text{RF}}/dt) / (I_b \cdot V_b) \quad (3.28)$$

Alternatively, the efficiency can also be calculated directly from the changing electron energy between the time-steps. This is done in the TWANG-code, where the trajectory-approach allows to directly compare the electron-energy at the cavity entrance and output for each electron. Finally, the time-dependent loaded diffractive quality-factor is calculated as:

$$Q_{\text{diff}} = \omega_0 W_{\text{RF}} / P_{\text{RF}}. \quad (3.29)$$

3.4.4 Benchmarking and confirmation of necessity for PIC-model

As a first step of code validation, the code TWANG-PIC was benchmarked against the original code TWANG. For this study, the case of the DNP-gyrotron was used.

The geometry of the cavity interaction region together with the inhomogeneous magnetic field profile were presented in Fig. 2.4. The typical system parameters for simulations describing the

3.4. 1D-PARTICLE-IN-CELL APPROACH: TWANG-PIC

Transverse mode	TE _{7,2}	
Magnetic field	B_0	9.45 – 9.70 T
Pitch-angle	α	1 – 2.4
Beam current	I_b	5 – 140 mA
Guiding center radius	R_g	1.394 mm
Beam energy	V_b	15.5 kV
Wall conductivity	σ	$2.9 \cdot 10^9$ S/m
Time step (TWANG-PIC)	Δt	1.8 ps = $3/\omega_0$
Time step (TWANG)	Δt	63 ps = $0.01 \cdot 2Q/\omega_0$
Injected particles (TWANG-PIC)	N_{inj}	32
Injected particles (TWANG)	N_{inj}	256
No. of time steps (TWANG-PIC)	N_t	240000
No. of time steps (TWANG)	N_t	10000
No. of points in z	N_z	500-2113
Pitch-angle spread	$\Delta\alpha$	0%
Energy spread	$\Delta\gamma$	0%
R_g -spread	ΔR_g	0%

Table 3.3: Typically used simulation parameters for simulations on the DNP-gyrotron.

wave-particle interaction are listed in table 3.3.

For this gyrotron, the operating region in the $(B_0 - I_b)$ -parameter plane has been shown in Fig. 2.7 in chapter 2. As described there, the forward-interaction region in the DNP-gyrotron is given by the region of magnetic field with $B_0 < 9.589$ T.

For a first comparison, a stationary operating point in the forward-wave regime was chosen, using the operating parameters $B_0 = 9.535$ T, $I_b = 20$ mA and $\alpha = 1.9$. For this operating point, Fig. 3.5 shows a comparison of the field amplitude and phase in the cavity between TWANG-PIC and TWANG. It is observed, that for both the amplitude and phase profile the result of the two codes matches very closely. The field profile corresponds to a stationary field profile, which is close to that of the cold-cavity axial mode $q=1$, shown in Fig. 3.1.

The same agreement is found for the particle evolution in energy and slow gyro-phase Ψ versus z , as it can be seen in Fig. 3.6. For TWANG, the electron distribution at the end of the simulation time is shown as lines, because the electron properties are calculated as trajectories of the injected electrons for each time step. In the PIC-version, the electron distribution is more uniform both in energy/phase and along the axial direction, since the electrons are no longer located on the grid points. However, the particle density in energy and phase over the interaction region is observed to be the same, so that the obtained bunching matches very well between the two codes. This clearly shows that the TWANG-PIC code is correctly simulating the beam-wave interaction for this considered cavity geometry and operating point.

In order to have a more complete comparison between the two codes, their behavior has been analysed not only for a single operating point, but over a range of parameters. Thus, the output parameters of the above-mentioned gyrotron were analysed at different values of the normalized

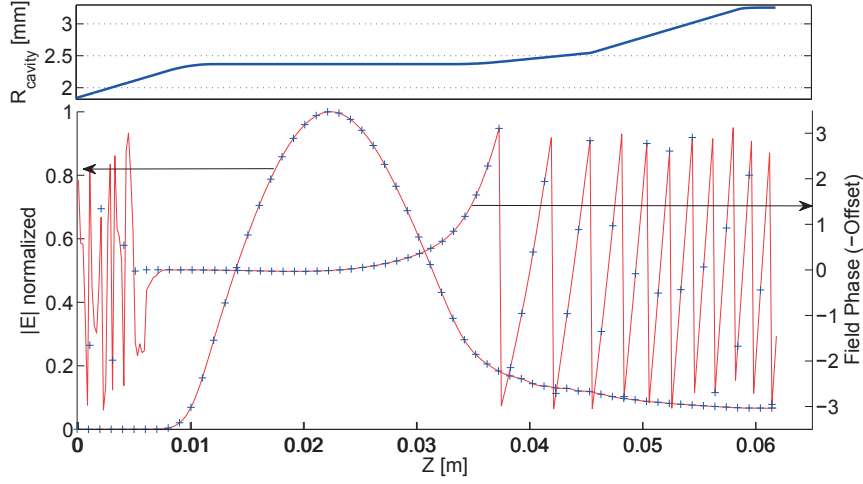


Figure 3.5: Top: Profile of the cavity wall radius as a function of the axial coordinate, as used in the simulations. Bottom: Self-consistent axial profile of the absolute value and phase of the electric field along the cavity. The profiles are a snapshot at the same instant from TWANG-PIC (red lines) and from TWANG (blue crosses). For a better visibility, only a certain number of points from TWANG are displayed and the offset of the field phase has been subtracted for both cases. The simulation parameters are $B_0 = 9.535\text{T}$, $I_b = 20\text{mA}$, $\alpha = 1.9$, $V_b = 15.5\text{kV}$.

detuning

$$\Delta_0 = \frac{\gamma_0 - s \frac{\Omega_c}{\omega_0}}{\hat{p}_{z,0}}, \quad (3.30)$$

which corresponds to the definition in Eq. (3.18a) using the initial relativistic factor $\gamma_0 = \gamma(z_{\text{in}})$ and parallel momentum $\hat{p}_{z,0} = \hat{p}_z(z_{\text{in}})$, as well as the angular reference-frequency ω_0 (set to cold-cavity frequency of the $q=1$ -axial mode). The scan in detuning was performed by varying the cavity magnetic field with a fixed beam current of $I_b = 20\text{mA}$ and a pitch-angle $\alpha = 1.9$.

The results of these simulations are presented in Fig. 3.7, showing the power (part a)) and the self-consistent oscillation frequency (part b)) as a function of the cavity magnetic field (bottom x -axis) and of the normalized detuning (top x -axis). At first, the reference frequency is chosen as the cold-cavity eigenmode frequency with the axial mode number $q=1$ (TWANG-PIC in blue, TWANG in red/dashed). For these simulations the results of TWANG and TWANG-PIC match very well in the forward-wave region. In the backward-wave region (detuning $\Delta_0 < 0$, higher B_0) however, the difference between the two codes is relatively large. If the reference frequency then is adjusted iteratively to the self-consistent oscillation frequency, it is observed, that both power and frequency of the TWANG-simulations (magenta/dotted line) converge towards the value from TWANG-PIC (green/dash-dotted line). The result of the latter code on the other hand stays nearly unchanged when changing the reference frequency towards the self-consistent oscillation frequency. This observation is independent of the chosen boundary condition.

The result shows, that the PIC-code is much less sensitive to the arbitrary choice of the reference frequency for stationary oscillation points. Recently the dependence of the simulation results

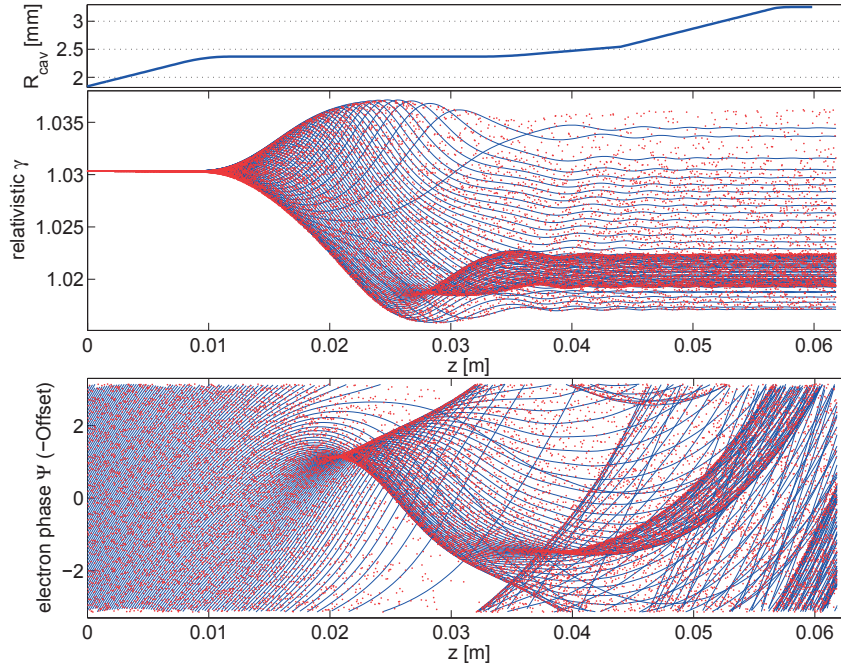


Figure 3.6: Instantaneous particle distribution in the relativistic γ -factor, corresponding to the particle energy, and in the slow gyro-phase Ψ along the interaction region. The snapshots are taken at the same simulation time as in Fig. 3.5 and for both codes $N_{\text{inj}} = 64$ particles were used. For the TWANG-simulation (blue lines) the electron trajectories are shown as lines. For TWANG-PIC (red points) however, for one simulation time only the instantaneous position, energy and phase are known and displayed. In the lower plot, again a constant phase offset between the result of the two codes has been subtracted.

on the reference frequency in the frame of the trajectory-approach has been studied in [122]. As suggested in [122], the reason for the dependency on the reference frequency is that the temporal variation of the field phase profile, which is present, if the reference frequency is not equal to the self-consistent RF-frequency, is not included in the equations of motion of TWANG. As it was described above in section 3.3, there the field profile (amplitude and phase) is supposed to be fixed during the electron transit time. If the reference frequency however matches exactly the oscillation frequency, the phase profile is constant in time, so that the field phase experienced by the electrons along the trajectory is the true phase.

Thus, the temporal variation of the field phase is expected to be stronger, if the self-consistent frequency deviates more from the reference frequency. By choosing the reference frequency equal to the cold-cavity frequency of the $q=1$ mode, the condition $f_{\text{RF}} = f_0$ is approximately fulfilled in the forward-wave region. In the backward-region however, where the self-consistent effects are dominant, this condition is no longer satisfied. This results in a deviation of the from TWANG-result from the correct result in the backward-region, if the reference frequency is not iteratively adjusted towards the self-consistent oscillation frequency.

Once the iterative frequency-adjustment in TWANG is converged, there is no significant differ-

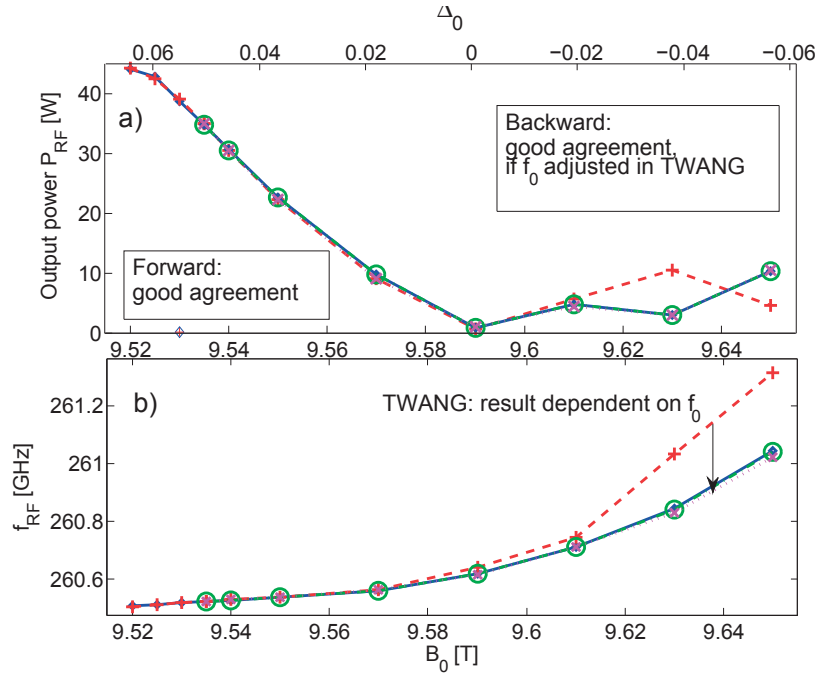


Figure 3.7: Radiated power (a) and self-consistent oscillation frequency (b) as a function of the cavity magnetic field (bottom x -axis) and of the normalized detuning (top x -axis). The red, dashed line ('+') corresponds to the radiation as simulated in TWANG with a reference frequency $f_0 = 260.507$ GHz, that corresponds to the cold-cavity eigenfrequency for the $TE_{7,2,1}$ -mode. The results from TWANG-PIC with the same input parameters are shown in blue (solid, diamonds). The TWANG-result with the reference frequency iteratively adapted to the RF-frequency is represented by the magenta/dotted line ('x') and the same for TWANG-PIC is shown as the green/dash-dotted line (circles). In the backward-region (higher B_0), the TWANG-result with a fixed f_0 deviates from the other results. In the hard-excitation-region (low B_0), only the result with a fixed f_0 is shown.

ence between the two results for such a case of mono-frequency oscillation.

Influence of reference frequency on non-stationary oscillations

Non-stationary regimes are associated with a multi-frequency or broadband spectrum. Because of this, the result of the previous paragraph is important for simulating non-stationary regimes. If in a broadband spectrum the reference frequency is chosen as the one corresponding to the dominant peak of the obtained spectrum, it might be well separated from the other relevant frequencies present in the oscillation, so that these frequency-components are not represented properly in TWANG. This means that there are two restrictions for simulating non-stationary regimes with a code as TWANG, based on the trajectory-approach. Firstly, the model assumption of time-scale separation is violated as explained in section 3.4.1 and secondly, in practice the reference frequency cannot be iteratively adjusted towards the oscillation frequency. Both

these restrictions are removed when moving towards a (reduced) PIC approach. In the previous subsection, it was already shown, that for single-frequency operating points the result of TWANG-PIC is much less sensitive to the reference frequency.

This is also the case for a non-stationary operating point, as it will be demonstrated here. The details and extent of the non-stationary regime in the discussed gyrotron will be discussed extensively in chapter 5, but at this point we will already use one of the operating points inside the non-stationary regime for demonstrating the necessity of the PIC-model for non-stationary oscillations. This is shown in Fig. 3.8 a) and b), which shows the spectrum obtained with TWANG-PIC (Fig. 3.8 a) and TWANG (Fig. 3.8 b) for the operating point $B_0 = 9.60$ T, $I_b = 67$ mA, $\alpha = 1.9$ with the cavity-geometry and parameters as above. The different colors and line styles corre-

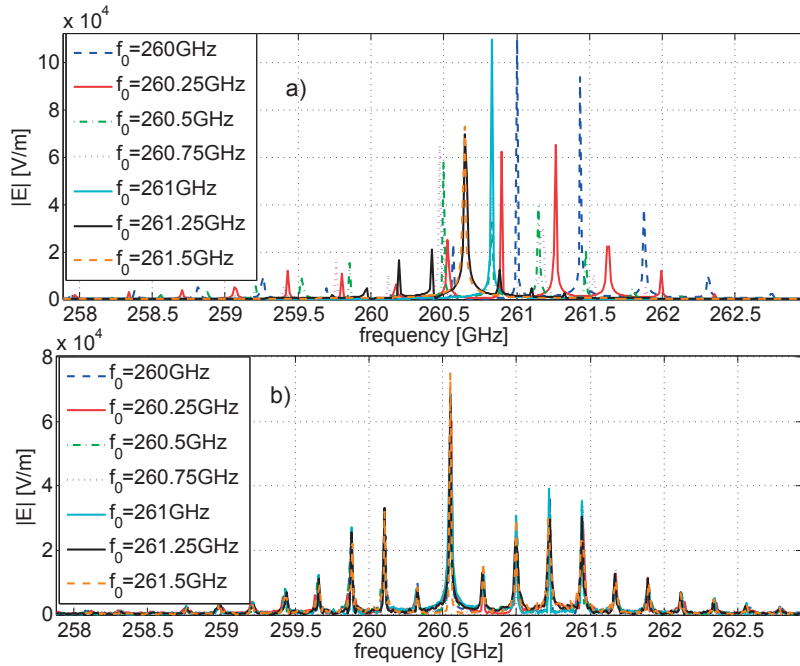


Figure 3.8: Spectra from TWANG-PIC (top part) and TWANG (bottom part) for the non-stationary operating point $B_0 = 9.60$ T, $I_b = 67$ mA, $\alpha = 1.9$. The different line styles and colors correspond to different reference frequencies (see legend).

spond to different reference frequencies, varied over the range of frequencies, that is present in the spectrum.

Again, the obtained spectrum is practically independent of the reference frequency for TWANG-PIC, but changes completely for TWANG-simulations, including a transition from nearly equal-amplitude sidebands (e.g. $f_0 = 260.25$ GHz) to stationary, mono-frequency oscillation (e.g. $f_0 = 261.0$ GHz). Unlike for stationary oscillations with a single RF-frequency, in this situation the reference frequency cannot be adjusted towards the oscillation frequency and there is no good choice of reference frequency, so that the simulation results are not reliable. The impossibility of choosing a correct reference frequency was observed to be a practical implication of the more abstract concern, that an inappropriate model is used for the beam-wave interaction. This

figure shows indeed that the model of the TWANG-code is inappropriate for simulating a multi-frequency oscillation and that in such a case the change towards a Particle-In-Cell approach is necessary.

3.5 Linear model and starting current calculations

The linear interaction model describes the beam-wave interaction in the limit of a small RF-field amplitude. The sign of the linear growth rate determines, whether a certain mode can grow from noise or would decay, if excited. The instability limit, where the change of sign occurs, depends on the parameters of the electron beam and is represented by the starting current. The linear analysis, and in particular the calculation of the starting current, plays a major role in gyrotron research [123, 124, 20]. However, this field is still being explored and has been subject to recent publications [125, 126, 127, 128, 129, 130].

The lowest order estimation for a linear model is that the profiles of the RF-mode are unchanged by the presence of the electron beam, which is supposed to only influence the field amplitude. If in addition to this assumption, the cold-cavity axial field profile is considered to interact with the beam inside a uniform-radius interaction structure, then an analytic solution exists for the calculation of the starting current. At SPC, this calculation is performed in the MATLAB-function SC by solving the equation, that is described in [28] (Eq. (5.40)), where the starting current I_{st} is explicitly expressed as:

$$\frac{1}{I_{st}} = - \left(\frac{QZ_0 e}{8\gamma_0 m_e c^2} \right) \left(\frac{\pi}{\lambda} \int_0^L |\hat{F}_q(z)|^2 dz \right)^{-1} \cdot \left(\frac{k_{\perp} C_{mp} G_{mp}}{\beta_{z0} (s-1)!} \right)^2 \cdot \left(\frac{ck_{\perp} \gamma_0 \beta_{\perp 0}}{2\Omega_c} \right)^{2(s-1)} \cdot \left(s + \frac{1}{2} \frac{\omega_{cold,q} \beta_{\perp 0}}{v_{z0}} \frac{\partial}{\partial \Delta_s} \right) \cdot \left| \int_0^L \hat{F}_q(z) e^{i\Delta_s z} dz \right|^2 \quad (3.31)$$

Here, the detuning is defined as $\Delta_s = \frac{\omega_{cold,q}}{v_{z0}} \left(1 - \frac{s\Omega_c(z)}{\omega_{cold,q}\gamma_0} \right)$ and the beam-wave coupling term is $G_{mp} = (\pm 1)^s J(k_{\perp} R_g)$ (with \pm for co- / counter- rotating mode) and $\hat{F}_q(z)$ is the fixed normalized field axial profile of the cold-cavity mode q . Additionally, λ expresses the vacuum wavelength and $\beta_{z0} = \frac{v_z(z_{in})}{c}$ and $\beta_{\perp 0}$ are the parallel and perpendicular component of the normalized initial velocity.

This way, the starting current for different longitudinal modes is calculated separately by using their axial profile from cold-cavity calculations performed by the code package CAVITY, described in section 3.1. This approach of first calculating a given eigenmode of the cold-cavity (i.e without electron beam) and using this solution for determining the starting current conditions is very commonly used in gyrotron modeling [131, 130, 129]. The non-self-consistent approach is satisfactory for situations in which the self-consistent effects are not dominant. This is often the case on the normal operating points of high power gyrotrons, where the RF-frequency is close to the cut-off frequency and the radiation properties are dominated by the cavity-geometry. Already in these situations, self-consistent effects start to be relevant for low quality factor gyrotron cavities [132].

For all other situations which are dominated by self-consistent effects the starting current calculations based on the cold-cavity RF-field profile fail to give a usable result. Especially in the gyro-BWO operating regime characterized by a negative detuning, it is known that the calculation of

3.5. LINEAR MODEL AND STARTING CURRENT CALCULATIONS

the starting current should be performed self-consistently [133, 134, 135, 136]. In this operating regime, the RF-field-profile in the cavity resonator develops fully self-consistently by an intrinsic coupling between the forward-moving electrons and the backward-moving wave, so that it strongly deviates from the cold-cavity RF-field profile [88, 127]. The linear self-consistent field profile should also be taken into account for the starting current calculation in gyrotron oscillators and/or the onset conditions of instabilities in gyro-amplifiers or beam-ducts [137, 138, 139]. Knowledge of the starting-current in the gyro-BWO regime is important for example for the development of low-power gyrotrons with continuous frequency-tunability, where the operation point is placed into the gyro-backward-wave regime suitable for performing the frequency tuning [31].

Also if the excitation of unwanted ('parasitic') modes outside the flat cavity section is studied, the self-consistent effects have to be included, because these modes may be excited in backward-interaction and/or because their RF-field profile is often strongly influenced by the presence of the electron beam. This is true both for parasitic instabilities in beam-ducts and for ACI in the after-cavity section [140, 141, 125].

When a linear self-consistent model is not available, a commonly applied method is the use of *non*-linear self-consistent models for the analysis of the linear behavior of a gyrotron [128, 126]. This can be problematic, firstly because, in contrast to linear simulations, the result of non-linear simulations depends on the initial conditions of the simulation [35] (of importance e.g. in the hard-excitation region), secondly because a non-linear code often fails to reach the required numerical accuracy necessary for modeling the linear regime.

Because of the above-described obvious need for self-consistent linear modeling, a new linear self-consistent beam-wave interaction model has been developed in the frame of this thesis and implemented in the code TWANGLIN. This approach for determining the linear behaviour and self-excitation conditions of a gyrotron oscillator represents an improvement with respect to the commonly used method for the calculation of starting currents [142, 124, 134, 133, 131] and is of importance both for the development of high power gyrotrons, as used for electron cyclotron resonance heating (ECRH) of magnetically confined plasmas, but also for the development of medium-power gyrotrons for other applications. This same approach can be used for studying absolute instabilities in gyro-amplifiers [143].

The simplified model, which is derived from the non-linear model described in section 3.3, and its resulting simulation code have been published in a journal article [99] and in a conference contribution [144] and will be described in detail in the following subsections.

3.5.1 TWANGLIN-model

Linearization of TWANG-model

In the following paragraphs, it will be shown how the linear model is obtained from a linearization of the self-consistent *non*-linear time-dependent equations of the TWANG-code with respect to a small amplitude of the RF-field.

The model of TWANG has been described in section 3.3, but for coherence we repeat the model

Eqs. (3.11)-(3.13) at this point:

$$\frac{d\mathcal{P}}{d\hat{z}} = \left(-i\Delta + \frac{s}{2} \frac{d(\ln B_0)}{d\hat{z}} \right) \mathcal{P} + s(-\gamma F^* + i\hat{p}_z F'^*) C_0 \frac{\hat{p}_\perp^{2s-2}}{\hat{p}_z}, \quad (3.32)$$

$$\frac{d\hat{p}_z}{d\hat{z}} = -\frac{C_0}{\hat{p}_z} \text{Im}(F' \mathcal{P}) - \frac{1}{2} \frac{\hat{p}_\perp^2}{\hat{p}_z} \frac{d(\ln B_0)}{d\hat{z}}. \quad (3.33)$$

$$\left(\frac{2i}{\omega_0} \frac{\partial}{\partial t} + \frac{\partial^2}{\partial \hat{z}^2} + \kappa_{||0}^2 \right) F = i\mathcal{I} \left\langle C_0 \frac{\mathcal{P}^*}{p_z} \right\rangle. \quad (3.34)$$

These equations are linearized by considering the amplitude of the RF-field, F , as a first-order perturbation on the electron motion. The zero-order equations are obtained by neglecting the influence of the electric field on the electron motion, i.e. setting $F = 0$:

$$\frac{d}{d\hat{z}} \mathcal{P}_0 = \left(-i \frac{\gamma_0 - s \frac{\Omega_c}{\omega_0}}{\hat{p}_{z0}} + \frac{s}{2} \frac{d(\ln B_0)}{d\hat{z}} \right) \mathcal{P}_0 \quad (3.35)$$

$$\frac{d\hat{p}_{z0}}{d\hat{z}} = -\frac{1}{2} \frac{p_{\perp 0}^2}{\hat{p}_{z0}} \frac{d(\ln B_0)}{d\hat{z}} \quad (3.36)$$

In these equations we can identify the conservation of magnetic moment in the real part of the 0th-order perpendicular equation of motion (Eq. (3.35)) and the conservation of kinetic energy in the 0th-order parallel equation of motion (Eq. (3.36)):

$$\frac{d}{d\hat{z}} \frac{\hat{p}_{\perp 0}^2}{B_0} = 0 \quad (3.37)$$

$$\frac{d}{d\hat{z}} (\hat{p}_{z0}^2 + \hat{p}_{\perp 0}^2) = 0, \quad (3.38)$$

where Eq. (3.37) has been used for deriving Eq. (3.38).

The imaginary part of the perpendicular equation (Eq. (3.35)) describes the axial dependence of the zero-order slow-timescale phase due to the mismatch between the electromagnetic wave and cyclotron angular frequencies:

$$\frac{d\Psi_0(\hat{z})}{d\hat{z}} = \Delta_{z0} = \frac{\gamma_0 - s \frac{\Omega_c(\hat{z})}{\omega_0}}{\hat{p}_{z0}(\hat{z})}, \quad (3.39)$$

where the zero-order, z -dependent normalized detuning Δ_{z0} has been introduced.

Treating the electric field F as a first order perturbation, we obtain the following set of linearized

first-order equations (linear perturbations indexed by 1):

$$\begin{aligned} \frac{d}{d\hat{z}} \mathcal{P}_1 &= \left(-i \frac{\gamma_0 - s \frac{\Omega_c}{\omega_0}}{\hat{p}_{z0}} + \frac{s}{2} \frac{d(\ln B_0)}{d\hat{z}} \right) \mathcal{P}_1 \\ &+ i \frac{(\gamma_0 - s \frac{\Omega_c}{\omega_0}) \frac{\hat{p}_{z1}}{\hat{p}_{z0}} - \gamma_1}{\hat{p}_{z0}} \mathcal{P}_0 \\ &+ s (-\gamma_0 F^* + i \hat{p}_{z0} F'^*) C_0 \frac{\hat{p}_{\perp 0}^{2s-2}}{\hat{p}_{z0}} \end{aligned} \quad (3.40)$$

$$\begin{aligned} \frac{d}{d\hat{z}} \hat{p}_{z1} &= -\frac{C_0}{\hat{p}_{z0}} \text{Im}(F' \mathcal{P}_0) \\ &+ \left(\frac{\frac{1}{2} p_{\perp 0}^2 \frac{\hat{p}_{z1}}{\hat{p}_{z0}} - p_{\perp 0} p_{\perp 1}}{\hat{p}_{z0}} \right) \frac{d(\ln B_0)}{d\hat{z}} \end{aligned} \quad (3.41)$$

$$\left(\frac{2i}{\omega_0} \frac{\partial}{\partial t} + \frac{\partial^2}{\partial \hat{z}^2} + \kappa_{\parallel}^2 \right) F = i \mathcal{I} \left\langle C_0 \left(\frac{\mathcal{P}_1^*}{\hat{p}_{z0}} - \frac{\mathcal{P}_0^* \hat{p}_{z1}}{\hat{p}_{z0}^2} \right) \right\rangle. \quad (3.42)$$

In these equations, the first-order perturbations γ_1 and $p_{\perp 1}$ are obtained as:

$$\begin{aligned} \gamma_1 &= \frac{1}{s \gamma_0 \hat{p}_{\perp 0}^{s-2}} \text{Re}(\mathcal{P}_1 e^{i\Psi_0}) + \frac{\hat{p}_{z0}}{\gamma_0} \hat{p}_{z1}, \\ \hat{p}_{\perp 1} &= \frac{1}{s \hat{p}_{\perp 0}^{s-1}} \text{Re}(\mathcal{P}_1 e^{i\Psi_0}). \end{aligned} \quad (3.43)$$

This system of zero-order and first-order equations (Eqs. (3.37)-(3.39) and Eqs. (3.33)-(3.34), solved for N electrons) represents a general self-consistent linear model, describing the gyrotron monomode dynamics in the linear regime.

Moment equations

Including these assumptions, the following sections will present the reduction of the electron equations of motion for N electrons to only two complex field-equations describing the wave-particle interaction dynamics as in a continuous medium by using a moment approach. The set of linearized Eqs. (3.33)-(3.34) can be reduced to a system of only 3 complex Partial Differential Equations (PDEs) under the approximations outlined below.

In the following, in the electron equations of motion no spread in velocity or guiding center radius is considered and the RF-magnetic field (terms including F') is neglected (this is justified for gyrotrons, since usually $k_{\parallel} \ll \omega/c$). Under these assumptions, the wave-particle interaction is dominated by the electron perpendicular motion and, in the following, we will neglect the perturbed parallel momentum by setting:

$$\hat{p}_{z1} = 0. \quad (3.44)$$

The wave equation depending only on the averaged perpendicular motion, we intend to average the remaining perpendicular equations of motion over the electron distribution. After replacing γ_1 and $\hat{p}_{\perp 1}$ (as given in Eq. (3.43)) in Eq. (3.33) and using the above-mentioned assumptions, the electron motion in Eqs.(3.33)-(3.34) reduces to the following N complex equations:

$$\begin{aligned} \frac{d\mathcal{P}_1}{d\hat{z}} = & (-i\Delta_{z0} + \delta)\mathcal{P}_1 - \frac{i\hat{p}_{\perp 0}^2}{2s\gamma_0\hat{p}_{z0}}(\mathcal{P}_1 + \mathcal{P}_1^* e^{-2i\Psi_0}) \\ & - C_0 \frac{s\gamma_0\hat{p}_{\perp 0}^{2s-2}}{\hat{p}_{z0}} F^*, \end{aligned} \quad (3.45)$$

where $\delta = \frac{s}{2} \frac{d}{d\hat{z}} \ln B_0$.

In this linearized model, the dynamics of the electrons is completely described by the 2 dynamic variables \mathcal{P}_1 and Ψ_0 . The electron phase-space distribution function can thus be defined by $\mathcal{F} = \mathcal{F}(\mathcal{P}_1, \Psi_0, z)$. With this, the average of any function $\mathcal{G}(\mathcal{P}_1, \Psi_0)$, introduced in Eq. (3.34), can be defined as:

$$\langle \mathcal{G} \rangle (z) = \frac{1}{N} \iint \mathcal{F}(\mathcal{P}_1, \Psi_0, z) \mathcal{G}(\mathcal{P}_1, \Psi_0) d\mathcal{P}_1 d\Psi_0, \quad (3.46)$$

where the \mathcal{F} is normalized to $N = \iint \mathcal{F} d\mathcal{P}_1 d\Psi_0$, the total number of electrons.

Considering now the average of \mathcal{P}_1^* and $\mathcal{P}_1 e^{2i\Psi_0}$, using Eq. (3.45) and Eq. (3.39) together with

$$\left\langle \frac{d\mathcal{G}}{d\hat{z}} \right\rangle = \frac{\partial}{\partial \hat{z}} \langle \mathcal{G} \rangle, \quad (3.47)$$

derived in [99], one can readily obtain the following closed system of equations for the two complex moments

$$\pi_1 = \langle \mathcal{P}_1^* \rangle \text{ and } \pi_2 = \langle \mathcal{P}_1 e^{2i\Psi_0} \rangle \quad (3.48)$$

and for the complex field F (from Eq. (3.34)):

$$\begin{aligned} \frac{\partial \pi_1}{\partial \hat{z}} &= (i\Delta_{z0} + iC_1 + \delta)\pi_1 + iC_1\pi_2 - C_2 C_0 F, \\ \frac{\partial \pi_2}{\partial \hat{z}} &= (i\Delta_{z0} - iC_1 + \delta)\pi_2 - iC_1\pi_1, \\ \left(\frac{2i}{\omega_0} \frac{\partial}{\partial t} + \frac{\partial^2}{\partial \hat{z}^2} + \kappa_{\parallel}^2 \right) F &= iC_3 C_0 \pi_1. \end{aligned} \quad (3.49)$$

The additional dimensionless parameters in these equations are:

$$\begin{aligned} C_1 &= \frac{\hat{p}_{\perp 0}^2}{2s\hat{p}_{z0}\gamma_0}, \quad C_2 = s\gamma_0 \frac{\hat{p}_{\perp 0}^{2s-2}}{\hat{p}_{z0}}, \\ C_3 &= \frac{eZ_0}{m_e c^2 \hat{p}_{z0}} \frac{I_b}{C_{mp}} \left(\frac{s^s}{2^s s!} \right)^2. \end{aligned} \quad (3.50)$$

Unlike the linearized model described by Eqs. (3.33)-(3.34), in which the equations of motion have to be solved for N electrons separately at each time step, the complete electron behavior

is now included in the field-variables π_1 and π_2 and only three complex equations need to be solved for π_1, π_2 and F .

In contrast to the self-consistent linear model described in [125], this model is time-dependent and expresses the electron motion by moments of the distribution function. Such a moment-based description for the linear electron response was used already in other works, such as in [142], but then with a greatly simplified model for the interaction region.

This set of equations can easily be implemented and is rapidly solved numerically, strongly reducing the numerical effort with respect to the solution of Eqs. (3.33)-(3.34). It has been implemented in the new code TWANGLIN, using the same numerical methods as for the non-linear code TWANG, which were described in section 3.3.1.

TWANGLIN-simulations give the self-consistent linear dynamics of the linearly most unstable mode. The temporal growth rate, the starting current, the linear self-consistent quality factor and the self-consistent frequency can also be calculated. This method is illustrated in the following, where the code is applied to the case of a gyrotron cavity, for which a comparison with experiment is possible.

In the frame of the master thesis by J er emy Genoud[145], this model has been developed further in order to solve the (modified) equations in the frequency-domain instead of in the time-domain. This way, the spectral model, that has been implemented into the code TWANGLIN-SPEC [146], allows obtaining directly the linear properties of all relevant modes instead of only the most unstable mode as in TWANGLIN.

3.5.2 TWANGLIN-benchmarking

A benchmarking of the new code TWANGLIN, solving this simplified set of linear equations, was performed by simulating the linear behavior of the DNP-gyrotron. The details of the interaction structure as well as the typical operating parameters have been mentioned in section 3.4.4 and in chapter 2.

As a first part of the benchmarking, for a specific operating point ($B_0 = 9.57$ T, $I_b = 9$ mA, $\alpha = 1.7$) the results of the linear code TWANGLIN and the *non*-linear version, TWANG, are compared. The simulated temporal behavior of the RF-field amplitude at the exit of the interaction space, $|E(\hat{z}_{\text{out}}, t)|$ is shown in Fig. 3.9. It is observed, that the evolution of the field amplitude predicted by TWANGLIN corresponds to the initial phase of the non-linear gyrotron dynamics predicted by TWANG. The bottom figure shows the temporal evolution of the field amplitude in the transient phase in the beginning of both simulations. In this phase, several axial modes can coexist, of which then only the most unstable one will persist. The growth time of the field amplitude E calculated with TWANGLIN ($\tau_{\text{TWANGLIN}} = 12.8$ ns) does well reproduce the one obtained with the initial linear phase of TWANG ($\tau_{\text{TWANG}} = 11.9$ ns), and the obtained self-consistent frequency in the linear phase is in both cases $f = 260.523$ GHz.

By determining the growth rate of E as a function of the beam current I_b , one can directly obtain the linear self-consistent starting current by finding the current, at which the growth rate changes sign. To illustrate this, the simulated growth rate Γ is represented as a function of the beam current in Fig. 3.10. For beam currents close to the starting current, the growth rate increases linearly with the beam current, as described for instance in [28].

These two results described above already show the proper functioning of the code TWANGLIN,

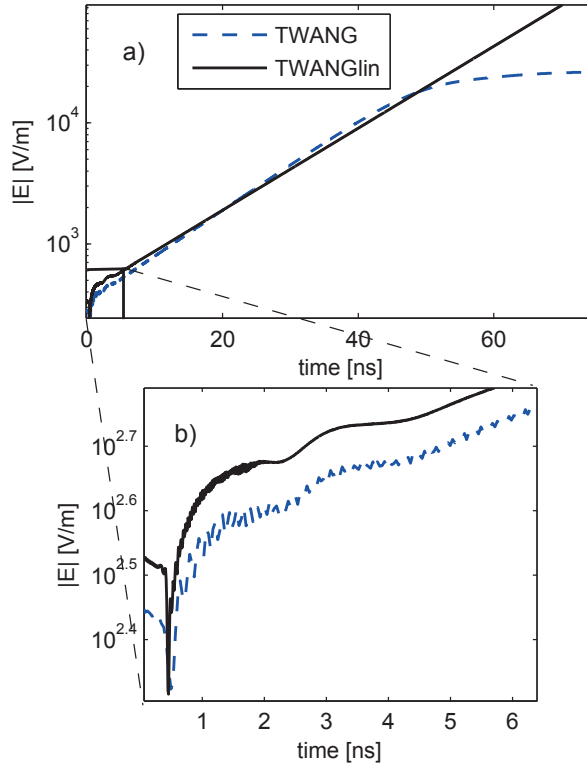


Figure 3.9: Comparison of temporal behavior in the initial phase of TWANG (in blue/ dashed) with the result of TWANGLIN (black). (Parameters: $B_0 = 9.57$ T, $I_b = 9$ mA, $\alpha = 1.7$). (a) Exponential growth of the absolute value of the RF-field at the output of the interaction region up to the saturated phase of the non-linear simulation, (b) Zoom of the transient phase of the simulation.

since it reproduces the behaviour of the benchmarked non-linear code TWANG and it shows the expected dependence of the growth rate on the beam current. A further validation of the code will be presented later on by a comparison of the starting current obtained with TWANGLIN with experimental results.

3.6 Summary of modeling

In this chapter, the available models and simulation codes at SPC have been introduced. It was shown, that within this thesis the available simulation tools were significantly extended. Based on the non-linear code TWANG and the model on which it is based, the codes TWANG-PIC and TWANGLIN were developed.

The code TWANG-PIC extends the applicability of the simulations to regimes with non-stationary oscillations, in which the field profile can vary on a time-scale, that is fast compared to the electron motion. For this, the equations and the numerical approach are changed from a trajectory-approach to a (reduced) PIC-approach. Due to the one-dimensional (3-D momentum) gyro-

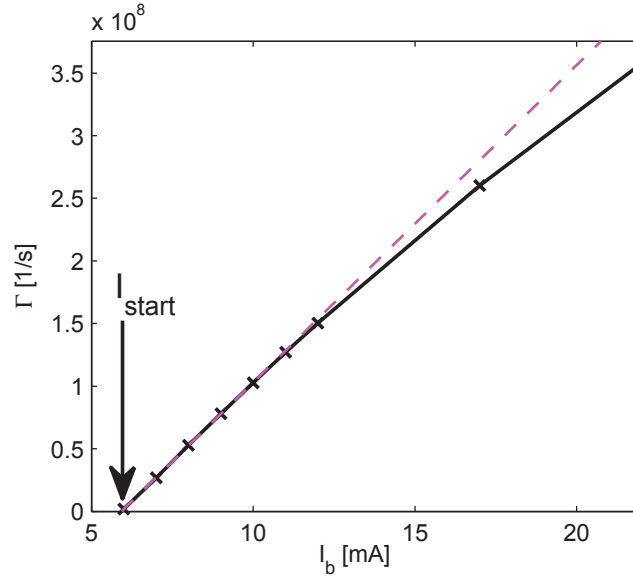


Figure 3.10: Growth rate of the field amplitude obtained from TWANGLIN (black) for a magnetic field of $B_0 = 9.55\text{T}$ versus the beam current. The point, where the growth rate reaches zero corresponds to the linear starting current

averaged description, this code remains numerically fast. It was demonstrated, that this modification was indeed necessary for simulating the non-stationary oscillations that appear in the DNP-gyrotron.

The code TWANGLIN introduces a fundamentally new approach for the linear beam-wave interaction. It is based on the linearized TWANG-model, expressed in a moment-approach with only two dynamic moment-variables describing the electron-motion. It represents a major advancement with respect to non-self-consistent calculations of the starting-current.

Chapter 4

The Stationary Gyrotron Operation Regime

In this chapter, the linear behavior and the stationary operating regime are described for the DNP-gyrotron. The linear behavior of the gyrotron includes the linear dispersion relation, the interaction start-up and the excitation limits which are described by the starting current.

The stationary regime is characterized by a saturated interaction exhibiting a radiation with a single RF-frequency (monomode) and a constant RF-power. Because this kind of operation is required for the gyrotron's basic application in DNP-enhanced NMR-spectroscopy, the stationary operation of the gyrotron was optimized in view of the requirements on this application. In particular the gyrotron operation is optimized, as desired for DNP [19, 147], for a fast or slow frequency-tuning over a maximum possible frequency-range, in combination with a sufficient RF-power (\sim several Watts). Additionally, the stability of RF-frequency and power as well as the achievable spectral purity are addressed.

The above-mentioned aspects of both the linear behavior and the stationary operating regime of the gyrotron will be characterized based on experimental measurements. The experimental results will then be analyzed and interpreted with numerical simulations using the modeling tools that were described in chapter 3.

The chapter is structured in the following way: first, in the linear analysis of section 4.1, the main attention is given to the starting current analysis. Section 4.2 is dedicated to a description of two phenomena close to the starting current in the forward and backward-region. After this, a detailed analysis of the different frequency tuning capabilities of the gyrotron is presented in section 4.3, together with a discussion of the microwave output power and a comparison of both frequency and power with simulations. The influence of the pitch-angle on oscillations and its correct value are discussed in section 4.4. Finally, the operation with pulsed microwave, via an external control of the system parameters, and the stability of the RF-frequency are discussed in sections 4.5 and 4.6 respectively.

4.1 Linear analysis

As a first very basic study, the RF-excitation of the gyrotron can be analyzed with the help of dispersion relations of the cavity field eigenmode and the beam mode. The lowest-order investigation consists in the analysis of the uncoupled dispersion relations in the cold-cavity description, as it was described in section 1.6.

A slightly more evolved estimate can be obtained from an examination of the coupled linear dis-

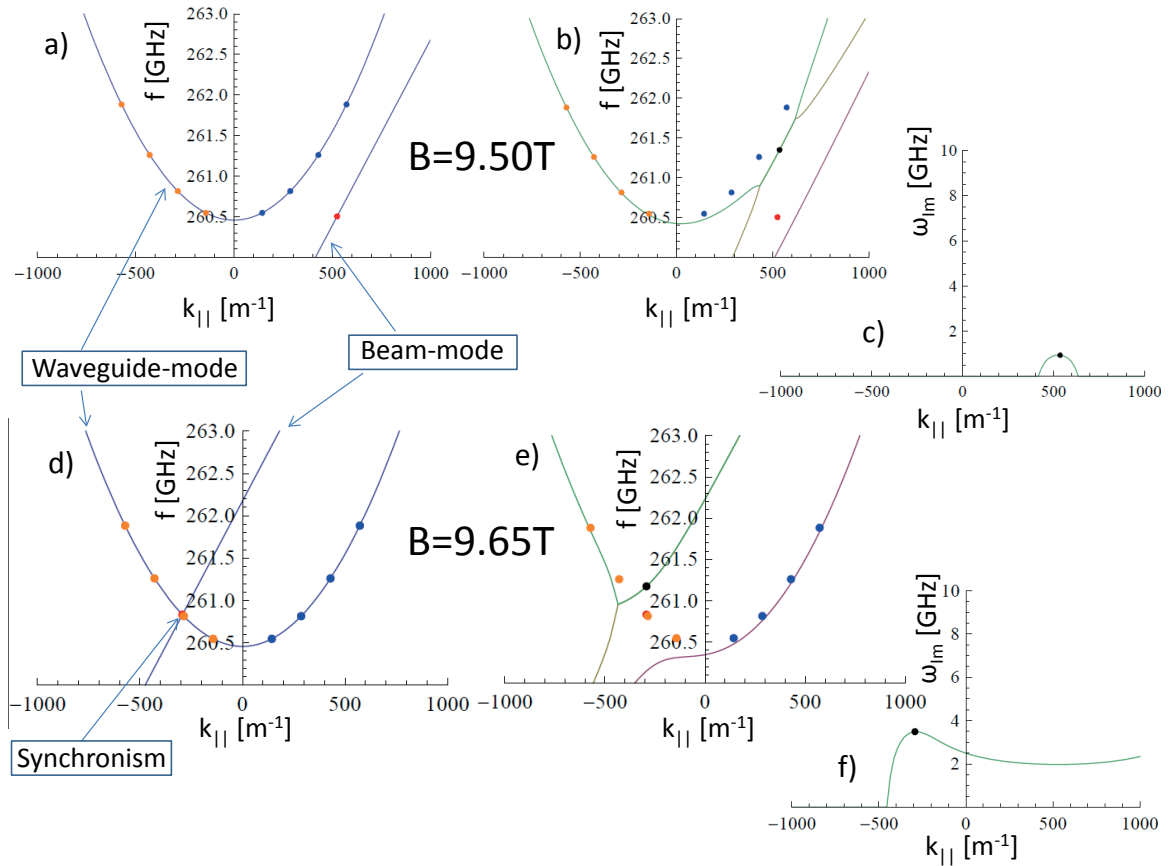


Figure 4.1: Uncoupled and coupled dispersion relations of an infinite system composed of a circular waveguide and an annular electron beam, shown in the plane of frequency and parallel wavenumber. The coupled dispersion relation is calculated as in [20] (Eq. (65)) and in [29] (Eq. (6.3)). In the coupled dispersion relation (b) / (c) and (e) / (f), $I_b = 65$ mA, the beam-wave interaction is supposed to occur at the parallel wavenumber, where the maximum growth rate occurs (black point). Here, the lines of different colors represent the different branches of the dispersion relation, where for the complex branch the real and imaginary part is shown. The points show the basic estimation for axial modes $k_{||} = \pm \frac{q\pi}{L_{\text{eff}}}$ on the uncoupled dispersion relation (q = axial index, L_{eff} = interaction length, '+' for forward-propagation (blue points) / '-' for backward-propagation (orange points)).

4.1. LINEAR ANALYSIS

persion relation in an approach describing the beam-wave interaction occurring in an infinitely long, longitudinally homogeneous system with circular cross-section. The equation for the resulting dispersion relations are described e.g. by Chu [20] (Eq. (65)) and by Nusinovich [29] (Eq. (6.3)).

Both the coupled and uncoupled dispersion relations have been analyzed for a cylindrical waveguide and a magnetized annular electron beam for the designated operating mode $TE_{7,2}$ in the DNP-gyrotron. The obtained dispersion relations are shown in Fig. 4.1, calculated in the forward-regime ($B_0 = 9.50\text{T}$) and in the backward-regime ($B_0 = 9.65\text{T}$), with a pitch-angle $\alpha = 2.3$ and with a current of $I_b = 65\text{mA}$ for the linear dispersion relation.

It shows that for the magnetic field $B_0 = 9.50\text{T}$ (top row) the uncoupled dispersion relation (Fig. 4.1a)) does not show any intersection, but with a linear coupling a region with positive growth rate appears (Fig. 4.1c)). A growing mode is expected from this calculation at $k_{||} \approx 530\text{m}^{-1}$ (maximum growth rate) / $f = 261.35\text{GHz}$ (same $k_{||}$, on dispersion relation). For $B_0 = 9.65\text{T}$, the uncoupled dispersion relations intersect at a negative wavenumber, which indicates a backward-interaction, and also the coupled dispersion relation indicates an interaction at a negative $k_{||}$.

4.1.1 Starting current analysis

The first step of the gyrotron characterization is to measure the excitation limits of the designated transverse mode. This starting current was determined for the operating mode $TE_{7,2}$ in the DNP-gyrotron, and is shown in Fig. 4.2 as a function of magnetic field / detuning Δ_0 (see Eq. (3.30)) with the other parameters fixed as in table 2.3.

Here, the experimentally measured starting current is compared to simulation results from TWANGLIN and to the starting current from linear analysis based on the cold-cavity field profiles of different axial modes calculated as from equation 3.31. Furthermore, the no-oscillation current is included, which defines the lower threshold of the hard-excitation region.

In Fig. 4.2 it is observed, that the starting current in the forward-region ($B_0 < 9.59\text{T}$) approximately follows the typical shape of the cold-cavity starting currents, but in the backward-region remains at low values over the entire operating range of magnetic field. A good agreement is found between the experimentally measured value and the one predicted by the linear self-consistent model (see section 3.5.1) used in the code TWANGLIN. In contrast, one clearly observes in Fig. 4.2, that the starting current based on the fixed-field approach fails to predict the correct values on many points across the considered magnetic field range. This is particularly true for operating points in the backward regime which is dominated by self-consistent effects.

From an inspection of the field profile in TWANGLIN-simulation close to the starting current one can determine, which linear axial mode is excited first at the starting current. A selection of these RF-electric field profiles (both amplitude and phase) is displayed in Fig. 4.3, where the field profiles are compared between TWANGLIN (solid lines) and the profiles of cold-cavity axial modes (dashed) for three magnetic field values, in the forward regime, close to zero-detuning and in the backward regime (compare Fig.4.2). It shows, that the field profiles from TWANGLIN do resemble the ones from the cold-cavity calculations, but with a strongly modified profile shape, both in amplitude and phase. In particular, the phase profile close to (Fig. 4.3 b)) and inside the backward region (Fig. 4.3 c)) clearly shows a backward-propagating behavior in the TWANGLIN-phase profiles, but not in the cold-cavity profiles.

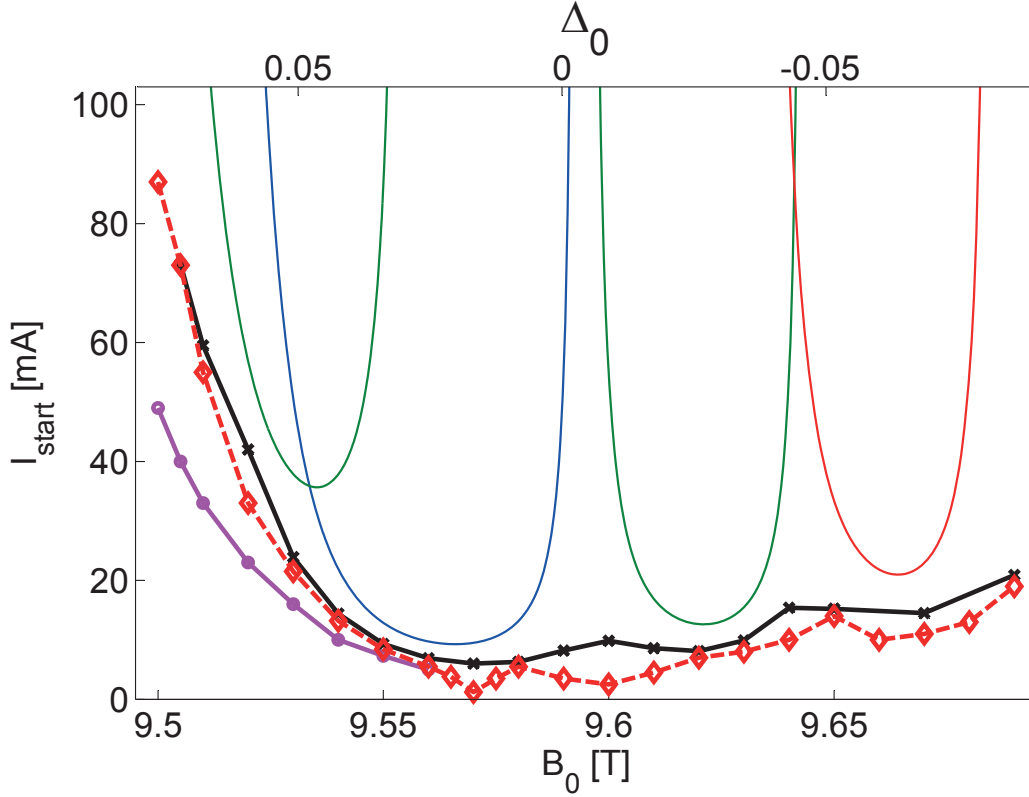


Figure 4.2: Starting current I_{st} for $TE_{7,2}$ -mode from experiment (red / dashed), TWANGLIN-simulations (black / solid) and linear analysis based on fixed-field calculations (thin solid) for axial modes $q=1$ (blue), $q=2$ (blue) and $q=3$ (red). The top x -axis shows the detuning Δ_0 (see Eq. (3.30)). The hard-excitation region from experiment is situated between the no-oscillation current (pink/solid) and the red / dashed and curve. The experimental system parameters are given in table 2.3, the anode-voltage is fixed at $V_a = 8.8$ kV, corresponding to a pitch-angle $\alpha \approx 1.8 - 2.0$ (see Fig. 2.5). Simulation parameters: see table 3.3, with $\alpha = 1.7$.

A further analysis of such field profiles from TWANGLIN showed, that the field profile for each value of magnetic field resembles the cold-cavity field-profile of the mode with the lowest starting current in the fixed-field calculation (thin lines in Fig. 4.2). Thus, the field profile along the starting current changes in the sequence of linear axial modes $q=2 \rightarrow q=1 \rightarrow q=2 \rightarrow q=3$ with increasing magnetic field. Here, the transition $q=2 \rightarrow q=1$ around $B_0 = 9.53$ T (see Fig. 4.2) corresponds to a sudden change from the field profile in Fig. 4.3 a) to the one in Fig. 4.3 b). The transition of the field profile $q=1 \rightarrow q=2$ and $q=2 \rightarrow q=3$ at higher magnetic field values however appears as a smooth transition between linear axial modes with a gradually changing field profile for an increasing magnetic field. This smooth transition between the modes leads to the field profile appearing in Fig. 4.3 c) from the region of transition between the linear modes $q=2 \rightarrow q=3$. Here only a smaller third maximum appears in the field amplitude, so that the field profile does neither completely resemble the cold-cavity profile of $q=2$ nor from $q=3$, due to the gradual

4.2. BEHAVIOR CLOSE TO STARTING CURRENT

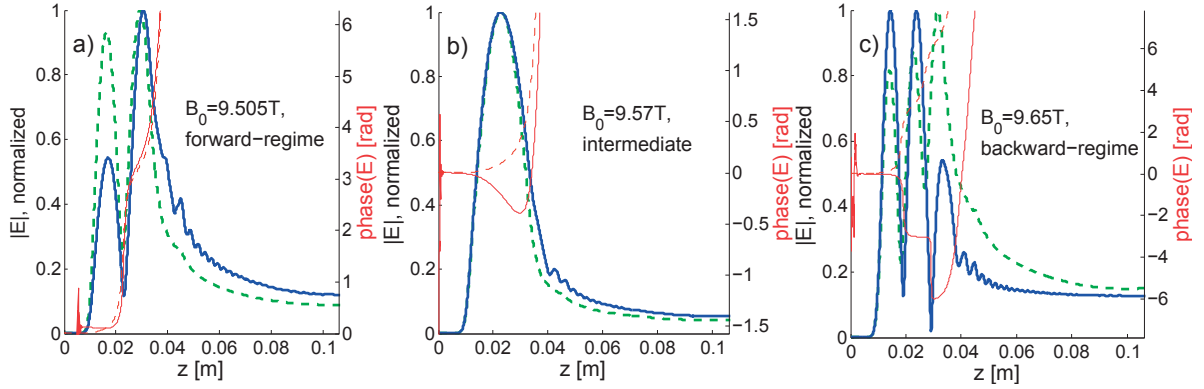


Figure 4.3: Normalized amplitudes (blue, left y-axis) and phases (red / fine line, right y-axis) of the electric field from TWANGLIN along the cavity axis for three different values of the magnetic field, at a current slightly exceeding the starting current (compare Fig.4.2). As a comparison, the amplitude (green/dashed) and phase (red/dashed) profiles of the corresponding cold-cavity modes has been added. a) $B_0 = 9.505$ T, forward regime, b) $B_0 = 9.57$ T, detuning close to zero, c) $B_0 = 9.65$ T, backward regime.

change of the field profile.

Comparing the TWANGLIN-starting current with the above-described electric field profiles, it shows, that the starting current shows a local minimum, where the field profile clearly corresponds to that of a certain linear axial mode ($B_0 \approx 9.57$ T, $B_0 \approx 9.62$ T and $B_0 \approx 9.67$ T), while the starting current has local maxima during the gradual transition of the field profile between these modes ($B_0 \approx 9.595$ T and $B_0 \approx 9.64$ T)

In earlier measurements, that have been included in publications [55, 99], the starting current in the backward-region was significantly higher than the one shown here (up to $I_{st} = 54.6$ mA at $B_0 = 9.65$ T). This difference was caused by the measurement method, that did not recognize the RF-output of very low powers ($P_{RF} \lesssim 20$ mW), that is emitted in the region of high magnetic fields and low currents, as it will be described in section 4.2.2.

In addition to this characterization of the designated transverse mode $TE_{7,2}$, also the starting current of the neighboring counter-rotating modes $TE_{-4,3}$ (lower magnetic fields) and $TE_{-2,4}$ (higher magnetic fields) was characterized experimentally. The results of this study are shown in Fig. 4.4. These measurements show that the starting currents of the other transverse modes are slightly higher, but of the same order as the starting current of $TE_{7,2}$. At the same time the overall shape of the starting current is similar for the different transverse modes.

4.2 Behavior close to starting current

4.2.1 Linear versus non-linear phase of interaction in forward-regime

In this section, the interaction will be analyzed in the the transition between the linear and the non-linear phase of the RF-startup at the starting current , comparing simulation with experi-

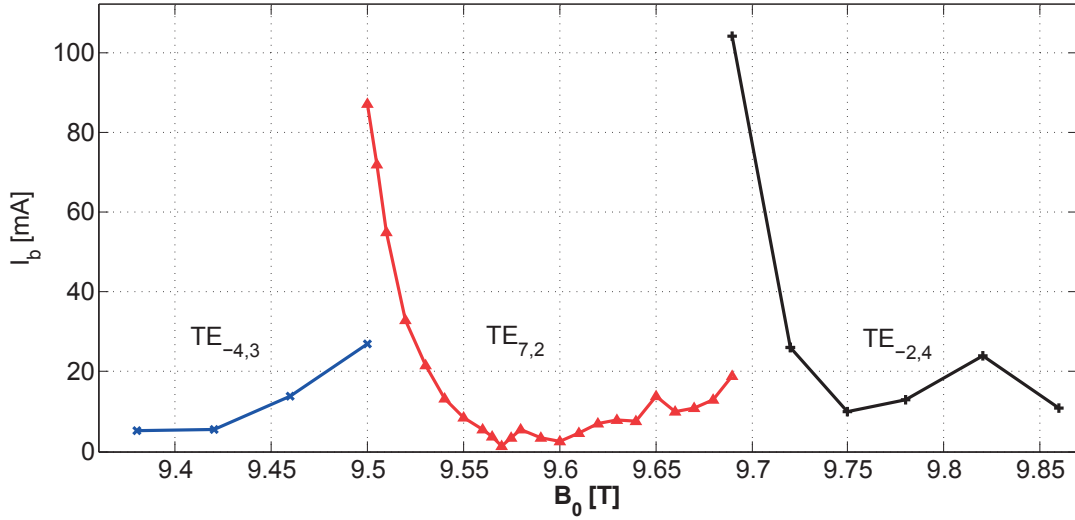


Figure 4.4: Experimental starting current versus magnetic field for designated operating transverse mode $TE_{7,2}$ (red) together with neighboring counter-rotating modes $TE_{-4,3}$ (blue) and $TE_{-2,4}$ (black). Parameters as in section 2.1.2, with $V_a = 8.8$ kV.

ment.

The presented analysis of linear axial modes based on the axial field profiles can be completed with the help of the self-consistent frequency in the linear regime from TWANGLIN-simulations. This RF-frequency from TWANGLIN is shown in Fig. 4.5, together the RF-frequency in the non-

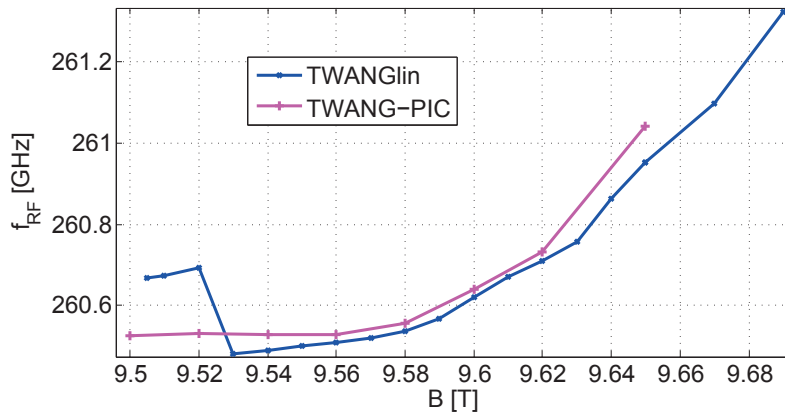


Figure 4.5: Self-consistent RF-frequency obtained from TWANGLIN (linear interaction) and TWANG-PIC (non-linear saturated regime) for a beam-current close to the starting current (compare Fig. 4.2), as a function of the magnetic field. Simulation parameters from table 3.3, ($\alpha_{twanglin} = 1.7$, $\alpha_{twangpic} = 1.89$).

linear regime predicted by TWANG-PIC for a current close to the starting current, versus the

4.2. BEHAVIOR CLOSE TO STARTING CURRENT

magnetic field.

In the region of higher magnetic fields (backward regime), where the field profiles in Fig. 4.3b)-c) showed a change between linear axial modes, a smooth behavior of the TWANGLIN-frequency is observed. This confirms the above-mentioned smooth transition between linear axial modes in the backward-regime. In the forward-region however, the frequency from TWANGLIN shows a step transition between the higher frequency of the linear $q=2$ -axial mode and lower frequency of the linear $q=1$ mode. This demonstrates the step-transition between these modes in the forward-region that was also described for the field profiles in Fig. 4.3a)-b).

The RF-frequency in the non-linear, stationary regime from TWANG-PIC generally slightly ex-

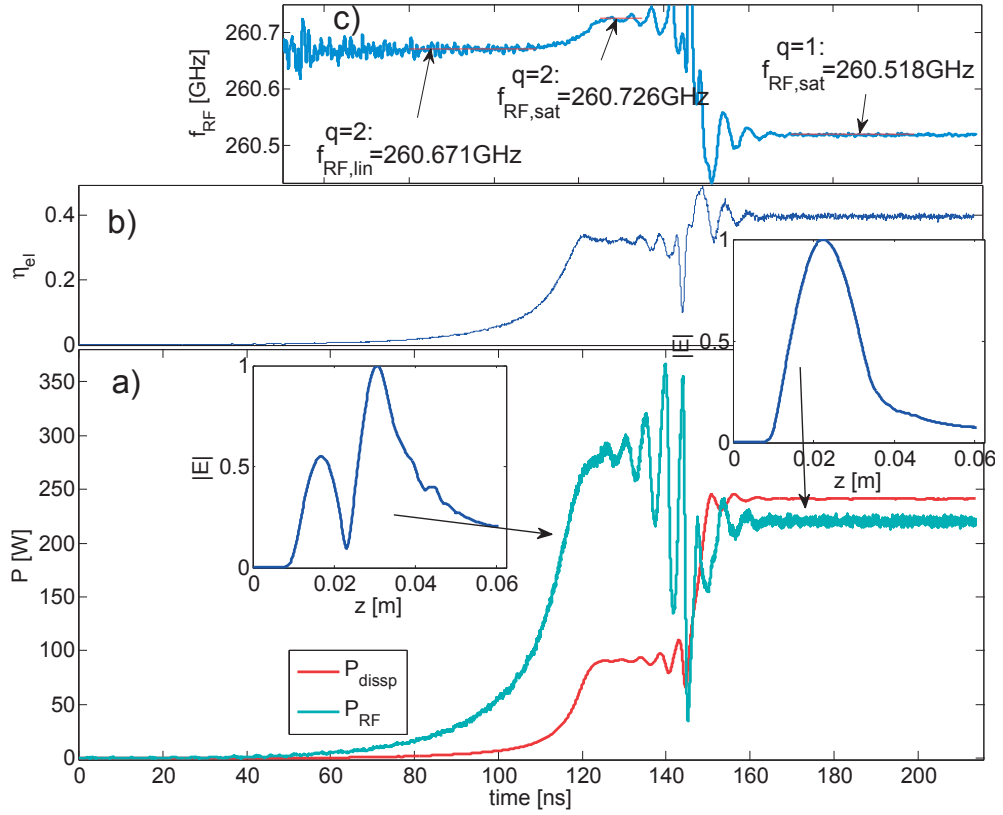


Figure 4.6: Longitudinal mode competition observed in TWANG-PIC-simulations for the operating point ($B_0 = 9.505\text{T}$ / $I_b = 75\text{mA}$ / $\alpha = 1.67$): ,a) evolution of RF-power and dissipated power, b) electron efficiency, c) instantaneous RF-frequency (from field phase derivative at output) and the corresponding field profiles (inlets) taken at times $t = 103\text{ns}$ (linear interaction) and at $t = 213\text{ns}$ (non-linear stationary regime). The $q=2$ -mode is observed in the phase of linear interaction (exponential growth) and in the short saturation phase ($t \sim 130\text{ns}$), whereas the non-linear $q=1$ -mode develops in the final stationary phase.

ceeds the frequency for linear interaction from TWANGLIN, except in the forward-region, where the frequency from TWANG-PIC does not show a step discontinuity. This illustrates, that in the non-linear, saturated phase of the interaction the $q=1$ -mode remains dominant also in the

forward-region.

The evolution from the linear phase of interaction to the non-linear phase is illustrated in Fig. 4.6. Here the TWANG-PIC-simulation close to the starting current in the forward-region shows, how the mode non-linearly evolves from the $q=2$ to the $q=1$ -mode. In the phase of linear interaction with exponential growth, a $q=2$ -mode appears with a frequency corresponding to the one from TWANGLIN in Fig. 4.5. In the short phase of saturation around $t \sim 130$ ns (with $P_{\text{RF}} = 280$ W) the interaction remains with a $q=2$ -like profile, whereas the frequency is slightly increased to the frequency of a saturated non-linear $q=2$ -mode. The interaction then non-linearly evolves towards a non-linear $q=1$ -axial mode with an RF-power $P_{\text{RF}} = 220$ W. This non-linear $q=1$ -mode shows a smaller RF-power than the non-linear $q=2$ -mode, but a higher electron efficiency, which is due to the elevated ohmic losses associated to a higher quality factor.

In experiment, it has been investigated whether such a transition from linear $q=2$ to non-linear

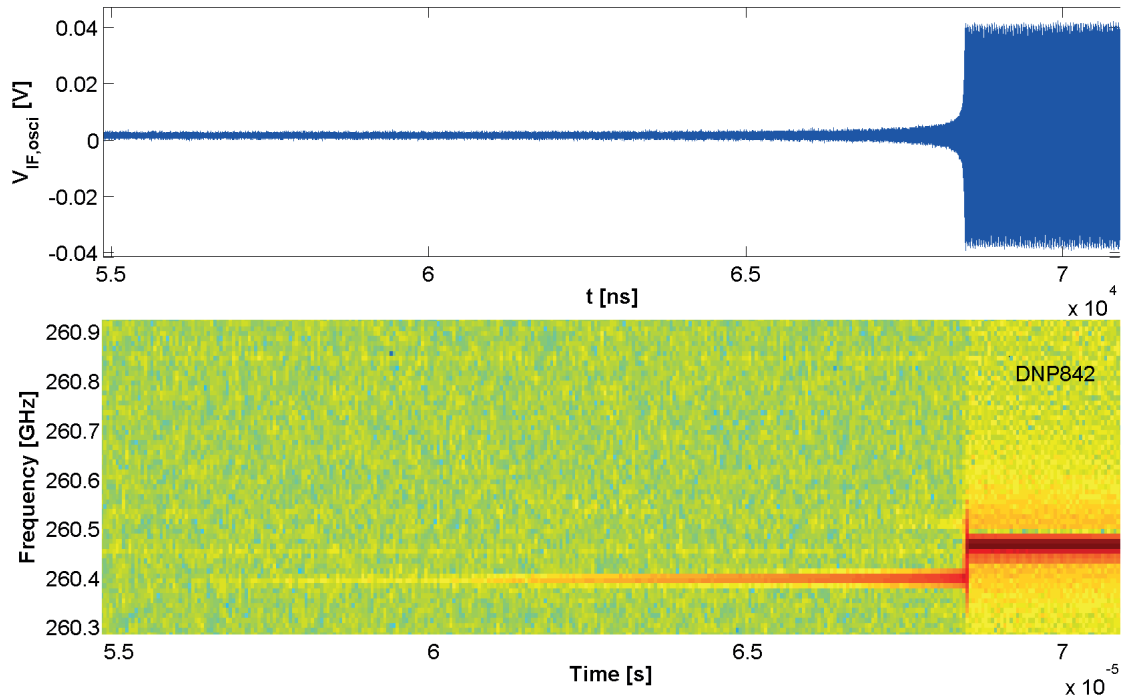


Figure 4.7: Experimental RF start-up on the IF-signal of the heterodyne receiver (top: raw signal on oscilloscope, bottom: spectrogram) for the operating point $B = 9.505$ T / $I_b = 75$ mA (slightly exceeding the starting current) / $V_a = 9.05$ kV (expected pitch-angle from DAPHNE: $\alpha \approx 1.69$, from Fig. 2.5). For these measurements, the oscillation was excited with a beam current crossing the starting current, keeping other parameters fixed.

$q=1$ -mode is also observable. A result of this study is shown in Fig. 4.7, where the RF-startup (same operating point as for TWANG-PIC above) is shown on the IF-signal of the heterodyne receiver, displayed as the raw signal and in a spectrogram. The spectrogram shows how the frequency changes in the process of saturation from $f_{\text{RF,lin}} \approx 260.40$ GHz to $f_{\text{RF,sat}} \approx 260.47$ GHz. This

4.2. BEHAVIOR CLOSE TO STARTING CURRENT

resembles the evolution from linear $q=2$ -mode to non-linear $q=2$ -mode observed in Fig. 4.6 (up to $t \sim 135$ ns). Such a frequency-increase of a similar amplitude is consistently observed in the transition from linear to non-linear phase for any RF-start-up without change of axial mode, in simulation and experiment. Thus, an evolution from the linear $q=1$ -mode to a non-linear $q=1$ -mode is observed, in contrast to the transition from linear $q=2$ -mode to non-linear $q=1$ -mode that was observed simulation.

The origin of this discrepancy is unknown. Either the linearly unstable mode in this region in experiment is the $q=1$ -axial mode instead of the $q=2$ -mode, or the growth in fact becomes non-linear very early in the start-up, with a transition $q=2 \rightarrow q=1$ at very small powers that are not measured here.

4.2.2 Behavior in backward-region: regime with low RF-power

In this subsection it will be shown, that in experiment a regime with very small RF-power and increased RF-frequency is measured in the backward-regime, that does not appear in simulations.

Fig. 4.8 shows the RF-frequency that has been measured experimentally in the *non-linear*,

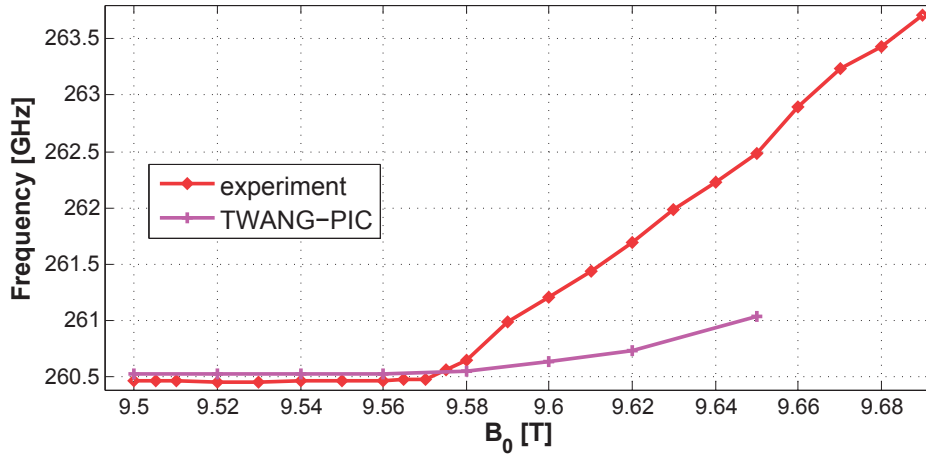


Figure 4.8: RF-frequency from experiment (red) and TWANG-PIC (pink, same as in Fig. 4.5) for currents slightly higher than the starting current versus magnetic field. Experimental parameters: table 2.3, $V_a = 8.8$ kV, simulation parameters: table 3.3, $\alpha = 1.89$

saturated regime close to the starting current versus the magnetic field. Here again the frequency from TWANG-PIC is shown for comparison. It is observed that in the forward-region ($B_0 < 9.59$ T) the frequency close to the starting current depends only very slightly on the magnetic field. Here, the frequencies from experiment and from TWANG-PIC-simulations are in close agreement. In the backward-regime however, the frequency from simulation remains at much smaller values than the experimental frequency, which increases up to $f_{RF} = 263.7$ GHz at $B_0 = 9.69$ T. In this measurement close to the starting current, the RF-power was extremely small ($P_{RF} < 16$ mW, less than the minimum power that can be reliably quantified with the present calorimeter-setup).

However, at a higher current, a threshold occurs where the power is abruptly increased to several 100 mW and the frequency is decreased. The threshold current separating these regimes is illus-

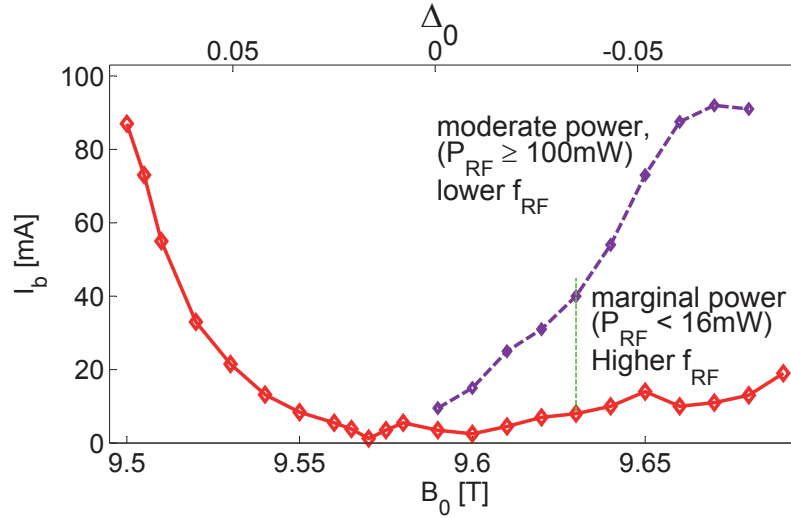


Figure 4.9: Threshold current (purple / dashed) for a transition to significant power and lower frequency in purple / dashed, together with starting current I_{st} in experiment (red / solid). The transition between the two regimes is illustrated in Fig. 4.10 in a scan in I_b along the green dashed line at $B_0 = 9.63$ T. The top x -axis shows the detuning Δ_0 .

trated in Fig. 4.9 together with the starting current.

The transition between the different regimes below and above the threshold current is shown in Fig. 4.10, which shows the RF-frequency and power for a scan in beam-current (trajectory indicated in Fig. 4.9). It is observed, how the power is increased in a step at the threshold current from marginal power (where the exact values for P_{RF} are unreliable) to $P_{RF} \approx 0.5$ W, whereas the frequency is decreased in a step by over 0.7 GHz.

The RF-frequency and power from TWANG-PIC close to the starting current, that are included in Fig. 4.10, are relatively close to the experimental values above the threshold current, whereas they are far from the experimental values at the same beam current. In the simulations, no threshold behavior with a step in power and frequency is observed with increasing current (not shown here). Therefore, the low-power / high-frequency mode from experiment below the threshold current is not observed in simulations, and the agreement between simulation and experiment above the threshold current, shown later on, is much better than the agreement close to starting current, shown in Figs. 4.8 and 4.10.

It has been investigated, whether in simulation such a low-power / higher-frequency regime can be reproduced with a deformed cavity, as for example from an iris in the constant-radius section, but without conclusive results. The reason for this discrepancy thus remains unknown and should be further investigated in the future. The fact that the discrepancy appears only in the backward-region may be due to the fact that there, the RF-properties are dominated by self-consistent effects [148, 20].

The marginally small power in the region of high magnetic fields and low currents was not de-

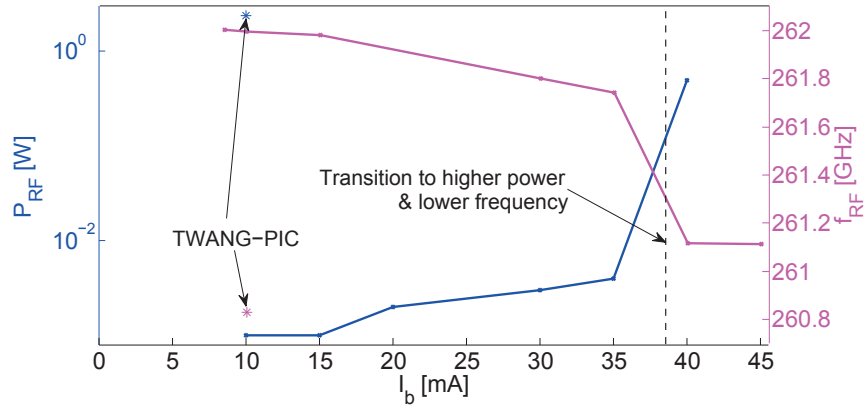


Figure 4.10: Experimentally measured RF-power (blue / left y -axis, logarithmic scale) and frequency (pink / right y -axis) versus beam current, showing the transition in RF-characteristics between the two regimes shown in Fig. 4.9 in the backward-regime ($B_0 = 9.63$ T). For comparison, the RF-frequency from TWANG-PIC has been added close to the starting current (symbol '*').

tected in earlier measurements, such that the threshold current in Fig. 4.9 (purple) was mistaken as the starting current, as it was mentioned earlier.

The extremely low RF-power in the region below the threshold current was regarded to be insufficient for an application in DNP-experiments. Therefore, in the next section 4.3, where the frequency tuning in view of the DNP-application is presented, this operating region is not included.

In the course of the measurement of the starting currents of the neighboring transverse modes, described earlier (Fig. 4.4), also the RF-frequency for currents close to the starting current was measured for these modes. This measurement (not shown here) confirmed the behavior as discussed above for the $TE_{7,2}$ -mode, equally showing a frequency that varies over several GHz with a very low power in the backward-interaction region. Therefore, the behavior of the other transverse modes is consistent with the one of the $TE_{7,2}$ -mode.

4.3 RF-Frequency and RF-power for DNP

In this section, the characteristics of the gyrotron frequency-tuning capabilities and the achievable RF-power will be described in detail in view of the application in DNP-enhanced NMR-spectroscopy. The experimental results are compared to simulation and interpreted with their help.

4.3.1 Frequency - tuning and RF-power: experimental results

During the gyrotron characterization the frequency tuning versus the magnetic field was maximized inside the stationary operating regime, which is a crucial feature of the gyrotron operation

for the application of DNP-NMR spectroscopy.

As already described in [70, 55], in the course of this measurement the power was maximized for each value of magnetic field. For this, a beam current of $I_b = 100$ mA close to the maximum beam current was chosen and the anode-voltage was varied (changing the pitch-angle) for finding the anode-voltage with maximum RF-power. The adjustment of the anode-voltage was however not only useful for maximizing the power but also necessary in order to avoid non-stationary oscillations, which restrained the available range of anode-voltage. Previously, e.g. Barnes et al. [149] equally showed an enhanced frequency-tuning by varying several operating parameters simultaneously.

The obtained frequency as a function of the magnetic field is shown in Fig. 4.11 together with

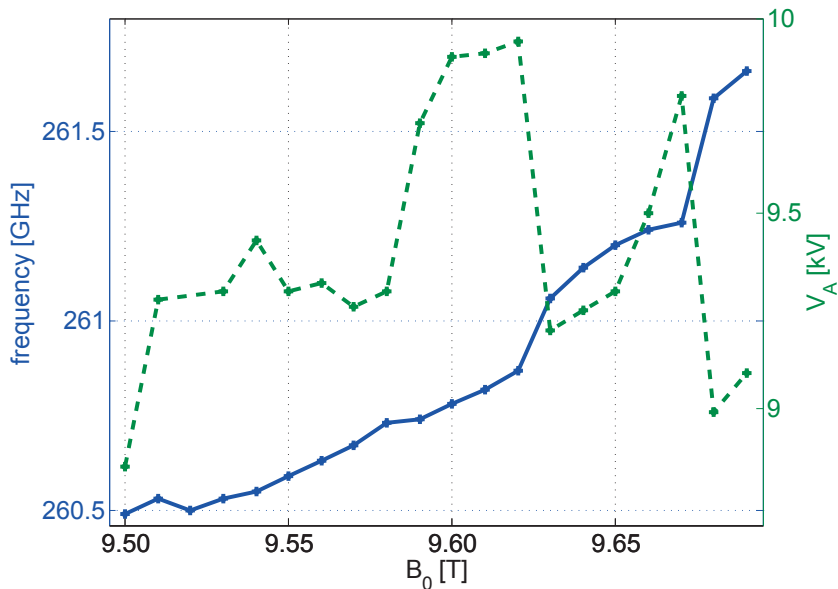


Figure 4.11: Experimental values for RF-frequency (blue, left y-axis) versus the cavity magnetic field, while varying the anode-voltage (green / dashed, right y-axis) for optimizing the power in stationary operation at each magnetic field. The beam current is $I_b = 100$ mA and the anode voltage V_a is adapted for maximum power in stationary operation ($V_a > V_{a,\text{nonstat}}$). The corresponding RF-power is shown in Fig. 4.12.

the adjusted anode-voltage. A frequency tuning of $\Delta f_{\text{RF}} \approx 1.17$ GHz over the range of $f_{\text{RF}} = 260.49 - 261.66$ GHz has been obtained with maximized power, for the magnetic field in the range of $B_0 = 9.50 - 9.69$ T.

The corresponding maximized RF-power is shown in Fig. 4.12. It is observed, that a maximum power of $P_{\text{RF,max}} = 150$ W can be achieved at the lower end of the magnetic field, where a frequency of $f_{\text{RF}} \approx 260.49$ GHz is obtained in Fig. 4.11. For higher values of magnetic field, the maximum achievable power is lower and in the minimum equals $P_{\text{RF}} = 1.5$ W, which is still adequate for application in DNP-NMR spectroscopy. Comparing the frequency-tuning and the corresponding RF-power (Figs. 4.11 and 4.12), it is observed that the achievable power is at

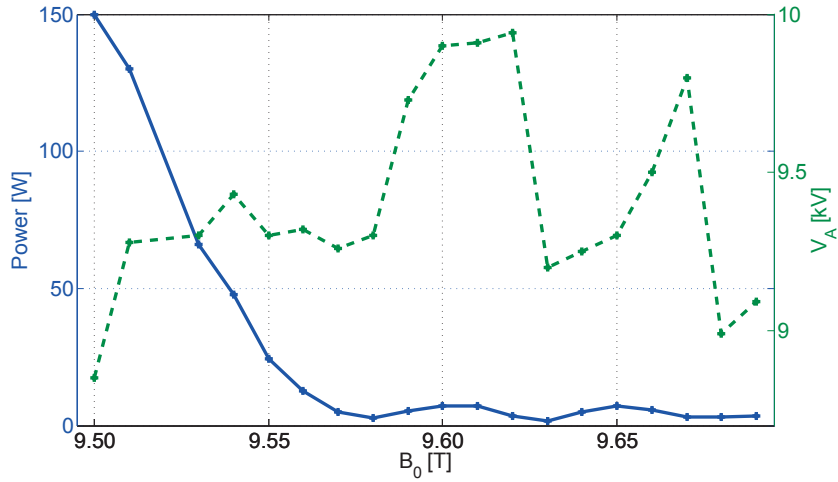


Figure 4.12: Experimental values for rf-power (blue, left y-axis) versus the cavity magnetic field, while varying the anode-voltage (green / dashed, right y-axis) for optimizing the power in stationary operation at each magnetic field. The beam current is $I_b = 100$ mA. Here, the measured power is increased by 10% as a correction for diffraction losses in the measurement and non-perfect absorption in the calorimeter.

its minimum, where step discontinuities are observed in the frequency-tuning ($B_0 = 9.63$ T and $B_0 = 9.68$ T).

It has to be stressed, that the available frequencies for DNP cover the entire range of 1.17 GHz, without gaps. If the desired frequency is in-between the steps shown in the frequency tuning graph (Fig. 4.11), stationary operating points can also be found for these frequencies. However, then the power of these operating points does not correspond to the maximized power and is lower than the one shown at $B_0 = 9.63$ T and $B_0 = 9.68$ T in Fig. 4.12.

4.3.2 Frequency - tuning and RF-power: experiment-theory comparison

The experimentally obtained frequency-tuning and the associated RF-power have been interpreted using TWANG-PIC. Since these simulations concern the stationary regime, also TWANG-simulations would give the same result. For this, the change in anode-voltage shown in Figs. 4.11 and 4.12 was translated to a change in pitch-angle using the DAPHNE-simulation results (Fig. 2.5).

In Fig. 4.13 the results of these simulations are compared to the experimental frequency-tuning, while the corresponding RF-powers are compared in Fig. 4.14. In both graphs, the variation of the pitch-angle has been included. It is observed that the frequency-tuning from simulation is slightly smaller than the experimental one, but qualitatively in good agreement. The simulation reproduces the two steps in frequency of the experimental results.

For the RF-power however, it can be observed in Fig. 4.14, that the power is largely over-estimated by the simulations. The results for the predicted power from simulation is higher than the results

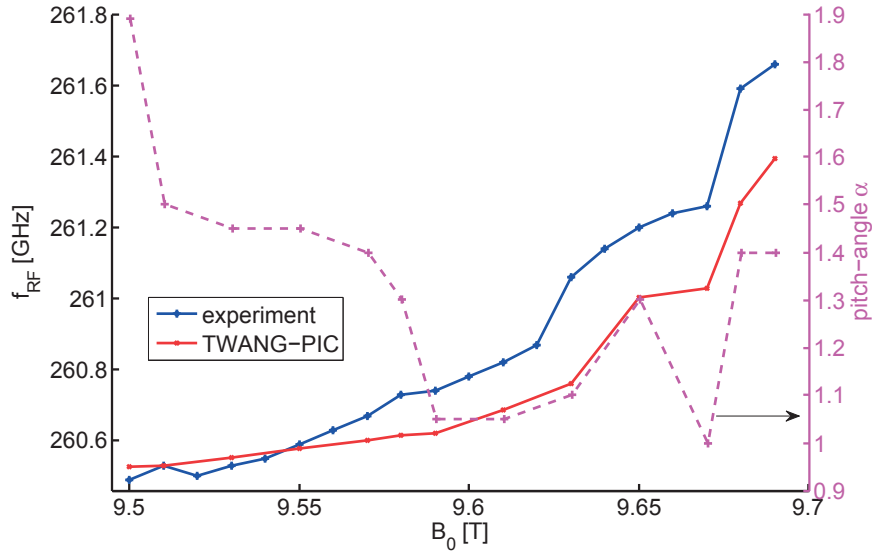


Figure 4.13: RF-frequency (left y-axis) from TWANG-PIC (red) and experiment (blue) versus the cavity magnetic field. The pitch-angle (pink / dashed, right y-axis) in simulation has been varied for reproducing approximately the anode-voltage dependence in the experimental measurements (see Fig. 4.11) and to avoid non-stationary oscillations. The beam current is $I_b = 100$ mA.

shown in [55], because in [55] a very low pitch-angle of $\alpha = 1.12$ was used. In the region of lower magnetic field, the power from simulations represents approximately the double of the experimental power, and in the backward-region the discrepancy is even larger.

The reason for this large discrepancy might be a combination of several factors. An obvious possibility is, that the systematic underestimate in the measurement is not taken into account sufficiently. The RF-power is decreased on its path from the cavity output (simulation) to the calorimeter (measurement) in the mode-conversion by the Vlasov-launcher, by diffraction losses at the internal mirrors, by reflection and absorption in the RF-window (4.7%, [55]), by diffraction losses on the beam path to the calorimeter and by reflection and absorption on the beam-splitter that was included during the measurements. Additionally the surface of the calorimeter is not perfectly absorbing in the present frequency-range ($\sim 3\%$ reflection, see section 2.5). Some of these effects, such as the Vlasov-converter, are frequency-dependent which can be responsible for a part of the forward-backward difference in experiment-simulation discrepancy. Another possibility is that the interaction structure is not perfectly modeled. The cavity radius, which includes a $30\ \mu\text{m}$ -deviation from manufacturing, might also be manufactured not completely flat, because of which the field formation would be not perfectly modeled. At powers higher than tens of watts, the formation of an iris is probable, as it has been discussed in [55]. Furthermore, some of the simulation parameters might deviate from reality, such as the wall-conductivity that has been estimated to $\sigma = \sigma_{\text{CU}}/2$ (see section 2.1.2).

Nevertheless, the power shows the same qualitative behavior as the experimental curve with three local minima. Just as for the experimental results, the minima of RF-power for the TWANG-

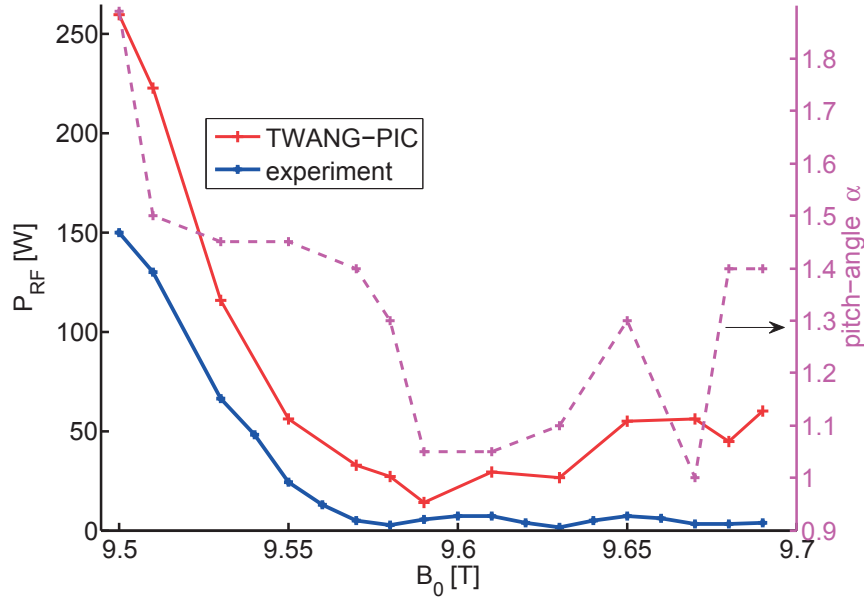


Figure 4.14: RF-power (left y-axis) from TWANG-PIC (red) and experiment (blue) versus the cavity magnetic field. The pitch-angle (pink / dashed, right y-axis) in simulation has been varied for reproducing approximately the anode-voltage dependence in the experimental measurements (see Fig. 4.12) and to avoid non-stationary oscillations. The beam current is $I_b = 100$ mA.

PIC-results ($B_0 = 9.63$ T and $B_0 = 9.68$ T) are located at the same magnetic field values as the steps in frequency-tuning.

The simulation results can help understanding the origin of these steps. For this, Fig. 4.15 shows a selection of electric field profiles (amplitude and phase), where each profile was chosen from another section of the step-wise increasing frequency of Fig. 4.13. These field profiles confirm, that the observed behavior of the frequency is the result of a gradual change of axial mode in the backward-region. At the magnetic field values, where the field profile changes from one non-linear axial mode to another, the achievable power is lowest and the frequency-tuning shows a step.

Similar characteristics for continuous frequency-tuning and RF-power, with an associated change of non-linear axial mode, have been described previously e.g. in [149, 150, 151, 152]. One may note, that for example in [151], the discrepancy between experimental power and prediction from simulation is comparable to the one shown above.

4.3.3 Frequency-modulation for DNP-spectroscopy

In the previous subsections the tuning of the RF-frequency was obtained via a variation of the magnetic field.

A fast modulation can be achieved by sweeping the anode-voltage over a relatively large range

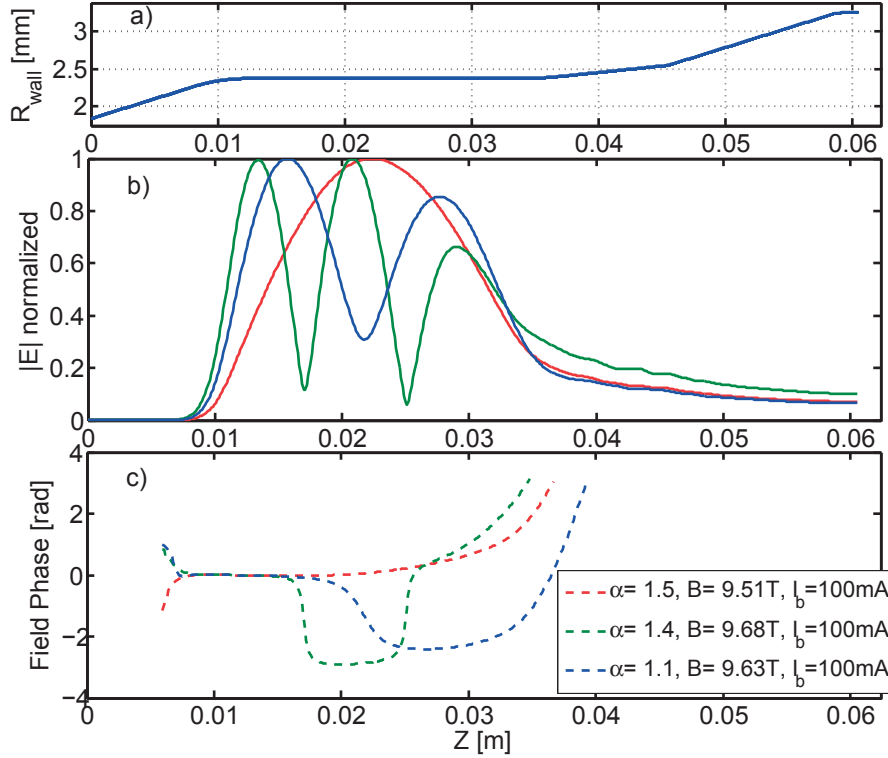


Figure 4.15: Selection of field profiles from simulations of which the frequency was shown in Fig. 4.13. a) Cavity wall profile, b) Amplitude profile of RF -field, c) Phase profile of RF -field. For the operating points, see legend in c).

and making use of the influence of the electron pitch-angle on the gyrotron frequency. The maximum modulation frequency of this approach is defined by the speed of the gyrotron control (program on FPGA and DACs), by anode-voltage power supply characteristics (slew rate, see section 2.1), by the effects associated to wiring of the anode and by the different internal capacitances and self-inductances of the triode-gun.

This kind of fast frequency modulation is illustrated in Fig. 4.16, showing the variation of the anode voltage set value and the time-dependent frequency on a spectrogram. Here, the currently fastest frequency-modulation is shown, sweeping over a frequency range $\Delta f_{\text{RF,fast}} \approx 110$ MHz on the minimum time scale of $\sim 30 \mu\text{s}$. It is observed that on this operating point a sweep over $\Delta f_{\text{RF,fast}} \approx 110$ MHz requires a variation of the anode voltage by $\Delta V_a \approx 640$ V, which is changed with a rate of $\Delta V_a / V_a \sim 20 \text{V} / \mu\text{s}$. During this sweep of the frequency however also the power is affected by the changing pitch-angle and varies in the range $P_{\text{RF}} = 0.4 - 1.6$ W.

A similar fast modulation of the gyrotron frequency via a sweep of the anode-voltage and with the goal of an application in DNP-NMR spectroscopy has been described in [153, 147].

In DNP-spectroscopy experiments at LPMN it was demonstrated for the first time by a change of the modulation frequency, that this frequency-modulation indeed has an increasing effect on the enhancement of the NMR-signal via the DNP process. A first description of the results obtained

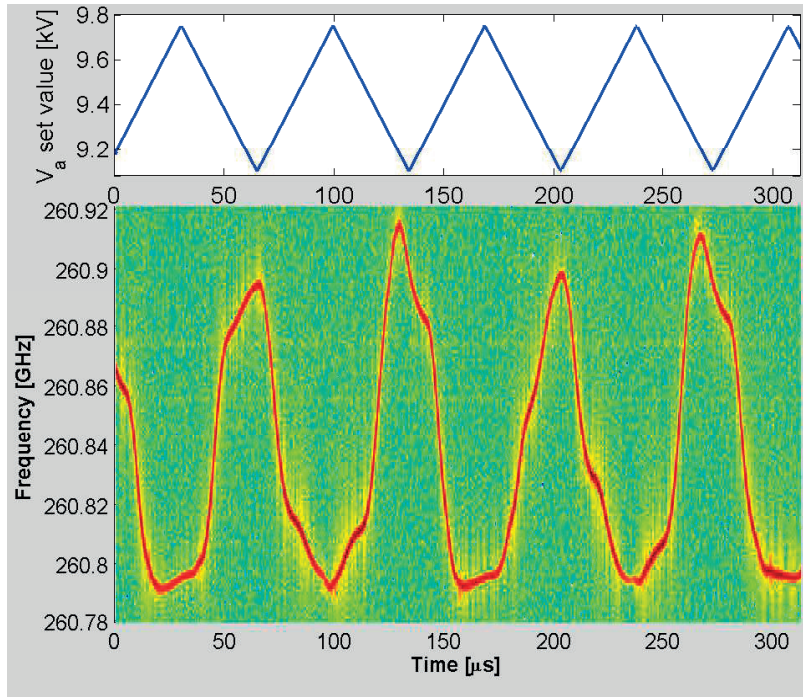


Figure 4.16: Time-dependent rf-spectrum (bottom) and set-value of anode voltage control (top) with fast frequency modulation ($f_{\text{sweep}} = 14.5 \text{ kHz}$, $\Delta f_{\text{RF,fast}} \approx 110 \text{ MHz}$).

with the gyrotron's novel features have been published recently in [17], from where a summarizing graph has been included in the Introduction in Fig. 1.4b). It clearly demonstrates that the enhancement of the NMR-signal through DNP can be significantly increased by applying the implemented frequency-modulation in spectroscopy.

4.4 Influence of pitch-angle

In section 2.1.2 it was described that the electron pitch-angle calculated by DAPHNE, which is also used in simulations presented above, corresponds to $\alpha \approx 1.82 - 2.02$ for $V_a = 8.8 \text{ kV}$ with a spread around 3%. However, additional experimental indications, presented below, suggest that this value is smaller than the one in experiment.

The pitch-angle in experiment is increased by decreasing the anode-voltage. However, with decreasing V_a , a limit $V_{a,\text{lim}}$ exists at which the first electrons reach an infinite pitch-angle and are reflected from the cavity-region in direction towards the cathode by the magnetic mirroring effect. Because some of the reflected electrons arrive at the anode, this effect can be detected by a precise measurement of the current delivered by the anode voltage power supply, also referred to as a 'body current'.

With this method, the limit $V_{a,\text{lim}}$ for the appearance of reflected electrons was determined for different values of magnetic field and beam current, which is shown in Fig. 4.17. These results

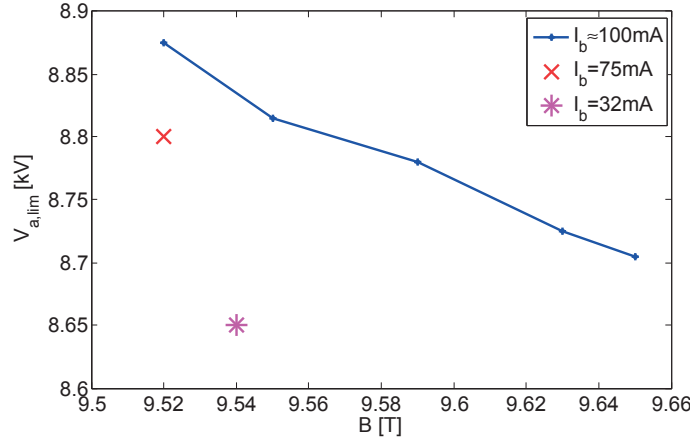


Figure 4.17: Anode voltage limit $V_{a,lim}$, below which reflected electrons are detected via an anode current, for different cavity magnetic field values. The blue line corresponds to a beam current of $I_b = 100$ mA, the red 'x' correspond to $I_b = 75$ mA and the pink star to $I_b = 32$ mA. For other parameters see table 2.3. The pitch-angle scales inversely with the anode-voltage, meaning that at higher I_b and lower B_0 the achievable pitch-angle is lower (because of a higher spread) or the pitch-angle is higher.

demonstrate that the usual operating point with $V_a = 8.8$ kV is very close to the voltage threshold at which the first reflected electrons appear. This is not consistent with the values from DAPHNE $\alpha(V_a=8.8\text{kV}) \lesssim 2$ and $\Delta\alpha \sim 3\%$, for which no electrons are expected to reach infinite pitch-angle. Therefore it is concluded, that the pitch-angle and (possibly also) its spread in experiment are higher than the value from DAPHNE. For this reason, in simulations of non-stationary oscillations presented in the next chapter, a slightly higher pitch-angle is used.

Furthermore, the measurements show, that at a higher beam current reflected electrons already appear at a higher anode-voltage. This means that a higher I_b decreases the achievable pitch-angle because of an increased spread, or that it increases directly the overall pitch-angle. This can be explained by increased DC-space charge fields at higher I_b , which decreases the electron axial velocity and increases the α -spread. Also the influence of the beam-wave interaction on the parallel electron momentum can play a role (increasing $\Delta\alpha$ in the region before B_0 -maximum). According to simulations with DAPHNE for the space-charge effects and with TWANG-PIC for the effect of interaction, both of these effects are expected to be small, but could lead to the mirroring of some electrons that already have a very high pitch-angle.

4.4.1 Pitch-angle variation from Anode-voltage fluctuation

As described earlier, the pitch-angle is essentially controlled by the anode-voltage.

During the gyrotron characterization it was realized that the anode voltage power supply consistently exhibits a periodic fluctuation with a peak-to-peak amplitude of approximately $\Delta V_a \approx 30$ V ($\frac{\Delta V_a}{V_a} \approx \frac{30\text{V}}{8800\text{V}} \sim 0.3\%$) and a period $T \approx 33 \mu\text{s}$. From DAPHNE-simulations (Fig. 2.5), this volt-

4.4. INFLUENCE OF PITCH-ANGLE

age fluctuation can be translated to a pitch-angle fluctuation with a peak-to-peak variation of $\sim 3\%$. In the monomode regime, this pitch-angle fluctuation causes a slight fluctuation of the RF-frequency.

This is illustrated in Fig. 4.18, which shows the variation of the anode-voltage from the high-

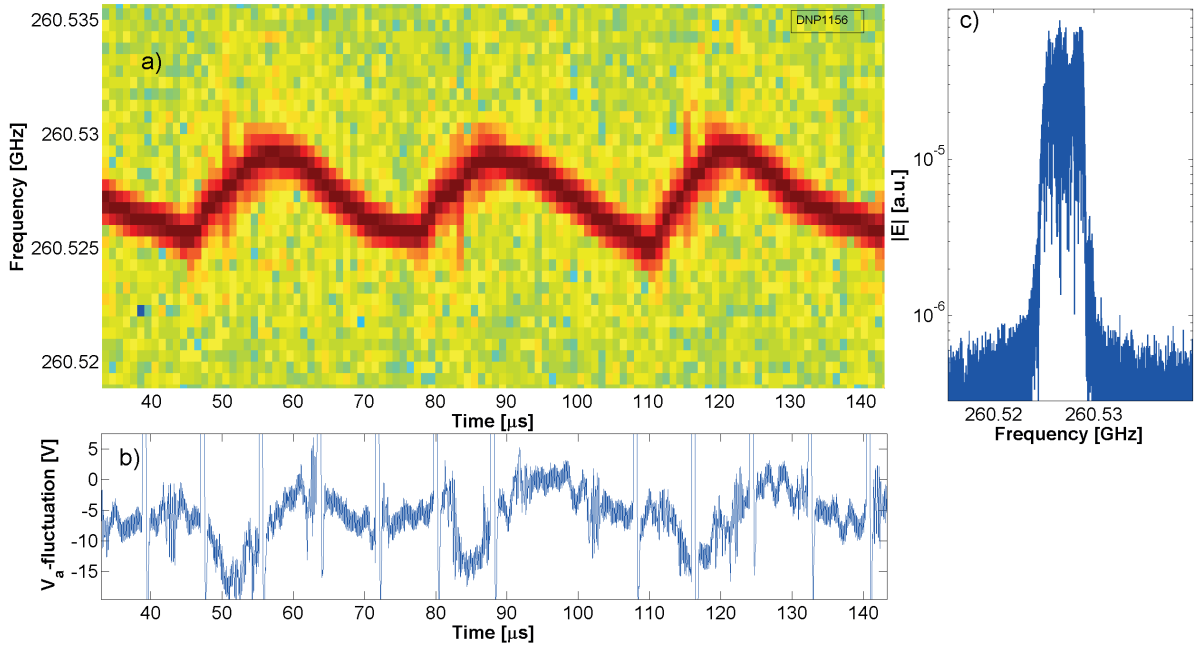


Figure 4.18: a) Fluctuation of rf-frequency with time in the monomode-regime, caused by anode-voltage fluctuation. From IF of heterodyne receiver. b) Fluctuation of anode-voltage, from front panel of anode-voltage power supply, numerically noise-filtered (-3dB at $\sim 7\text{MHz}$). c) RF-spectrum, FFT of same signal as in a), over entire shown time window. IF-signal and V_a synchronously acquired on 13GHz analogue bandwidth LeCroy-oscilloscope (see section 2.5).

voltage power supply in Fig. 4.18b), the resulting frequency-variation in time in Fig. 4.18a) and a spectrum in Fig. 4.18c). It has to be mentioned, that the spikes in the anode-voltage time trace are probably a voltage-fluctuation appearing only on the V_a -monitoring value, which is created internally in the anode voltage power supply. They cannot be actual V_a -fluctuations, because the self-inductance of the system would not allow for such rapid voltage variations in the anode. In the next subsection, additionally it will be shown, that these fluctuations do not have an influence on the RF-emission.

It is observed, that the temporal variation of the RF-frequency is correlated to the fluctuation of the anode-voltage. In the shown case, the consequence of the V_a -fluctuation is a variation of the monomode frequency over 3.5MHz. If the FFT is taken over a time that is longer than the V_a -fluctuation time-scale, the peak in the frequency-spectrum is broadened as shown in Fig. 4.18c). Thus, the spectral purity in such spectra is determined by the fluctuation of a system parameter. Such effects have also been studied in literature earlier [154, 29, 19], where it was found that the instantaneous linewidth of the gyrotron can be as low as 1 kHz and smaller. In the DNP-gyrotron,

the minimum linewidth due to the fluctuation is ~ 1.4 MHz, as shown in Fig. 4.19. However, the

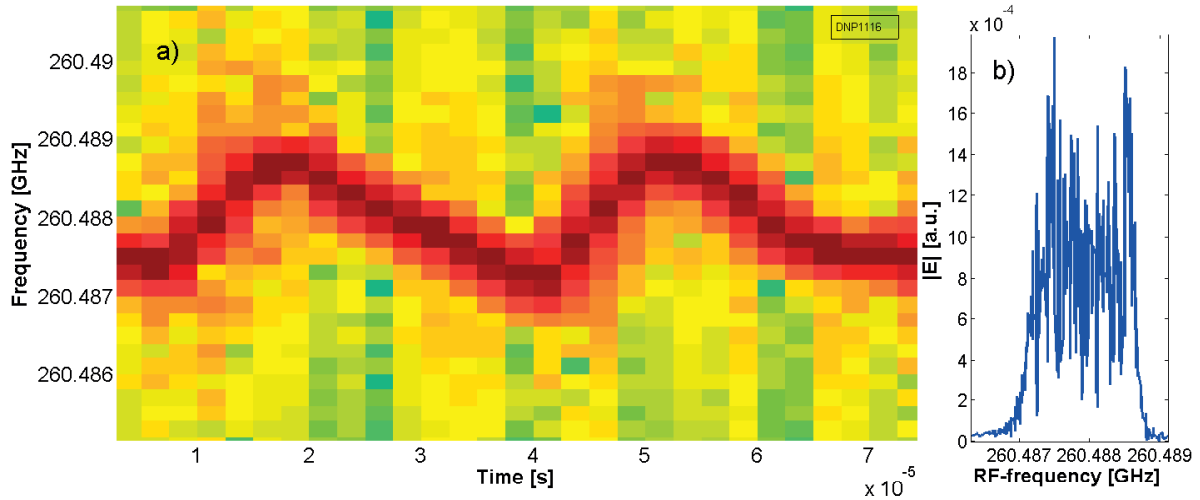


Figure 4.19: Spectrogram and time-averaged spectrum (windowing over longer time) of IF-signal from heterodyne receiver, showing the fluctuation due to anode voltage fluctuation. On this stationary operating point ($B = 9.54$ T / $I_b = 20$ mA / $V_a = 8.80$ kV) the frequency fluctuation in a) and the spectral width in b) were among the smallest observed of all operating points.

importance of the frequency-fluctuation depends strongly on the operating point. because both the influence of the anode-voltage on the pitch-angle and the influence of the pitch-angle on the RF-frequency depend on the operating point. In monomode-operation the measured excursion of the RF-frequency due to the anode-voltage fluctuation was approximately in the range of 1.4 – 20 MHz.

4.5 Pulsed operation

For the application of the gyrotron in DNP-enhanced NMR spectroscopy, in most cases microwave pulses are requested instead of CW-operation. Due to this, a pulsed mode has been implemented in the gyrotron control program, that allows arbitrary pulse lengths and duty-cycles of microwave. In contrast to the nanosecond-pulsed regime, which will be introduced in section 5.7.1 and where pulses are created self-consistently from the interaction, the principle of this pulsed mode is a triggering of the microwave emission via the anode-voltage. For this, in the off-mode the pitch-angle is decreased by an increase in anode-voltage enough to suppress the RF-emission (equivalent to decreasing current below starting current). Then, for pulsing the microwave a negative pulse is applied to the anode voltage.

This mode of pulsed operation allows fast microwave pulses, where the minimum pulse length is given by the fastest possible sweep of anode-voltage, with the same limitations as described in section 4.3.3 for the frequency-modulation. The fastest pulses that were achieved with this method are of the order of $30 \mu\text{s}$, which is presented in Fig. 4.20, showing the instantaneous power level from a Schottky-diode and the simultaneously measured anode-voltage.

Here again spikes are observed on the anode-voltage signal. The fact, that these spikes have

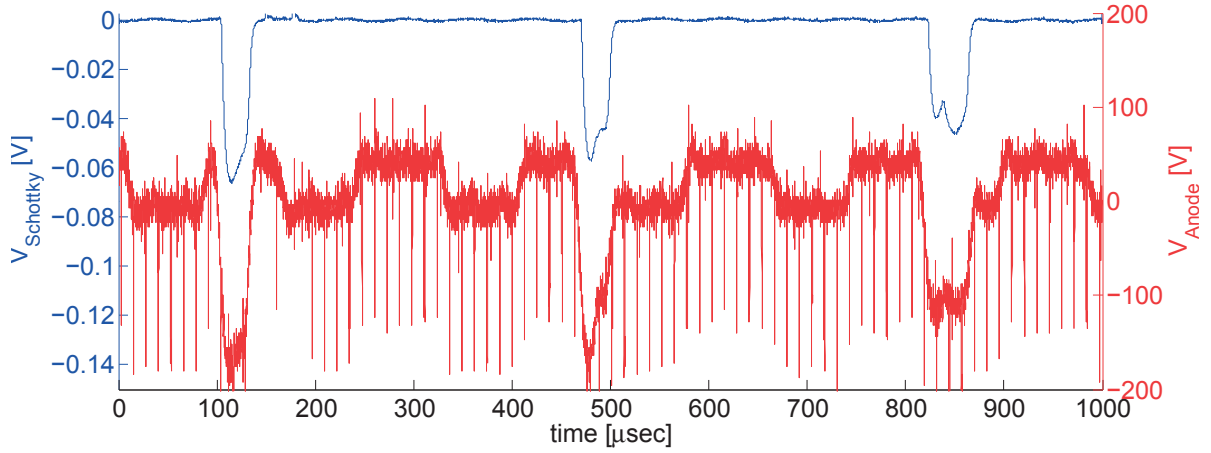


Figure 4.20: Fast microwave-pulses via anode-voltage pulses: Signal from fast Schottky-diode (blue, left y-axis) and from anode-voltage (red, right y-axis) on 300MHz Agilent oscilloscope. The negative Schottky-signal corresponds to the instantaneous RF-power.

no influences on the instantaneous RF-power confirms, that they are not present on the anode-voltage inside the gyrotron. A real spike of the anode-voltage with the shown amplitude would have been measured as a spike in instantaneous RF-power, since both the beam-wave interaction and the diagnostics have a faster reaction time than the $\sim 0.5 \mu\text{s}$ -duration of the V_a -spikes. During the short $30 \mu\text{s}$ V_a -pulses, the RF-power is already influenced by an anode-voltage. Such pulses can be obtained with an arbitrary duty cycle.

4.6 Frequency and power stabilization

In section 2.3.2, it has been described, that the beam current is stabilized through a feedback loop acting on the heating current of the cathode filament, in order to counteract the variation of the cathode emission over time. Naturally, a non-stable beam current also influences the RF-characteristics. In Fig. 4.21 it is illustrated, that the beam current stabilization was in fact necessary in order to stabilize the RF-frequency and RF-power.

The graph shows the evolution of frequency-position of the RF spectral peak both without a current feedback-control (keeping filament heating current constant) and with a feedback-control, as well as the RF-power without controller, for an operation of nearly one hour. The shown frequency corresponds to the drift in frequency of a $\sim 3 \text{MHz}$ wide peak as the one that has been shown in Fig. 4.18c). It shows, that without a current feedback-control the frequency peak shows a drift of 6.5MHz due to a drift of the beam-current. At the same time the RF-power varies over $\sim 17\%$. With the current feedback-control on the other hand, both frequency and RF-power (not shown here) are very stable over the time-scale of one hour and longer.

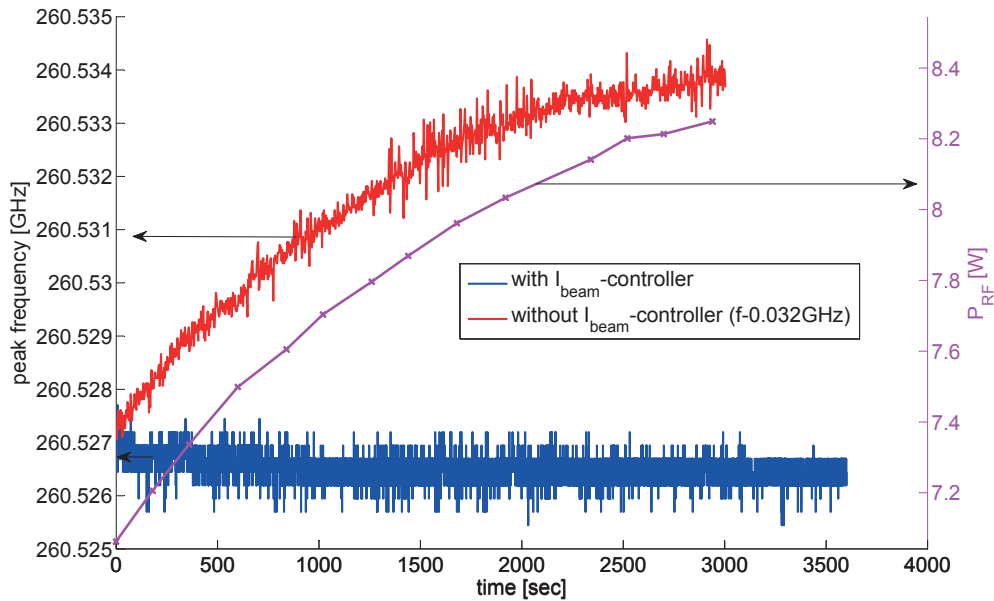


Figure 4.21: Effect of current stabilization on RF-frequency (blue and red, left y-axis) and power (pink, right axis) stability during CW-operation of one hour. The displayed frequency-drift corresponds to the change of frequency-position of a peak with ~ 3 MHz spectral width (see section 4.4.1). The RF-frequency without current-control (red), which has been acquired on a slightly different operating point than the blue curve, has been shifted by 32 MHz for better comparison.

4.7 Summary of characterization of stationary operating regime

In this chapter, a detailed characterization of the stationary gyrotron operating regime has been presented. It is shown, that the starting current can be accurately predicted with the help of the new simulation code TWANGLIN. These simulations can also be used to interpret the details of the starting current. A detailed analysis of the RF-startup allows a theory-experiment comparison of the mode that is linearly excited first at the starting current and of its evolution to the non-linear phase of the interaction.

It is shown, that the DNP-gyrotron is well-designed, characterized and prepared for matching and outmatching all necessary requirements for the application in DNP-NMR spectroscopy. A frequency-tuning over $\Delta f_{\text{RF}} \sim 1.2$ GHz is achieved via a magnetic field sweep with sufficient RF-power over the entire frequency-range. Additionally, the innovative feature of a fast frequency-modulation via a sweep in anode-voltage has been implemented and proofed its capabilities in DNP-experiments.

The broadening of the frequency-peak over >1 MHz is explained as being caused by a fluctuating instantaneous frequency due to a fluctuation of anode-voltage. Additionally, the possibility to create pulses as short as $30 \mu\text{s}$ has been implemented. A well-performing stabilization of the RF-frequency and power over long operation times is achieved via a feedback-control of the beam current.

4.7. SUMMARY OF CHARACTERIZATION OF STATIONARY OPERATING REGIME

In the presented characterization of the stationary operating regime, the results could be interpreted using simulations. The simulations can explain details in the starting current, the frequency-tuning and the power-dependency, as being caused by a smooth transition between different axial modes in the backward-region, both in the linear and in the non-linear interaction.

Chapter 5

Analysis of the non-stationary regime

In the DNP-gyrotron it was observed, that for a certain range of operating points, a regime of non-stationary oscillation is observed. As mentioned earlier, this non-stationary regime is characterized by a multi-frequency or broadband RF-spectrum with a bandwidth of typically less than 3GHz and a power which fluctuates self-consistently in time. The typical dominant timescale of this fluctuation is of the order of 4 – 5 ns, corresponding to a typical oscillation frequency of 200 – 250 MHz.

In this chapter, this experimentally observed non-stationary regime will be introduced and analyzed in detail. The experimental results will be compared to results from theoretical modeling and interpreted with their help.

The chapter is structured as follows: First, in section 5.1 the non-stationary oscillations will be introduced as opposed to stationary oscillations by describing the thresholds of the non-stationary regime. Then, in section 5.2 the observed variety of non-stationary oscillations will be categorized into the major types.

Non-stationary simulations with their peculiarities and the important simulation parameters are introduced in section 5.3. Here, also a comparison between the experimental categorization and a categorization of simulation results is included, followed by a comparison between the observed dependencies of RF-power and frequency in section 5.4

After this general overview, the attention is given to different specific operating points. In section 5.5 the effect of the experimentally observed anode-voltage fluctuation on the non-stationary oscillation is illustrated. The chaotic regime will be introduced in section 5.6, including a description of the observed route(s) to chaos. In section 5.7 a specific dynamical regime with a spectrum composed of sidebands will be studied in depth, including the first experimental observation of a nanosecond pulsed regime.

Finally, section 5.9 presents an attempt for interpreting the origin of the non-stationary regime. The experimental and numerical results of this chapter will be discussed with respect to previously published results. It will be shown that some general properties of non-stationary regimes need to be reconsidered in the light of the new results.

5.1 The non-stationary regime: Operational domain

In this section, the threshold will be characterized, where the RF-emission in experiment passes from the stationary regime, where the RF-power is constant over time and the RF-spectrum is monochromatic, towards the non-stationary regime, which is characterized by fast-varying RF-power and a multi-frequency or broadband RF-spectrum.

The commonly used operating parameters of the DNP-gyrotron were presented in section 2.1.2 (table 2.3). Compared to the stationary regime described in chapter 4, the non-stationary regime was observed in a region of higher beam-current and lower anode-voltage $V_a = 8.8\text{ kV}$, leading to a higher pitch-angle. In particular, the elevated pitch-angle $\alpha \sim 1.9\text{--}2.5$ is close to the limit given by reflected electrons (see section 4.4) and plays an important role in the non-stationary regime dynamics.

The operating region, in which non-stationary oscillations are observed in this configuration is

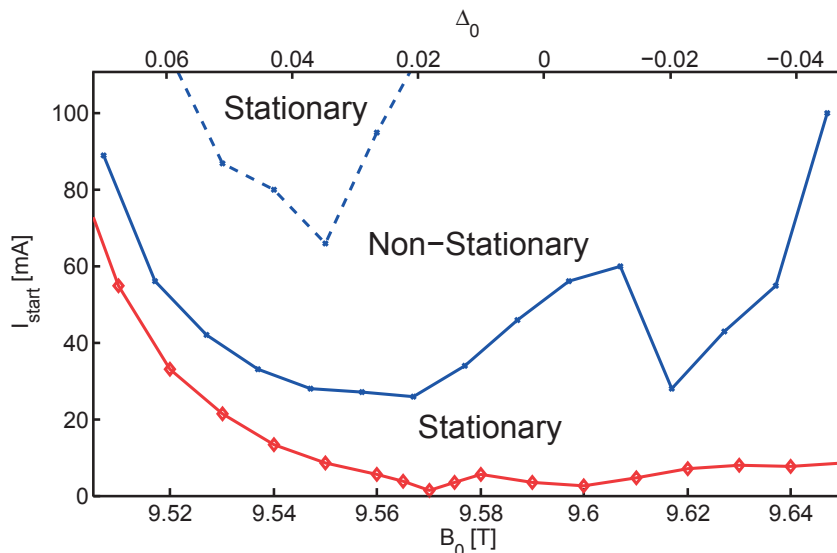


Figure 5.1: Starting current (red) and non-stationary onset current (blue). The non-stationary regime is observed above the solid blue line and below the dashed blue line. Above the dashed threshold current, a second stationary regime is observed.

presented in Fig. 5.1, showing the beam current thresholds distinguishing the different dynamical regimes in the $(I_b\text{-}B_0)$ -parameter space. The lower limit of stationary/monomode operation corresponds to the starting current, above which the lower limit of the non-stationary region is displayed. For high beam currents, a second transition to stationary oscillation appears, limited by a second threshold current (blue/dashed). The regime changed mostly via a hard transition, with a sudden appearance of other frequency-components in the RF-spectrum.

It can be observed, that the non-stationary oscillations appear already for a current that is relatively close to the starting current, as for example in the forward-region for $B_0 = 9.51\text{--}9.52\text{ T}$ where the non-stationary onset current is less than twice the starting-current.

The detailed measurements of the non-stationary operating region is a very important result. To our knowledge, this is the first time that in a gyrotron oscillator, a second stationary region (above dashed blue in Fig. 5.1) was experimentally observed. It is unclear, if the alternating stationary and non-stationary operating points described for a B_0 -scan on a gyro-BWO in [53] and [155] are a signature of such a second stationary regime. Similar alternating regions of the stationary and non-stationary regime have only been described experimentally on devices, where a feedback mechanism has been added specifically for producing non-stationary oscillations [156, 157]. In simulation however, such alternating stationary and non-stationary regions have been predicted and described in a quite large series of publications [158, 159, 60, 160, 53, 117], which will be further discussed in section 5.3.1.

5.2 Categorization of non-stationary oscillations

Within the non-stationary regime the details of the RF-characteristics can vary strongly between different operating points.

The large variety of non-stationary oscillations that were observed on the parameter space described in the previous section was characterized and categorized, and is presented in Fig. 5.2. Here, the oscillation types are shown via color-coding with a characteristic spectrum shown for each category. The oscillations were categorized by visual inspection of the spectra measured with a spectrum analyzer (see section 2.5). Because of its limited acquisition rate ($\lesssim 30$ Hz) these measurements cannot include possible faster variations in the RF-spectrum.

It has to be stressed that the method of visual inspection of spectra only gives an approximate categorization, since the transition between different categories is generally smooth and the choice of a specific category based on the spectrum is sometimes ambiguous, as it will be illustrated later on.

5.2.1 Sideband category

The most common non-stationary category, which is also always excited first when the non-stationary onset-current is exceeded, is the regime where equidistant sidebands appear in the RF-spectrum. An example of the corresponding spectrum for this oscillation type is shown in Fig. 5.2c) and a typical example of the corresponding time-trace of the power is shown in Fig. 5.3a). The appearance of such equidistant peaks in the spectrum corresponds to a temporal evolution of the power in which a fluctuation with mostly a single periodicity appears. The relative height of the sidebands, which depends on the operating point, influences the modulation depth of the power fluctuation.

5.2.2 Period doubling category

If starting from the sideband regime at the non-stationary onset current the system is driven more strongly by an increase in beam current or pitch-angle, the system on some occasions follows a route of transition towards chaotic oscillation.

The first step towards chaos is often a transition to a regime characterized by period doubling,

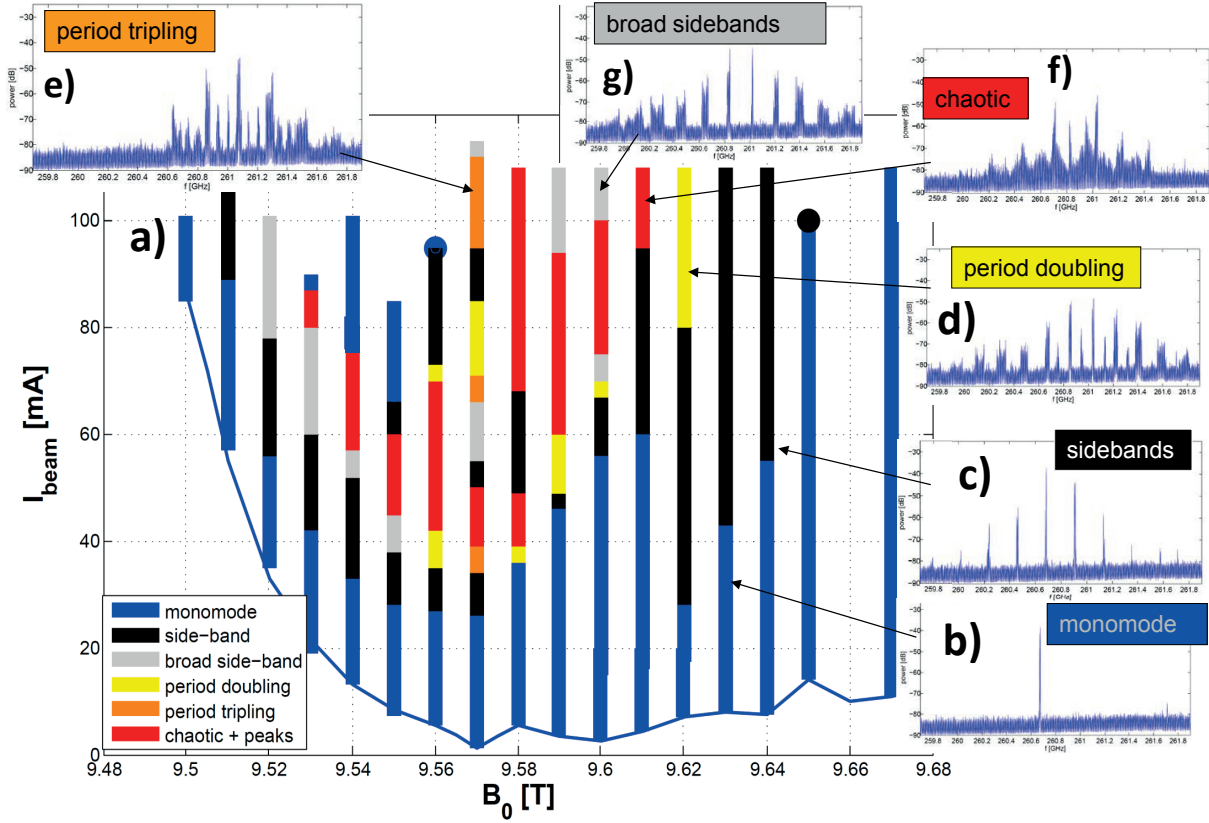


Figure 5.2: Categorization of non-stationary oscillation on plane of beam current and magnetic field, for other experimental parameters fixed ($V_a = 8.8\text{ kV} \rightarrow$ DAPHNE: $\alpha \approx 1.8 - 2$). The categorization is obtained by visual inspection of spectra measured with the spectrum analyzer, as they are shown in the insets b)-g).

defined by the appearance of an intermediate frequency peak at the central position between each two adjacent sidebands in the RF-spectrum, as shown in Fig. 5.2d). In the temporal trajectory of the power, shown on an example in Fig. 5.3b), the oscillation passes from a one-period oscillation to a two-period oscillation by the appearance of a further local maximum inside each period.

5.2.3 Period tripling category

For certain operating points, the period tripling type was observed, appearing in Fig. 5.2a) and e). This type of period tripling is related to the simultaneous appearance of two intermediate peaks between the sideband peaks in the spectrum, coupled to the appearance of (mostly) two additional periodicities in the the power oscillation in addition to the dominant oscillation from

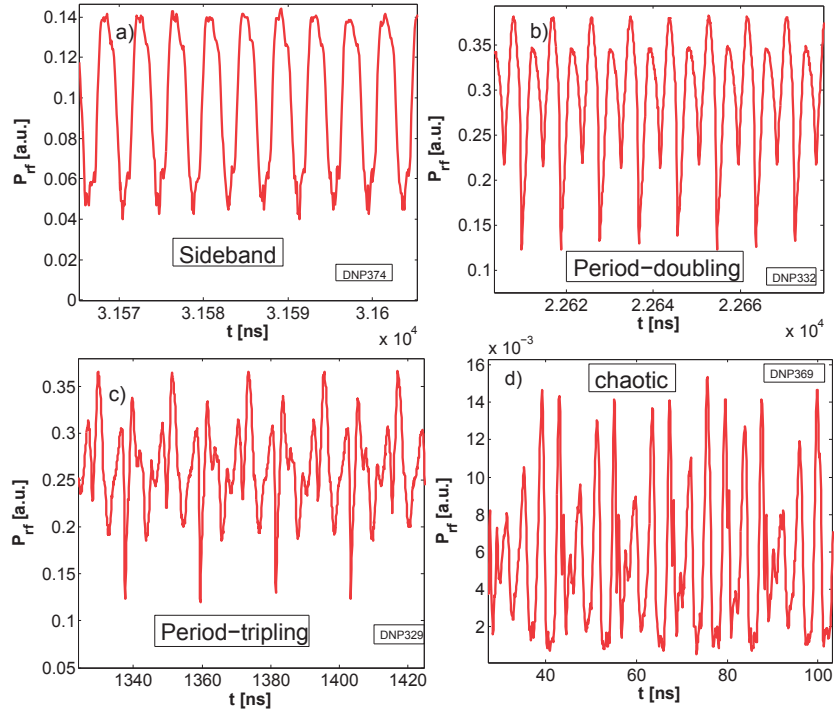


Figure 5.3: Examples of power time-traces, measured with fast Schottky-diode on fast oscilloscope (categories indicated in each inlet). The measurements are short excerpts of situations, in which the corresponding category was present, from longer acquisitions. It is observed, how the power is not constant in the non-stationary regime, with a single fluctuation periodicity in the sideband category, a double and triple periodicity in period doubling and tripling. In the chaotic time-trace then, the strict periodicity is broken.

the sidebands, as suggested by the power evolution shown in Fig. 5.3c).

5.2.4 Chaotic category

If the beam-current is increased beyond the period-doubling / tripling regime, the oscillation often changes its behavior towards chaotic oscillation. In this category, the RF-spectrum acquires a continuous broadband component, on top of which mostly distinct peaks persist (e.g. Fig. 5.2f). As shown in Fig. 5.3d), this spectrum is caused by a power oscillation, in which the main oscillation still persists, but the strict periodicity of the oscillation is broken.

With a further increase of the beam-current, the chaotic regime is generally followed by a transition back to a more stable oscillation with period doubling, period tripling or sidebands. In the region $B_0 = 9.53 - 9.56$ T, the system even returns to stationary oscillation with a monomode rf-spectrum and constant power for an elevated beam current ($I_b \geq 66$ mA at $B_0 = 9.55$ T).

5.2.5 Broad sideband category

In addition to the non-stationary types described so far, the category of broad sidebands appears in the categorization of Fig. 5.2. This category, for which a typical spectrum is included into Fig. 5.2g), is characterized by broadened sideband peaks in the RF-spectrum with an increased broadening for the peaks further away from the dominant peak. The origin of this category, which is actually part of the sideband category, will be explained in section 5.4.

5.3 Simulation of non-stationary oscillations

In this section, the simulation of non-stationary oscillations will be introduced with an investigation of the adequate simulation parameters. As discussed in chapter 3, the model of TWANG-PIC is adequate for simulating the non-stationary regime and therefore will be used throughout this chapter.

For reducing the simulation run times with the PIC-code, the cavity in simulations was shortened to the wall profile and B_0 -profile in Fig. 5.4 with a flattened cavity output in order to match the radiation boundary condition. It was verified, that the behavior on a non-stationary operating point is unchanged with the shortened cavity.

Most of the simulation parameters that will be used throughout this chapter have been pre-

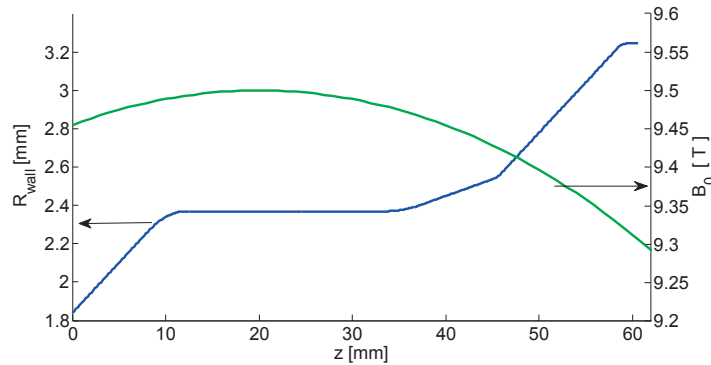


Figure 5.4: Cavity wall radius (blue, left y-axis) and magnetic field profile (green, right y-axis) as used in TWANG-PIC-simulations.

sented in table 3.3.

As described in section 4.4, the pitch-angle α , which is a derived quantity, was not exactly known for a given configuration of anode-voltage, cathode-voltage and magnetic field. The threshold for the appearance of a leakage current to the anode suggests that the true pitch-angle is slightly higher than the values from DAPHNE-simulation shown in Fig. 2.5 (corresponding to $\alpha = 1.939$ for $B_0 = 9.54\text{T}$). Thus, the pitch-angle to be used in the TWANG-PIC-simulations was determined by comparing the range of beam-current, where the non-stationary regime is observed experimentally, to the I_b -range predicted by simulations.

The results of this study ($B_0 = 9.54\text{T}$) are shown in Fig. 5.5, representing the frequency of the peak with highest amplitude in the RF-spectrum, and indicating the non-stationary regime by

5.3. SIMULATION OF NON-STATIONARY OSCILLATIONS

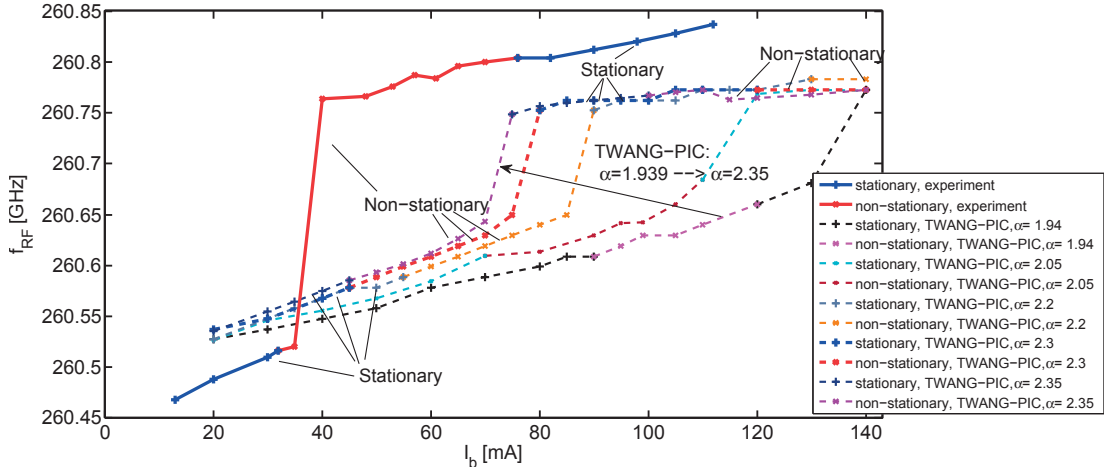


Figure 5.5: Indirect determination of the pitch-angle to be used in simulations by comparing the I_b -range with non-stationary oscillations to experiment (solid line): Dominant RF-frequency (highest amplitude in spectrum) for I_b -scan at $B_0 = 9.54$ T. In TWANG-PIC, the pitch-angle α is varied between $\alpha = 1.94$ (value from DAPHNE) and $\alpha = 2.35$. The best match of the non-stationary regions is achieved for $\alpha = 2.3$ (thicker dashed line), since for $\alpha = 2.35$ a non-stationary zone re-appears at $I_b \geq 100$ mA. See pointers (only selected lines) and legend for different colors and line styles.

a different color. Based on these results, the best match of the non-stationary range is obtained for $\alpha = 2.3$, because with $\alpha = 2.35$ the non-stationary regime reappears for $I_b \geq 100$ mA. The frequency jump in this graph occurs, where one sideband achieves a slightly higher amplitude than the previously dominant peak, so that the exact location of this jump should not be taken as reference for matching the correct pitch-angle.

The pitch-angle dependence on magnetic field as shown in Fig. 2.5 has been included in the TWANG-PIC simulations by multiplying the pitch-angle that was obtained from DAPHNE by a constant factor as $\alpha_{\text{optim}}(B_0) = \frac{\alpha_{\text{optim}}(B_0=9.54\text{T})}{\alpha_{\text{daphne}}(B_0=9.54\text{T})} \cdot \alpha_{\text{daphne}}(B_0) = \frac{2.3}{1.94} \cdot \alpha_{\text{daphne}}(B_0)$, leading to values ranging between $\alpha_{\text{optim}}(B_0 = 9.50\text{T}) = 2.365$ and $\alpha_{\text{optim}}(B_0 = 9.65\text{T}) = 2.134$.

In further simulations, the effect of pitch-angle spread in simulations was investigated, presented in Fig. 5.6. Here, a comparison between simulations with ($\Delta\alpha = 5\%$, exceeding DAPHNE-predictions of Fig. 2.5) and without α -spread is shown for RF-power and RF-frequency as well as the region of non-stationary oscillation, for an I_b -scan. It is observed that the inclusion of a realistic pitch-angle spread changes only minor details such as the exact transition point to the higher-power oscillation mode at $I_b = 80$ mA and $I_b = 130$ mA, but neither the overall behavior nor the range of beam-current, where the non-stationary regime appears. The weak influence of $\Delta\alpha$ on the non-stationary regime is consistent with the results of Airila et al. [60].

In addition to the influence of velocity-spread, also the influence of a spread in guiding center radius and the influence of the wall conductivity have been tested. The results are summarized in Fig. 5.7. Here, an exaggerated velocity-spread (in this case defined by the axial momentum) of $\Delta p_z = 10\%$ and a (according to DAPHNE) realistic guiding center radius spread of $\Delta R_g = 2\%$ are

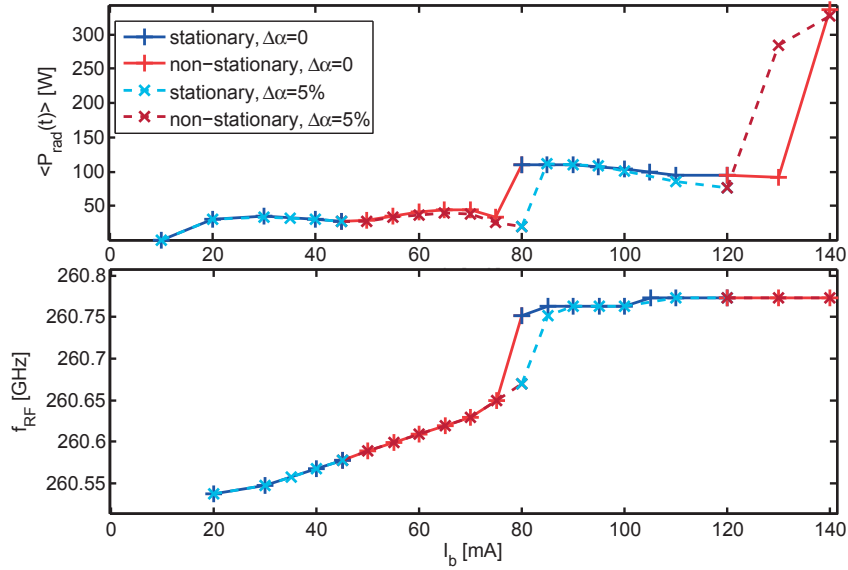


Figure 5.6: Influence of pitch-angle spread on TWANG-PIC results: time-averaged power and dominant RF-frequency (highest peak in spectrum) for I_b -scan at $B_0 = 9.54 \text{ T}$ / $\alpha = 2.3$. Other parameters as in table 3.3. (blue/red, solid line, '+'): Stationary / non-stationary oscillation without spread; (Light blue/dark red, dashed line, 'x'): Stationary / non-stationary oscillation with spread $\Delta\alpha = 5\%$.

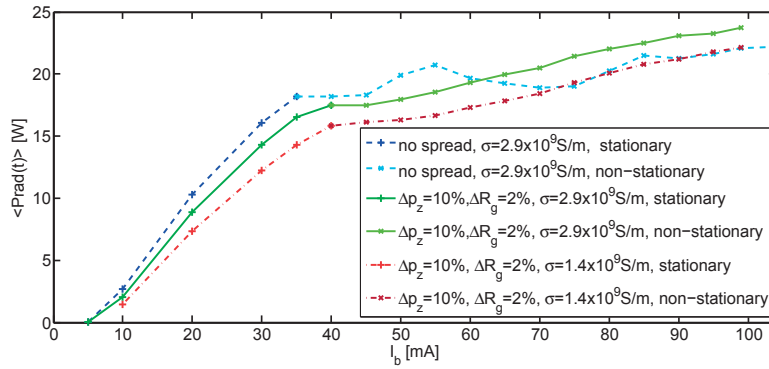


Figure 5.7: Influence of spread in velocity and guiding center radius and of the wall conductivity on TWANG-PIC results. The time-averaged RF-power is shown for I_b -scan at $B_0 = 9.65 \text{ T}$, with $\alpha = 2.05$. Other parameters as in table 3.3. The non-stationary regime is shown by a different color. For different colors and line styles see legend.

used. It is observed, that the influence of the spreads is only minor, since even in this non-stationary simulation in the backward-region, the power is only deviating by a maximum of $\lesssim 12\%$ and since the non-stationary oscillation appears approximately at the same threshold. Because the spreads in pitch-angle and guiding center radius have only minor influence on the

5.3. SIMULATION OF NON-STATIONARY OSCILLATIONS

results, both spreads are not included in any of the following non-stationary simulations, in order to facilitate the analysis of the occurring beam-wave interaction. A doubling of the wall resistance with respect to the usual value leads to exactly the same behaviour but with a power that is reduced by $\sim 9\%$.

Previously, several publications were dedicated to the effect of end reflections on non-stationary oscillations in simulations [161, 162, 163] and also in experiment there were devices, where the non-stationary oscillations were observed as a result of artificially increased reflections [157, 164]. Thus, it was investigated whether the result with the single-frequency Boundary Conditions (B.C.) Eq. (3.20) is different from the result with the broadband non-reflecting B.C. (see section 3.3.1). The simulated RF-power evolutions with these two B.C.s on a non-stationary operating point are compared in Fig. 5.8. It shows that in contrast to the references above, the

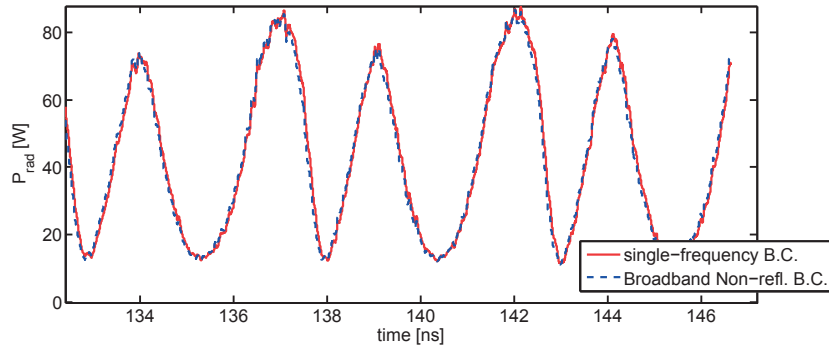


Figure 5.8: Influence of radiation boundary condition on non-stationary TWANG-PIC results. The temporal evolution of the RF-power at the end of the simulation is shown for $I_b = 65 \text{ mA}$ / $B_0 = 9.54 \text{ T}$ / $\alpha = 2.3$ with single-frequency boundary condition and broadband non-reflecting boundary condition. It shows, that the result is independent of the choice of boundary condition.

oscillation is unchanged by using the broadband non-reflecting B.C., probably because also the single-frequency B.C. provides very small reflections ($< 1\%$) over the bandwidth of the non-stationary oscillations. Thus, it was decided to use the single-frequency B.C. in the following simulations in order to facilitate the setup of the simulations and to reduce the runtime.

Finally, the influence of the magnetic field profile has been analyzed by comparing the results for the generally used B_0 -profile with the case of an axially uniform magnetic field. The resulting comparison of power and operating regimes is shown in Fig. 5.9. It can be observed, that the simulations with uniform magnetic field show a small shift in the non-stationary I_b -range with a slightly smaller power. The overall result however is similar to the one including the magnetic field tapering.

5.3.1 Experiment-theory comparison of non-stationary regime categories

In order to compare the experimental categorization to simulations, a full parameter-scan has been performed with TWANG-PIC, using the parameters described above ($\alpha(B_0=9.50\text{T}) = 2.365$ to $\alpha(B_0=9.65\text{T}) = 2.134$, elevated pitch angle with a constant anode voltage). In Fig. 5.10, the

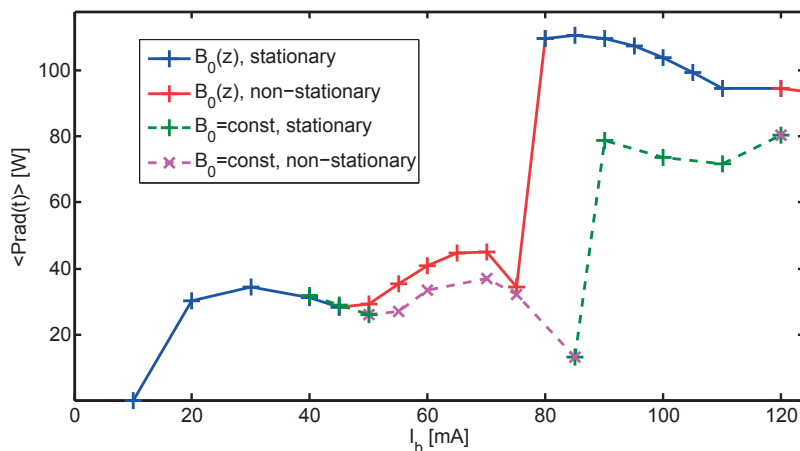


Figure 5.9: Influence of realistic magnetic field profile on TWANG-PIC results. The time-averaged RF-power is shown for I_b -scan at $B_0 = 9.54$ T, with $\alpha = 2.3$ for the usually used realistic B_0 -profile (blue / red) and for a uniform magnetic field (green / magenta). The non-stationary regime is shown by a different color.

main results of this simulation study are compared to the experimental results.

The conclusion from these simulations is that the same kinds of oscillation are observed as in experiment, including sidebands, period doubling, period tripling etc. and chaos. In this case, the thresholds of the non-stationary regime are relatively close to the measurements in the forward-region, but match less well in the backward-region where the threshold is significantly lower in simulations. This comparison suggests also, that the exact shift for matching the experimental magnetic field could be slightly smaller than the value of $\Delta B_0 = 0.05$ T that was added in this graph.

Also the overall pattern of the non-stationary types is reproduced, although the exact location of each category is different in simulations. In particular, like in experiment the category which appears first above the non-stationary threshold is always the sideband regime. Furthermore, the chaotic region in the central part of the operating plane is relatively well reproduced in simulation. Also the stationary region above a non-stationary region at lower B_0 values is reproduced, although the re-appearance of non-stationary oscillations above this second stationary regime has not yet been observed in experiment.

Thus, we can conclude, that the simulations with the appropriate PIC-model can well reproduce all the details of oscillation that appear within the non-stationary regime. The weaker agreement in the backward-interaction region is a well-known behaviour of both the codes at SPC and elsewhere (see e.g. [31]), which still needs further investigation in the future.

As mentioned earlier, the regions of the stationary and non-stationary regimes on a plane of operating parameters have been the subject of a series of publications [117, 53, 158, 159, 60, 160]. Most of these simulations however used a model based on the time-scale separation between field and particle (Eq. (3.10)) as well as a strongly simplified cavity. Here we showed that, like these earlier publications, the TWANG-PIC-simulations show the appearance of alternating sta-

5.3. SIMULATION OF NON-STATIONARY OSCILLATIONS

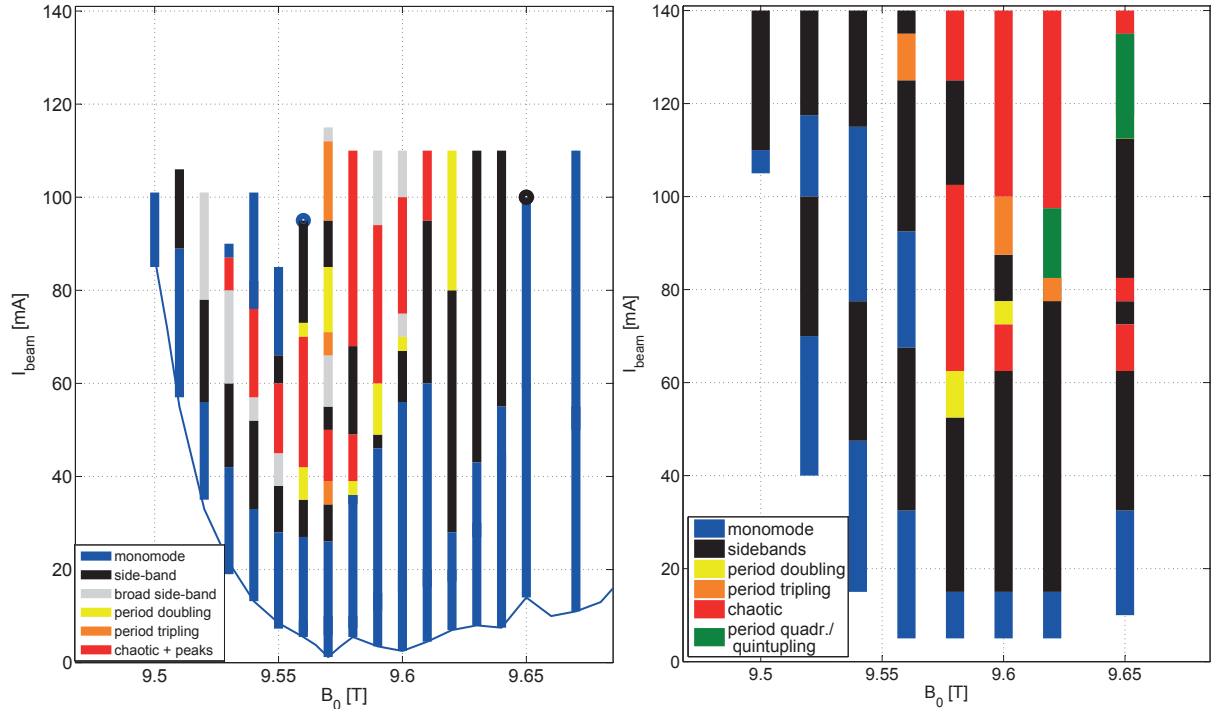


Figure 5.10: Comparison of the categorization of the occurring type of RF-oscillation from experiment (left) and TWANG-PIC-simulation. In simulations, the same non-stationary oscillation types appeared as in experiment. For the PIC-simulations, the pitch-angle was chosen to vary between $\alpha = 2.365$ ($B_0 = 9.50\text{T}$) and $\alpha = 2.134$ ($B_0 = 9.65\text{T}$) in the same way as in DAPHNE-results for a constant anode-voltage.

tionary and non-stationary regions in the $(B_0 - I_b)$ -plane. However, in this work, for the first time such simulations results could be compared directly to experimental results, and this comparison proved to be successful.

Despite the disagreement in some details when comparing the simulation results with experiment, these simulations already show a considerable improvement with respect to previously published theoretical results by other authors. In this context we compare our results with the relatively general study of the non-stationary regime that was performed by Airila [64]. In this work, the appearance of different non-stationary categories was studied while again using a model based on the usual time-scale separation between field and particle (Eq. (3.10)) as well as a simplified geometry of a uniform cavity wall radius with artificial reflections in the radiation B.C.. The parameters of this study are normalized variables, where the dependency on the pitch-angle is included into the three independent normalized parameters Δ , I and μ .

The main results, that have been published e.g. in [60] are shown in Fig. 5.11, where the detuning in this study is defined as $\Delta = \frac{2}{\beta_{\perp}^2} \left(1 - \frac{\Omega_c}{\omega_0}\right)$. Here, on top of Airila's results, the non-stationary threshold current measured in the DNP-gyrotron is included (as in Fig. 5.1). For this, the no-oscillation current from Airila's results is approximately reproduced (blue curve) and shown in

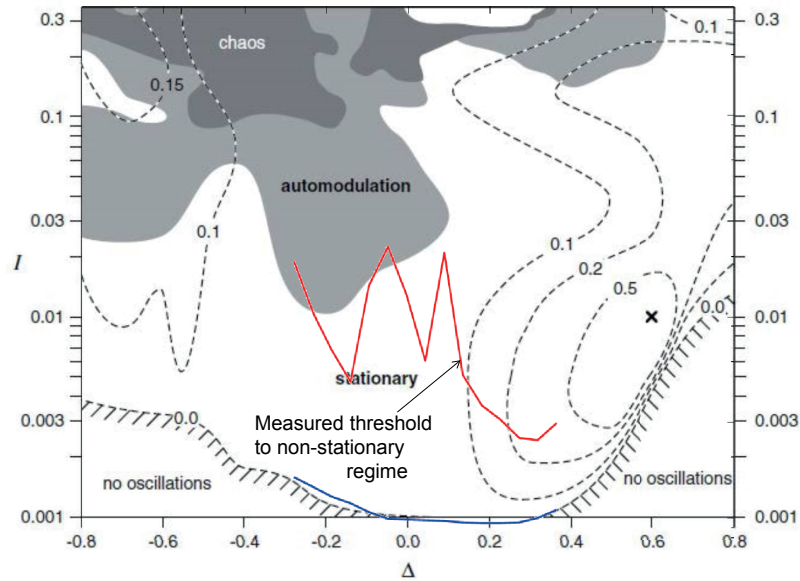


Figure 5.11: From Airila et al. [60]: Map of operating regimes in the plane of detuning and normalized current. Remark, that the non-stationary onset current corresponds to at least ten times the no-oscillation current (far backward-region). The red curve shows the non-stationary threshold current measured in the DNP-gyrotron, included by fitting the measured no-oscillation current to the one in the graph (blue, $I_{\text{no-osc}}$) and reproducing the fraction of non-stationary threshold current over no-oscillation current as $I_{\text{no-osc}} = (I_{\text{nonst}}/I_{\text{no-osc}})_{\text{exp}} \cdot I_{\text{no-osc}}$.

an axis with the same dimensions as the original figure. Then, a current is displayed that is the same ratio above the no-oscillation current as in our experimental results (red).

It can be seen that in the general study of Airila, the non-stationary regime is predicted to appear at a current that is by a large factor above the no-oscillation current. In the range of detuning values relevant for our case, the minimum non-stationary threshold current is a factor 100 above the starting current. As opposed to these studies, our simulations showed, in agreement with the experiment, that non-stationary oscillations can appear at a current that exceeds the starting current by less than a factor two (less than factor 2.5 above no-oscillation current).

None of the previously published simulations on gyrotrons have predicted a non-stationary threshold as low as observed in our case both in experiment and simulation, although for a gyro-BWO such a low threshold was presented in [155, 53]. This is a very important result since it shows the capabilities of the newly developed simulation model and because it shows that non-stationary oscillations can play a more important role in gyrotron operation than previously reported.

5.4 Dependency of rf-characteristics on operating parameters

Complementary to the comparison of the non-stationary categories, the dependency of the RF-characteristics on the operating point is compared between experiment and simulation.

In Fig. 5.12, the time-averaged RF-power and the dominant RF-frequency (highest peak in RF-spectrum) are analyzed as a function of the beam-current. The parameters are the ones, that were used in section 5.3 for finding the optimum α ($B_0 = 9.54$ T, $\alpha = 2.3$, other parameters as in table 3.3). For the power-comparison in Fig. 5.12a) the time-average of a fluctuating power is shown on the non-stationary operating points. Furthermore, the experimental power-values have been doubled for an easier comparison. In order to interpret the frequency-dependence shown in Fig. 5.12 b), the cavity-field profiles of three specific beam current values are shown in part c) with the corresponding beam-currents indicated in part b).

The power-dependence in TWANG-PIC reproduces roughly the characteristics of the experimental results. Both curves show an initial increase of power with current, the following plateau of the power with increasing I_b around the first non-stationary region (experiment: $I_b = 32 - 76$ mA, simulation: $I_b = 45 - 80$ mA) and a following power-increase at the end of this non-stationary region. The experimental current-dependence is probably smeared out by a pitch-angle fluctuation, that will be explained in more detail in the next section 5.5, so that no discrete jump in power is observed there.

Regarding the power in the first non-stationary region, one might get the impression that with the appearance of non-stationary oscillation the efficiency is strongly degraded. This however is contradicted by the strongly non-stationary operating point (pulses with 97% power modulation) at $I_b = 140$ mA, where simulations predict a time-averaged ($\langle \cdot \rangle_t$) power of $\langle P_{RF} \rangle_t = 336$ W (out of the limits of the graph) and an average electronic efficiency of $\langle \eta_{el} \rangle_t = 23.5\%$ (against e.g. $\eta_{el} \approx 14\%$ at $I_b = 95$ mA). In experiment, this region of currents has not yet been explored, because the maximum current has been limited to $I_{b,max} \sim 115$ mA. Because of this high-efficiency non-stationary operating point, no simple conclusion can be made regarding the influence of the non-stationary regime on RF-power and efficiency.

Also the overall dependency of the dominant RF-frequency can be reproduced by TWANG-PIC, as shown in Fig. 5.12b). In both simulation and experiment, a jump of this frequency can be observed inside the non-stationary region. In this step the position of maximum amplitude in the spectrum changes from one sideband to the neighboring one. The exact position within the non-stationary region, at which the sideband peak with the higher frequency becomes dominant, is however different for simulation. The step in frequency can be further explained using field profiles from the simulation results.

Such instantaneous field profiles are shown in Fig. 5.12c), for beam currents in the lower stationary region ($I_b = 30$ mA), in the first non-stationary region ($I_b = 65$ mA, snapshot of oscillating profile) and in the second stationary region ($I_b = 100$ mA). Comparing these amplitude and phase profiles, one can clearly identify a change of the non-linear axial mode within the non-stationary region, from a field-profile with a single maximum, resembling the cold-cavity $q=1$ -axial mode towards a $q=2$ -like mode with two amplitude maxima inside the cavity. Thus, the frequency before the step (lower I_b) can be identified as the one belonging to the $q=1$ -like mode, while the frequency after the step corresponds to the frequency of the $q=2$ -like mode. For beam cur-

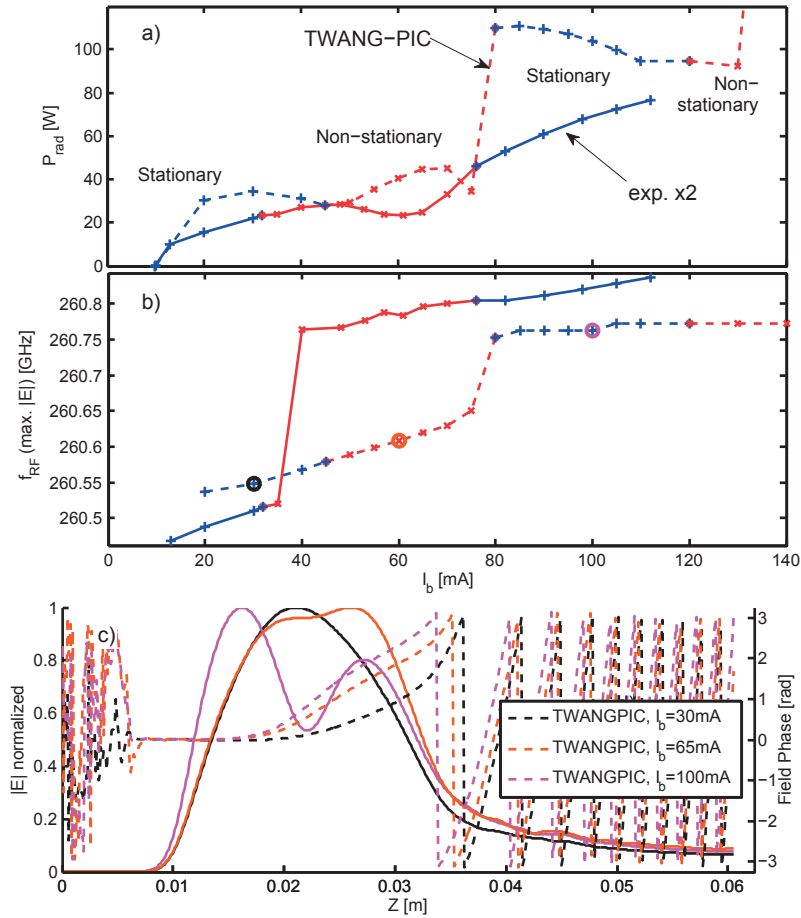


Figure 5.12: Comparison between experiment (solid) and TWANG-PIC (dashed) for a scan in beam current on $B_0 = 9.54 T / \alpha = 2.3$. a) Time-averaged RF-power versus I_b with experimental value doubled. $P_{\text{RFpic}}(I_b = 140 \text{ mA}) = 336 \text{ W}$. b) Dominant RF-frequency versus I_b with indications of the current values at which the profiles are analysed. c) Snapshot of field amplitude at the end of the simulation time (solid, left y-axis) and phase profiles (dashed, right y-axis) from TWANG-PIC, for the currents indicated by the same color in part b). Stationary / Non-stationary regime in blue / red, respectively.

rents in the range $45 \text{ mA} < I_b < 80 \text{ mA}$ exhibiting a non-stationary oscillation, the axial profile of the wave electric field oscillates between the two modes.

In order to analyze the field profile oscillation on a non-stationary operating point, a series of snapshots has been created in order to represent a full cycle of the non-stationary oscillation. This evolution is shown in Fig. 5.13, showing in 6 graphs the evolution of the field amplitude and phase profile inside the cavity profile. In each graph the field profile passes from one point of time (dashed lines) to the next instant (solid lines) in the oscillation cycle. It is observed, how from Fig. 5.13 e) the field amplitude increases strongly while the shape of the profile resembles

5.4. DEPENDENCY OF RF-CHARACTERISTICS ON OPERATING PARAMETERS

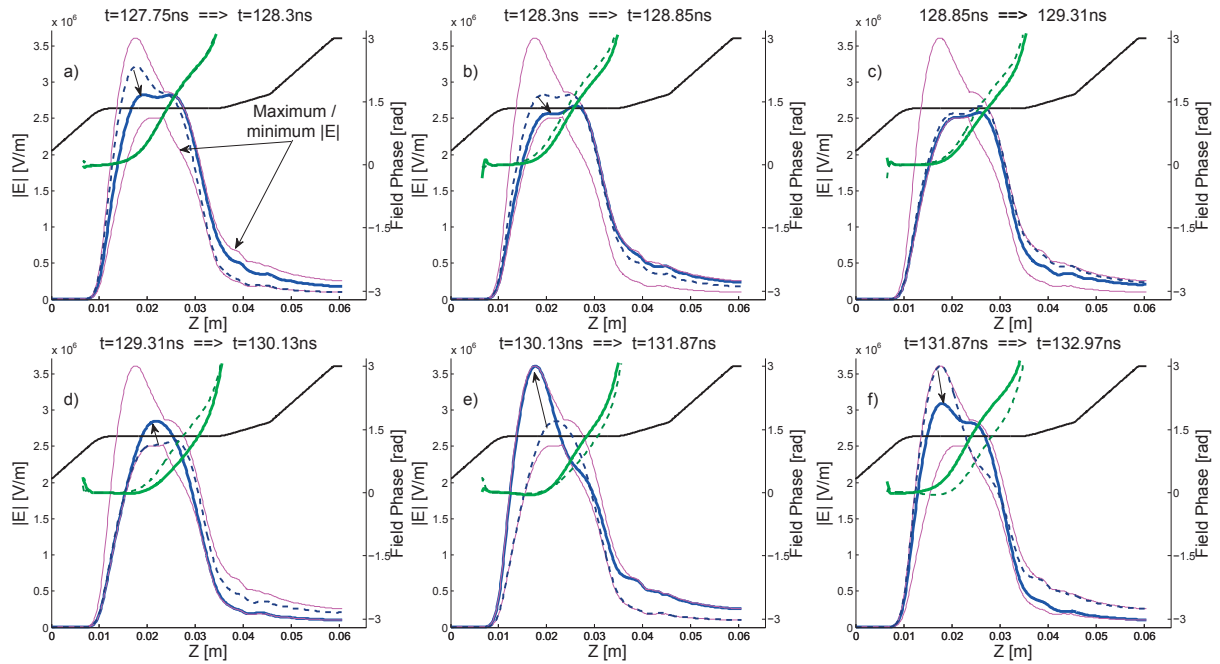


Figure 5.13: Evolution of field profile on non-stationary operating point at $I_b = 65 \text{ mA}$ / $B_0 = 9.54 \text{ T}$, $\alpha = 2.3$ over an entire oscillation cycle. Field amplitude (blue, left y-axis) and phase (green, right y-axis) inside the cavity profile (black, normalized) from previous point of time (dashed lines) to the next instant (solid lines). The minimum and maximum amplitude value at each axial position are shown by pink lines.

a cold-cavity $q=1$ -profile and the maximum moves towards the cavity entrance in a contraction of the field profile. In the following evolution series f) to c) the large maximum at the entrance decays and the profile resembles more and more a $q=2$ -profile where in the end the second maximum along z , exceeds the first. From this small-amplitude $q=2$ -like profile, in part d) the field again tends towards a $q=1$ -like profile that grows and contracts.

Such a forward-and backward bouncing field amplitude maximum has also been presented in [51] in the energy equilibration process in the RF-startup. Therein it was also described, that this equilibration process eventually transforms into the non-stationary oscillation at higher currents. This cycle of field profile oscillation not only shows the oscillation between $q=1$ / $q=2$ -like profiles, but can also be used in order to extract information about the underlying mechanism of non-stationary oscillation, which will be done in more detail in section 5.9.

In summary, we can conclude that the PIC-simulations can qualitatively reproduce the overall complex dynamics of the measurements for this scan in beam-current and that they confirm a competition between two longitudinal modes. Furthermore, as shown in Fig. 5.12, simulations predict the existence of a second region exhibiting non-stationary oscillations at high beam-currents with a strongly increased power inside the non-stationary region.

In order to explore, what is expected for much higher beam currents, a continuation of the above-shown I_b -scan has been performed in TWANG-PIC-simulations. The result of this study is pre-

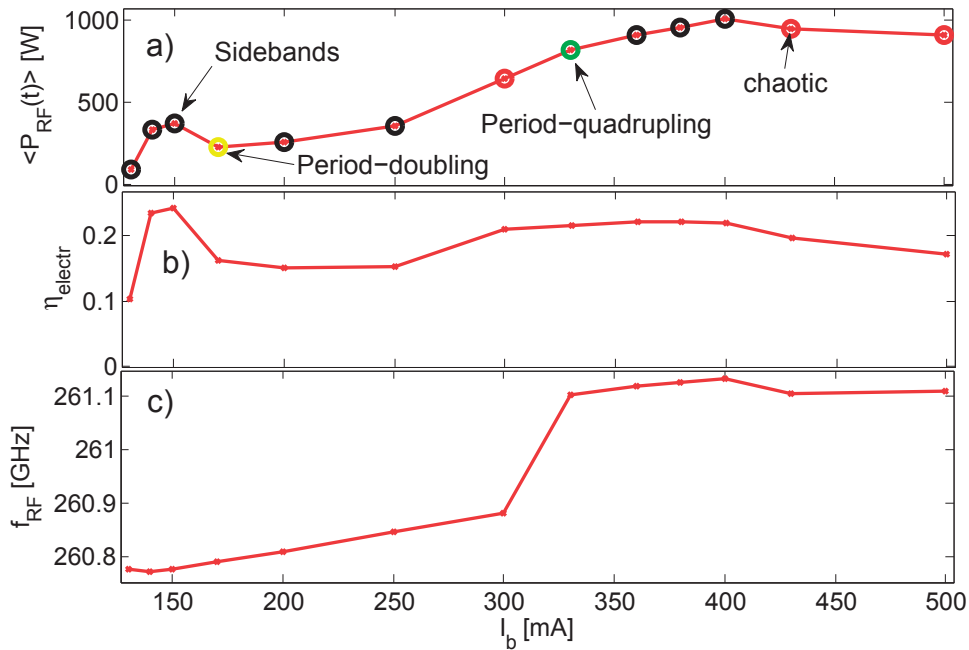


Figure 5.14: Continuation of Fig. 5.12 at high beam current (TWANG-PIC, $B_0 = 9.54 T / \alpha = 2.3$). a) Time-averaged RF-power versus I_b . Here, the category of non-stationary oscillation has been added as circles around the power-markers with the colors defined in Fig. 5.10. b) Time-averaged electronic efficiency. c) Dominant RF-frequency versus I_b . The first two I_b -values corresponds to the last two I_b 's in Fig. 5.12.

sented in Fig. 5.14, showing the time-averaged RF-power, the time-averaged electronic efficiency and the dominant RF-frequency for operating points up to $I_b = 500$ mA. Additionally, in inlet a) for a comparison with the categorization of Fig. 5.10, the color of the corresponding non-stationary category has been added as rings around the markers of each operating point. It is observed, that no more stationary operating point is observed, but that the non-stationary category varies, with mainly sideband and chaotic category. The RF-power remains at the elevated level of the last I_b -value in Fig. 5.12, which also results in an elevated efficiency.

In addition to the discrete frequency-jump at $I_b = 80$ mA in the previous graph, here another discrete frequency-jump is observed at $I_b = 330$ mA, between the two regions with sidebands. This again indicates a change of mode around this region, which is also observed in the corresponding field profiles (not shown here).

5.5 Temporal variation of spectra induced by anode voltage fluctuations

In the following it will be shown that different dynamical regimes (sideband, chaotic, etc.), that were described above for different operating points, can even be observed sequentially in time

5.5. TEMPORAL VARIATION OF SPECTRA INDUCED BY ANODE VOLTAGE FLUCTUATIONS

for a fixed operating point. This is due to the $\sim 30\text{kHz}$ anode-voltage fluctuation described in section 4.4 ($\frac{\Delta V_a}{V_a} \approx \frac{30\text{V}}{8800\text{V}}$), which induces a fluctuation of the electron pitch-angle, and thus of the RF-properties. This V_a -fluctuation has a large effect on the non-stationary regime.

An example of the consequences of this anode-voltage fluctuation on the frequency spectrum in

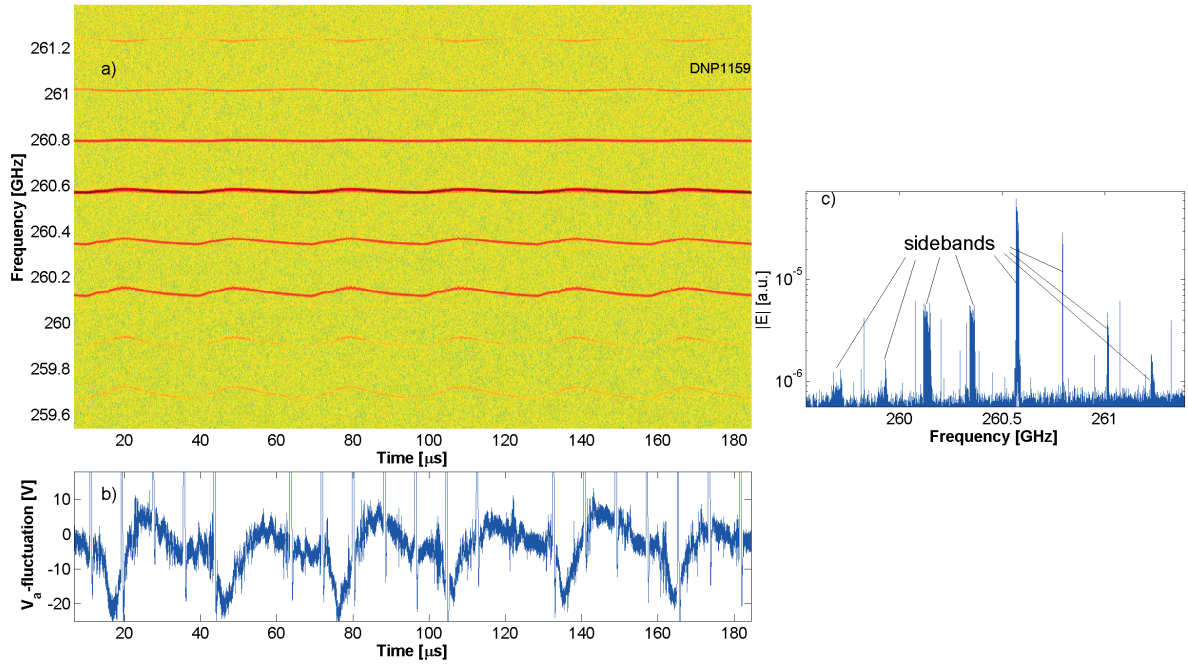


Figure 5.15: a) Fluctuation of RF-frequencies with time in the sideband-regime, caused by anode-voltage fluctuation. b) Fluctuation of anode-voltage from power supply, numerically noise-filtered (-3dB at $\sim 7\text{MHz}$). c) Spectrum from FFT of heterodyne IF-signal over entire time window. In c), additional artificial peaks become visible (e.g. at $f_{\text{IF}} = 2.5\text{GHz}$), apparent as single-pixel peaks, that are not affected by the V_a -fluctuation.

the sideband-regime can be seen in the spectrogram shown in Fig. 5.15, for which the IF-signal of the heterodyne system (see section 2.5) has been acquired simultaneously with the measurement of the anode-voltage on the fast LeCroy-oscilloscope (13 GHz analogue bandwidth).

On the displayed operating point, the sidebands frequency variations are synchronous with the anode-voltage fluctuation (Fig. 5.15b). As it has been mentioned in section 4.4.1, the spikes in the anode-voltage time trace are probably not a measurement of actual V_a -fluctuations. As shown in Fig. 5.15c), in a spectral analysis of this oscillation over a longer time-window this fluctuation of the sideband-frequencies causes a slight broadening of the sidebands on the low-frequency side. Here, for the RF-spectrum an FFT-window of the entire displayed acquisition time was chosen.

An example of spectrum-variation due to V_a -fluctuation for a partly chaotic operating point is shown in Fig. 5.16. Again, the fluctuation of the spectrum follows the fluctuation of the anode-voltage, which confirms the correlation between the two phenomena. In the spectrogram it

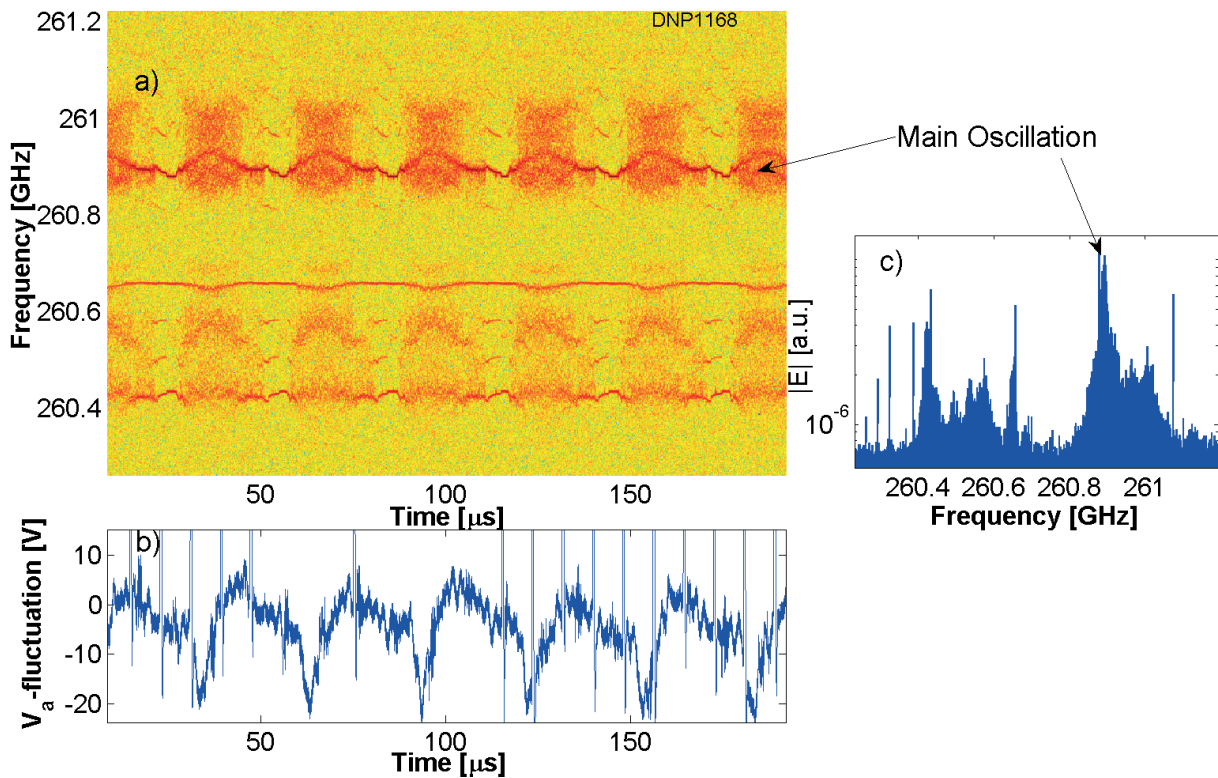


Figure 5.16: a) Fluctuation of RF-frequencies with time on an operating point, where the spectrum shows transitions between period doubling and chaotic oscillation, caused by anode-voltage fluctuation. b) Fluctuation of anode-voltage from power supply, numerically noise-filtered (-3 dB at ~ 7 MHz). c) RF-spectrum from FFT of heterodyne IF-signal over entire time window.

is observed, that the system oscillates between strongly time-varying sidebands and a chaotic broadband oscillation with the period of the voltage fluctuation. This combination of the two regimes causes a superposition of distinct peaks in the spectrum on top of a broadband background, as it is shown in Fig. 5.16 c).

These two examples show, that the spectra that were analyzed for the categorization in Fig. 5.2 do only include part of the information of the non-stationary oscillation type, that appears on each operating point. The spectrum only represents a superposition of the various spectra that sequentially appear during the V_a -fluctuation. The system often changes between different types of non-stationary oscillation during the fluctuation, whereas the spectrum had to be categorized into a single type. Such is the case for Fig. 5.16, which is categorized into chaotic oscillation because of the broadband spectral background.

5.6 Analysis of chaotic regime and the route towards chaos

The chaotic regime was already shortly introduced during the categorization of non-stationary oscillation in section 5.2. As it could be seen in Figs. 5.2f) and 5.3d), the chaotic oscillation is characterized by a broadband-spectrum, that is continuous over some frequency-range, and a power-evolution that is irregular.

This irregularity was expressed in the power-evolutions in Fig. 5.3 by the fact, that for all regimes except the chaotic regime, the power-evolution at any point of time recurs in the same way at a later instance of the time-trace. The irregular temporal behavior in the final asymptotic state fundamentally distinguishes the chaos from all the other types of oscillation. The non-recurrent behavior is illustrated here on the chaotic power-evolution, but in the chaotic regime this is a general property of any trajectory of a variable or state in phase-space.

Chaos and the transition to chaos has been observed and analyzed in many fields of physics [165, 166, 167] and have also been analyzed in publications by several research groups in gyrotrons [168, 60, 169, 170]. Here, we will analyze several aspects of the experimentally observed chaotic regime, in particular we will classify the route(s) to the chaotic state and determine the dominant chaotic timescale.

5.6.1 Routes to Chaos

The route to chaos in gyrotrons has been analyzed in a series of earlier publications on gyrotrons and similar devices. A period-doubling route to chaos was observed in numerical simulations for instance in [51, 158], sometimes classed as the Ruelle-Takens route, in which chaos appears after a finite number of bifurcations (period multiplications), whereas the Feigenbaum period doubling sequence has an infinite number of bifurcation. Also an experimental investigation of non-stationary oscillation in a gyro-BWO [52], a transition from sidebands to stochastic behavior (continuous spectrum) via period multiplication was observed with increasing beam current. The subject has then been studied in detail both by a group at Saratov University [168, 171] and by Airila et al. [60]. These publications are purely based on numerical simulations, in which the underlying assumption of time-scale separation between the electron transit time and RF-wave evolution (see Eq. (3.10)) is marginally violated. Despite this inconsistency, the authors agree on the observation of two types of the route towards chaos, of which the more common is the above-mentioned transition to chaos via a period-doubling bifurcation series, also known as the Feigenbaum period-doubling cascade [172, 167]. For larger positive detuning [168], the transition to chaos was classified as intermittency, where a nearly periodic system shows irregularly spaced bursts of chaos [173].

The categorization of the non-stationary oscillations in experiment and simulation (Figs. 5.2 and 5.10) showed the period doubling type in vicinity of the chaotic region, suggesting the period doubling route to chaos.

The period doubling sequence can be observed even more clearly by analyzing the transition towards chaos directly as a temporal evolution during the anode-voltage fluctuations. The thus induced fluctuation of the pitch-angle creates a sequence of changes between different non-stationary categories and often shows part or the entire sequence of transition towards chaos.

A particularly clear case is shown in the spectrogram of Fig. 5.17, showing a transition from

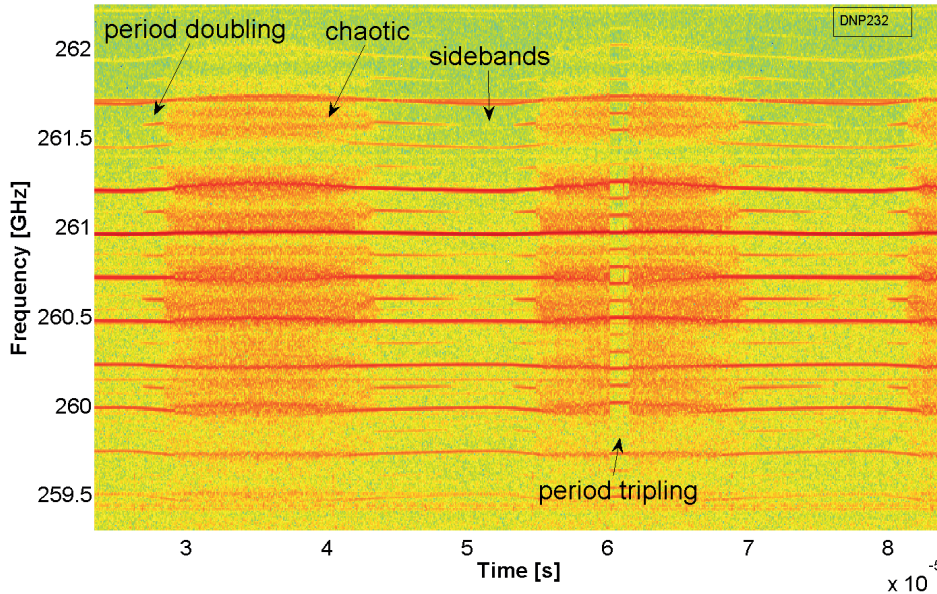


Figure 5.17: Spectrogram for an operating point, where during the anode-voltage fluctuation a transition from the sideband regime to the period-doubling regime and then towards chaos is observed. A short period-tripling phase is observed starting at $60 \mu\text{s}$.

the sideband regime to the period-doubling regime and then towards chaos, where some of the sideband-peaks are still present in the chaotic section. Later in the spectrogram (around $t = 45 \mu\text{s}$), this sequence is reversed to go back towards a sideband oscillation. Thus, in this case the transition towards chaos can be classified as the period-doubling bifurcation type, as predicted in the above-mentioned theoretical publications.

For a full period-doubling route to chaos one would however expect more steps of period multiplication than only sideband - period doubling - chaos. Such higher orders of period multiplication are also observed in the DNP-gyrotron, but as it will be shown in the following, the transition towards chaos usually doesn't strictly follow the even ordering of the period bifurcation sequence (doubling, quadrupling, etc.). This circumstance is illustrated in the more typical spectrogram with a transition to chaos shown in Fig. 5.18, where the dominant peak and the sidebands are indicated by arrows in order to distinguish them from intermediate peaks.

In this spectrogram, the non-stationary regimes follow the sequence of period doubling ($\Delta f_{\text{SB}} \approx 140 \text{ MHz}$) - period quadrupling - chaos - period quintupling - chaos - period tripling - chaos - period doubling. The fact, that period tripling and quintupling appears in the sequence, is quite untypical since it represents an odd number of intermediate frequencies between sidebands, which is not included in the Feigenbaum period-doubling sequence [166]. It has however been observed on other physical systems and was in a general way described for anharmonic oscillators [174, 175, 176].

The most common type of odd period multiplication is the period tripling regime. Interestingly,

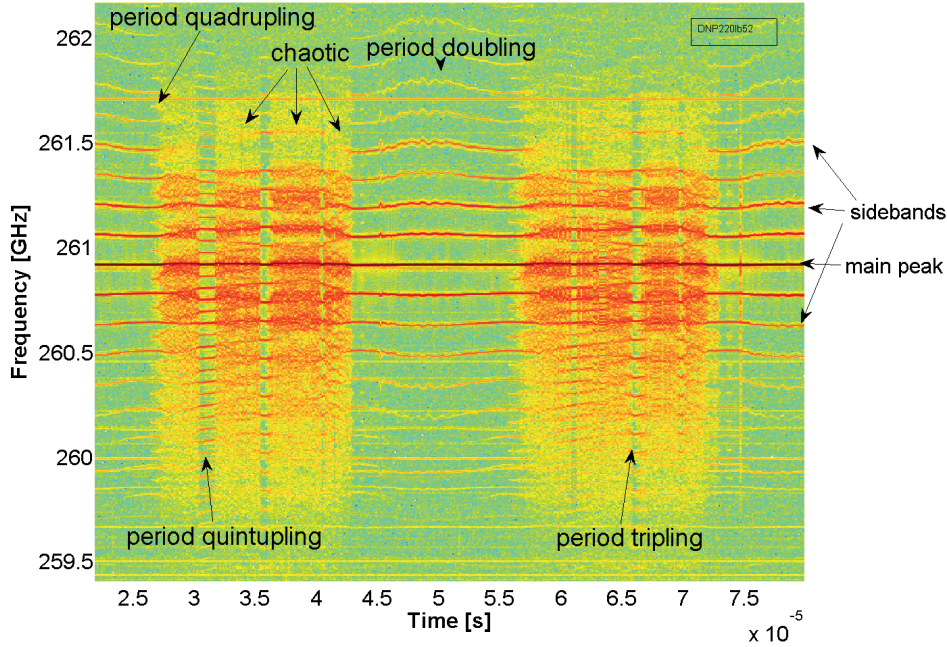


Figure 5.18: Spectrogram for an operating point, where during the anode-voltage fluctuation a transition from the sideband regime to the period-doubling regime and then towards chaos is observed.

the period-tripling regime can appear both with equidistant peaks in the spectrum and with non-equidistant intermediate peaks. This character is illustrated in Fig. 5.19, where the system passes from period-doubling to tripling in a continuous splitting of the intermediate peak. This shows, that the intermediate sidebands cannot be equidistant at all instances of the shown spectrogram. The performance of the TWANG-PIC-simulation is underlined by the fact, that also in simulations a period tripling appears, that is mostly but not always equidistant. A spectrum with such a non-equidistant period tripling from PIC simulations is shown in Fig. 5.20 for the operating point $B_0 = 9.62 \text{ T} / I_b = 80 \text{ mA} / \alpha = 2.178$.

Other typical examples for the routes to chaos are included in Fig. 5.21. The route to chaos often follows the sequence sidebands - period doubling - period tripling - chaos, such as it is observed in Fig. 5.21b). However, the system also shows a sidebands to chaos such as in Fig. 5.21a) (also including period doubling \rightarrow chaos).

Thus, one can conclude, that in experiment, the period doubling bifurcation-type of transition to chaos is confirmed, but that it doesn't follow the strict sequence of doubling the number of intermediates peaks each time. As indicated above, this can be reproduced from TWANG-PIC simulation, where in the categorization map in Fig. 5.10 all three types of sidebands, period doubling and period tripling appear in direct vicinity of the chaotic type.

Here, it has to be stressed, that the entire sequences of non-stationary oscillation types in the spectrograms are caused by a fluctuation of the anode voltage of only $\Delta V_a / V_a \sim 0.3\%$, corre-

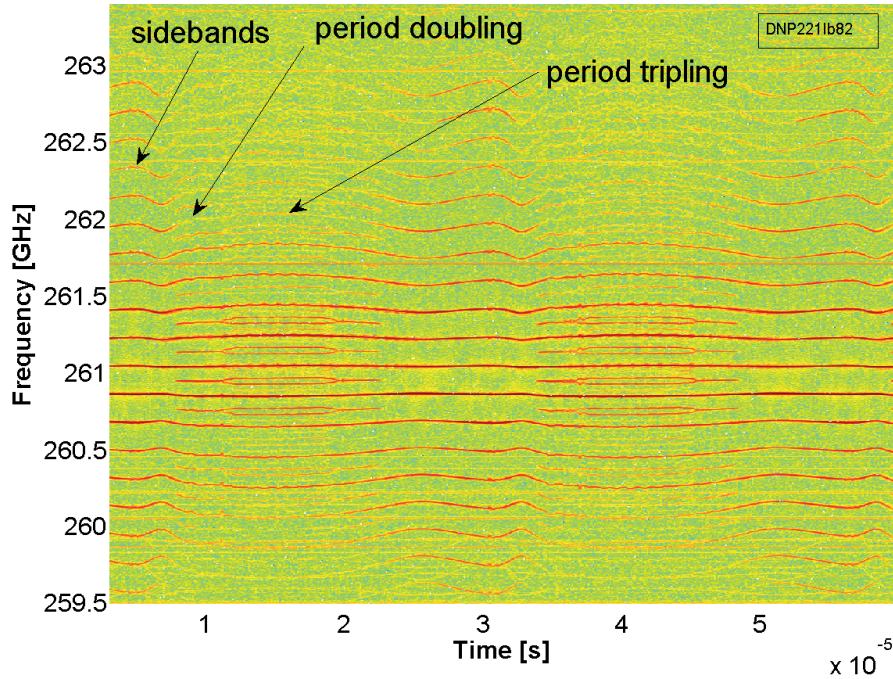


Figure 5.19: Spectrogram showing a continuous transition from period doubling to period-tripling with non-equidistant intermediate frequency peaks.

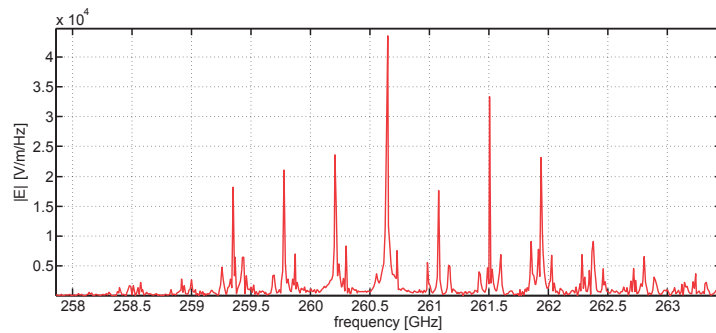


Figure 5.20: RF-spectrum showing non-equidistant period-tripling from FFT on TWANG-PIC simulations at the operating point $B_0 = 9.62 \text{ T} / I_b = 80 \text{ mA} / \alpha = 2.178$.

sponding to a fluctuation in pitch-angle of $\Delta\alpha/\alpha \sim 3\%$. This emphasizes the fact that, close to the chaotic state, systems are very sensitive to the external parameters, which is a characteristic property of a chaotic system.

In addition to this characterization of the period doubling type of transition to chaos, it has been investigated, if also the intermittency-type of transition to chaos is observed in our experiment. Although there were no clear evidences for this regime, the chaotic state was sometimes ob-

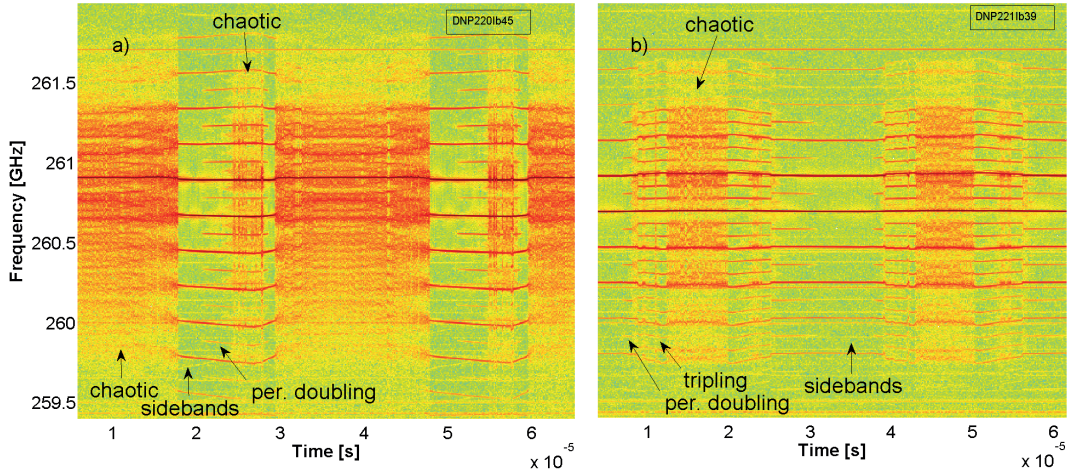


Figure 5.21: Spectrograms with different routes to chaos: a) sidebands-chaos and sidebands - period doubling - chaos and b) sidebands - period doubling - period tripling - chaos.

served in an intermittent way. In order to demonstrate this observation, a new analysis method of a bifurcation diagram is introduced. Following the analysis used in [60] and [177], extrema of the power-evolution are used in order to analyse the transition to chaos. For this, the temporal evolution of the power amplitude $V_{\text{schott}}(t)$ from the fast Schottky-diode (see section 2.5) is analysed, as it is illustrated in the small time-window with slightly chaotic power-evolution of Fig. 5.22b). Here, the extrema of the power-evolution (where $\frac{dV_{\text{schott}}}{dt}(t) = 0$) are detected (red crosses) and their amplitude $V_{\text{schott}}\left(\frac{dV_{\text{schott}}}{dt}(t) = 0\right)$ is then displayed as points in the temporal bifurcation diagram shown in Fig. 5.22 a). In this graph, a stationary oscillation would correspond to a constant power and thus a single horizontal line, while sidebands correlate (mostly) with an ordinary power-oscillation having one maximum and one minima with always the same amplitude position and thus two lines.

A comparison of Fig. 5.22a) with the corresponding spectrogram for the same time section in part c) shows, how the bifurcation at $24 \mu\text{s}$ is due to the appearance of period doubling. The period doubling / tripling sections can be well distinguished from the chaotic section, where the extrema are randomly distributed within a certain range of values. The transitions that appear in this bifurcation diagram should be compared with the different categories of routes to chaos, that have been described in earlier publications.

Fig. 5.23 presents examples of such a diagram from [64], displaying bifurcation diagrams as a function of the beam current and of the detuning, as examples of a period doubling route to chaos and of the intermittency route to chaos. A comparison with our results show that there the second transition to chaos at $t \sim 57 \mu\text{s}$ is identified as the period-doubling type, since the transition is initiated by an unstable period-doubling oscillation. The first transition at $t \sim 42 \mu\text{s}$ appears to be a combination of intermittency and the period doubling type, since the system passes from the sideband-regime to the chaotic regime by a transition, which seems to include the intermittent bursts of chaotic oscillation.

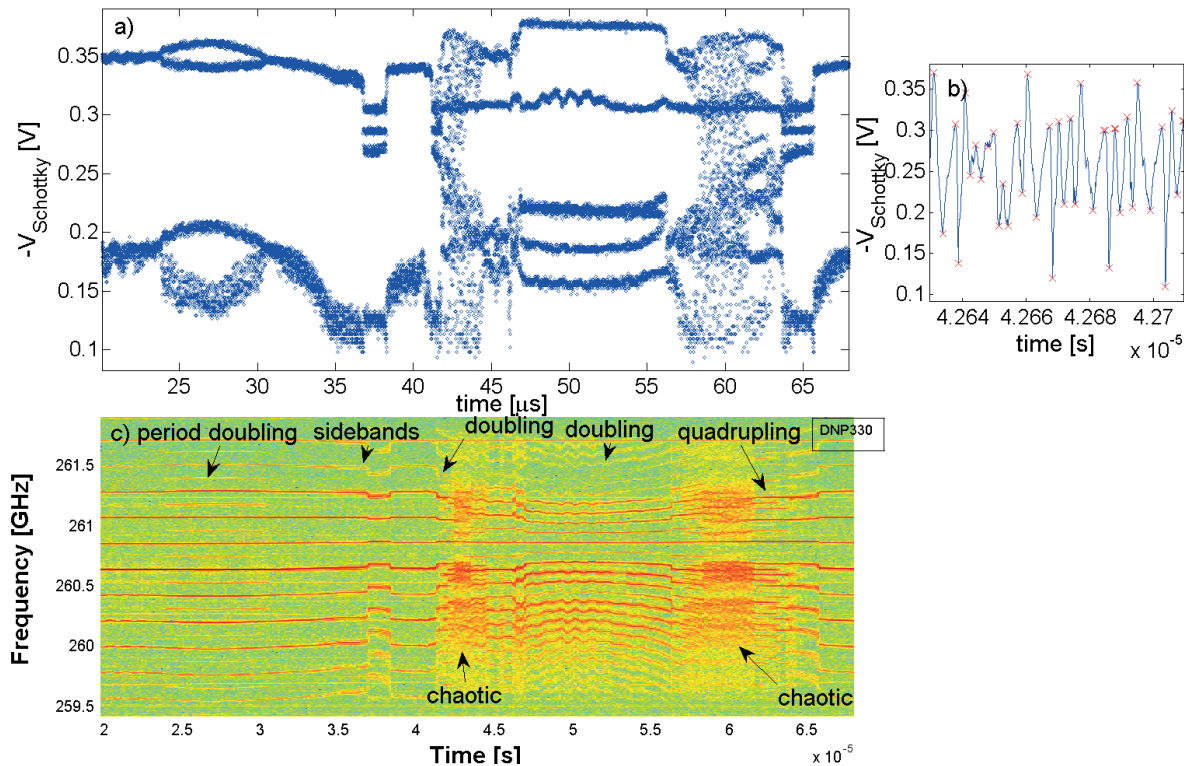


Figure 5.22: a) Temporal bifurcation diagram: Temporal evolution of extrema amplitude $V\left(\frac{dV}{dt}(t) = 0\right)$ in measured time-trace of fast Schottky-diode, corresponding to instantaneous power. b) Illustration of method how extrema (red points) are obtained from power time trace inside a slightly chaotic section (see $t = 42.65 \mu\text{s}$ in part a)). c) Spectrogram of same oscillation of which temporal bifurcation diagram is shown part a).

Another example, which includes elements of the intermittency-type transition to chaos is shown in Fig. 5.24. This bifurcation diagram includes sections of sidebands, period doubling, period tripling and chaos and the transitions to chaos around $t = 25 \mu\text{s}$ and around $t = 55 \mu\text{s}$ resemble the transitions of the intermittent type from [64] in Fig. 5.23b). Nevertheless, it cannot be decided with certainty, if any of the bursts of chaos are inherent from the system or come from the anode-voltage fluctuation.

It can thus be concluded, that the transition to chaos in experiment is governed by a modified period-doubling bifurcation route to chaos, in which elements of intermittency seem to be present.

5.6.2 Calculation of the Lyapunov-exponent

After this analysis of the transition route towards chaos, the attention will be devoted to the chaotic oscillation itself. One important method for describing the behavior of a system within the chaotic regime is based on the fact, that if the system is initiated at two neighboring points

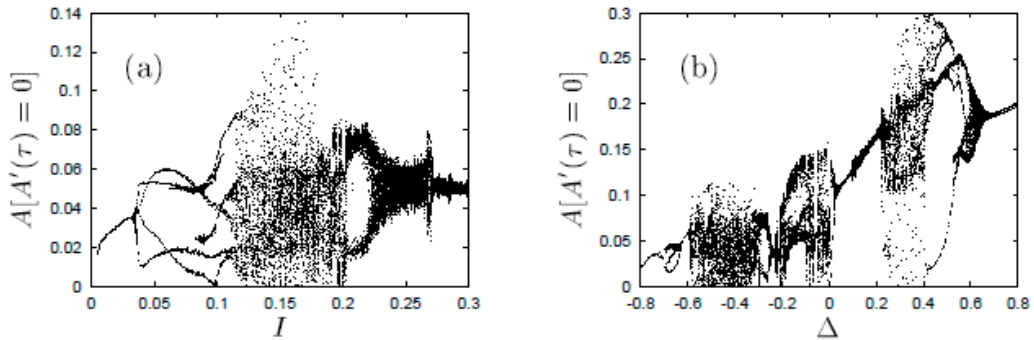


FIGURE 3.10. Routes to chaos. (a) Along the line $\Delta = -0.30$ in figure 3.9, traces of period doubling are seen. (b) Along the line $I = 0.20$, traces of intermittency appear. [95]

Figure 5.23: Airila [64]: Bifurcation diagrams from extrema in RF-power evolution, using numerical simulations. Left: period-doubling route to chaos, Right: intermittency-type route to chaos. To be compared with Fig. 5.22.

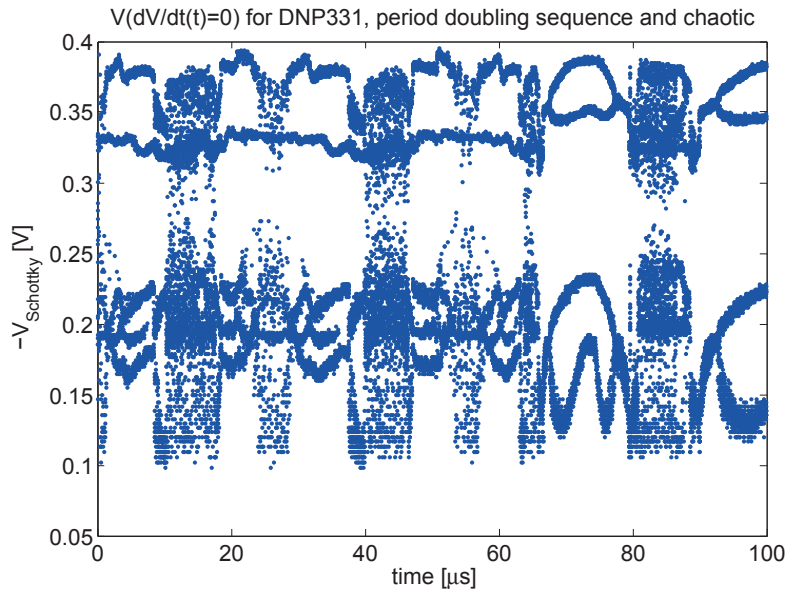


Figure 5.24: Temporal bifurcation diagram (extrema $V\left(\frac{dV}{dt}(t)=0\right)$ of instantaneous power). Here, the appearance of chaos seems to include elements of intermittency.

in phase space (setting all system properties), the following phase-space trajectories diverge exponentially from each other [165, 166].

This is expressed by the spectrum of Lyapunov-exponents, which are a measure of the temporal growth of a given volume in the phase space of the considered system [178]. A system has as many Lyapunov-exponents λ_i as dimensions in phase space, each of which describing the evo-

lution of the corresponding dimension in phase space. The gyrotron being a system with an infinite number of degrees of freedom, there exists also an infinite number of Lyapunov-exponents [160].

For a given phase space dimension, the Lyapunov-exponent gives the average rate at which two points, that initially start infinitesimally close to each other, diverge (exponentially) in time.

The mathematical definition can be expressed as [178]:

$$\lambda_i = \lim_{t \rightarrow \infty} \frac{1}{t} \log \frac{l_i(t)}{r(t=0)}, \quad (5.1)$$

from an exponential divergence $l_i(t) = r(t=0)e^{\lambda_i t}$, where $r(t=0)$ represents an initial reference volume and $l_i(t)$ is the length of the i^{th} dimension in phase space of this volume element at time t .

If the system is of purely oscillatory nature (not necessarily sinusoidal oscillation), the Lyapunov-exponents equal zero $\lambda_i = 0$, and they are negative, $\lambda_i < 0$ for a dissipative system, where trajectories converge to a single point in phase space.

The system exhibits chaos already, if there is one positive Lyapunov-exponent. Because, by convention, Lyapunov-exponents are ordered by their magnitude as $\lambda_1 > \lambda_2 > \lambda_3 > \dots$, this is equivalent to the condition $\lambda_1 > 0$. This means that the largest Lyapunov-exponent determines, whether the system is chaotic or not: λ_1 measures, how quickly linear distances in phase space grow, meaning that the average distance of two initially neighboring points evolves as $l(t) = \epsilon e^{\lambda_1 t}$, with an initially infinitesimally close distance, ϵ .

If there is more than one positive Lyapunov-exponent, the state of the system is called hyperchaos. It was found with self-consistent simulations [168], however based on the separation of time-scale between particles and field (Eq. (3.10)), that both weak chaos (only $\lambda_1 > 0$) and hyperchaos can be present in a gyrotron.

The largest Lyapunov-exponent λ_1 , which determines the dominant chaotic timescale, was calculated for the experimentally observed chaotic regime in the DNP-gyrotron. Much of this study has been described in [179, 104].

The method that was used to obtain the Lyapunov-exponent was described by Rosenstein et al. [180]. In this method a time trace of N_{sample} points is analyzed, as it will be illustrated in Fig. 5.25 on a chaotic power-evolution acquired with the fast Schottky-diode. Within this time trace, two neighboring points in phase space are represented by two time intervals with very similar signal evolution from different places in the time trace. This can be seen in Fig. 5.25, where the signal inside the shaded areas is close to identical.

These similar signal sections are represented by an m -tuple of points $X_{j=1,\dots,m}$ and $\hat{X}_{j=1,\dots,m}$, shown in the figure by the three connected blue points ($m = 3$). One can see, that the difference $d(0)$ between the two 3-tuples is very small, so that these two trajectories can be considered as nearest neighbors. Now, the m -tuples \mathbf{X} and $\hat{\mathbf{X}}$ are in parallel advanced in time, calculating the temporal evolution of the difference between the two vectors

$$d(t) = \|\mathbf{X}(t) - \hat{\mathbf{X}}(t)\|. \quad (5.2)$$

Initially, this difference is expected to grow exponentially and the exponent of this growth gives

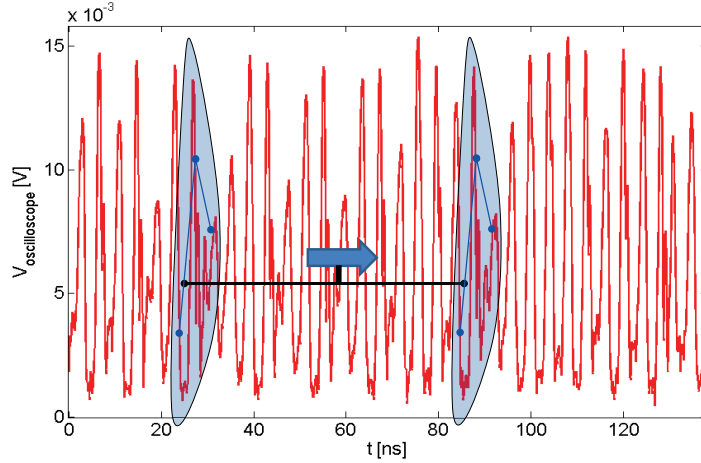


Figure 5.25: Illustration of method for calculation of largest Lyapunov-exponent: Two similar signal trajectories (encircled regions) are represented by $m = 3$ points $X_{j=1,2,3}$ and $\hat{X}_{j=1,2,3}$ separated by a properly chosen delay $(t(X_2) - t(X_1))$, corresponding to J points in the time-trace. Then these 3-tuples are advanced in time and the temporal growth of the initially small distance between X and \hat{X} is used to obtain the Lyapunov-exponent.

the largest Lyapunov-exponent:

$$d(t) = d(0)e^{\lambda_1 t}$$

$$\Rightarrow \lambda_1 = \frac{d}{dt} \left(\ln \frac{d(t)}{d(0)} \right). \quad (5.3a)$$

Thus, the Lyapunov exponent is obtained as the linear slope of the logarithm of the difference between the initially similar vectors.

In this method, several parameters have to be chosen carefully in order to obtain a valid result for the Lyapunov-exponent, such as the delay (J points in time-trace in interval $t(X_j) - t(X_{j-1})$) between two neighboring points in the m -tuple. With a delay that is too small, two neighboring points in the tuple will always have similar values, while with a too large delay the m -tuple is not representative for the signal section (see Fig. 5.25: with a larger delay, the 3-tuple could not represent the similar signal section in the shaded area). Here, a robust criterion was used, defining the optimum delay with the help of the autocorrelation function as described in [181, 182].

Additionally, m has to be chosen, the number of elements in the m -tuple ($m = 3$ in Fig. 5.25). Here, a larger number of points is preferable, since longer signal sections give a better representation of the position of the system in phase space.

Thus, a random segment of signal section is chosen, represented by an m -tuple of points each separated by the delay J . Matching to this m -tuple, a similar section is found (finding the second, matching 3-tuple in Fig. 5.25) by the 'closest neighbor' criterion, namely by finding within all other possible m -tuples (separated from the reference tuple by a minimum distance) the one

with the minimum difference:

$$d(0) = \min_{\text{all } \hat{\mathbf{X}}_s} \|\mathbf{X} - \hat{\mathbf{X}}\|, \quad (5.4)$$

This procedure is executed for many reference trajectories, resulting in many pairs of closest neighbors. The Lyapunov-exponent is then obtained from the average temporal evolution of the difference of all these pairs of m -tuples.

This procedure is shown in Fig. 5.26, where the logarithm of the average difference between

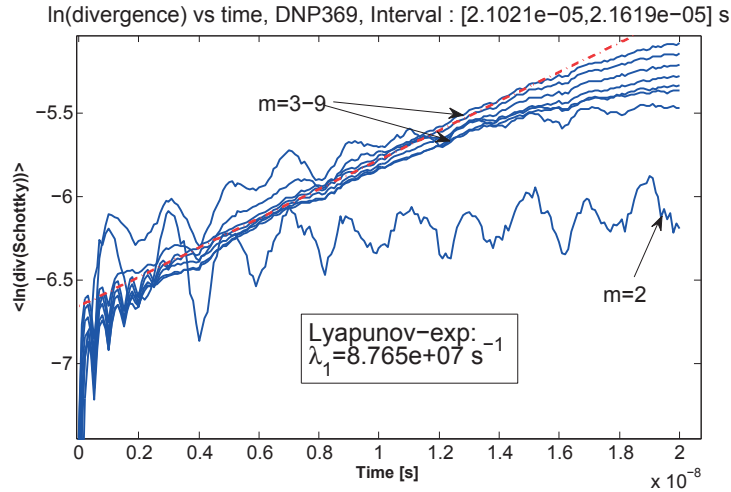


Figure 5.26: Average value of logarithmic divergence between two initially similar signal trajectories over time. The analyzed signal was acquired with the fast Schottky-diode. For finding similar signal trajectories, the number of points to represent this signal section was varied in the range $m = 2 - 9$. With more points, the divergence shows a behavior that is more clearly exponential. The slope of the fit to the traces with higher m gives the Lyapunov-exponent $\lambda_1 = 8.765 \cdot 10^7 \frac{1}{s}$.

two similar trajectories (m -tuples) is displayed for different m 's. It can be seen, that for the analyzed power evolution at least $m = 4$ is necessary to properly represent the temporal evolution, resulting in a linear behavior of the logarithm and a reliable Lyapunov-exponent. The result of this analysis, obtained as the slope of the fit (red), is $\lambda_1 = 8.765 \cdot 10^7 \frac{1}{s}$. Thus, the time-scale, over which similar signal trajectories diverge, is slightly larger than the timescale of the fluctuation induced by the sidebands ($\sim 250 \text{ MHz} = 25 \cdot 10^7 \frac{1}{s}$). An important outcome of this analysis is however, that the behavior of the system in this case is indeed chaotic, since at least the largest Lyapunov-exponent is positive.

This analysis was applied to several cases of chaotic oscillation, both from experimental data (from fast Schottky-diode) and from TWANG-PIC-simulation. Within the analyzed cases, the observed timescales were as follows:

$$\text{experiment: } \tau_{\text{chaos}} = \frac{1}{\lambda_1} \approx 7.7 - 56 \text{ ns} \quad (5.5a)$$

$$\text{simulation: } \tau_{\text{chaos}} = \frac{1}{\lambda_1} \approx 9 - 70 \text{ ns.} \quad (5.5b)$$

Thus, a good agreement between experiment and simulation is observed, with a slightly shorter chaotic timescale from experimental time-traces than from measurements. To our knowledge, this is the first quantitative experiment-theory comparison for the chaotic behavior in gyrotrons. Although the spectrum of Lyapunov-exponents was analysed in the study by Blokhina et al. [183, 168, 184, 160], the highest Lyapunov-exponent could not be retrieved from these studies in physical quantities, for comparison with the results shown here.

5.7 Analysis of the sideband-regime

The categorization, shown in section 5.2, showed that the most common type of non-stationary oscillation is that of frequency-equidistant sidebands, which results in a fast power modulation, having (mostly) a single periodicity. In this section, this category will be analyzed in more detail. In the previous sections it was mentioned, that the sidebands appear to be equidistant in the spectra, whereas section 5.5 also showed that the sideband spectrum can vary in time due to an anode-voltage fluctuation. With the help of the fluctuation, the equidistance of the sidebands can be further verified, as it will be shown in the following.

The spectrogram in Fig. 5.27 shows the time-varying spectrum on an operating point, where the sideband frequencies vary strongly in time due to the V_a -fluctuation, resulting in the same periodicity as this fluctuation. Here one observes, that the frequency variation is symmetric with respect to the dominant frequency (highest peak amplitude at $f_{\max} = 260.791$ GHz), with a higher sideband amplitude towards the lower frequencies. The frequency oscillation becomes the larger the further the sideband is away from the dominant peak, because the sidebands remain frequency-equidistant with a varying frequency-separation.

To illustrate this, the frequency separation between the sidebands has been measured in the spectrogram by a peak detection method for two points of time and included into the figure at the corresponding times in-between the corresponding sidebands. This quantitatively demonstrates the continuous frequency-equidistance of the sidebands for the case of temporally varying sideband-frequencies, within the frequency-resolution (1 MHz) of the spectrogram. The strict equidistance in frequency leads to the question, whether the sideband modes are phase-locked, which will be investigated later on.

As mentioned earlier, if the RF-frequencies are shown in a spectrum that covers a time longer than the V_a -fluctuation period, the fluctuating frequencies in Fig. 5.27 are observed as sideband peaks that are broadened in frequency. This is illustrated in the spectrum in Fig. 5.28 showing the same oscillation as the spectrogram, measured with the spectrum analyzer (acquisition time $\gtrsim 30$ ms, see section 2.5). Such spectra have been classed into the category of 'broad sidebands' in the categorization of Fig. 5.2, so that this category shows the region, where sideband frequencies are more prone to the pitch-angle fluctuation. If most of the peaks overlap in the spectrum, as they do for the lower frequency end in Fig. 5.28, the broadband spectrum leads to the somewhat unprecise categorization into the chaotic type.

The oscillation of the sideband frequencies can be very large. An extreme case of such a sideband fluctuation is shown in the spectrogram of Fig. 5.29, where the sideband separation varies in the range $\Delta f_{\text{SB}} \approx 25 - 135$ MHz.

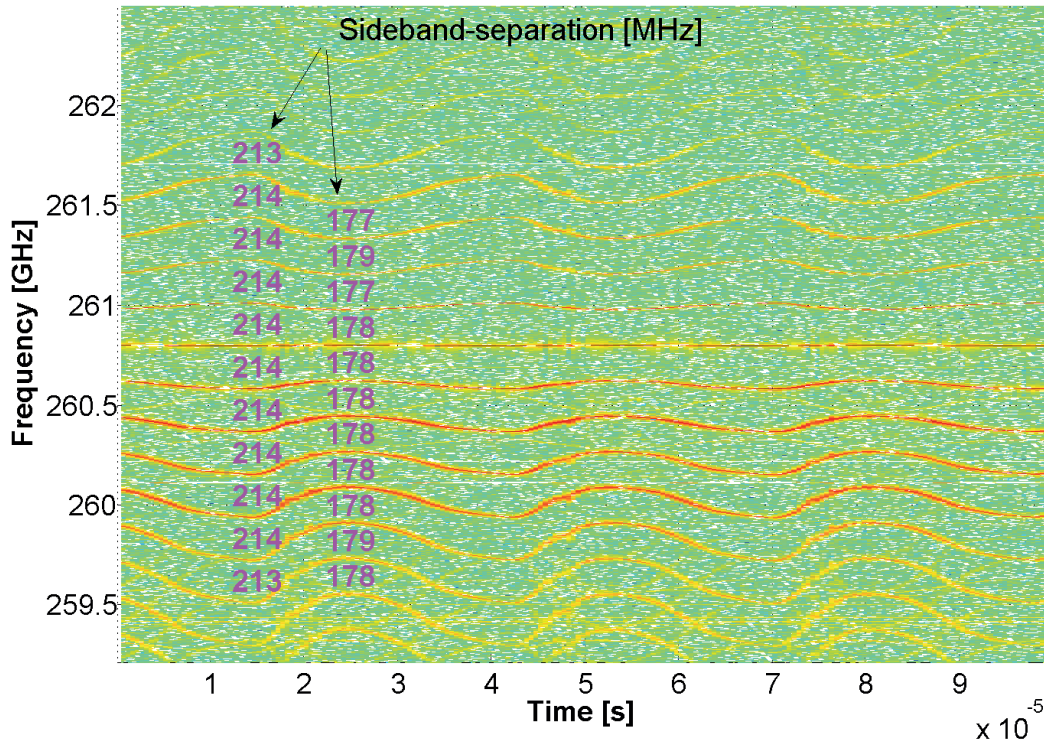


Figure 5.27: Demonstration of sideband-equidistance: Spectrogram showing temporal fluctuation of rf-frequencies (due to V_a -fluctuation) on an operating point, where the sideband frequencies vary strongly. For highlighting the equidistance at each point of time, the frequency separation between neighbouring sidebands has been added as numbers (unit [MHz]) for the times $t_1 = 1.41 \cdot 10^{-5}$ and $t_2 = 2.40 \cdot 10^{-5}$ s. The equidistance is confirmed within the spectrogram resolution of 1 MHz.

5.7.1 Nanosecond power pulses in non-stationary oscillation

Within the sideband-regime, the temporal evolution of the power and the relative height of the sidebands strongly depends on the operating point. For certain operating points, a nanosecond-pulsed regime is observed, which is characterized by a deep power-modulation and by the appearance of several dominant sidebands of comparable amplitude in the spectrum. This kind of oscillation was analyzed in [103] with an explanation of the phenomenon through a so-called Self-consistent Q-Switch (SQS) mechanism, that will be elaborated in the following.

The spectrogram of a typical operating point for this regime ($B_0 = 9.59$ T, $I_b = 75$ mA, $V_a = 8.8$ kV $\rightarrow \alpha \approx 2.2$) is shown in Fig. 5.30. The oscillation was analyzed in more detail for two points in time, namely for $t_1 = 58 \mu\text{s}$ and $t_2 = 65 \mu\text{s}$, indicated in the spectrogram by the blue and black line respectively. The details of the oscillation at these moments are shown in Fig. 5.31, showing the time-trace of the instantaneous power from the fast Schottky-diode, together with the simultaneously acquired IF-signal (on oscilloscope) from the heterodyne system in the top half and

5.7. ANALYSIS OF THE SIDEBAND-REGIME

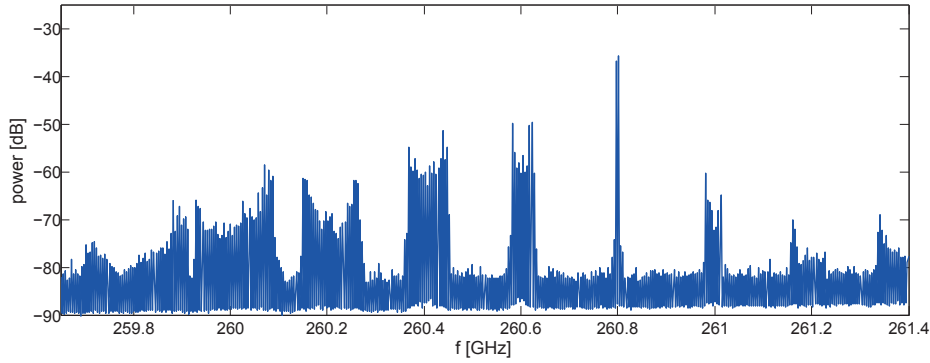


Figure 5.28: Broadened sidebands: RF-spectrum from spectrum analyzer, corresponding a measurement of the temporally varying spectrum shown in Fig. 5.27 over a longer acquisition time.

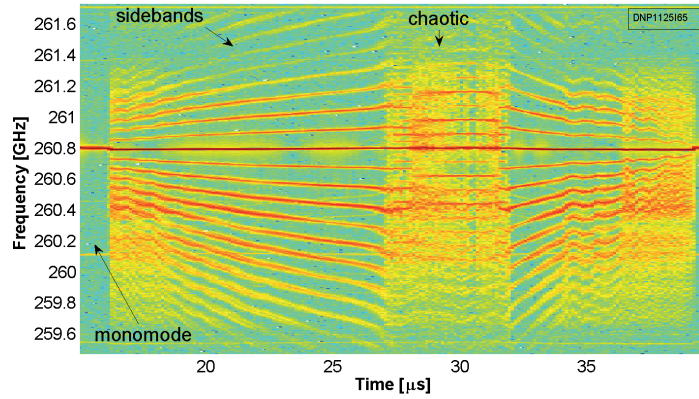


Figure 5.29: Spectrogram with very strong variation of sideband-frequency.

the spectrum for a small time-window around t_1 and t_2 in the bottom half.

The instantaneous power is strongly pulsed, with a Full Width Half Maximum (FWHM) of ~ 1.2 ns and a repetition period of 4.2 ns, corresponding to the inverse of the frequency distance between the sidebands. The average power on this point is $\langle P_{\text{RF}} \rangle = 1.2$ W and from the modulation depth of 90% and the duty cycle it can be inferred that the peak power is approximately 5 W.

Such nanosecond-pulses of the power with a large modulation depth are observed on different other operating points distributed over the non-stationary region. A second example ($B_0 = 9.575$ T, $I_b = 100$ mA, $V_a = 8.8$ kV) is shown in Fig. 5.32, showing again the spectrogram and the instantaneous power together with the IF-signal, at the time that is indicated in the spectrogram. Here, the nanosecond-pulses show to be even narrower and more pronounced than on the operating point shown above.

For interpreting the measurements, the same operating point as in Fig. 5.30-5.31 has also been analyzed in TWANG-PIC simulations. These simulation results are presented in Fig. 5.33, show-

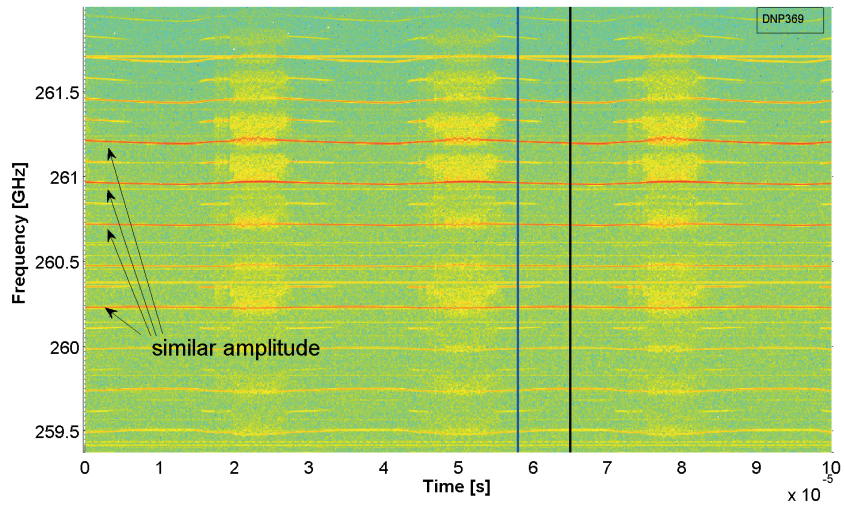


Figure 5.30: Spectrogram for nanosecond-pulsed regime. Indicating times, at which time-traces and spectras are taken for the following figures ($t_1=58\mu\text{s}$ in blue and $t_2=65\mu\text{s}$ in black)

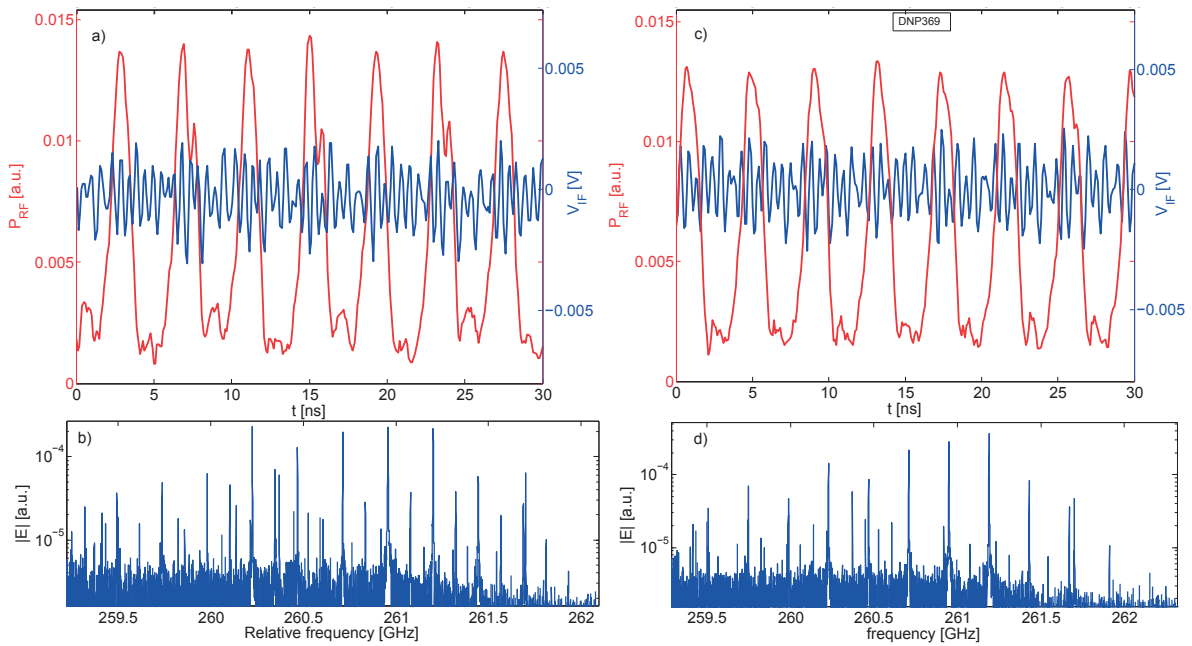


Figure 5.31: Nanosecond-pulses: Details of oscillation corresponding to $t_1=58\mu\text{s}$ (a) and b)) and $t_2=65\mu\text{s}$ (c) and d)) in the spectrogram shown in Fig. 5.30. a)/c) Instantaneous RF-power, experimentally measured with fast Schottky-diode and compared to IF-signal from heterodyne system on fast oscilloscope. b)/d) Spectrum from FFT in a time-window around the same time as the time-trace in a)/c)

5.7. ANALYSIS OF THE SIDEBAND-REGIME

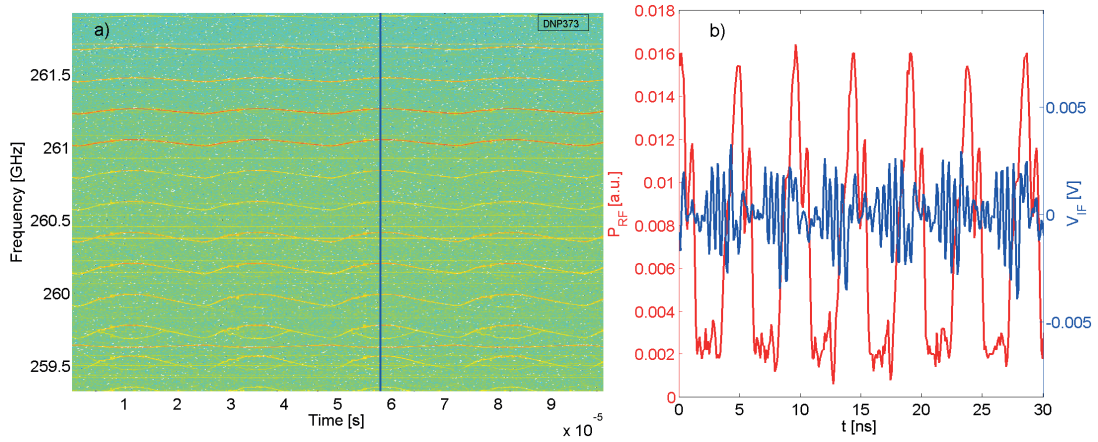


Figure 5.32: Nanosecond-pulses: a) Spectrogram for typical point where nanosecond-pulsed power was observed ($B_0 = 9.575$ T, $I_b = 100$ mA, $V_a = 8.8$ kV, $V_c = 15.5$ kV) and b) Signal from fast Schottky-diode (negative) and heterodyne-system (plus offset) at the time $t_1 = 58 \mu\text{s}$ marked by the blue line in the spectrogram. There is a time-delay between the two time-traces, caused by different signal path lengths.

ing the integrated field energy W_{RF} , the electron efficiency η_{el} , the output power P_{RF} and the loaded diffractive quality factor Q_{diff} (all calculated as in section 3.4.3).

The temporal behavior of the RF-power is very similar to the one observed in experiment. Although the power-level is not comparable to experiment, the power from simulations reproduces nanosecond-pulses with very deep modulation, with a FWHM of ~ 0.6 ns and a repetition period of ~ 4.6 ns. The fact, that subsequent pulses have a slightly different shape indicates, that the oscillation is on the verge of the chaotic regime, just as in experiment (see spectrogram Fig. 5.30).

A characteristic phenomenon of the nanosecond-pulses in simulations is, that the electron efficiency is negative for periods of time during the oscillation, corresponding to re-absorption of energy by the beam from the field.

It is also observed, that the diffractive quality factor varies self-consistently over *three* orders of magnitude, with a close correlation to the creation of the nanosecond-pulses, since the temporarily lowered quality factor allows the sudden release of the wave energy in a pulse of RF-output. This did lead to the terminology of Self-Consistent Q-Switch (SQS) regime as an explanation of the pulsed regime [103].

These results show, that nanosecond-pulses of RF-power with a large modulation depth can be created by equidistant sidebands of similar amplitude. According to a theoretical work by McCurdy [185], nanosecond-pulses can be created in a gyrotron by modes that are equidistant in frequency, if they are locked in phase. In [185] the sideband modes corresponded to the cold-cavity axial modes, which satisfy an equidistance in frequency-separation by a specific cavity design. In [185] it is then proposed to phase-lock these eigenmodes by modulating the beam current with a modulation frequency equal to the intermediate frequency between the modes. Performing this in a real experiment is however by far not evident, since the electron beam should

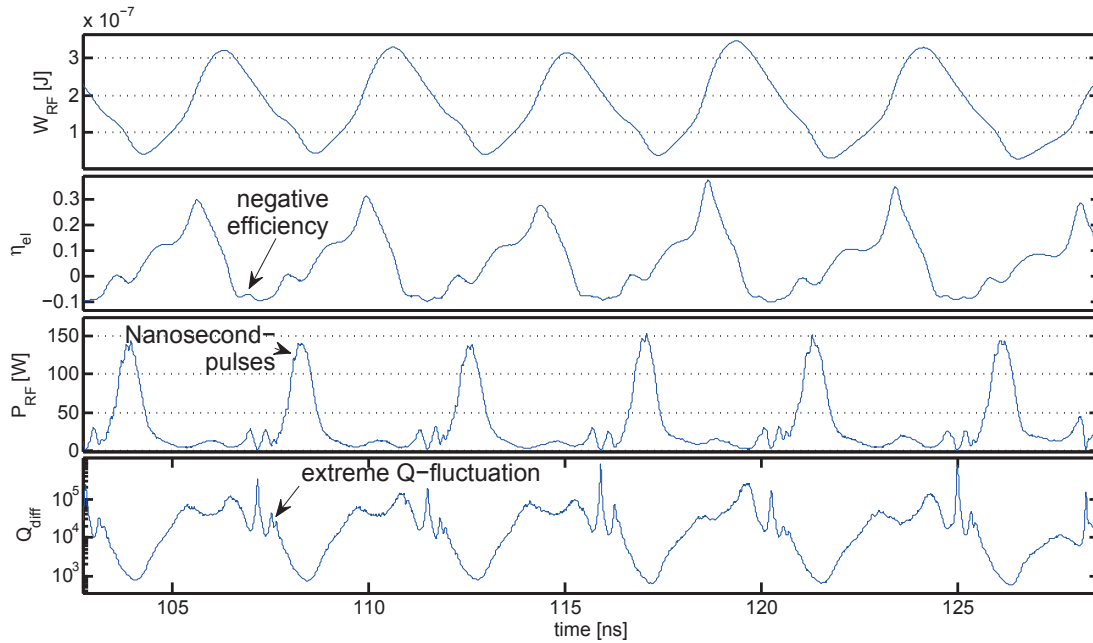


Figure 5.33: Nanosecond-pulses in TWANG-PIC simulation: Results for operating point corresponding to experimentally measured nanosecond-pulses in Fig. 5.31 ($B_0 = 9.60\text{ T}$ / $I_b = 70\text{ mA}$ / $\alpha = 2.208$). a) Temporal variation of RF-energy stored in field inside cavity b) electron interaction efficiency c) radiated RF-power at end of interaction region d) diffractive quality-factor, calculated from field profile.

be modulated at 250 MHz.

A very similar approach was studied by Denisov et al. [186] on a slow-wave BWO between two mirrors. Therein the axial modes are locked by Q-switching via a modulation of the reflection of a mirror with a modulation frequency corresponding to the frequency-separation of the axial modes. In [186] it is explained, that the artificial modulation can lock the axial modes in order to achieve a superposition of the modes to super-radiant pulses, where the peak power of the pulse can exceed the power of the operating electron beam. Such super-radiant pulses can also be created in a gyrotron with very fast start-up [187].

In the following it will be tested, whether a correspondence can be made between such theoretical ideas and the here-described self-consistently created pulses. Therefore, firstly, it is investigated whether the sideband modes that are observed in the DNP-gyrotron are phase-locked. Secondly, in section 5.7.4, it is analyzed, whether also in the DNP-gyrotron the equidistant sideband modes can be identified as axial modes, even if their cold-cavity frequencies are not frequency-equidistant.

5.7.2 Analysis of phase relation between sidebands

The phase-relation between the spectral components of two different sidebands has been determined using a numerical homodyne receiver.

In the analysis, it was assumed that the signal of the two relevant frequencies within the experimental IF-signal from the heterodyne system can be written as:

$$S(t) = A_1 \cos(\omega_1 t + \varphi_1(t)) + A_2 \cos(\omega_2 t + \varphi_2(t)), \quad (5.6)$$

where the subscripts '1' and '2' refer to two chosen sidebands and where the phases φ_1 and φ_2 of the two components are assumed to vary slowly with respect to ω_1 and ω_2 .

The squared signal can be written as:

$$S^2(t) = A_1^2 \cos^2(\omega_1 t + \varphi_1) + 2A_1 A_2 \cos(\omega_1 t + \varphi_1) \cos(\omega_2 t + \varphi_2) + A_2^2 \cos^2(\omega_2 t + \varphi_2) \quad (5.7a)$$

$$= \frac{A_1^2}{2} (1 + \cos(2\omega_1 t + 2\varphi_1)) + \frac{A_2^2}{2} (1 + \cos(2\omega_2 t + 2\varphi_2)) \quad (5.7b)$$

$$+ A_1 A_2 [\cos((\omega_1 + \omega_2)t + \varphi_1 + \varphi_2) + \cos((\omega_1 - \omega_2)t + \varphi_1 - \varphi_2)], \quad (5.7c)$$

Here, one is interested in the phase difference $\varphi_1(t) - \varphi_2(t)$ between the two modes, which appears in the term that oscillates with the frequency $\omega_1 - \omega_2$. This phase difference can be extracted by multiplying $S^2(t)$ by a numerical test signal of the form

$$x(t) = B \cos((\omega_1 - \omega_2)t). \quad (5.8)$$

One then obtains the new signal:

$$S_1(t) = S^2(t) \cdot x(t) \quad (5.9a)$$

$$= \frac{A_1^2 B}{2} [\cos((\omega_1 - \omega_2)t) + \cos(2\omega_1 t + 2\varphi_1) \cos((\omega_1 - \omega_2)t)] \quad (5.9b)$$

$$+ \frac{A_2^2 B}{2} [\cos((\omega_1 - \omega_2)t) + \cos(2\omega_2 t + 2\varphi_2) \cos((\omega_1 - \omega_2)t)] \quad (5.9c)$$

$$+ A_1 A_2 B [\cos((\omega_1 + \omega_2)t + \varphi_1 + \varphi_2) \cos((\omega_1 - \omega_2)t) + \cos((\omega_1 - \omega_2)t + \varphi_1 - \varphi_2) \cos((\omega_1 - \omega_2)t)] \quad (5.9d)$$

$$= \frac{A_1^2 B}{4} [2\cos((\omega_1 - \omega_2)t) + \cos((3\omega_1 - \omega_2)t + 2\varphi_1) + \cos((\omega_1 + \omega_2)t + 2\varphi_1)] \quad (5.9e)$$

$$+ \frac{A_2^2 B}{4} [2\cos((\omega_1 - \omega_2)t) + \cos((\omega_1 + \omega_2)t + 2\varphi_1) + \cos((3\omega_2 - \omega_1)t + 2\varphi_1)] \quad (5.9f)$$

$$+ \frac{A_1 A_2 B}{2} [\cos(2\omega_1 t + \varphi_1 + \varphi_2) + \cos(2\omega_2 t + \varphi_1 + \varphi_2) + \cos(2(\omega_1 - \omega_2)t + \varphi_1 - \varphi_2) + \cos(\varphi_1 - \varphi_2)] \quad (5.9g)$$

This shows, that the only term without an explicit time-dependence is the last term $\frac{A_1 A_2 B}{2} \cos(\varphi_1 - \varphi_2)$ and that the slowest-oscillating terms with an explicit time-dependence, $\frac{A_i^2 B}{2} \cos((\omega_1 - \omega_2)t)$ (with $i = 1, 2$), have the time-dependence of the reference signal and do not

include any phase-dependence. Thus, one can obtain the phase relation between the two sidebands by low-pass filtering this signal, with a cut-off frequency below the sideband separation frequency. Thus, a filtering-frequency of 150MHz was used. This allows detecting variations of the phase difference slower than this frequency, which is sufficient to analyze, if the phase difference is constant or not.

The phase difference is then obtained by calculating

$$\varphi_1(t) - \varphi_2(t) = \arccos\left(\frac{2 \cdot \tilde{S}_1(t)}{A_1 A_2}\right), \quad (5.10)$$

using a reference signal with an amplitude $B = 1$ and where $\tilde{S}_1(t)$ is the low-pass filtered signal $S_1(t)$. For this analysis, the amplitude of the two modes as well as the frequency difference are retrieved from the spectrum. Due to the anode-voltage fluctuation, the distance between the sidebands is never exactly constant in experiment. This causes the obtained phase difference to be constant only over a certain period of time, because the frequency difference that is used in the reference signal only fits for a certain time-window. Thus, the phase difference was calculated with this algorithm for several frequency differences in the reference signal.

An example of this analysis is shown in Fig. 5.34, showing a spectrogram of the signal with

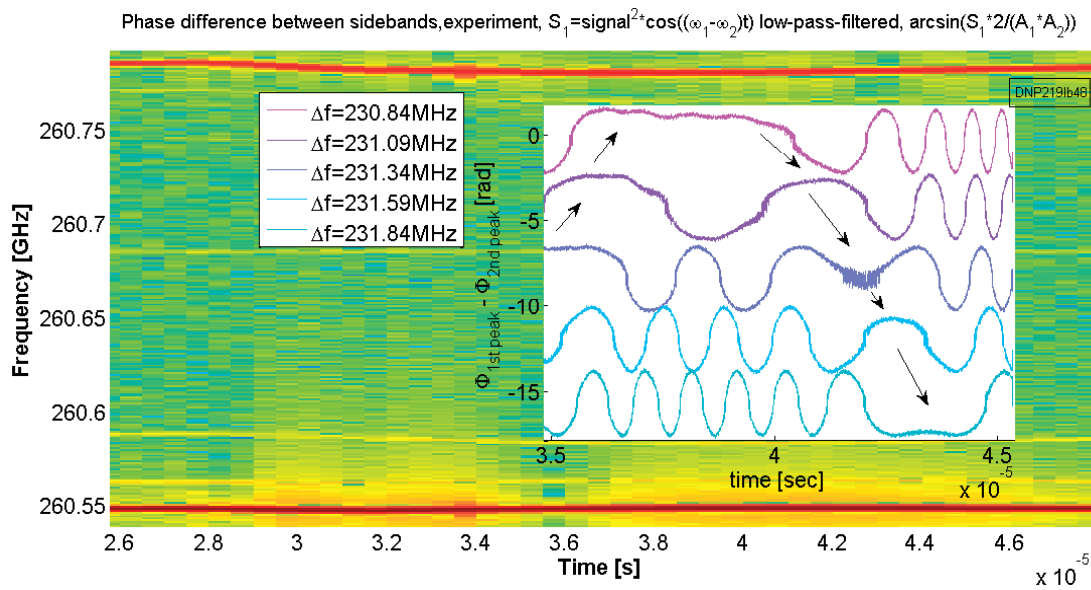


Figure 5.34: Result of analysis of phase difference between sidebands. As it can be seen from the spectrogram, the distance between the two analysed sidebands is slowly varying, so that the phase difference is constant only for a certain period for each frequency difference in the reference. The result of the phase difference is shown with different offsets for different frequency differences and is placed within the analysed time section of the spectrogram.

the two analysed sidebands and in an inset the obtained phase difference, placed in the analysed time section. For the analysis, a time window with relatively little variation of the sideband frequency separation was chosen. It is observed that at each instant, the phase difference of a

certain reference frequency is practically constant, typically varying over less than $\sim 0.3 \text{ rad} \approx 17$ degrees over the time-scale of one or several microseconds. At each instant, this trace with a nearly constant phase corresponds to the reference signal with the currently correct frequency difference, while the sideband separation is varying from $\Delta f = 231.35 \text{ MHz}$ to 230.84 MHz and back to 231.84 MHz . Thus, the entire variation of the phase difference between two sidebands can be completely attributed to the variation of the frequency separation between the sidebands. Therefore, this analysis confirms, that the sidebands are indeed locked in phase. Applying this analysis to sidebands in simulations, where the frequency-separation does not vary, showed a completely constant phase difference.

5.7.3 Dependence of sideband frequency separation on operating parameters

The frequency-distance between equidistant sidebands, Δf_{SB} , represents an important parameter for describing the non-stationary regime. It represents the (inverse of the) period of power oscillation in the sideband-regime and is therefore of practical importance for any potential application of non-stationary oscillations.

It can also be used to gain understanding of the mechanisms and origins of the non-stationary regime, and its scaling allows obtaining and testing theories on the basic principles of non-stationary oscillations. For this reason, it has received considerable attention in previous publications on non-stationary oscillation. In this section, we will analyze the dependency of Δf_{SB} on parameters and compare the results with some of the scaling laws from literature.

Chang et al. [52] presented a dependence of Δf_{SB} on the wave group velocity as $\Delta f_{\text{SB}} = \frac{1}{2\tau_w} = \frac{v_{\text{gr}}}{2L}$, where τ_w represents the wave transit time, v_{gr} the wave group velocity and L the interaction length. The origin of this scaling is an explanation of the sidebands as being caused by a wave energy packet bouncing back and forth in the cavity over a length L . This expression was adopted by Chu et al. [20] for the forward-interaction region (positive detuning), but extended by the expression $\Delta f_{\text{SB}} = \frac{1}{\tau_w + \tau_{\text{el}}}$ for the backward region (τ_{el} electron transit time), because there the feedback loop of the energy bouncing is composed of a traveling wave packet in backward-direction combined with the electron transit in forward-direction. Remarkably, in [188] a sideband separation is mentioned that equals two third of this value for a slow-wave BWO.

The more recent publication on the gyro-BWO interaction by Chen et al. [189] proposes a scaling with the maximum amplitude of the field profile as $\Delta f_{\text{SB}} \sim \sqrt{|\hat{F}|_{\text{max}}}$ ($|\hat{F}|_{\text{max}}$ obtained from simulations). The explanation in [189] is that a secondary electron bunch forms at the end of the cavity, with a relativistic factor that, with respect to its initial value γ_0 , is increased by the difference $\Delta\gamma$, proportional to $\sqrt{|\hat{F}|_{\text{max}}}$. This secondary bunching is claimed to be responsible for the creation of the sidebands and their frequency separation would be proportional to $\Delta\gamma$ and thus to $\sqrt{|\hat{F}|_{\text{max}}}$.

Here it has to be stressed, that the interaction in a gyrotron is not the same as that in a gyro-BWO (as in [189]) or in a slow-wave BWO (as [188]), but because there are many similarities, these scaling laws could nevertheless be valid for gyrotrons.

The scaling on the field amplitude can be compared to the dependency of the sideband frequency-separation on the beam current, which controls the interaction strength and thus has an impact on the field amplitude. The I_b -dependency is summarized in Fig. 5.35, showing Δf_{SB} from both

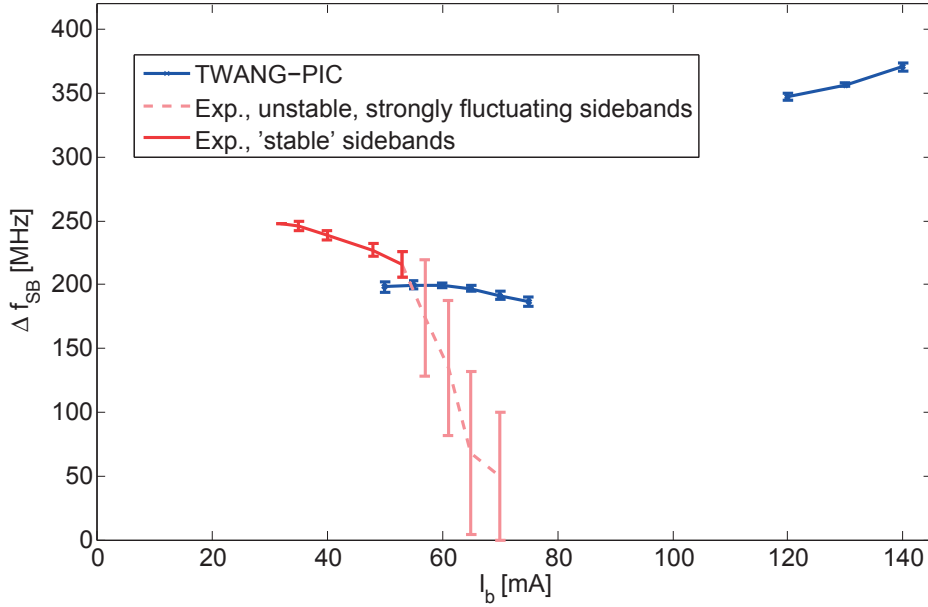


Figure 5.35: Distance between equidistant sidebands in RF-spectrum for I_b -scan at $B_0 = 9.54$ T (simulation: $\alpha = 2.3$). In experiment (red/light red), the sidebands become very strongly fluctuating and the radiation nearly chaotic for $I_b > 57$ mA, indicated by a dashed/light red line. The experimental error bars show the range of fluctuation of sideband frequencies due to the V_a -fluctuation, those for simulation are due to an uncertainty in peak detection.

experiment and simulation, for the I_b -scan that has been analyzed in section 5.4. In the range of $I_b = 57 - 70$ mA, the sidebands in experiment were strongly fluctuating and unstable due to the V_a -fluctuation, which is shown as a light red/dashed line. This sideband-fluctuation is illustrated in Fig. 5.36, which shows the spectrogram for one of the involved operating points at $I_b = 61$ mA. The simulation results show two non-stationary regimes around $50 - 75$ mA and at $120 - 140$ mA, while the measurements can only show the lower of the two non-stationary regimes, because the experimental current was limited to $I_b < 115$ mA.

In the region of stable sidebands, the experimental result of the frequency separation shows only a slight dependence on the current, but decreases monotonically. The results from TWANG-PIC also show only a slight variation with current within the lower non-stationary region ($I_b = 57 - 70$ mA), first slightly increasing then decreasing. The upper non-stationary regime ($120 - 140$ mA) however shows a much higher sideband separation.

The scaling law $\Delta f_{SB} \sim \sqrt{|\hat{F}|_{\max}}$ will be compared to these simulation results, for which the field profile is known. In [189], a field profile from stationary simulation on a non-stationary operating point was used for obtaining $|\hat{F}|_{\max}$. Instead of this, here for each I_b -value the temporally varying field profile (for non-stationary) was time-averaged to the profile $\langle |\hat{F}| \rangle_t(z) = \langle |\hat{F}(z, t)| \rangle_t$ (time-averaging the amplitude on each point in z , over entire simulation time excluding transient; examples in Fig. 5.38), which is used for obtaining the maximum field amplitude. With the maximum amplitude of each of these profiles, the scaling law can be tested against the results of

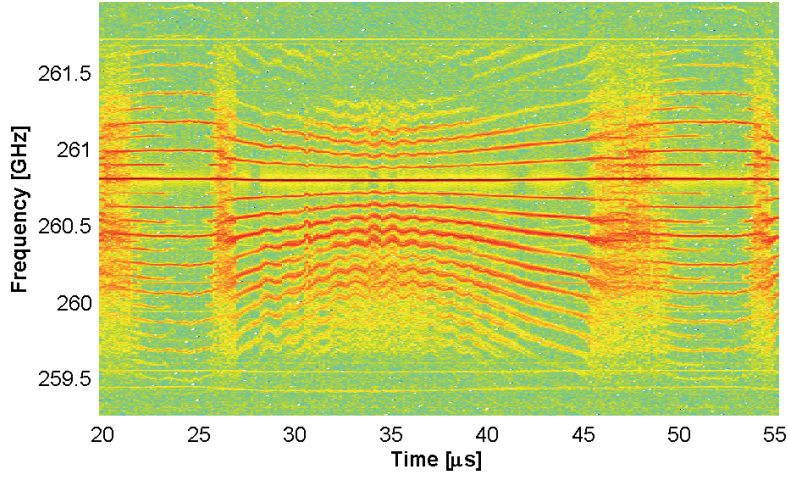


Figure 5.36: Spectrogram to illustrate the strongly fluctuating sidebands that are shown in Fig. 5.35 in light red/dashed on the example of $I_b = 61$ mA.

Δf_{SB} .

Fig. 5.37 displays the scaling, that would be expected from $\Delta f_{\text{SB}} \sim \sqrt{|\hat{F}|_{\text{max}}}$ with the maximum

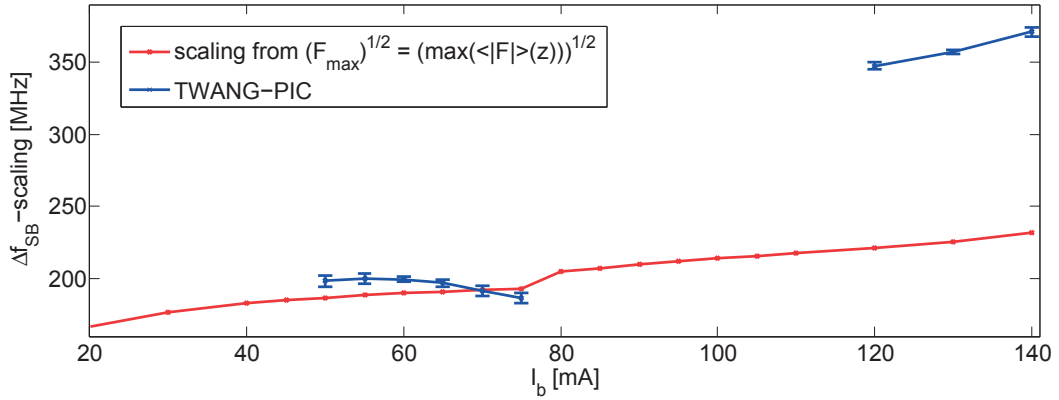


Figure 5.37: Sideband frequency-separation (TWANG-PIC): Scaling from maximum field amplitude of time-averaged field profiles $\sqrt{|\hat{F}|_{\text{max}}} = \sqrt{\max(\langle |\hat{F}|(z, t) \rangle_t)}$ (with factor 1/9), compared to Δf_{SB} from RF-spectra. On operating points with $B_0 = 9.54$ T / $\alpha = 2.3$ and varying beam current. This shows that the scaling law in [189] is not consistent with our simulation-results.

field amplitudes from TWANG-PIC ($\sqrt{|\hat{F}|_{\text{max}}}$ rescaled with constant factor for a better comparison), compared to Δf_{SB} from the RF-spectra of the same simulations, as a function of the beam-current. This shows that the scaling law from [189] can neither reproduce the behavior inside the lower non-stationary region ($I_b = 50 - 75$ mA) nor the jump in Δf_{SB} between the lower ($I_b = 50 - 75$ mA) and upper non-stationary regime (120 – 140 mA).

Regarding a comparison of the scaling law with the experimental sideband separation, only a rough estimation is possible. In Fig. 5.12 it was shown, that the experimental power increases in the region $I_b = 32 - 48$ mA with current inside the non-stationary region. The maximum field amplitude is related to the RF-power and should thus increase with the beam current, too. Since the experimental frequency-separation decreases with I_b , it does thus probably not scale as $\Delta f_{\text{SB}} \sim \sqrt{|\hat{F}|_{\text{max}}}$ in experiment either. This suggests, that the scaling law of the sideband frequency separation proposed by Chen for a gyro-BWO, does not apply to the case of the DNP-gyrotron, which is possibly because of the difference in interaction between a gyro-BWO and a gyrotron.

Moreover, the sideband separation from TWANG-PIC in Fig. 5.35 shows a very different sideband separation between the two regions of non-stationary oscillation. This difference in sideband separation can be tentatively explained with an analysis of the field profiles in the described I_b -scan.

Fig. 5.38 displays time-averaged profiles for four different beam currents located in each of

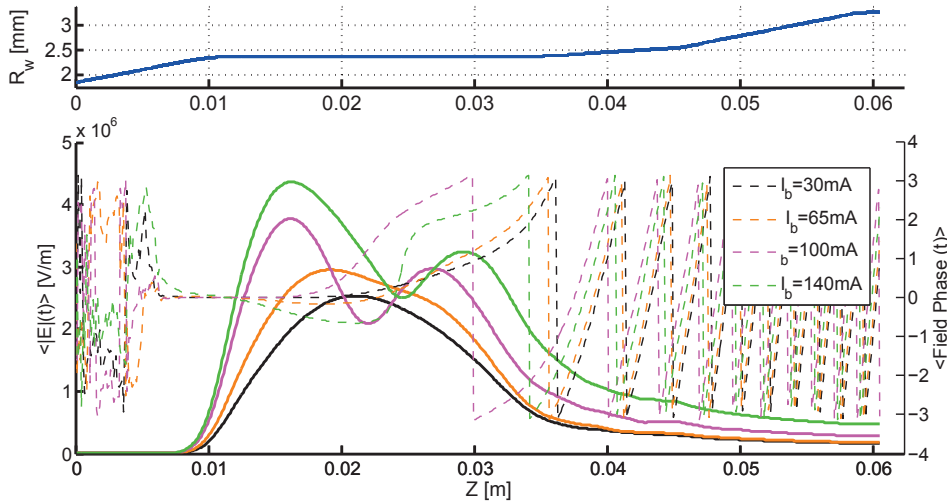


Figure 5.38: Time-averaged field profiles from simulations for different beam currents from each of the regions of stationary and non-stationary oscillation that were shown in the I_b -scan of Fig. 5.12 ($B_0 = 9.54$ T / $\alpha = 2.3$ / I_b see legend). Amplitudes (left y-axis) are shown as solid lines, phases (right y-axis) as dashed lines. The top part shows the cavity wall profile for a better coordination.

the regions of stationary and non-stationary oscillation that were shown in Fig. 5.12. As described earlier, the field profile changes from one maximum ($q=1$ -like) in the stationary region with $I_b \leq 45$ mA to two maxima ($q=2$ -like) in the upper stationary region ($I_b = 80 - 120$ mA). Inside the non-stationary region between these stationary regimes ($I_b = 45 - 80$ mA), the time-varying field profile (was shown in Fig. 5.13) oscillates between one and two maxima, leading to an intermediate profile in the time-averaged profile of Fig. 5.38. The time-averaged profile at $I_b = 140$ mA then shows a change towards a third maximum inside the upper non-stationary region and the time-varying profile in this region shows an oscillation between profiles with two and with three

maxima (not shown here).

The change of field profile indicates, that inside the non-stationary regime a competition between two non-linear modes takes place. These non-linear modes have field profiles, that resemble the field profiles of cold-cavity / linear axial modes. As already in the mode-competition during RF-startup and in the discussion of the frequency-tuning (sections 4.2.1 and 4.3.2), it may thus be assumed, that these modes are the non-linear equivalent of the cold-cavity / linear axial modes. Therefore, the non-linear modes can be identified as different non-linear axial modes.

The non-linear axial modes that are involved in the field profile oscillation inside the differ-

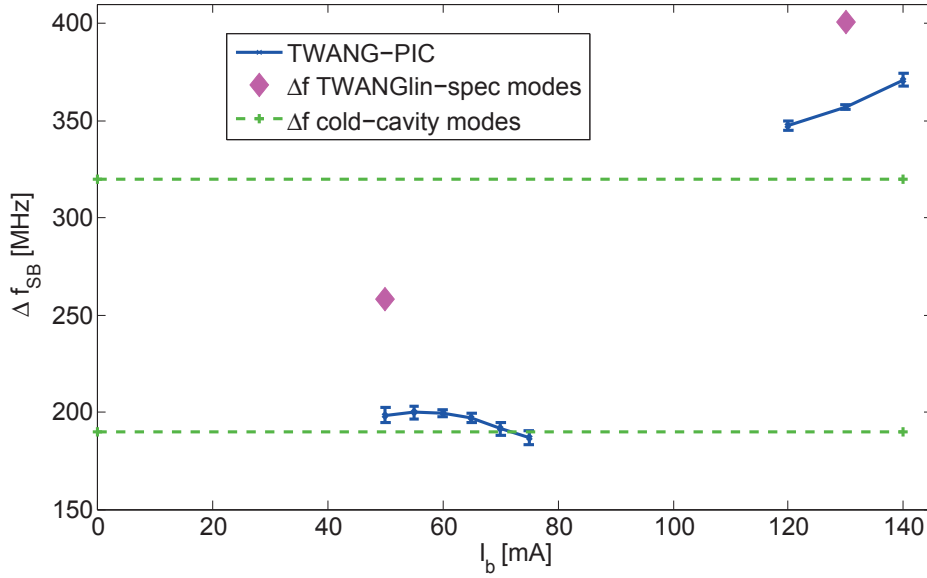


Figure 5.39: Distance between equidistant sidebands from TWANG-PIC for I_b -scan at $B_0 = 9.54$ T (simulation: $\alpha = 2.3$), compared to the frequency difference between the cold-cavity axial modes $q=2/q=1$ (190 MHz) and $q=3/q=2$ (320 MHz) as dashed/green lines, and to the frequency separation from TWANGLIN-SPEC (pink diamonds), between the two most unstable modes ($q=2/q=1$ -like) for $I_b = 50$ mA, and between the second and third most unstable modes ($q=3/q=2$ -like) for $I_b = 130$ mA (same parameters as TWANG-PIC). Error bars are due to an uncertainty in peak detection.

ent non-stationary regions are directly related to Δf_{SB} in these regions. This is shown in Fig. 5.39, comparing the dependency of Δf_{SB} on the beam current from TWANG-PIC-simulation with the frequency separation between the corresponding cold-cavity / linear axial modes from cold-cavity calculation (green horizontal lines) and from TWANGLIN-SPEC [146, 145] (magenta diamonds), where the frequencies of all axial modes are obtained simultaneously in the linear self-consistent regime. The cold-cavity frequencies, that were shown in Table 2.2 have a separation of $\Delta f_{cold}(q=1/q=2) \approx 190$ MHz and $\Delta f_{cold}(q=2/q=3) \approx 320$ MHz. It becomes apparent, that Δf_{SB} from TWANG-PIC in both upper and lower non-stationary region ($I_b = 45 - 80$ mA and $I_b \geq 120$ mA) is very close to the difference in cold-cavity frequency of the involved axial modes. Because the linear axial modes from self-consistent linear simulations should represent the fre-

frequencies of axial modes more realistically than the cold-cavity frequencies, Fig. 5.39 includes the frequency-difference Δf_{lin} of the involved axial modes from TWANGLIN-SPEC simulations for two representative values of I_b . A comparison of these values with the TWANG-PIC sideband separation shows, that Δf_{SB} is between cold-cavity results Δf_{cold} and TWANGLIN-SPEC-results Δf_{lin} both in the lower non-stationary region with $q=2/q=1$ and for the upper non-stationary region with $q=3/q=2$. This is also true for experiment in the non-stationary region observed there (compare Fig. 5.35).

This correlation between Δf_{SB} and the frequency-separation of axial modes (cold-cavity or linear) gives a very strong indication, that the interfering non-linear axial modes play an important role for the formation of non-stationary oscillations and of the sidebands.

Additionally, also the dependence of the sideband frequency separation on the magnetic field and therefore on the detuning was studied, which allows a comparison to the scaling laws of Δf_{SB} with a dependence on the wave group velocity.

In Fig. 5.40, the sideband frequency separation as a function of the magnetic field is com-

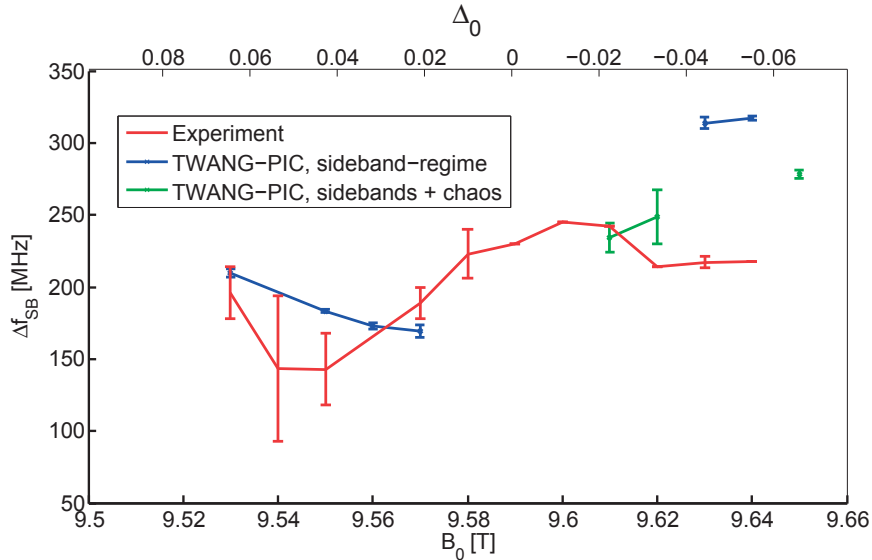


Figure 5.40: Distance between equidistant sidebands in RF-spectrum for B_0 -scan at $I_b \sim 65$ mA (simulation: varying α , as described in section 5.3). The normalized detuning was added as the top y-axis. The experimental error bars show the range of fluctuation of sideband frequencies due to the V_a -fluctuation, those for simulation an uncertainty in peak detection. Where sidebands appeared in simulation on top of a chaotic spectrum, Δf_{SB} is shown in green. In simulation, the oscillation on operating points in the range $B_0 = 9.58 - 9.60$ T was chaotic. In experiment, Δf_{SB} was extracted from spectrograms in temporal sections of the sideband-type.

pared between experimental measurements and TWANG-PIC simulation, for a current close to $I_b = 65$ mA. The results show a qualitative agreement between simulation and experiment for the forward-interaction ($B_0 = 9.53 - 9.57$ T). In the backward-region however, the simulation results show a sudden increase in sideband frequency separation, that does not appear in the experi-

5.7. ANALYSIS OF THE SIDEBAND-REGIME

mental results.

An inspection of the corresponding field profiles in simulation shows, that the behavior with changing magnetic field is similar to the one observed in the I_b -scan shown in Fig. 5.35 and Fig. 5.38. The field profile oscillates between ones that resemble the cold-cavity axial modes $q=1 / q=2$ in the forward-region and the modes $q=2 / q=3$ in the backward-region ($B_0 = 9.63 - 9.64$ T). As in the I_b -scan, the sideband frequency separation from TWANG-PIC is again close to the difference of the cold-cavity frequencies of the corresponding modes: $\Delta f_{\text{cold}}(q=1/q=2) \approx 190$ MHz and $\Delta f_{\text{cold}}(q=2/q=3) \approx 320$ MHz.

In experiment, the sideband separation is also generally slightly larger in the backward-region than in the forward-region, but the increase is smaller and not abrupt. This implies that the experimental Δf_{SB} does not match the difference of cold-cavity frequencies of the $q=2 / q=3$ -modes in the backward-region. The reason for this discrepancy between experiment and TWANG-PIC-simulation is unknown and it is thus unclear, if in experiment the non-stationary oscillation in the backward region is still caused by $q=1 / q=2$ -like profiles.

The observed behavior should be compared to the above-mentioned scaling laws by Chu et al. [20], that include the group velocity: $\Delta f_{\text{SB}} = \frac{1}{2\tau_w} = \frac{v_{\text{gr}}}{2L}$ in the forward-region and $\Delta f_{\text{SB}} = \frac{1}{\tau_w + \tau_{\text{el}}}$ in the backward-region. However, as discussed in [103], the results of these scaling laws strongly depend on the evaluation method of both the group velocity $v_{\text{gr}} = \frac{\partial \omega}{\partial k_{\parallel}}$ and of the length of the interaction region. In fact, in the experimental results the sideband regime is most present in the region around zero-detuning. Theoretically, from a cold-cavity approach at this point one would expect a group velocity that approaches zero, which would result in Δf_{SB} of both scaling laws tending to zero.

The group velocity was calculated from the cold-cavity dispersion relation for the operating points $B_0 = 9.50$ T and $B_0 = 9.65$ T (with $\alpha = 2.3$), on interaction points that have been obtained from the linearly coupled dispersion relation in Fig. 4.1.

For the interaction length L two possibilities exist that give a very similar result $L \approx 20$ mm, choosing either the width of the maximum in a $q=1$ -like field profile or the entire length of the section with constant wall radius.

A summary of these estimations and of the resulting sideband-separation is presented in table

	Forward ($B_0 = 9.50$ T)	Backward ($B_0 = 9.65$ T)
Group velocity v_{gr}	$\sim 2.9 \cdot 10^7$ m/s	$\sim 1.6 \cdot 10^7$ m/s
Wave transit time $\tau_w = \frac{L}{v_{\text{gr}}}$	~ 1.3 ns	~ 0.7 ns
Electron transit time $\tau_{\text{el}} = \frac{L}{v_{z,e^-}}$	~ 0.7 ns	~ 0.7 ns
Sideband frequency separation Δf_{SB}	$f_{\text{SB}} \sim \frac{1}{2\tau_w}$ ~ 400 MHz	$f_{\text{SB}} \sim \frac{1}{\tau_w + \tau_{\text{el}}}$ ~ 720 MHz

Table 5.1: Results of sideband frequency separation from scaling in [20] with the help of the cold-cavity dispersion relation (see Fig. 4.1).

5.1. It shows that this estimation gives a sideband frequency separation, that is at least a factor 2 larger than both the experimental values and the simulation results on the analyzed operating points.

In summary, we can conclude that the scaling laws of the sideband frequency separation both by

Chen and by Chang / Chu (established for gyro-BWO) do not agree with our observations from experiment and simulation. However, the simulation results help to give a new interpretation of the sideband separation as being close to the frequency separation (cold-cavity or linear) of the non-linear axial modes, that are involved in the non-stationary field oscillation.

5.7.4 The axial profiles of sideband-modes

In the earlier subsections the question was raised, whether different sidebands can be identified as a non-linear manifestation of different cold-cavity axial modes. In order to answer this question, this section will present an analysis of the field profiles that can be assigned to each of the sideband modes and which will be compared to the field profiles of the cold-cavity axial modes. For this, the spectral components of the field profile have been analyzed using non-stationary TWANG-PIC simulations. By Fourier-transforming the field-profile of these simulations, one can assign a field profile to each frequency:

$$\hat{F}(z, t) \xrightarrow{\text{FFT}} \hat{F}(z, f) \quad (5.11)$$

The frequency-position of the sidebands $f_{\text{SB},j}$ (for j^{th} sideband) can then be determined from the RF-spectrum at the cavity output $|\hat{F}|(z_{\text{out}}, f)$, which allows us to determine the complex field profile at the sideband-frequencies $\hat{F}(z, f_{\text{SB},j})$.

For this analysis, the simulation results for the operating point ($B_0 = 9.54 \text{ T} / I_b = 65 \text{ mA} / \alpha = 2.3$) (compare results shown in Fig. 5.13, Fig. 5.12 and Fig. 5.10) in the sideband-regime was chosen. The RF-spectrum for determining the frequency-positions of the sidebands is shown in Fig. 5.41, where the sidebands are labeled in the ordering of their peak amplitude and where the cutoff-frequency in the flat-cavity section is indicated by a red / dashed vertical line. This labeling is also used for the field profiles $\hat{F}(z, f_{\text{SB},j})$ of the sidebands in Fig. 5.42. There, in addition to the field amplitude and phase profiles, the flat-cavity section is indicated by a red bar at the bottom of each graph and the diffractive quality-factor $Q_{\text{diff}} = \omega_0 W_{\text{RF}} / P_{\text{RF}}$ for each sideband profile is included as text.

The figures show, that the sideband modes with frequencies below cutoff in the flat-cavity section (peak number 3-4 and 6-8) have a fundamentally different profile from the ones located above cutoff. The field profile of the sidebands above cutoff, especially the dominant peak at $f_{\text{SB}1} = 260.620 \text{ GHz}$ and peak number 2 at $f_{\text{SB}2} = 260.814 \text{ GHz}$, but also number 5 at $f_{\text{SB}5} = 261.016 \text{ GHz}$, have field profiles that resemble those of the cold-cavity axial modes with one, two and three maxima (compare Fig. 3.1), corresponding to $q=1$, $q=2$ and $q=3$, respectively. This identification of the sidebands with cold-cavity axial modes cannot be sustained for the sidebands below the cutoff frequency of the constant-radius section. With the exception of sideband no. 4, that is located very close to the cutoff-frequency, the lower sidebands have their maxima close to the start of the uptaper-section. The reason for this is that the field of the corresponding modes cannot penetrate into the constant-radius section, because their frequency is below the corresponding cutoff frequency. The suppression of the high field amplitude in the constant-radius section results in a reduction of the stored field energy in the cavity W_{RF} and thus in a smaller Q_{diff} for the sidebands with lower frequencies.

Because their maximum is pushed entirely outside the flat-cavity section, the presence of these

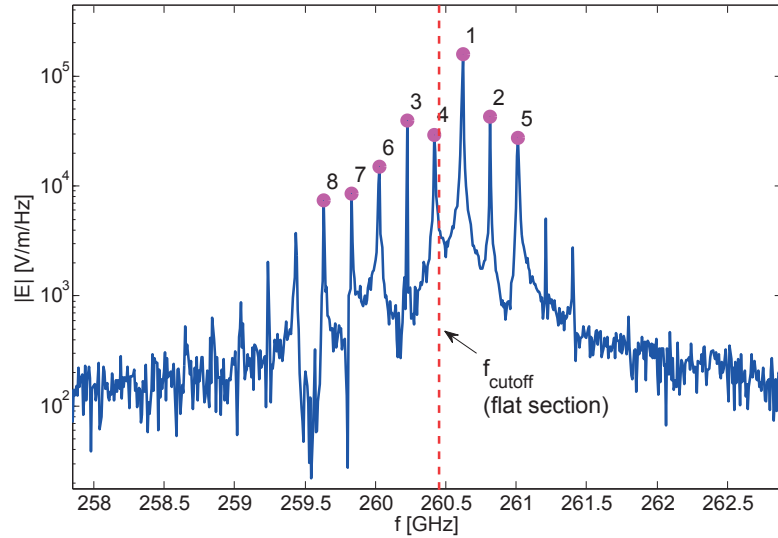


Figure 5.41: RF-spectrum from end of interaction region with frequency peaks corresponding to the field profiles shown in Fig. 5.42. The ordering in peak amplitude and the numbering corresponds to the order of the profiles.

sidebands shows, that the initial uptaper section (0.85° -taper) plays an important role in the formation of the sidebands and of the non-stationary oscillations in general.

In the previous subsection 5.7.3, it was shown that the sideband frequency separation is close to the difference in cold-cavity frequency of the non-linear axial modes that appear in the field profile oscillation, which in the present case are the modes $q=1$ and $q=2$ (see Fig. 5.13). Due to the field profiles in Fig. 5.42, these two non-linear axial modes can be identified as the two dominant sideband modes. This would indicate, that the frequency-positions of all the equidistant sidebands are determined by the frequency-position and separation of the two involved axial modes.

The origin of the non-dominant sidebands can be illustrated on the case of nanosecond-pulses of section 5.7.1. The non-sinusoidal variation of power implies that the radiation has to include other spectral components than the two dominant, original sideband modes. However, the frequency-separation between these components is still determined by the pulse-frequency, which corresponds to the frequency-separation of the two originally involved modes, thus leading to equidistant sidebands.

The frequency-position of the corresponding non-dominant sideband modes then may directly determine also their field profile. In [190], a linear analysis was described, that assigns a field profile for any frequency on a linear dispersion relation. At the frequencies of the linear axial eigenmodes, the field profiles from this analysis match the field profiles of the modes, whereas for intermediate frequencies the field profile shows a gradual transition. The field profiles that are observed in this analysis resemble those assigned to the sidebands in Fig. 5.42.

In summary, the frequency location of all the sidebands is likely to be determined by the domi-

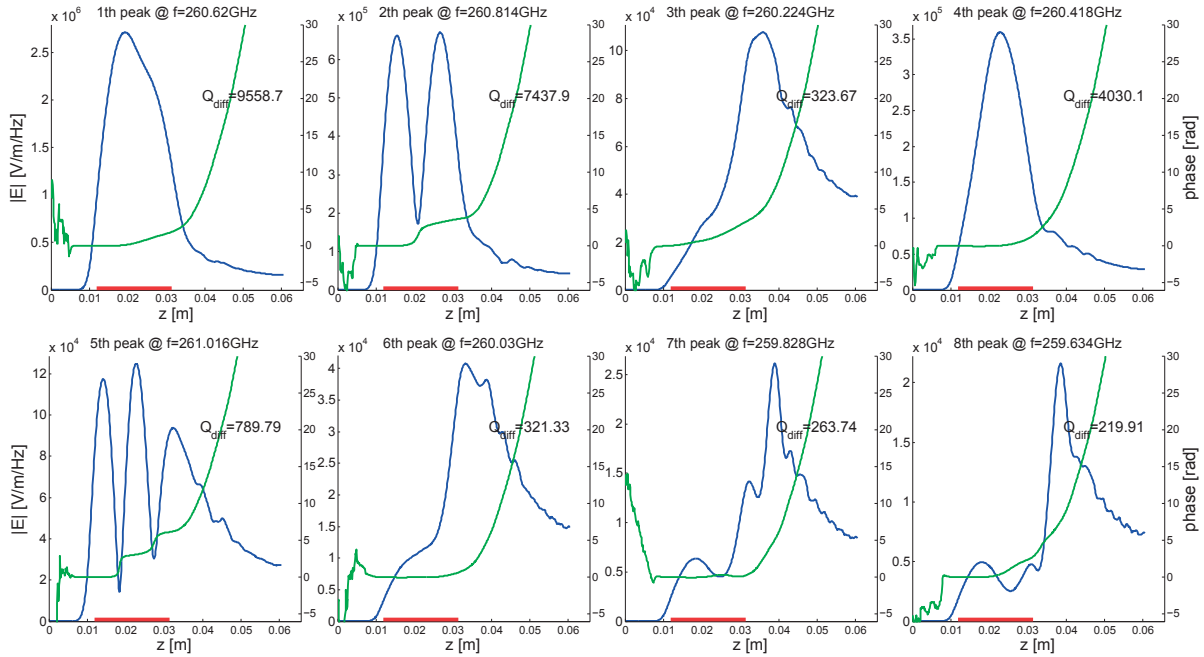


Figure 5.42: Field profile for sidebands: Field amplitude (blue / left y-axis) and phase (green / right y-axis) profiles of different frequency-components in RF-output from TWANG-PIC on operating point with sidebands $I_b = 65 \text{ mA}$ / $B_0 = 9.54 \text{ T}$ / $\alpha = 2.3$. The profiles correspond to the height in the FFT of each spectral peak along the axial direction and the graphs are ordered by the peak amplitude in the spectrum that is displayed in Fig. 5.41. The diffractive quality-factor has been calculated for each profile and is included as text in the graph. The flat-cavity section is indicated by a red bar at the bottom of the profiles. For the peak ordering and frequency of the peak see figure titles.

nant sidebands, which would correspond to non-linear axial modes involved in the field-profile oscillation. The frequency location would then determine the field profiles that were observed in Fig. 5.42.

The field profiles of the sidebands shown above also impose the question, how the field profile of the intermediate peaks are related to the field profile of cold-cavity axial modes in the regime of period doubling, period tripling etc.. Therefore, the same analysis was repeated for the operating point $B_0 = 9.58 \text{ T}$ / $I_b = 55 \text{ mA}$, that had been identified as a period doubling type. The resulting field profiles are shown in Fig. 5.44 and the spectrum, that is used for identifying the corresponding peak-frequencies, is shown in Fig. 5.43, where again the cutoff-frequency in the flat-cavity section is indicated (red / dashed).

On this operating point, the highest peak corresponds to a $q=2$ -like profile with two axial maxima, followed by a $q=1$ -like and a $q=3$ -like profile with their maximum close to the beginning of the flat-cavity section. The sideband peaks no. 6, 7 and 8 on the lower-frequency side are similar to the lower-frequency peaks shown previously in Fig. 5.42, with a maximum further towards the

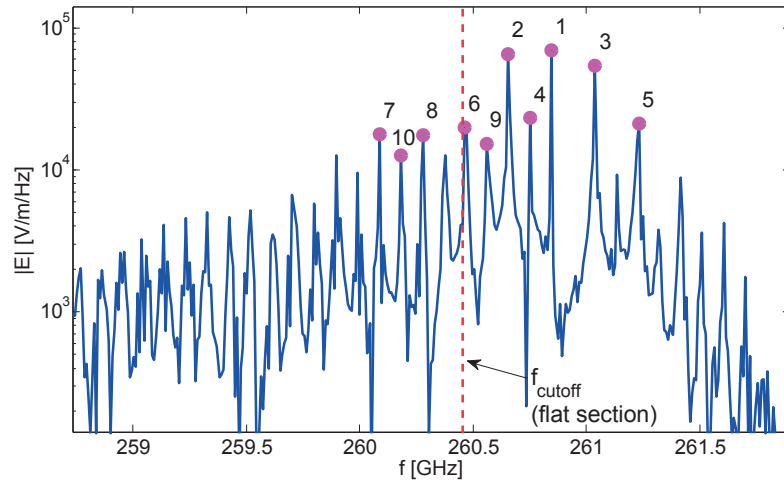


Figure 5.43: RF-spectrum for operating point with period-doubling, from end of interaction region with frequency peaks corresponding to the field profiles shown in Fig. 5.44. The ordering in peak amplitude and the numbering corresponds to the order of the profiles.

end of the flat-cavity section for lower frequencies. Sideband no. 5 shows, that the field profiles of the lateral sidebands do not necessarily resemble the profiles of successive cold-cavity axial modes. This shows, that these sidebands do not correspond to successive axial modes and affirms that their profile is rather determined by their frequency-position.

The intermediate period-doubling peaks no. 4, no. 9 and no. 10 show, that the profiles of intermediate peaks are close to the profiles of the adjacent sidebands, but pushed further towards the end of the interaction region and with a much lower quality-factor than these sidebands.

In summary, the analysis on this second operating point confirms, that the dominant sidebands show a field profile, that is close to that of the cold-cavity axial modes, while the other sidebands and the intermediate peaks cannot be definitely related to any of these axial modes.

5.8 Non-stationary oscillations in high-power gyrotrons

In a brief simulation study it has been analyzed, whether the phenomenon of non-stationary oscillations described is also relevant for the operation of high-power gyrotrons. These gyrotrons differ from the DNP-gyrotron substantially and in several aspects. An important aspect is, that the available range of operating parameters is dictated by a competition between different transverse modes and not by the characteristics of a single transverse mode. Therefore, the region close to zero-detuning, where the majority of the non-stationary regime appears in the DNP-gyrotron, can never be accessed in a high-power gyrotron, because it would result in the excitation of a different transverse mode.

Thus, the relevance of the non-stationary oscillations for high-power gyrotrons was tested by increasing the beam current, starting from the designated standard operating point in the forward-region. The results for the cavity of European 1 MW ITER gyrotron are presented in Fig. 5.45,

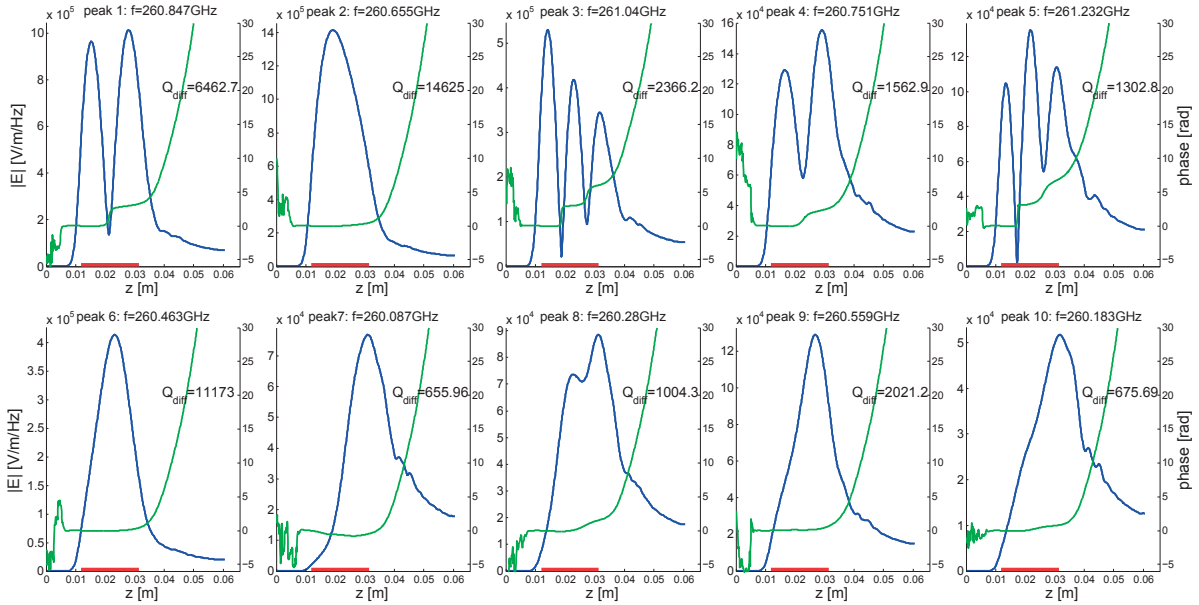


Figure 5.44: Field profile for sidebands (period doubling): Field amplitude (blue / left y-axis) and phase (green / right y-axis) profiles of different frequency-components in RF-output from TWANG-PIC on operating point with period-doubling $I_b = 55 \text{ mA}$ / $B_0 = 9.58 \text{ T}$ / $\alpha = 2.238$. The profiles correspond to the height in the FFT of each spectral peak along the axial direction and the graphs are ordered by the peak amplitude in the spectrum that is displayed in Fig. 5.44. The flat-cavity section is indicated by a red bar at the bottom of the profiles. The diffractive quality-factor has been calculated for each profile and is included in the graph.

showing the RF-power evolution and RF-spectrum for beam-currents of approximately 3 times ($I_b = 100 \text{ A}$) and 6 times ($I_b = 200 \text{ A}$) the no-oscillation current (lower limit of hard-excitation region). Notice that these are artificially high beam currents with the nominal beam current being $I_b = 40 \text{ A}$.

The spectrum and power of the non-stationary oscillation at $I_b = 200 \text{ A}$ shows a different behavior from the one in the DNP-gyrotron, namely a single-frequency oscillation with a higher and higher broadband background, leading to a chaotic power-modulation.

The current, where this non-stationary regime appears is about a factor $I_b / I_{\text{no-osc}} \sim 5\text{-}6$ above the no-oscillation current (detuning $\Delta_0 \sim 0.11$), compared to a factor of 2.5 in the forward-region of the DNP-gyrotron ($\Delta_0 \lesssim 0.07$). A similar analysis in the cavity of the 140 GHz-gyrotron for Wendelstein 7-X did not show any significant non-stationary behavior up to even higher currents. Thus, it can be concluded, that the phenomenon of non-stationary oscillation is probably not relevant for the operation of high-power gyrotrons.

However, a direct comparison of high-power gyrotrons with the DNP-gyrotron is difficult. Some of the most important differences are, that their operation is generally restricted to a small operating space in the forward-region, that the cavity-profile with a relatively short flat-cavity section is designed for a low-Q field profile and that the pitch-angle is generally much smaller than the

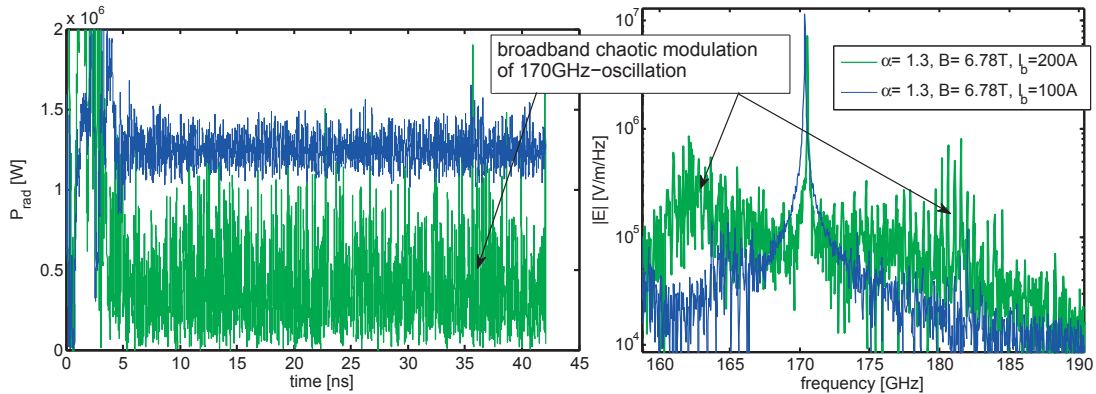


Figure 5.45: Non-stationary oscillation in cavity of European 1 MW ITER gyrotron: RF-power evolution (left) and RF-spectrum on operating points with approximately 3 times (blue, $I_b = 100\text{A}$) and 6 times (green, $I_b = 200\text{A}$) the no-oscillation current, with other parameters as on the designated operating point: $B_0 = 6.78\text{T}$, $\alpha=1.3$, $V_b = 79.5\text{kV}$. With broadband non-reflecting boundary conditions.

one in the DNP-gyrotron.

5.9 Interpretation of non-stationary oscillations with simulations

In this section, an investigation will be presented, trying to identify the basic mechanisms and the source of the non-stationary regime observed in the DNP-gyrotron. For this, a survey of literature is presented, showing attempts for explaining non-stationary oscillations published in earlier works. Finally, merging the analysis presented in this chapter, a tentative interpretation of the origin of non-stationary oscillations will be given and compared to the explanations found in literature.

5.9.1 Possible interpretations from literature

Non-stationary oscillations as the ones described above have been investigated in gyrotron research for almost 30 years.

As described earlier, a series of theoretical studies have put their attention on describing the regions of the parameter-space, where the non-stationary regime appears [60, 158, 159, 60, 160, 53, 117], where most often the non-stationary threshold current is investigated. Additionally, the chaotic regime and the transition to chaos have been investigated in detail in gyrotron simulations [160, 60]. Nevertheless, although many different have been presented, it is still not fully understood. In the following the most important publications will be presented, that include attempts for explaining the mechanism responsible for the non-stationary oscillations, for gyrotrons and devices with a similar interaction mechanism, starting in chronological order.

The first detailed research work on non-stationary oscillations in gyrotrons was published by

Nusinovich [49], Ginzburg et al. [50] and Lin et al. [51]. In [50], based on simulations the regimes of periodic automodulation (sideband regime) and the stochastic regime (chaotic) were described, however without an analysis of their origin. In [51] an interpretation of the non-stationary oscillations was attempted using a PIC-model, arguing that their origin is an uneven energy deposition of the beam on the forward- and on the backward-components of the excited wave. The energy deposition would be equilibrated through axial propagation and end reflections, explaining the observed modulation period close to the bounce period.

In a publication on a slow-wave BWO, Levush et al. [188] extended this study and postulated the existence of two non-stationary oscillation categories, of which one is caused by the so-called self-modulation instability and the other is caused by a so-called cross-excitation instability. The first mechanism is explained to be 'associated with overbunching of the electrons under the influence of a large electric field amplitude in the RF structure'. The cross-excitation instability however is described as being caused by axial mode-competition, where the presence of one growing mode triggers the excitation of another mode, which then cannot be sustained and decays, so that an oscillatory behavior appears.

On a gyro-BWO, Nusinovich et al. [158] emitted the idea that self-modulation could be caused by a competition between two modes with different axial field structure. Furthermore, it was argued that in such gyro-BWOs the detailed geometry of the uptaper at the upstream end plays a determining role in the formation of non-stationary oscillations. This study however included artificially induced reflections for studying the effect of the uptaper.

Such reflections have been described later to play a dominant role in the origin of the non-stationary regime [161, 162, 163]. In the DNP-gyrotron however one can conclude, that the observed dynamics are not due to reflections, since the experimental results are well reproduced by simulations, where the reflections are negligible and where a further reduction of the remaining reflections has no influence on the results (see section 5.3).

Another hypothesis that could explain non-stationary oscillation in gyro-BWOs has been published by Chang and Fang et al. It relies on the 'self-consistent non-linear contraction of the axial field profile' [155, 53, 148]. Due to the field profile contraction, a further interaction at a different frequency occurs at the end of the interaction region, causing the appearance of a 'trailing field structure' [189] and at the same time causing the non-stationary oscillations. This phenomenon is also closely related to the overbunching process, where the interaction at the end of the cavity is important.

At this point it has to be underlined, that the vast majority of the mentioned theoretical publications were obtained with models based on the time-scale separation (Eq. (3.10)) between field and electron transit, so that their applicability to non-stationary oscillations is questionable. However, in the publications discussed above, some models were based on a more first-principle set of equations solved using a PIC-approach [51, 162, 163]. Additionally, many of the publications were obtained with an unrealistic cavity, that only consists of a section with uniform wall radius. Then, at the cavity output either a non-reflecting B.C. or some imposed reflections are used. Such a cavity model however does not include the important role of the uptaper section for the excitation of non-stationary oscillations.

Thus, the variety of interpretations of the non-stationary regime in gyrotrons and similar devices shows, that there is not yet a single accepted explanation for the origin of non-stationary

oscillations. This is also apparent in the failure of predicting regimes of non-stationary oscillation [20, 53].

An understanding and prediction of non-stationary regimes would be of great importance for gyrotron development, e.g. for the development of continuously frequency-tunable gyrotrons [155, 53, 191, 149].

5.9.2 Interpretation of observed non-stationary oscillation

Summarizing the results described in this chapter, a coherent picture can be obtained of the characteristics, background and mechanism of the non-stationary regime in the DNP-gyrotron. The dependencies of RF-frequency and power indicate a competition between non-linear modes within the non-stationary region, both in experiment and simulation. A change of modes within the non-stationary region is confirmed by an analysis of the field profiles in the stationary and non-stationary regions, showing a transition between modes that resemble cold-cavity modes (e.g. $q=1 \rightarrow q=2$) and thus justifying an identification of the modes as non-linear axial modes. Within the non-stationary regime, the temporally changing field profile suggests a competition between these non-linear axial modes.

The analysis of the frequency-separation of sidebands at the same time shows a disagreement with previously established scaling laws for gyro-BWOs and suggests that the frequency-separation is dictated by the frequencies of the two non-linear axial modes, that are involved in the mode-competition. The analysis of the field profile of the sideband modes shows, that these two non-linear axial modes correspond to the dominant sidebands, while the other sidebands cannot be clearly identified as axial modes.

In the analysis of the temporally varying field profile in Fig. 5.13 it has been observed, that the non-stationary cycle can be summarized in two phases of the oscillating field profile. In the first phase, the field amplitude increases strongly while resembling a cold-cavity $q=1$ -profile, undergoing a field profile contraction. At the point of maximum field amplitude and field contraction, the field profile starts resembling a cold-cavity $q=2$ -profile. In this shape however, the field profile decreases, during which the field contraction is reversed.

An interpretation of this cycle is, that the presence of a high-amplitude $q=1$ -like oscillation triggers a transition to a $q=2$ -like mode, which would non-linearly dominate over the $q=1$ -like mode. Such a transition was also observed in the process of the saturation in the RF-startup (see section 4.2.1, with $q=2 \rightarrow q=1$). This $q=2$ -like mode however cannot sustain itself at this point, so that the field profile decays, when the $q=2$ -like mode is reached.

Such a situation of a mode, that would be the preferred state but that cannot yet sustain itself, reminds of the situation in the hard-excitation region, where the highest efficiency can be reached [192]. In this region, the oscillation can only be sustained, if it is accessed already with a sufficient power. In this case, the field in simulation decays when initiated with a small field amplitude, but settles into a high-power oscillation when it is initiated with a high field amplitude (exceeding the amplitude of stationary state).

It was thus tested, whether the $q=2$ -like mode is in the same situation in the non-stationary regime. Fig. 5.46 shows the evolution of the RF-power and the RF-spectrum for an operat-

ing point ($I_b = 70 \text{ mA}$ / $B_0 = 9.54 \text{ T}$ / $\alpha = 2.3$) located inside the non-stationary region ($I_b = 45 - 80 \text{ mA}$) of the I_b -scan presented earlier (e.g. in Fig. 5.12). The shown curves are simulations with identical parameters, but once initiated with a low-amplitude cold-cavity $q=1$ -profile (initial output-power $P_0 = 0.15 \text{ W}$, as also in all other simulations in this document) and once initiated with a high-amplitude cold-cavity $q=2$ -profile ($P_0 = 180 \text{ W}$). Both the power and the spec-

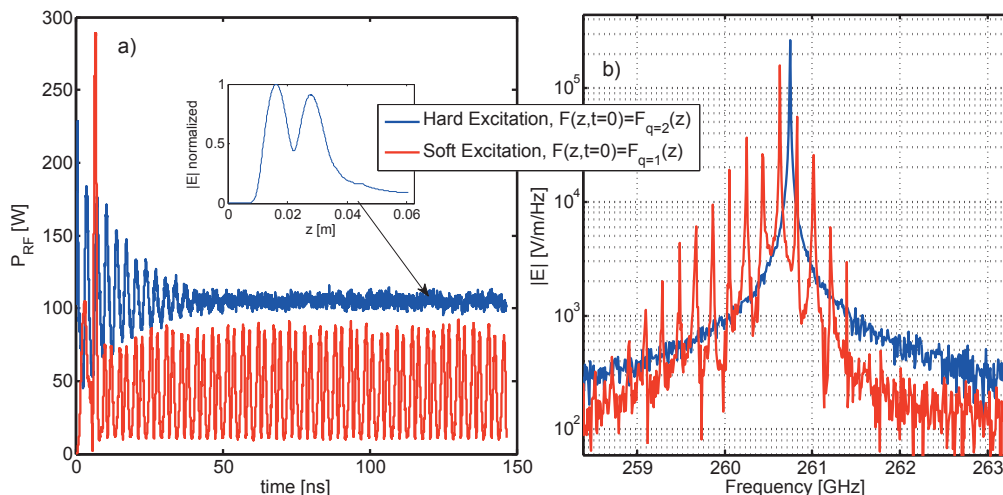


Figure 5.46: Hard-excitation of non-linear $q=2$ -mode on non-stationary operating point: a) Temporal evolution of RF-power and b) RF-spectrum on operating point $I_b = 70 \text{ mA}$ / $B_0 = 9.54 \text{ T}$ / $\alpha = 2.3$ with different initial conditions. The simulation in red is initiated with a cold-cavity $q=1$ field profile and a power $P_0 = 0.15 \text{ W}$. The simulation in blue is initiated with high power $P_0 = 180 \text{ W}$ and a field profile of the cold-cavity $q=2$ -mode. An inlet shows the field amplitude profile of the blue curves.

trum show, that instead of the non-stationary oscillation now a stable oscillation is obtained on the mode that previously existed only for higher beam currents $I_b \geq 80 \text{ mA}$. The fact, that a stable monomode oscillation is achieved, if the simulation is initiated with a high-power ($P_0 = 180 \text{ W}$) $q=2$ -mode shows, that this operating point indeed corresponds to a hard-excitation region of the non-linear $q=2$ axial mode.

This important and new result strengthens the argumentation above, that this non-stationary regime is caused by the situation, where the $q=2$ -mode is dominant but not self-sustained. It shows, that the non-stationary oscillation at least partly appears in a region, where the $q=2$ -like mode can exist and dominate over the $q=1$ -like mode, but where it cannot be reached from a lower-power $q=1$ -like oscillation.

This hard-excitation leads to a hysteresis-effect, where the oscillation on a given operating point depends on the previous oscillation or on preceding operating points. Such a hysteresis effect could not be observed with varying beam-current experimentally on the DNP-gyrotron, probably because the V_a -fluctuation leads to a premature transition towards the stationary or non-stationary regime in each direction. In a publication by Pao et al. [191] however, such a hysteresis effect between different axial modes has been described in a gyro-BWO for changing beam cur-

rent.

This additional analysis further strengthens the reasoning above, that the non-stationary regime in the DNP-gyrotron is caused by a competition of non-linear axial modes. As mentioned earlier, this corresponds to the cross-excitation mechanism described by Levush et al. [188], but also e.g. in [158, 53] a competition of modes with different axial structure is described in the non-stationary regime.

For generating this competition of non-linear axial modes in the gyrotron, several other parameters play a role, that have been described as the dominating effect in other publications. A non-linear contraction of the field profile is observed during the rise of the $q=1$ -like field profile in the non-stationary cycle. Also the initial uptaper-region, that was analyzed in [158] plays an important role, as it was observed in the analysis of the field profiles assigned to sidebands. Furthermore, also a strong overbunching, as described e.g. in [188, 189, 193] is observed in the interaction during the non-stationary cycle.

This is shown in Fig. 5.47, which shows the time-averaged profiles of the (forward-directed) RF-

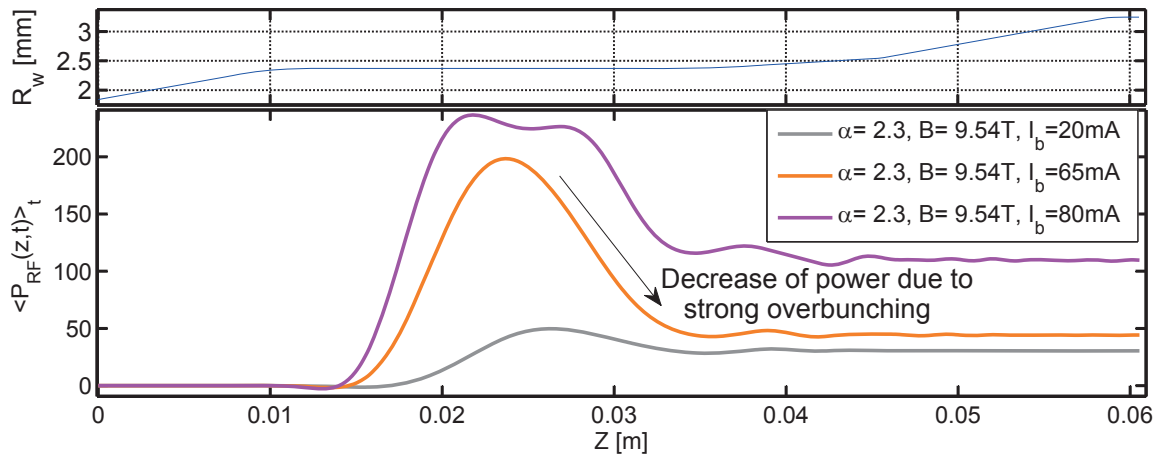


Figure 5.47: Overbunching in non-stationary regime: Top: Cavity wall profile. Bottom: Axial profile of (forward-directed) time-averaged RF-power from TWANG-PIC for operating points with $B_0 = 9.54\text{T} / \alpha = 2.3$. A negative power means backward-propagation (initial small dip at $z \approx 0.011 - 0.015\text{m}$), a decreasing power (with increasing z) shows energy re-absorption by the electrons, due to overbunching. A stronger overbunching is observed in the non-stationary region and a smaller one in the surrounding stationary regions.

power as a function of z , for different operating points in the I_b -scan analyzed earlier (e.g. in Fig. 5.12). This graph can be compared to Fig. 1.8 in the introduction, where the overbunching was explained. An axially decreasing power means, that the electrons re-gain energy. It shows, that the overbunching is relatively small for smaller currents ($I_b = 20\text{mA}$), large in the non-stationary regime ($I_b = 65\text{mA}$), and again reduced for the stationary regime at higher currents ($I_b = 80\text{mA}$). The correlation of this overbunching with the axial mode competition should be further investigated in a future study.

5.10 Summary and conclusions of non-stationary oscillations

In this chapter, the regime of non-stationary oscillations has been characterized in detail and compared to simulations. Basically the entire chapter is composed of novel results, that either represent the first analysis of this kind or are much more detailed than previously published results.

The characterization of the threshold between stationary and non-stationary regime showed a stationary region surrounded by a non-stationary regime, as it has been predicted earlier in simulations, but never clearly shown in a gyrotron experiment. The categorization of experimentally measured non-stationary oscillations showed for the first time a map of operating points with different types, including the sideband regime, period multiplication (doubling, tripling, etc.) and the chaotic regime.

The results are directly compared to simulations based on a model, that is appropriate for non-stationary oscillations, with positive results.

Due to the fluctuation of the anode voltage, the variety of different regimes and the transition to chaos can be directly observed as a temporal evolution in spectrograms. The transition to chaos could be mainly identified as the period-doubling bifurcation route, but with an appearance of period tripling and quintupling.

The analysis of the sideband regime, which allowed the first experimental observation of nano-second-pulses in a gyrotron, also revealed new insights into the regime of non-stationary regime. It showed, that the sidebands are strictly equidistant and that they appear to be locked in phase. An analysis of their frequency-separation suggested them to be associated to the difference in frequency of two axial modes. It was shown, that these two non-linear axial modes are also involved in an oscillation of the field profile. Finally, a novel method of analyzing the field profile of the sidebands suggested, that the non-linear axial modes can be identified as the two dominant sidebands.

In summary, a combination of the simulation results allows the interpretation of the non-stationary regime as being caused and governed by the competition of two non-linear axial modes.

Chapter 6

Summary and Conclusions

This thesis presented a complete characterization, analysis and interpretation of the phenomena observed in a gyrotron designed for DNP-enhanced NMR-spectroscopy. In particular, the characteristics of a non-stationary regime with self-consistently oscillating power and a multi-frequency or broadband RF-spectrum have been described and investigated.

The gyrotron is designed for CW-operation on the $TE_{7,2}$ -mode and is currently routinely operated on a 400 MHz NMR-experiment. The characterization shows a maximum RF-power of $P_{RF} = 150\text{ W}$ at a frequency of $f_{RF} = 260.5\text{ GHz}$. A frequency-tuning over 1.2 GHz with a minimum power of 1.5 W is obtained by changing the magnetic field, which determines the detuning, and simultaneously optimizing the pitch-angle (via the anode-voltage). A careful comparison with numerical simulations indicated that the features observed in this frequency-tuning can be related to a gradual change of the axial field profile. Additionally, a frequency-modulation over a frequency-range $\Delta f_{RF} > 100\text{ MHz}$ with a modulation frequency of $\leq 14.5\text{ kHz}$ was implemented and already proves an increase of the enhancement in DNP-experiments. For the DNP-application, a feedback-controller on the beam current has been installed for stabilizing RF-power and frequency. A pulsed operation (via pulses on anode-voltage) has been implemented with a pulse-length $\gtrsim 30\ \mu\text{s}$ and an arbitrary duty-cycle.

In order to improve the modeling of the RF-characteristics of the DNP-gyrotron, new models and simulation codes have been developed. A linear model has been developed by linearizing the model of the code TWANG and modifying it towards a novel moment-based approach. In this model, implemented in the linear self-consistent time-dependent code TWANGLIN, the electron equations of motion are reduced to only two complex moment-equations. It has been shown, that in contrast to fixed-field calculations, TWANGLIN-simulations can accurately reproduce the experimentally measured starting current of the DNP-gyrotron.

Also for modeling the observed non-stationary oscillations, a new model has been developed on the basis of the model of TWANG. Here, a time-scale separation assuming a constant field during the electron transit is removed. As a consequence, instead of the trajectory approach the model is based on a (spatially) 1-D PIC-model, implemented in the code TWANG-PIC. In contrast to the TWANG-code and to an entire group of gyrotron codes used elsewhere, the TWANG-PIC-results are independent of the choice of the arbitrary reference frequency. This demonstrates, that the

development of the PIC-model is indeed necessary for reliably simulating non-stationary oscillations.

The thesis presents for the first time an extensive analysis and characterization of the non-stationary regime. A novel detailed categorization of non-stationary oscillation types is presented on a plane of operating parameters, with the types of a sideband regime, period doubling, tripling etc. as well as a chaotic type. In a categorization of TWANG-PIC-simulations, all important features of the experimental categorization can be reproduced. It is shown, that the route to chaos is generally that of the period doubling bifurcation type, modified by the appearance of period tripling and quintupling, and that the chaotic time-scale is slightly larger than the time-scale of power-oscillation in the sideband-regime.

Within the sideband-regime, nanosecond-pulses could be observed for the first time in a gyrotron experiment, where it is demonstrated that they are related to a strongly self-consistently varying diffractive quality-factor. It is shown, that the sidebands are always strictly equidistant and that they appear to be phase-locked. An analysis of the dependence of the sideband-frequency separation shows a relatively small variation in experiment, whereas the dependence from simulations can be used to relate the sideband separation with the separation of axial-mode frequencies (linear/cold-cavity). The importance of axial modes is supported by a novel analysis assigning a field profile to each sideband. In the study, the dominant sidebands are identified as different non-linear axial modes. The correlation between the appearance of non-stationary oscillations and a competition of two non-linear axial modes is also confirmed by an analysis of the varying and averaged field profile in different stationary and non-stationary regions, by the dependence of the dominant RF-frequency and the RF-power on the beam-current, as well as by the existence of a hard-excitation region of the non-linear $q=2$ -mode.

In summary, the results presented in this thesis represent a significant progress in the modeling and the understanding of beam-wave interaction in a low-power gyrotron. For the first time, experimentally measured non-stationary oscillations have been compared directly to a model that is appropriate for this simulation. At the same time, the results call into question the validity of previously published simulation studies.

Nevertheless, several open issues would require to further pursue the presented study. Despite the numerous presented strong indications for an origin of the non-stationary regime in a competition of non-linear axial modes, the precise mechanism responsible for the phenomenon still needs to be understood. In particular, the details of beam-wave interaction such as the bunching-process should be further investigated in the non-stationary regime. It would be desirable to identify the term(s) in the equations responsible for the occurrence of the non-stationary regime and to identify a threshold value for the transition between the stationary and non-stationary regimes.

Additionally, some discrepancies between experiment and simulation should be further investigated. Especially the differences in the backward-regime remain to be explained, as well as the overestimated RF-power.

Appendix A

Numerical Implementation of TWANG

This appendix is an excerpt of the SPC-internal report [194] and describes the details of the numerical implementation that has been used in TWANG and TWANG-PIC for the solution of the wave-equation, and that has been introduced in sections 3.4.2 and 3.3.1.

The TWANG-equations that have to be implemented are:

$$\begin{aligned}
 \frac{d\mathcal{P}}{d\hat{z}} &= \left[-i \frac{\gamma - s\Omega_c/\omega_0}{\hat{p}_z} + \frac{s}{2} \frac{d}{d\hat{z}} \ln B_0 \right] \mathcal{P} + s \left[-\gamma F^* + i \hat{p}_z F'^* \right] \frac{C_0}{\hat{p}_z} \hat{p}_\perp^{2s-2} \\
 \frac{d\hat{p}_z}{d\hat{z}} &= - \left[\frac{C_0}{\hat{p}_z} \text{Im}(F' \mathcal{P}) + \frac{1}{2} \frac{\hat{p}_\perp^2}{\hat{p}_z} \frac{d}{d\hat{z}} \ln B_0 \right] \\
 \left[\frac{i}{Q} \frac{\partial}{\partial \tau} + \frac{\partial^2}{\partial \hat{z}^2} + \kappa_{\parallel 0}^2 \right] F &= i \mathcal{S} \frac{1}{N_j} \sum_{p=1}^{N_j} \frac{C_{0j}}{\hat{p}_{zj}} \mathcal{P}_j^*
 \end{aligned} \tag{A.1}$$

with the definitions of section 3.3 and the time-normalization $\tau \equiv \frac{\omega_0}{2Q} t$.

A.1 Numerical discretization

A.1.1 Space discretization using Finite Elements

Multiplying the last equation of (A.1) by a *test function* $g(z)$ and integrating yields:

$$\frac{i}{Q} \frac{d}{d\tau} \int_{z_{in}}^{z_{out}} d\hat{z} g F - \int_{z_{in}}^{z_{out}} d\hat{z} \frac{\partial F}{\partial \hat{z}} \frac{dg}{d\hat{z}} + \frac{\partial F}{\partial \hat{z}} g \Big|_{z_{in}}^{z_{out}} + \int_{z_{in}}^{z_{out}} d\hat{z} \kappa_{\parallel}^2 F g = i \frac{\mathcal{I}}{Q} \int_{z_{in}}^{z_{out}} d\hat{z} \mathcal{S} g \tag{A.2}$$

where we introduce the source term \mathcal{S} defined as

$$\mathcal{S}(z, \tau) = \frac{1}{N_j} \sum_{j=1}^{N_{inj}} C_{0p} \mathcal{P}_j^*$$

Discretizing $[z_{in}, z_{out}]$ using the grid $[\hat{z}_0, \dots, \hat{z}_N]$ and setting

$$g(\hat{z}) = \Lambda_k^p(\hat{z}), \quad k = 1, \dots, N+p \quad (\text{A.3})$$

$$F(\hat{z}, \tau) = \sum_{j=1}^{N+p} f_j(\tau) \Lambda_j^p(\hat{z}), \quad (\text{A.4})$$

where the *B-splines* $\Lambda^p(\hat{z})$ of order p are used as *test functions* and *basis functions* in the expansion for the field F and finally using the boundary conditions

$$\left. \frac{\partial F}{\partial \hat{z}} \right|_{z_{in}} = -i \frac{k_{\parallel}}{k} F \Big|_{z_{in}}, \quad \Lambda_k^p(z_{in}) = \delta_{k1}, \quad (\text{A.5})$$

$$\left. \frac{\partial F}{\partial \hat{z}} \right|_{z_{out}} = i \frac{k_{\parallel}}{k} F \Big|_{z_{out}}, \quad \Lambda_k^p(z_{out}) = \delta_{kN} \quad (\text{A.6})$$

we obtain the following linear system of ODEs for the unknowns $\mathbf{f} = (f_1, \dots, f_{N+p})^T$:

$$\frac{i}{Q} \mathbf{M} \cdot \frac{d\mathbf{f}}{d\tau} + \mathbf{N} \cdot \mathbf{f} = i \frac{\mathcal{S}}{Q} \mathbf{s} \quad (\text{A.7})$$

where the matrices \mathbf{M} , \mathbf{N} are given by:

$$M_{kj} = \int \Lambda_k^p \Lambda_j^p d\hat{z}, \quad (\text{A.8})$$

$$N_{kj} = \int \left(\kappa_{\parallel}^2 \Lambda_j^p \Lambda_k^p - \frac{d\Lambda_k^p}{d\hat{z}} \frac{d\Lambda_j^p}{d\hat{z}} \right) d\hat{z} + i \frac{k_{\parallel}}{k} \Big|_{z_{out}} \delta_{jk} \delta_{kN} + i \frac{k_{\parallel}}{k} \Big|_{z_{in}} \delta_{jk} \delta_{k1} \quad (\text{A.9})$$

and the vector \mathbf{s} computed from:

$$s_k(\tau) = \int_{z_{in}}^{z_{out}} d\hat{z} \mathcal{S}(\hat{z}, \tau) \Lambda_k^p(\hat{z}) \quad (\text{A.10})$$

By pushing the particles, [the first 4 equations in (A.1)] using the field $F(\hat{z}, \tau)$ given by (A.4) and a **fourth order Runge-Kutta integrator** (described in subsection below), the source term $S(\hat{z}, \tau)$ can be computed on the grid points \hat{z}_j , and thus can be written as an expansion of *linear splines*;

$$\mathcal{S}(\hat{z}, \tau) = \sum_{j=1}^{N+1} \mathcal{S}_j(\tau) \Lambda_j^1(\hat{z}). \quad (\text{A.11})$$

After integration:

$$s_k(\tau) = \sum_{j=1}^{N+1} M_{kj}^x \mathcal{S}_j(\tau), \quad k = 1, \dots, N+p, \quad (\text{A.12})$$

where the *cross mass matrix* \mathbf{M}^x is defined as

$$M_{kj}^x = \int \Lambda_k^p \Lambda_j^1 d\hat{z}. \quad (\text{A.13})$$

Note that \mathbf{M}^x is a *rectangular* $(N+p) \times (N+1)$ matrix which reduces to the square mass matrix \mathbf{M} when linear splines are used to discretize the RF field.

A.1.2 Time integration

The second order time centered discretization applied to Eq.(A.7) on the interval $[\tau_n, \tau_{n+1} = \tau_n + \Delta\tau]$ yields:

$$\frac{i}{Q} \mathbf{M} \cdot \frac{\mathbf{f}^{n+1} - \mathbf{f}^n}{\Delta\tau} + \mathbf{N} \cdot \frac{\mathbf{f}^{n+1} + \mathbf{f}^n}{2} = \frac{i\mathcal{J}}{Q} \mathbf{s}^{n+1/2}, \quad (\text{A.14})$$

which reduces to

$$\underbrace{\left(\mathbf{M} - i \frac{Q\Delta\tau}{2} \mathbf{N} \right)}_{\mathbf{A}} \mathbf{f}^{n+1} = \underbrace{\left(\mathbf{M} + i \frac{Q\Delta\tau}{2} \mathbf{N} \right)}_{\mathbf{B}} \mathbf{f}^n + \mathcal{J} \Delta\tau \mathbf{s}^{n+1/2} \quad (\text{A.15})$$

This can be solved using the following Predictor-Corrector two steps procedure:

1. Predictor step

- Push particles using field \mathbf{f}^n and compute \mathbf{s}^n .
- Compute the *predicted* field \mathbf{f}^* from

$$\mathbf{A}\mathbf{f}^* = \mathbf{B}\mathbf{f}^n + \mathcal{J} \Delta\tau \mathbf{s}^n \quad (\text{A.16})$$

2. Corrector step

- Push particles using field \mathbf{f}^* and compute \mathbf{s}^{n+1} .
- Compute the *time centered* coupling

$$\mathbf{s}^{n+1/2} = \frac{\mathbf{s}^n + \mathbf{s}^{n+1}}{2} \quad (\text{A.17})$$

- Compute the *new* field \mathbf{f}^{n+1} from

$$\mathbf{A}\mathbf{f}^{n+1} = \mathbf{B}\mathbf{f}^n + \mathcal{J} \Delta\tau \mathbf{s}^{n+1/2} \quad (\text{A.18})$$

The corrector step can be applied repeatedly by replacing \mathbf{f}^* with \mathbf{f}^{n+1} that is just computed to push the particles.

A.1.3 Implementation of equations of motion with 4th order Runge-Kutta method

The particles are advanced in z in the first 2 equations in (A.1) by using the field $F(\hat{z}, \tau)$, that was obtained as described above and a **fourth order Runge-Kutta integrator**.

The equations to solve have the form $dp/dz = f(z, p)$, where f stands for a function representing the RHS of the first two equations in (A.1) being solved stepwise (in a loop $iz=1:nz$) along the trajectory. The Runge-Kutta approach uses the approximation [195]

$$p(z_i + 1) = p(z_i) + \frac{1}{6} \cdot (k_1 + 2k_2 + 2k_3 + k_4) \quad (\text{A.19})$$

$$\text{with:} \quad (\text{A.20})$$

$$k_1 = \Delta z \cdot f(z_i, p(z_i)) \quad (\text{A.21})$$

$$k_2 = \Delta z \cdot f(z_{center}, p(z_i) + \frac{1}{2}k_1) \quad (\text{A.22})$$

$$k_3 = \Delta z \cdot f(z_{center}, p(z_i) + \frac{1}{2}k_2) \quad (\text{A.23})$$

$$k_4 = \Delta z \cdot f(z_i + 1, p(z_i) + k_3) \quad (\text{A.24})$$

For implementing this algorithm, a memory-saving approach was used.

Appendix B

Symbol List

The following table summarizes all the symbols of quantities, parameters and constants that were used in this document.

Imaginary unit ($\sqrt{-1}$)	i	
Electron mass	m_e	[kg]
Electron charge	e	[C]
Vacuum impedance	Z_0	[Ω]
Speed of light	c	[m/s]
Vacuum permeability	μ_0	[N/A ²]
Vacuum permittivity	ϵ_0	[F/m]
Time	t	[s]
Axial spatial variable	z	[m]
Normalized axial variable	\hat{z}	
Radial spatial variable	r	[m]
Azimuthal angle spatial variable	φ	[rad]
Normalized time	τ	
Time step	Δt	[s]
Normalized time step	$\Delta \tau$	
Azimuthal mode number of transverse eigenmode	m	
Radial mode number of transverse eigenmode	p	
Bessel-zero(p^{th} root of $J'_m(x) = 0$)	v_{mp}	
Bessel-function of order m	$J_m(x)$	
Mode-number of axial mode	q	
Electron current density	\mathbf{J}	[A/m ²]
Electron charge density	ρ_e	[C/m ³]
RF-electric field vector	\mathbf{E}	[V/m]
RF-magnetic field vector	\mathbf{B}	[T]
Transverse transverse field vector of TE _{m,p} -mode, normalized	$\hat{\mathbf{e}}_{mp}$	
Axial profile of the field amplitude	$\hat{F}(z)$	[V/m]
Normalized axial field amplitude profile	$F(z)$	[V/m]

Normalized axial cold-cavity field amplitude profile	$F_{\text{cold}}(z)$	
Cyclotron harmonic number	s	
Vacuum wavelength	λ	[m]
Quality-factor, general	Q	
Diffraction Q-factor	Q_{diff}	
Ohmic quality factor	Q_{ohm}	
Total Q-factor	Q_{tot}	
Angular frequency	ω	[rad/s]
Reference angular frequency	ω_0	[rad/s]
Imaginary angular frequency	ω_i	[1/s]
Cold-cavity angular frequency	ω_{cold}	[rad/s]
RF angular frequency	ω_{RF}	[rad/s]
Cutoff-angular frequency / transverse angular eigenfrequency	ω_{co}	[rad/s]
Non-relativistic angular cyclotron frequency	Ω_c	[rad/s]
Reference frequency	f_0	[Hz]
Cold-cavity frequency	f_{cold}	[Hz]
RF-frequency	f_{RF}	[Hz]
RF-power	P_{RF}	[W]
Dissipated power in cavity wall	P_{dissp}	[W]
Dissipated power in cavity wall	P_{dissp}	[W]
Efficiency	η	
Electron interaction efficiency	η_{el}	
Cutoff frequency / transverse eigenfrequency	f_{co}	[Hz]
Guiding center radius	R_g	[m]
Cavity wall radius	R_w	[m]
Larmor-radius	r_L	[m]
Skin depth	δ_{sk}	[m]
Cavity wall conductivity	σ	[S/m]
Wave number	k	[1/m]
Reference wavenumber	k_0	[1/m]
Perpendicular wavenumber	k_{\perp}	[1/m]
Parallel wave number	k_{\parallel}	[1/m]
Reference parallel wavenumber	$k_{\parallel,0}$	[1/m]
Phase-velocity	v_{ph}	[m/s]
Group velocity	v_{gr}	[m/s]
Electron transit time	τ_{el}	[s]
Wave transit time	τ_w	[s]
Interaction length	L	[m]
Effective interaction length	L_{eff}	[m]
Characteristic bandwidth of RF-field profile variation	$\Delta\omega_F$	[rad/s]
Characteristic instability bandwidth	$\Delta\omega_{\text{ib}}$	[rad/s]
Timescale of field profile variation	τ_F	[s]
Electron momentum vector	\mathbf{p}_j	[kg·m/s]

Electron velocity vector	\mathbf{v}_j	[m/s]
Axial electron velocity	v_z	[m/s]
Perpendicular electron velocity	v_\perp	[m/s]
Axial electron momentum	p_z	[kg·m/s]
Perpendicular electron momentum	p_\perp	[kg·m/s]
Normalized axial electron velocity	β_z	[m/s]
Normalized perpendicular electron velocity	β_\perp	[m/s]
Normalized axial electron momentum	\hat{p}_\perp	
Normalized perpendicular electron momentum	\hat{p}_\perp	
Complex slow-timescale normalized perpendicular el. momentum	\mathcal{P}	
Slow-timescale electron gyro-phase	Ψ	
Relativistic factor a macro-electron	γ_j	
Axial position of entrance/output of interaction region	$z_{\text{in/out}}$	[m]
No. of injected macro-electrons per time step (simulations)	N_{inj}	
Normalized detuning	Δ	
Normalized beam current	\mathcal{I}	
Normalized complex axial wavenumber w. Ohmic losses	$\kappa_{\parallel 0}^2$	
Beam-wave coupling factor	C_0	
Normalizing constant for $\text{TE}_{m,p}$ -mode	C_{mp}	
No. of time steps	N_t	
No. of points in z	N_z	
Pitch-angle spread	$\Delta\alpha$	%
Energy spread	$\Delta\gamma$	%
R_g -spread	ΔR_g	%
Spread of axial momentum	Δp_z	%
First-order perturbation of electron relativistic factor	γ_1	
Normalized moment of perpendicular electron motion in TWANGLIN	π_1	
Normalized moment of perpendicular electron motion in TWANGLIN	π_2	
Normalized quantity in TWANGLIN	C_1	
Normalized quantity in TWANGLIN	C_2	
Normalized quantity in TWANGLIN	C_3	
In TWANGLIN: normalized variation of magnetic field	δ	
Normalized detuning at cavity entrance (w. reference-frequency)	Δ_0	
Normalized interaction length	$\hat{\mu}$	
Fresnel-parameter	C_F	
Normalized detuning from [63, 59]	$\hat{\Delta}$	
Detuning from [28]	Δ_s	
Normalized beam current from [63, 64, 55]	\hat{I}	
Beam-wave coupling term from [28]	G_{mp}	
Beam current	I_b	[A]
Beam-voltage / beam energy	V_b	[V]
External magnetic field	B_0	[T]
Anode voltage	V_a	[V]

Cathode voltage	V_c	[V]
Cathode filament heating current	I_{gc}	[A]
Gun coil current	I_{gc}	[A]
DNP-enhancement	ϵ	
Starting current	I_{st}	[A]
No-oscillation current (I_{st} or lower limit of hard excitation)	I_{no-osc}	[A]
Sideband frequency	f_{SB}	[Hz]
Sideband frequency separation	Δf_{SB}	[Hz]
Relative permittivity	ϵ_r	[F/m]
Dielectric loss-tangent	$\tan \delta$	
RF-beam minimum waist horizontally / vertically	$w_{0,x} / w_{0,y}$	
Intermediate frequency between RF and reference frequency	f_{IF}	[Hz]
Reference frequency	f_{ref}	[Hz]
Local oscillator frequency	f_{LO}	[Hz]
Sampling frequency	f_{sample}	[Hz]
Number of points in sample	N_{sample}	
Threshold-current to non-stationary regime	I_{nonst}	[A]
Largest Lyapunov-exponent	λ_1	[1/s]
m -tuple for Lyapunov-exp. calculation ($m \neq$ mode number)	$X_{j=1,\dots,m}$	
Integrated field energy in interaction region	W_{RF}	[J]
Output-power of initial field profile (simulations)	P_0	[W]

Table B.1: Summary of constants and quantities used in this thesis.

List of Figures

1.1	Schematic view of half-torus of TCV with plasma-cross-section. Height of vacuum vessel: 1.54 m.	3
1.2	Concept of ECRH on resonant layer in plasma.	4
1.3	a) Transitions between energy-levels of the proton, induced by gyrotron RF (red and blue). The radiation changes the orientation of electron spin and nuclear spin simultaneously. b) Dependence of enhancement on tuning of the gyrotron frequency, through change between the different transitions. The frequencies are ω_n : resonance for nuclear spin-flip, ω_e : resonance for electron spin-flip, and the two combinations of simultaneous spin-flips correspond to the DNP-frequencies. From [14].	6
1.4	Enhancement of the NMR-signal due to the irradiation with RF and the DNP-effect. a) Black: signal without RF from gyrotron. Red: signal with gyrotron. From [16]. b) Black: signal without RF from gyrotron. Red: signal with gyrotron. Blue: Enhancement increased via frequency-modulation of gyrotron-RF. Maximum enhancement $\epsilon \approx 80$. From [17].	7
1.5	Schematic view of a gyrotron. The RF-radiation is excited in the cavity resonator shaded in red and is directed out of the window (black arrows). The circular cross-section beam of gyrating electrons from cathode to collector is shown in orange.	9
1.6	Amplitude profile of RF-electric field for $TE_{7,2,q}$ -eigenmode inside cavity structure in transverse cross-section (left) and axial direction (right, two different axial modes). In the transverse profile, the direction-independent amplitude of the field is shown as color-coding, whereas on the right, the represented field amplitude at each axial position corresponds to the maximum value of the transverse field profile at the electron guiding center radius. In the axial view, the interaction with the electron beam takes place in the cavity-region shaded in red around the region of constant wall-radius (compare setup in Fig. 1.5). The position of the electron beam is indicated in both views.	10
1.7	a) Snapshot of electrons and RF-field in electron velocity-space. The electron velocity rotates with approximately the same angular frequency as the oscillation of the RF-electric field vector (ω for field at electron position, Ω_c/γ for electrons). b) Concept of snapshots at integer multiple of field period. In this view, the field direction stays fixed and the bunch forms at the top of the graph. From: [20].	11

1.8	Typical interaction efficiency and snapshots of the bunching process as a function of the field phase ωt , following the electrons along their trajectory. The snapshots are taken at integer multiples of the field phase, so that the field direction is always in \mathbf{e}_x -direction. A detuning between field frequency and gyration-frequency makes the bunch gather in the decelerating phase. From: [20].	12
1.9	Uncoupled dispersion relations (frequency versus parallel wavenumber) for electron beam (two examples with different cyclotron frequencies) and of cylindrical waveguide TE-mode. An intersection of the dispersion relations (red points) shows a synchronism between wave and particle with possible interaction. An interaction with an intersection at positive wavenumbers is called forward-interaction and occurs for $\omega_{\text{RF}} > \Omega_c/\gamma$ while backward interaction means $k_{\parallel} < 0$ and $\omega_{\text{RF}} < \Omega_c/\gamma$	14
2.1	Schematic view of gyrotron setup with the main components. The approximate size is shown by the scale on the left.	20
2.2	Density of transverse modes in frequency and their coupling factors for the DNP-gyrotron. The red and blue dots correspond to co- and counter-rotating modes respectively, which are separated only for clarity.	21
2.3	Schematic view of the triode-Magnetron Injection Gun (MIG) with an example of beam propagation and the applied voltages. V_{fil} defines the voltage driving the filament current I_{fil} for heating the cathode emitter, V_c is the cathode voltage and V_a the anode-voltage.	22
2.4	Axial profile of cavity wall radius (blue) and of magnetic field B_0 (green).	23
2.5	Average pitch-angle α and relative spread $\Delta\alpha$ versus the anode voltage V_a for different cavity magnetic field values, cold-cavity values from DAPHNE. Note that α is decreased by increasing V_a . Beam-current $I_b = 100$ mA (unless indicated differently), for other parameters see table 2.3. Here, the gun-coil currents $I_{\text{gc,top}} = -1$ A for the top coil and $I_{\text{gc,bot}} = -2$ A for the bottom coil were used.	25
2.6	Average pitch-angle α (blue) and relative spread (green) versus gun coil currents. $I_{\text{gun coil}}$ in the x -axis shows the average of the two gun coils for a fixed difference $I_{\text{gc,top}} - I_{\text{gc,bot}} = 1$ A, cold-cavity values from DAPHNE. Generally, in this document the operating point with the average value $I_{\text{gc}} = -1.5$ A was used. $V_a = 8.8$ kV, $B_0 = 9.51$ T, $I_b = 100$ mA, for other parameters see table 2.3.	26
2.7	Starting currents as a function of the magnetic field, calculated with Eq. (5.40) in [28], using the fixed field profiles of the cold-cavity eigenmodes with axial mode number $q=1$ to $q=4$. The normalized detuning Δ_0 and the normalized beam-current \hat{I} are shown as top-axis and right vertical axis. Zero-detuning at $B_0 = 9.589$ T. Pitch-angle: $\alpha = 1.7$	27
2.8	Normalized detuning Δ_0 as in Eq. (2.1) and $\hat{\Lambda}$ as in Eq. (2.2) for typical values of magnetic field and pitch-angle for the DNP-gyrotron. Beam voltage: $V_b = 15.5$ kV.	28

LIST OF FIGURES

2.9	Dependence of a) normalized beam current \hat{I} and b) normalized interaction length $\hat{\mu}$ on the pitch-angle for DNP-gyrotron with parameters as described in subsection 2.1.2. In part a), a beam current of $I_b = 100$ mA was used and in b) an effective length $L_{\text{eff}} = 20$ mm was used.	29
2.10	Integration of DNP-gyrotron (on the right) in its present environment for use in DNP-NMR experiments.	30
2.11	Rack with power supplies (PSs) and other auxiliaries for gyrotron operation.	31
2.12	Interface in Labview-program for gyrotron control, screenshot of version for gyrotron experts. The white (active) number fields on the right show the control parameters, whereas the grey fields show indications and the red fields show limitations. The main parameters are monitored as time-traces on the window on the left.	31
2.13	Interface of Labview-program for gyrotron control, version for application in DNP-spectroscopy. The gyrotron is essentially controlled by the buttons, which trigger a sequence for gyrotron start or stopping, together with external triggering.	33
2.14	Long-term drift of beam current with a fixed operating parameters (fixed filament heating current). This shows, that a feedback control for the current is necessary.	34
2.15	Reaction of feedback-controller on application of steps of I_b set-value. a) Measured I_b (red) compared to set value (blue). b) Filament heating current, adapted by feedback-controller to act on beam-current.	35
2.16	Beam profile at a distance $z = 90$ mm from window, from perspective-corrected, centered and filtered temperature-profile measurement with the help of an IR-camera. Methods described in [69].	36
2.17	Measured (perspective-corrected) beam amplitude profile (left, at $z = 120$ mm), compared to beam amplitude and phase profile from phase-reconstruction, propagated to a distance $z = 120$ mm from window. Methods described in [69].	36
2.18	a) Displacement of center of gravity of the RF-beam as a function of the distance from the window, x -direction (positive=right, looking onto window): original (red) from unshifted IR-camera images and after alignment of images onto straight line (blue). b) center of gravity, y -direction (positive=up). c) Evolution of spot size in x - and y -direction as function of distance from window.	37
2.19	Beam pattern (blackened spot) of $TE_{2,4}$ -mode, captured with temperature-sensitive paper directly in front of the window. The window circumference is indicated by a line. Operating point at $B_0 = 9.75$ T.	38
2.20	Diagnostic setup (left) and its context in LPMN-laboratory (right, compare Fig. 2.10). The RF is directed into the overmoded waveguide and from there distributed to the diagnostics by the beam splitters.	38
2.21	Schematic view of diagnostic setup, shown as a photograph in Fig. 2.20.	39
2.22	VDI-heterodyne receiver: photograph and schematic.	39

2.23	Example for spectrogram, showing the change of frequency during an RF-startup in the DNP-gyrotron. Here, the IF-signal amplitude on the oscilloscope was approximately $3.5\text{mV}_{\text{RMS}}$	41
3.1	Cold-cavity axial eigenmodes for the $\text{TE}_{7,2}$ -mode in the DNP-gyrotron: a) Cavity wall-profile. b) Cold-cavity field amplitude profile for different axial modes (for colors and line-styles see legend) from code package CAVITY, normalized to output value. c) Cold-cavity field phase profiles. Frequencies and quality-factors: see table 2.2. Here, for the Ohmic losses, a wall conductivity of $\sigma = \sigma_{\text{Cu}}/2 = 2.9 \cdot 10^7 \text{ S/m}$ was used.	47
3.2	Sketch of the relevant time-scales in gyrotron interaction and in gyrotron modeling. The positions of the different time-scales apply to the here-described DNP-gyrotron and are different in other gyrotrons.	47
3.3	Algorithm for solving the system of equations in the code TWANG. The equations of motion are advanced over the entire interaction region using a 4 th -order Runge-Kutta method and the field profile is updated in the parabolic wave equation by using a combination of a finite-difference predictor-corrector approach in time-domain with a finite-element approach in spatial domain.	53
3.4	PIC-algorithm for solving the system of equations in the code TWANG-PIC. The equations of motion are advanced in time using a 4 th -order Runge-Kutta method and the field profile is updated in the parabolic wave equation using a combination of a finite-difference predictor-corrector numerical scheme in time-domain with a finite-element scheme in spatial domain.	56
3.5	Top: Profile of the cavity wall radius as a function of the axial coordinate, as used in the simulations. Bottom: Self-consistent axial profile of the absolute value and phase of the electric field along the cavity. The profiles are a snapshot at the same instant from TWANG-PIC (red lines) and from TWANG (blue crosses). For a better visibility, only a certain number of points from TWANG are displayed and the offset of the field phase has been subtracted for both cases. The simulation parameters are $B_0 = 9.535 \text{ T}$, $I_b = 20 \text{ mA}$, $\alpha = 1.9$, $V_b = 15.5 \text{ kV}$	60
3.6	Instantaneous particle distribution in the relativistic γ -factor, corresponding to the particle energy, and in the slow gyro-phase Ψ along the interaction region. The snapshots are taken at the same simulation time as in Fig. 3.5 and for both codes $N_{\text{inj}} = 64$ particles were used. For the TWANG-simulation (blue lines) the electron trajectories are shown as lines. For TWANG-PIC (red points) however, for one simulation time only the instantaneous position, energy and phase are known and displayed. In the lower plot, again a constant phase offset between the result of the two codes has been subtracted.	61

LIST OF FIGURES

3.7 Radiated power (a) and self-consistent oscillation frequency (b) as a function of the cavity magnetic field (bottom x -axis) and of the normalized detuning (top x -axis). The red, dashed line ('+') corresponds to the radiation as simulated in TWANG with a reference frequency $f_0 = 260.507$ GHz, that corresponds to the cold-cavity eigenfrequency for the TE_{7,2,1}-mode. The results from TWANG-PIC with the same input parameters are shown in blue (solid, diamonds). The TWANG-result with the reference frequency iteratively adapted to the RF-frequency is represented by the magenta/dotted line ('x') and the same for TWANG-PIC is shown as the green/dash-dotted line (circles). In the backward-region (higher B_0), the TWANG-result with a fixed f_0 deviates from the other results. In the hard-excitation-region (low B_0), only the result with a fixed f_0 is shown. 62

3.8 Spectra from TWANG-PIC (top part) and TWANG (bottom part) for the non-stationary operating point $B_0 = 9.60$ T, $I_b = 67$ mA, $\alpha = 1.9$. The different line styles and colors correspond to different reference frequencies (see legend). 63

3.9 Comparison of temporal behavior in the initial phase of TWANG (in blue/ dashed) with the result of TWANGLIN (black). (Parameters: $B_0 = 9.57$ T, $I_b = 9$ mA, $\alpha = 1.7$). (a) Exponential growth of the absolute value of the RF-field at the output of the interaction region up to the saturated phase of the non-linear simulation, (b) Zoom of the transient phase of the simulation. 70

3.10 Growth rate of the field amplitude obtained from TWANGLIN (black) for a magnetic field of $B_0 = 9.55$ T versus the beam current. The point, where the growth rate reaches zero corresponds to the linear starting current 71

4.1 Uncoupled and coupled dispersion relations of an infinite system composed of a circular waveguide and an annular electron beam, shown in the plane of frequency and parallel wavenumber. The coupled dispersion relation is calculated as in [20] (Eq. (65)) and in [29] (Eq. (6.3)). In the coupled dispersion relation (b) / c) and e) / f), $I_b = 65$ mA), the beam-wave interaction is supposed to occur at the parallel wavenumber, where the maximum growth rate occurs (black point). Here, the lines of different colors represent the different branches of the dispersion relation, where for the complex branch the real and imaginary part is shown. The points show the basic estimation for axial modes $k_{||} = \pm \frac{q\pi}{L_{\text{eff}}}$ on the uncoupled dispersion relation ($q =$ axial index, $L_{\text{eff}} =$ interaction length, '+' for forward-propagation (blue points) / '-' for backward (orange points)). 74

4.2 Starting current I_{st} for TE_{7,2}-mode from experiment (red / dashed), TWANGLIN-simulations (black / solid) and linear analysis based on fixed-field calculations (thin solid) for axial modes $q=1$ (blue), $q=2$ (blue) and $q=3$ (red). The top x -axis shows the detuning Δ_0 (see Eq. (3.30)). The hard-excitation region from experiment is situated between the no-oscillation current (pink/solid) and the red / dashed and curve. The experimental system parameters are given in table 2.3, the anode-voltage is fixed at $V_a = 8.8$ kV, corresponding to a pitch-angle $\alpha \approx 1.8-2.0$ (see Fig. 2.5). Simulation parameters: see table 3.3, with $\alpha = 1.7$ 76

- 4.3 Normalized amplitudes (blue, left y-axis) and phases (red / fine line, right y-axis) of the electric field from TWANGLIN along the cavity axis for three different values of the magnetic field, at a current slightly exceeding the starting current (compare Fig.4.2). As a comparison, the amplitude (green/dashed) and phase (red/dashed) profiles of the corresponding cold-cavity modes has been added. a) $B_0 = 9.505$ T, forward regime, b) $B_0 = 9.57$ T, detuning close to zero, c) $B_0 = 9.65$ T, backward regime. 77
- 4.4 Experimental starting current versus magnetic field for designated operating transverse mode $TE_{7,2}$ (red) together with neighboring counter-rotating modes $TE_{-4,3}$ (blue) and $TE_{-2,4}$ (black). Parameters as in section 2.1.2, with $V_a = 8.8$ kV. 78
- 4.5 Self-consistent RF-frequency obtained from TWANGLIN (linear interaction) and TWANG-PIC (non-linear saturated regime) for a beam-current close to the starting current (compare Fig. 4.2), as a function of the magnetic field. Simulation parameters from table 3.3, ($\alpha_{\text{twanglin}} = 1.7$, $\alpha_{\text{twangpic}} = 1.89$). 78
- 4.6 Longitudinal mode competition observed in TWANG-PIC-simulations for the operating point ($B_0 = 9.505$ T / $I_b = 75$ mA / $\alpha = 1.67$): ,a) evolution of RF-power and dissipated power, b) electron efficiency, c) instantaneous RF-frequency (from field phase derivative at output) and the corresponding field profiles (inlets) taken at times $t = 103$ ns (linear interaction) and at $t = 213$ ns (non-linear stationary regime). The $q=2$ -mode is observed in the phase of linear interaction (exponential growth) and in the short saturation phase ($t \sim 130$ ns), whereas the non-linear $q=1$ -mode develops in the final stationary phase. 79
- 4.7 Experimental RF start-up on the IF-signal of the heterodyne receiver (top: raw signal on oscilloscope, bottom: spectrogram) for the operating point $B = 9.505$ T / $I_b = 75$ mA (slightly exceeding the starting current) / $V_a = 9.05$ kV (expected pitch-angle from DAPHNE: $\alpha \approx 1.69$, from Fig. 2.5). For these measurements, the oscillation was excited with a beam current crossing the starting current, keeping other parameters fixed. 80
- 4.8 RF-frequency from experiment (red) and TWANG-PIC (pink, same as in Fig. 4.5) for currents slightly higher than the starting current versus magnetic field. Experimental parameters: table 2.3, $V_a = 8.8$ kV, simulation parameters: table 3.3, $\alpha = 1.89$ 81
- 4.9 Threshold current (purple / dashed) for a transition to significant power and lower frequency in purple / dashed, together with starting current I_{st} in experiment (red / solid). The transition between the two regimes is illustrated in Fig. 4.10 in a scan in I_b along the green dashed line at $B_0 = 9.63$ T. The top x-axis shows the detuning Δ_0 82
- 4.10 Experimentally measured RF-power (blue / left y-axis, logarithmic scale) and frequency (pink / right y-axis) versus beam current, showing the transition in RF-characteristics between the two regimes shown in Fig. 4.9 in the backward-regime ($B_0 = 9.63$ T). For comparison, the RF-frequency from TWANG-PIC has been added close to the starting current (symbol '*'). 83

LIST OF FIGURES

4.11	Experimental values for RF-frequency (blue, left y-axis) versus the cavity magnetic field, while varying the anode-voltage (green / dashed, right y-axis) for optimizing the power in stationary operation at each magnetic field. The beam current is $I_b = 100\text{ mA}$ and the anode voltage V_a is adapted for maximum power in stationary operation ($V_a > V_{a,\text{nonstat}}$). The corresponding RF-power is shown in Fig. 4.12. . . .	84
4.12	Experimental values for rf-power (blue, left y-axis) versus the cavity magnetic field, while varying the anode-voltage (green / dashed, right y-axis) for optimizing the power in stationary operation at each magnetic field. The beam current is $I_b = 100\text{ mA}$. Here, the measured power is increased by 10 % as a correction for diffraction losses in the measurement and non-perfect absorption in the calorimeter. . .	85
4.13	RF-frequency (left y-axis) from TWANG-PIC (red) and experiment (blue) versus the cavity magnetic field. The pitch-angle (pink / dashed, right y-axis) in simulation has been varied for reproducing approximately the anode-voltage dependence in the experimental measurements (see Fig. 4.11) and to avoid non-stationary oscillations. The beam current is $I_b = 100\text{ mA}$	86
4.14	RF-power (left y-axis) from TWANG-PIC (red) and experiment (blue) versus the cavity magnetic field. The pitch-angle (pink / dashed, right y-axis) in simulation has been varied for reproducing approximately the anode-voltage dependence in the experimental measurements (see Fig. 4.12) and to avoid non-stationary oscillations. The beam current is $I_b = 100\text{ mA}$	87
4.15	Selection of field profiles from simulations of which the frequency was shown in Fig. 4.13. a) Cavity wall profile, b) Amplitude profile of RF -field, c) Phase profile of RF -field. For the operating points, see legend in c).	88
4.16	Time-dependent rf-spectrum (bottom) and set-value of anode voltage control (top) with fast frequency modulation ($f_{\text{sweep}} = 14.5\text{ kHz}$, $\Delta f_{\text{RF,fast}} \approx 110\text{ MHz}$).	89
4.17	Anode voltage limit $V_{a,\text{lim}}$, below which reflected electrons are detected via an anode current, for different cavity magnetic field values. The blue line corresponds to a beam current of $I_b = 100\text{ mA}$, the red 'x' correspond to $I_b = 75\text{ mA}$ and the pink star to $I_b = 32\text{ mA}$. For other parameters see table 2.3. The pitch-angle scales inversely with the anode-voltage, meaning that at higher I_b and lower B_0 the achievable pitch-angle is lower (because of a higher spread) or the pitch-angle is higher. .	90
4.18	a) Fluctuation of rf-frequency with time in the monomode-regime, caused by anode-voltage fluctuation. From IF of heterodyne receiver. b) Fluctuation of anode-voltage, from front panel of anode-voltage power supply, numerically noise-filtered (-3 dB at $\sim 7\text{ MHz}$). c) RF-spectrum, FFT of same signal as in a), over entire shown time window. IF-signal and V_a synchronously acquired on 13 GHz analogue bandwidth LeCroy-oscilloscope (see section 2.5).	91
4.19	Spectrogram and time-averaged spectrum (windowing over longer time) of IF-signal from heterodyne receiver, showing the fluctuation due to anode voltage fluctuation. On this stationary operating point ($B = 9.54\text{ T}$ / $I_b = 20\text{ mA}$ / $V_a = 8.80\text{ kV}$) the frequency fluctuation in a) and the spectral width in b) were among the smallest observed of all operating points.	92

4.20	Fast microwave-pulses via anode-voltage pulses: Signal from fast Schottky-diode (blue, left y-axis) and from anode-voltage (red, right y-axis) on 300MHz Agilent oscilloscope. The negative Schottky-signal corresponds to the instantaneous RF-power.	93
4.21	Effect of current stabilization on RF-frequency (blue and red, left y-axis) and power (pink, right axis) stability during CW-operation of one hour. The displayed frequency-drift corresponds to the change of frequency-position of a peak with ~ 3 MHz spectral width (see section 4.4.1). The RF-frequency without current-control (red), which has been acquired on a slightly different operating point than the blue curve, has been shifted by 32 MHz for better comparison.	94
5.1	Starting current (red) and non-stationary onset current (blue). The non-stationary regime is observed above the solid blue line and below the dashed blue line. Above the dashed threshold current, a second stationary regime is observed.	98
5.2	Categorization of non-stationary oscillation on plane of beam current and magnetic field, for other experimental parameters fixed ($V_a = 8.8\text{kV} \rightarrow$ DAPHNE: $\alpha \approx 1.8 - 2$). The categorization is obtained by visual inspection of spectra measured with the spectrum analyzer, as they are shown in the insets b)-g).	100
5.3	Examples of power time-traces, measured with fast Schottky-diode on fast oscilloscope (categories indicated in each inlet). The measurements are short excerpts of situations, in which the corresponding category was present, from longer acquisitions. It is observed, how the power is not constant in the non-stationary regime, with a single fluctuation periodicity in the sideband category, a double and triple periodicity in period doubling and tripling. In the chaotic time-trace then, the strict periodicity is broken.	101
5.4	Cavity wall radius (blue, left y-axis) and magnetic field profile (green, right y-axis) as used in TWANG-PIC-simulations.	102
5.5	Indirect determination of the pitch-angle to be used in simulations by comparing the I_b -range with non-stationary oscillations to experiment (solid line): Dominant RF-frequency (highest amplitude in spectrum) for I_b -scan at $B_0 = 9.54\text{T}$. In TWANG-PIC, the pitch-angle α is varied between $\alpha = 1.94$ (value from DAPHNE) and $\alpha = 2.35$. The best match of the non-stationary regions is achieved for $\alpha = 2.3$ (thicker dashed line), since for $\alpha = 2.35$ a non-stationary zone re-appears at $I_b \geq 100\text{mA}$. See pointers (only selected lines) and legend for different colors and line styles.	103
5.6	Influence of pitch-angle spread on TWANG-PIC results: time-averaged power and dominant RF-frequency (highest peak in spectrum) for I_b -scan at $B_0 = 9.54\text{T}$ / $\alpha = 2.3$. Other parameters as in table 3.3. (blue/red, solid line, '+'): Stationary / non-stationary oscillation without spread; (Light blue/dark red, dashed line, 'x'): Stationary / non-stationary oscillation with spread $\Delta\alpha = 5\%$	104

LIST OF FIGURES

5.7 Influence of spread in velocity and guiding center radius and of the wall conductivity on TWANG-PIC results. The time-averaged RF-power is shown for I_b -scan at $B_0 = 9.65\text{ T}$, with $\alpha = 2.05$. Other parameters as in table 3.3. The non-stationary regime is shown by a different color. For different colors and line styles see legend. 104

5.8 Influence of radiation boundary condition on non-stationary TWANG-PIC results. The temporal evolution of the RF-power at the end of the simulation is shown for $I_b = 65\text{ mA}$ / $B_0 = 9.54\text{ T}$ / $\alpha = 2.3$ with single-frequency boundary condition and broadband non-reflecting boundary condition. It shows, that the result is independent of the choice of boundary condition. 105

5.9 Influence of realistic magnetic field profile on TWANG-PIC results. The time-averaged RF-power is shown for I_b -scan at $B_0 = 9.54\text{ T}$, with $\alpha = 2.3$ for the usually used realistic B_0 -profile (blue / red) and for a uniform magnetic field (green / magenta). The non-stationary regime is shown by a different color. 106

5.10 Comparison of the categorization of the occurring type of RF-oscillation from experiment (left) and TWANG-PIC-simulation. In simulations, the same non-stationary oscillation types appeared as in experiment. For the PIC-simulations, the pitch-angle was chosen to vary between $\alpha = 2.365$ ($B_0 = 9.50\text{ T}$) and $\alpha = 2.134$ ($B_0 = 9.65\text{ T}$) in the same way as in DAPHNE-results for a constant anode-voltage. 107

5.11 From Airila et al. [60]: Map of operating regimes in the plane of detuning and normalized current. Remark, that the non-stationary onset current corresponds to at least ten times the no-oscillation current (far backward-region). The red curve shows the non-stationary threshold current measured in the DNP-gyrotron, included by fitting the measured no-oscillation current to the one in the graph (blue, $I_{\text{no-osc}}$) and reproducing the fraction of non-stationary threshold current over no-oscillation current as $I_{\text{no-osc}} = (I_{\text{nonst}}/I_{\text{no-osc}})_{\text{exp}} \cdot I_{\text{no-osc}}$ 108

5.12 Comparison between experiment (solid) and TWANG-PIC (dashed) for a scan in beam current on $B_0 = 9.54\text{ T}$ / $\alpha = 2.3$. a) Time-averaged RF-power versus I_b with experimental value doubled. $P_{\text{RF,pic}}(I_b = 140\text{ mA}) = 336\text{ W}$. b) Dominant RF-frequency versus I_b with indications of the current values at which the profiles are analysed. c) Snapshot of field amplitude at the end of the simulation time (solid, left y -axis) and phase profiles (dashed, right y -axis) from TWANG-PIC, for the currents indicated by the same color in part b). Stationary / Non-stationary regime in blue / red, respectively. 110

5.13 Evolution of field profile on non-stationary operating point at $I_b = 65\text{ mA}$ / $B_0 = 9.54\text{ T}$, $\alpha = 2.3$ over an entire oscillation cycle. Field amplitude (blue, left y -axis) and phase (green, right y -axis) inside the cavity profile (black, normalized) from previous point of time (dashed lines) to the next instant (solid lines). The minimum and maximum amplitude value at each axial position are shown by pink lines. 111

5.14 Continuation of Fig. 5.12 at high beam current (TWANG-PIC, $B_0 = 9.54 T / \alpha = 2.3$).
 a) Time-averaged RF-power versus I_b . Here, the category of non-stationary oscillation has been added as circles around the power-markers with the colors defined in Fig. 5.10. b) Time-averaged electronic efficiency. c) Dominant RF-frequency versus I_b . The first two I_b -values corresponds to the last two I_b 's in Fig. 5.12. 112

5.15 a) Fluctuation of RF-frequencies with time in the sideband-regime, caused by anode-voltage fluctuation. b) Fluctuation of anode-voltage from power supply, numerically noise-filtered (-3 dB at ~ 7 MHz). c) Spectrum from FFT of heterodyne IF-signal over entire time window. In c), additional artificial peaks become visible (e.g. at $f_{IF} = 2.5$ GHz), apparent as single-pixel peaks, that are not affected by the V_a -fluctuation. 113

5.16 a) Fluctuation of RF-frequencies with time on an operating point, where the spectrum shows transitions between period doubling and chaotic oscillation, caused by anode-voltage fluctuation. b) Fluctuation of anode-voltage from power supply, numerically noise-filtered (-3 dB at ~ 7 MHz). c) RF-spectrum from FFT of heterodyne IF-signal over entire time window. 114

5.17 Spectrogram for an operating point, where during the anode-voltage fluctuation a transition from the sideband regime to the period-doubling regime and then towards chaos is observed. A short period-tripling phase is observed starting at $60 \mu s$. 116

5.18 Spectrogram for an operating point, where during the anode-voltage fluctuation a transition from the sideband regime to the period-doubling regime and then towards chaos is observed. 117

5.19 Spectrogram showing a continuous transition from period doubling to period-tripling with non-equidistant intermediate frequency peaks. 118

5.20 RF-spectrum showing non-equidistant period-tripling from FFT on TWANG-PIC simulations at the operating point $B_0 = 9.62 T / I_b = 80 \text{ mA} / \alpha = 2.178$ 118

5.21 Spectrograms with different routes to chaos: a) sidebands-chaos and sidebands - period doubling - chaos and b) sidebands - period doubling - period tripling - chaos. 119

5.22 a) Temporal bifurcation diagram: Temporal evolution of extrema amplitude $V\left(\frac{dV}{dt}(t) = 0\right)$ in measured time-trace of fast Schottky-diode, corresponding to instantaneous power. b) Illustration of method how extrema (red points) are obtained from power time trace inside a slightly chaotic section (see $t = 42.65 \mu s$ in part a)). c) Spectrogram of same oscillation of which temporal bifurcation diagram is shown part a). 120

5.23 Airila [64]: Bifurcation diagrams from extrema in RF-power evolution, using numerical simulations. Left: period-doubling route to chaos, Right: intermittency-type route to chaos. To be compared with Fig. 5.22. 121

5.24 Temporal bifurcation diagram (extrema $V\left(\frac{dV}{dt}(t) = 0\right)$ of instantaneous power). Here, the appearance of chaos seems to include elements of intermittency. 121

LIST OF FIGURES

5.25 Illustration of method for calculation of largest Lyapunov-exponent: Two similar signal trajectories (encircled regions) are represented by $m = 3$ points $X_{j=1,2,3}$ and $\hat{X}_{j=1,2,3}$ separated by a properly chosen delay ($t(X_2) - t(X_1)$, corresponding to J points in the time-trace). Then these 3-tuples are advanced in time and the temporal growth of the initially small distance between X and \hat{X} is used to obtain the Lyapunov-exponent. 123

5.26 Average value of logarithmic divergence between two initially similar signal trajectories over time. The analyzed signal was acquired with the fast Schottky-diode. For finding similar signal trajectories, the number of points to represent this signal section was varied in the range $m = 2 - 9$. With more points, the divergence shows a behavior that is more clearly exponential. The slope of the fit to the traces with higher m gives the Lyapunov-exponent $\lambda_1 = 8.765 \cdot 10^7 \frac{1}{s}$ 124

5.27 Demonstration of sideband-equidistance: Spectrogram showing temporal fluctuation of rf-frequencies (due to V_a -fluctuation) on an operating point, where the the sideband frequencies vary strongly. For highlighting the equidistance at each point of time, the frequency separation between neighbouring sidebands has been added as numbers (unit [MHz]) for the times $t_1 = 1.41 \cdot 10^{-5}$ and $t_2 = 2.40 \cdot 10^{-5}$ s. The equidistance is confirmed within the spectrogram resolution of 1 MHz. 126

5.28 Broadened sidebands: RF-spectrum from spectrum analyzer, corresponding a measurement of the temporally varying spectrum shown in Fig. 5.27 over a longer acquisition time. 127

5.29 Spectrogram with very strong variation of sideband-frequency. 127

5.30 Spectrogram for nanosecond-pulsed regime. Indicating times, at which time-traces and spectras are taken for the following figures ($t_1=58 \mu s$ in blue and $t_2=65 \mu s$ in black) 128

5.31 Nanosecond-pulses: Details of oscillation corresponding to $t_1=58 \mu s$ (a) and b)) and $t_2=65 \mu s$ (c) and d)) in the spectrogram shown in Fig. 5.30. a)/c) Instantaneous RF-power, experimentally measured with fast Schottky-diode and compared to IF-signal from heterodyne system on fast oscilloscope. b)/d) Spectrum from FFT in a time-window around the same time as the time-trace in a)/c) 128

5.32 Nanosecond-pulses: a) Spectrogram for typical point where nanosecond-pulsed power was observed ($B_0 = 9.575T$, $I_b = 100mA$, $V_a = 8.8kV$, $V_c = 15.5kV$) and b) Signal from fast Schottky-diode (negative) and heterodyne-system (plus offset) at the time $t_1=58 \mu s$ marked by the blue line in the spectrogram. There is a time-delay between the two time-traces, caused by different signal path lengths. 129

5.33 Nanosecond-pulses in TWANG-PIC simulation: Results for operating point corresponding to experimentally measured nanosecond-pulses in Fig. 5.31 ($B_0 = 9.60T$ / $I_b = 70mA$ / $\alpha = 2.208$). a) Temporal variation of RF-energy stored in field inside cavity b) electron interaction efficiency c) radiated RF-power at end of interaction region d) diffractive quality-factor, calculated from field profile. 130

- 5.34 Result of analysis of phase difference between sidebands. As it can be seen from the spectrogram, the distance between the two analysed sidebands is slowly varying, so that the phase difference is constant only for a certain period for each frequency difference in the reference. The result of the phase difference is shown with different offsets for different frequency differences and is placed within the analysed time section of the spectrogram. 132
- 5.35 Distance between equidistant sidebands in RF-spectrum for I_b -scan at $B_0 = 9.54\text{ T}$ (simulation: $\alpha = 2.3$). In experiment (red/light red), the sidebands become very strongly fluctuating and the radiation nearly chaotic for $I_b > 57\text{ mA}$, indicated by a dashed/light red line. The experimental error bars show the range of fluctuation of sideband frequencies due to the V_a -fluctuation, those for simulation are due to an uncertainty in peak detection. 134
- 5.36 Spectrogram to illustrate the strongly fluctuating sidebands that are shown in Fig. 5.35 in light red/dashed on the example of $I_b = 61\text{ mA}$ 135
- 5.37 Sideband frequency-separation (TWANG-PIC): Scaling from maximum field amplitude of time-averaged field profiles $\sqrt{|\hat{F}|_{\max}} = \sqrt{\max(\langle |\hat{F}|(z, t) \rangle_t)}$ (with factor $1/9$), compared to Δf_{SB} from RF-spectra. On operating points with $B_0 = 9.54\text{ T} / \alpha = 2.3$ and varying beam current. This shows that the scaling law in [189] is not consistent with our simulation-results. 135
- 5.38 Time-averaged field profiles from simulations for different beam currents from each of the regions of stationary and non-stationary oscillation that were shown in the I_b -scan of Fig. 5.12 ($B_0 = 9.54\text{ T} / \alpha = 2.3 / I_b$ see legend). Amplitudes (left y-axis) are shown as solid lines, phases (right y-axis) as dashed lines. The top part shows the cavity wall profile for a better coordination. 136
- 5.39 Distance between equidistant sidebands from TWANG-PIC for I_b -scan at $B_0 = 9.54\text{ T}$ (simulation: $\alpha = 2.3$), compared to the frequency difference between the cold-cavity axial modes $q=2/q=1$ (190 MHz) and $q=3/q=2$ (320 MHz) as dashed/green lines, and to the frequency separation from TWANGLIN-SPEC (pink diamonds), between the two most unstable modes ($q=2/q=1$ -like) for $I_b = 50\text{ mA}$, and between the second and third most unstable modes ($q=3/q=2$ -like) for $I_b = 130\text{ mA}$ (same parameters as TWANG-PIC). Error bars are due to an uncertainty in peak detection. 137
- 5.40 Distance between equidistant sidebands in RF-spectrum for B_0 -scan at $I_b \sim 65\text{ mA}$ (simulation: varying α , as described in section 5.3). The normalized detuning was added as the top y-axis. The experimental error bars show the range of fluctuation of sideband frequencies due to the V_a -fluctuation, those for simulation an uncertainty in peak detection. Where sidebands appeared in simulation on top of a chaotic spectrum, Δf_{SB} is shown in green. In simulation, the oscillation on operating points in the range $B_0 = 9.58 - 9.60\text{ T}$ was chaotic. In experiment, Δf_{SB} was extracted from spectrograms in temporal sections of the sideband-type. 138

LIST OF FIGURES

5.41 RF-spectrum from end of interaction region with frequency peaks corresponding to the field profiles shown in Fig. 5.42. The ordering in peak amplitude and the numbering corresponds to the order of the profiles. 141

5.42 Field profile for sidebands: Field amplitude (blue / left y-axis) and phase (green / right y-axis) profiles of different frequency-components in RF-output from TWANG-PIC on operating point with sidebands $I_b = 65 \text{ mA} / B_0 = 9.54 \text{ T} / \alpha = 2.3$. The profiles correspond to the height in the FFT of each spectral peak along the axial direction and the graphs are ordered by the peak amplitude in the spectrum that is displayed in Fig. 5.41. The diffractive quality-factor has been calculated for each profile and is included as text in the graph. The flat-cavity section is indicated by a red bar at the bottom of the profiles. For the peak ordering and frequency of the peak see figure titles. 142

5.43 RF-spectrum for operating point with period-doubling, from end of interaction region with frequency peaks corresponding to the field profiles shown in Fig. 5.44. The ordering in peak amplitude and the numbering corresponds to the order of the profiles. 143

5.44 Field profile for sidebands (period doubling): Field amplitude (blue / left y-axis) and phase (green / right y-axis) profiles of different frequency-components in RF-output from TWANG-PIC on operating point with period-doubling $I_b = 55 \text{ mA} / B_0 = 9.58 \text{ T} / \alpha = 2.238$. The profiles correspond to the height in the FFT of each spectral peak along the axial direction and the graphs are ordered by the peak amplitude in the spectrum that is displayed in Fig. 5.44. The flat-cavity section is indicated by a red bar at the bottom of the profiles. The diffractive quality-factor has been calculated for each profile and is included in the graph. 144

5.45 Non-stationary oscillation in cavity of European 1 MW ITER gyrotron: RF-power evolution (left) and RF-spectrum on operating points with approximately 3 times (blue, $I_b = 100 \text{ A}$) and 6 times (green, $I_b = 200 \text{ A}$) the no-oscillation current, with other parameters as on the designated operating point: $B_0 = 6.78 \text{ T}$, $\alpha = 1.3$, $V_b = 79.5 \text{ kV}$. With broadband non-reflecting boundary conditions. 145

5.46 Hard-excitation of non-linear $q=2$ -mode on non-stationary operating point: a) Temporal evolution of RF-power and b) RF-spectrum on operating point $I_b = 70 \text{ mA} / B_0 = 9.54 \text{ T} / \alpha = 2.3$ with different initial conditions. The simulation in red is initiated with a cold-cavity $q=1$ field profile and a power $P_0 = 0.15 \text{ W}$. The simulation in blue is initiated with high power $P_0 = 180 \text{ W}$ and a field profile of the cold-cavity $q=2$ -mode. An inlet shows the field amplitude profile of the blue curves. 148

5.47 Overbunching in non-stationary regime: Top: Cavity wall profile. Bottom: Axial profile of (forward-directed) time-averaged RF-power from TWANG-PIC for operating points with $B_0 = 9.54 \text{ T} / \alpha = 2.3$. A negative power means backward-propagation (initial small dip at $z \approx 0.011 - 0.015 \text{ m}$), a decreasing power (with increasing z) shows energy re-absorption by the electrons, due to overbunching. A stronger overbunching is observed in the non-stationary region and a smaller one in the surrounding stationary regions. 149

List of Tables

2.1	Design specifications of the DNP-gyrotron.	19
2.2	Cold cavity frequencies and quality factors of the first 3 axial modes ($q=1-3$) of the nominal transverse mode $TE_{7,2}$ both with and without Ohmic losses. A copper conductivity, $\sigma = \sigma_{Cu}/2 = 2.9 \cdot 10^7$ S/m corresponding to half of the ideal conductivity has been considered for calculating the Ohmic losses.	24
2.3	Experimental operating parameters in the usual operating region of the DNP-gyrotron. R_g and α are derived quantities, that are controlled mainly by the anode-voltage and the current in the gun coils.	24
3.1	Summary of standard constants and quantities used in this section. Other quantities are defined in the text and can be found in Appendix B.	52
3.2	TWANG-PIC runtime on two different compute nodes, using a different number of processor-cores. The speedup with increasing number of cores is not perfect because of MPI-communication.	57
3.3	Typically used simulation parameters for simulations on the DNP-gyrotron.	59
5.1	Results of sideband frequency separation from scaling in [20] with the help of the cold-cavity dispersion relation (see Fig. 4.1).	139
B.1	Summary of constants and quantities used in this thesis.	160

Glossary

ARIADNE Advanced Electron optics simulation code for beam property simulations with possibility to calculate e.g. voltage depression and non-axisymmetric effects, developed at HELLAS and presently used at KIT. 44

COLD Fortran-code for finding cold-cavity eigenmodes. It calculates the value of the determinant of the source-free wave equation in the adiabatically varying interaction structure. Combined with code EIGM to package CAVITY.. 46

DAPHNE 2D axisymmetric electron gun simulation code at SPC [62]. 24–26, 44, 54, 80, 85, 89, 90, 100, 102, 103, 106, 162, 166, 168, 169

DEMO a planned nuclear fusion reactor to demonstrate the feasibility of a commercial fusion power plant. 175

EGUN Electron optics code [73] developed at Stanford University and used e.g. at KIT. 44

EIGM Fortran-code for finding cold-cavity eigenmodes from the source-free wave equation. Starting from a close guess, it converges towards the correct eigenvalue (frequency) and eigenvector (field) by using Muller's method. Combined with code EIGM to package CAVITY.. 46, 177

Fortran an imperative programming language especially suited for numeric computation and scientific computing. 177

HELLAS Hellasfusion is a section of the Greek contribution to research on controlled magnetic fusion, coordinated by National Technical University of Athens (NTUA). 177

MPI Message Passing Interface (MPI) is a standardized and portable message-passing system designed for different computer programming languages such as Fortran, C, C++ and Java. By ruling the communication between different cores computing in parallel, it allows the parallelization of computer codes and programs.. 54

spread RMS of electron distribution in velocity, pitch-angle, energy or guiding center radius. 44

tokamak The most researched and successful Magnetic fusion device type; russian acronym translating to toroidal chamber with magnetic coils. 3

TWANG Non-linear slow-timescale monomode self-consistent gyrotron simulation code at SPC. Advancement of the code TWA [196]. [197]. 2, 16, 27, 44, 46, 48, 50, 51, 53–65, 69–71, 85, 151, 153, 164, 165, 178

TWANGLIN Linear version of TWANG. [99]. i, iii, 2, 17, 44, 46, 65, 69–71, 75–80, 94, 151, 159, 165, 166, 178

TWANGLIN-SPEC Spectral version of TWANGLIN, spectral linear version of TWANG. [145]. 44, 69, 136, 137, 172

TWANG-PIC 1D reduced Particle-In-Cell version of the code TWANG. [110]. i–iv, 2, 16, 44, 46, 55–63, 70, 78–83, 85–87, 90, 101–110, 112, 117, 118, 124, 127, 130, 134–139, 141, 143, 149, 151–153, 164–173, 175

Acronyms

2D two-dimensional. 44, 177

3D three-dimensional. 45

AC Alternating Current. 7, 49

ACI After-Cavity Interaction. 54, 65

B.C. Boundary Conditions. 103, 107, 146

BWO Backward-Wave Oscillator. 14, 26, 64, 99, 107, 114, 128, 133, 135, 139, 145–147

CW continuous wave. 15, 32, 92, 94, 151, 168

DAC Digital Analog Converter. 88

DC Direct Current. 49, 90

DNP Dynamic Nuclear Polarization. iii, iv, 1, 2, 5–7, 15–17, 19, 21, 24, 25, 27–30, 32, 33, 35, 41, 46, 47, 54, 58, 59, 69, 71, 73, 75, 83–85, 88, 89, 91, 92, 94, 97, 98, 107, 108, 116, 121, 129, 135, 143–148, 151, 160–164, 169, 175

ECCD Electron Cyclotron Current Drive. 4

ECM Electron Cyclotron Maser. 7, 8, 10, 43

ECRH Electron Cyclotron Resonant Heating. 1, 3, 4, 15, 161

EGYC European Gyrotron Consortium. 15

EPFL École Polytechnique Fédérale de Lausanne. i, 19, 29

ESR Electron Spin Resonance. 5

FEM Finite Element Method. 53

FFT Fast Fourier Transform. 41, 91, 112, 143, 167, 173

- FPGA** Field-Programmable Gate Array. 29, 32, 34, 88
- FWHM** Full Width Half Maximum. 127
- HVPS** High-Voltage Power Supply. 22, 32
- IF** Intermediate Frequency. 38–41, 80, 91, 92, 112–114, 126–128, 164, 166, 167, 170, 171
- IR** InfraRed. 35–37, 163
- KIT** Karlsruhe Institut für Technologie. 44, 48, 177
- LO** Local Oscillator. 39, 40
- LPMN** Laboratoire de Physique des Matériaux Nanostructurés. 19, 28, 38, 88, 163
- MIG** magnetron injection gun. 21
- MIT** Massachusetts Institute of Technology. 6
- MOU** matching optics unit. 29, 36
- NMR** Nuclear Magnetic Resonance. iv, 1, 5–7, 19, 29, 30, 32, 36, 73, 83, 84, 88, 89, 92, 94, 151, 161, 163
- ODE** Ordinary Differential Equation. 50, 53
- OFHC** Oxygen-Free High thermal conductivity Copper. 22
- PDE** Partial Differential Equation. 67
- PI** Proportional-Integral. 34
- PIC** Particle-In-Cell. iii, 43, 47, 48, 55–60, 63, 70, 101, 106, 107, 110, 117, 145, 146, 151, 152, 164, 169
- r.h.s.** right hand side. 13
- RF** radio-frequency. 3–17, 19, 24, 27, 29, 32–41, 43–46, 48–52, 54, 58, 61–67, 69, 70, 73–75, 77–88, 91–94, 97–106, 108–115, 118, 125–128, 130, 133–136, 138–149, 151, 152, 161, 163–173
- RMS** root mean square. 41, 164
- SPC** Swiss Plasma Center. i, 3, 19, 28, 29, 44, 46, 48, 64, 70, 107, 153, 177, 178
- TCV** Tokamak à Configuration Variable. 3, 4

TWT Traveling-Wave Tube. 8, 26

VNA Vector Network-Analyzer. 40

w.r.t. with respect to. 21

Bibliography

- [1] R. Prater. Heating and current drive by electron cyclotron waves. *Physics of Plasmas*, 11(5):2349–2376, 2004.
- [2] S. Alberti, G. Arnoux, L. Porte, J.-P. Hogge, B. Marletaz, P. Marmillod, Y. Martin, S. Nowak, and T. Team. Third-harmonic, top-launch, ECRH experiments on TCV tokamak. *Nuclear Fusion*, 45(11):1224, 2005.
- [3] E. Poli, C. Angioni, F. Casson, D. Farina, L. Figini, T. Goodman, O. Maj, O. Sauter, H. Weber, H. Zohm, G. Saibene, and M. Henderson. On recent results in the modelling of neoclassical-tearing-mode stabilization via electron cyclotron current drive and their impact on the design of the upper EC launcher for ITER. *Nuclear Fusion*, 55(1):013023, 2015.
- [4] T. Idehara and S. P. Sabchevski. Development and Applications of High-Frequency Gyrotrons in FIR FU Covering the sub-THz to THz Range. *Journal of Infrared Millimeter Terahz Waves*, 33:667–694, 2012.
- [5] M. Glyavin, G. Denisov, V. Zapevalov, A. Kuftin, A. Luchinin, V. Manuilov, M. Morozkin, A. Sedov, and A. Chirkov. Terahertz gyrotrons: State of the art and prospects. *Journal of Communications Technology and Electronics*, 59(8):792–797, 2014.
- [6] S. Mitsudo, T. Tanaka, C. Umegaki, and Y. Fujii. Intense and short millimeter wave pulse generation by using a gyrotron as a light source. In *Infrared, Millimeter, and Terahertz waves (IRMMW-THz), 2014 39th International Conference on*, pages 1–1. IEEE, 2014.
- [7] Aripin, S. Mitsudo, T. Shirai, K. Matsuda, T. Kanemaki, T. Idehara, and T. Tatsukawa. Sub-millimeter Wave ESR Measurement for Cr³⁺ in Ruby Crystal Using a Gyrotron as a Radiation Source. *International Journal of Infrared and Millimeter Waves*, 20(11):1875–1888, 1999.
- [8] A. Miyazaki, T. Yamazaki, T. Suehara, T. Namba, S. Asai, T. Kobayashi, H. Saito, Y. Tatematsu, I. Ogawa, and T. Idehara. First millimeter-wave spectroscopy of ground-state positronium. *Progress Of Theoretical And Experimental Physics*, 1, Jan 2015.
- [9] A. Miyazaki, T. Yamazaki, T. Suehara, T. Namba, S. Asai, T. Kobayashi, H. Saito, Y. Tatematsu, I. Ogawa, and T. Idehara. The sub-THz direct spectroscopy of positronium hyperfine splitting. *Journal of Physics: Conference Series*, 443(1):012002, 2013.

-
- [10] S. Mitsudo, K. Sakai, T. Idehara, T. Saito, and V. Zapevalov. 300 GHz gyrotron material processing system. In *Infrared Millimeter Waves and 14th International Conference on Terahertz Electronics, 2006. IRMMW-THz 2006. Joint 31st International Conference on*, pages 572–572, Sept 2006.
- [11] Y. Yamaguchi, T. Saito, Y. Tatematsu, S. Ikeuchi, V. N. Manuilov, J. Kasa, M. Kotera, T. Idehara, S. Kubo, T. Shimozuma, K. Tanaka, and M. Nishiura. High-power pulsed gyrotron for 300 GHz-band collective Thomson scattering diagnostics in the Large Helical Device. *Nuclear Fusion*, 55(1):013002, 2015.
- [12] E. M. Purcell, H. C. Torrey, and R. V. Pound. Resonance Absorption by Nuclear Magnetic Moments in a Solid. *Physical Review*, 69:37–38, January 1946.
- [13] J. Keeler. *Understanding NMR Spectroscopy*. John Wiley and Sons, Inc., 2 edition, April 2010.
- [14] E. Rej, T. Gaebel, T. Boele, D. E. Waddington, and D. J. Reilly. Hyperpolarized nanodiamond with long spin-relaxation times. *Nature Communications*, 6:–, October 2015.
- [15] C. P. Slichter. The discovery and renaissance of dynamic nuclear polarization. *Reports On Progress In Physics*, 77(7), Jul 2014.
- [16] T. Maly, G. T. Debelouchina, V. S. Bajaj, K.-N. Hu, C.-G. Joo, M. L. Mak-Jurkauskas, J. R. Sirigiri, P. C. A. van der Wel, J. Herzfeld, R. J. Temkin, and R. G. Griffin. Dynamic nuclear polarization at high magnetic fields. *Journal Of Chemical Physics*, 128(5), Feb 7 2008.
- [17] D. Yoon, M. Soundararajan, P. Cuanillon, F. Braunmueller, S. Alberti, and J.-P. Ansermet. Dynamic nuclear polarization by frequency modulation of a tunable gyrotron of 260 {GHz}. *Journal of Magnetic Resonance*, 262:62 – 67, 2016.
- [18] L. R. Becerra, G. J. Gerfen, R. J. Temkin, D. J. Singel, and R. G. Griffin. Dynamic nuclear polarization with a cyclotron resonance maser at 5 T. *Physical Review Letters*, 71:3561–3564, Nov 1993.
- [19] V. S. Bajaj, M. K. Hornstein, K. E. Kreischer, J. R. Sirigiri, P. P. Woskov, M. L. Mak-Jurkauskas, J. Herzfeld, R. J. Temkin, and R. G. Griffin. 250 GHz CW gyrotron oscillator for dynamic nuclear polarization in biological solid state NMR. *Journal of Magnetic Resonance*, 189(2):251–279, Dec 2007.
- [20] K. R. Chu. The electron cyclotron maser. *Reviews of Modern Physics*, 76:489–540, 2004.
- [21] R. Q. Twiss. Radiation Transfer and the Possibility of Negative Absorption in Radio Astronomy. *Australian Journal of Physics*, 11(1):564–579, 1958.
- [22] J. Schneider. Stimulated Emission of Radiation by Relativistic Electrons in a Magnetic Field. *Physical Review Letters*, 2:504–505, Jun 1959.
- [23] A. V. Gaponov. Excitation of the Transmission Line by a Non-Straight Electron Beam. *Izv. Vyssh. Uchebn. Zaved., Radiofizika*, 2(3):443, 1959.

BIBLIOGRAPHY

- [24] A. V. Gaponov. Addendum izvestia. *Izv. VUZ. Radiofizika*, 2:450–462, 1959.
- [25] J. L. Hirshfield and J. M. Wachtel. Electron Cyclotron Maser. *Physical Review Letters*, 12:533–536, May 1964.
- [26] V. Flyagin, A. Gaponov, M. Petelin, and V. Yulpatov. The Gyrotron. *Microwave Theory and Techniques, IEEE Transactions on*, 25(6):514–521, Jun 1977.
- [27] G. S. Nusinovich, M. K. A. Thumm, and M. Petelin. The Gyrotron at 50: Historical Overview. *Journal of Infrared, Millimeter, and Terahertz Waves*, 35(4):325–381, 2014.
- [28] M. Kartikeyan, E. Borie, and M. Thumm. *Gyrotrons*. Springer-Verlag, 2004.
- [29] G. S. Nusinovich. *Introduction to the physics of gyrotrons*. The John Hopkins University Press, 2004.
- [30] C. Edgecombe, editor. *Gyrotron Oscillators*. Taylor & Francis Ltd, London, 1993.
- [31] T. H. Chang, T. Idehara, I. Ogawa, L. Agus, and S. Kobayashi. Frequency tunable gyrotron using backward-wave components. *Journal of Applied Physics*, 105(6), Mar 2009.
- [32] J. Franck, K. Avramidis, I. Pagonakis, S. Illy, G. Gantenbein, M. Thumm, and J. Jelonnek. Multi-frequency design of a 2 MW coaxial-cavity gyrotron for DEMO. In *Infrared, Millimeter, and Terahertz waves (IRMMW-THz), 2015 40th International Conference on*, pages 1–2, Aug 2015.
- [33] T. Rzesnicki, G. Gantenbein, S. Illy, J. Jelonnek, J. Jin, I. Pagonakis, B. Piosczyk, A. Schlaich, and M. Thumm. 2 MW, 170 GHz coaxial-cavity short-pulse gyrotron - Investigations on electron beam instabilities and parasitic oscillations. In *38th International Conference on Infrared, Millimeter, and Terahertz Waves (IRMMW-THz)*, pages 1–2, Sept 2013.
- [34] D. Tax, O. Sinitsyn, W. Guss, G. Nusinovich, M. Shapiro, and R. Temkin. Experimental Study of the Start-Up Scenario of a 1.5-MW, 110-GHz Gyrotron. *Plasma Science, IEEE Transactions on*, 41(4):862–871, April 2013.
- [35] G. S. Nusinovich, L. Sinitsyn, O. V. and Velikovich, M. Yeddulla, T. M. Antonsen, A. N. Vlasov, S. R. Cauffman, and K. Felch. Startup-scenarios in high-power gyrotrons. *IEEE Transactions On Plasma Science*, 32(3, Part 1):841–852, Jun 2004.
- [36] J. Jin, G. Gantenbein, J. Jelonnek, T. Rzesnicki, and M. Thumm. Development of Mode Conversion Waveguides at KIT. *EPJ Web of Conferences*, 87:04003, 2015.
- [37] G. Dammertz, S. Alberti, A. Arnold, D. Bariou, P. Brand, H. Braune, V. Erckmann, O. Dumbrajs, G. Gantenbein, E. Giguet, R. Heidinger, J.-P. Hogge, S. Illy, J. Jin, W. Kasperek, K. Koppenburg, H. Laqua, F. Legrand, W. Leonhardt, C. Lievin, G. Michel, G. Neffe, B. Piosczyk, O. Prinz, T. Rzesnicki, M. Schmid, M. Thumm, M. Q. Tran, X. Yang, and I. Yovchev. High-power gyrotron development at Forschungszentrum Karlsruhe for fusion applications. *Plasma Science, IEEE Transactions on*, 34(2):173–186, April 2006.

- [38] K. Sakamoto, A. Kasugai, K. Kajiwara, K. Takahashi, Y. Oda, K. Hayashi, and N. Kobayashi. Progress of high power 170GHz gyrotron in JAEA. *Nuclear Fusion*, 49(9):095019, 2009.
- [39] A. G. Litvak, G. G. Denisov, V. E. Myasnikov, E. M. Tai, E. A. Azizov, and V. I. Ilin. Development in Russia of Megawatt Power Gyrotrons for Fusion. *Journal of Infrared, Millimeter, and Terahertz Waves*, 32(3):337–342, 2011.
- [40] K. Felch, M. Blank, P. Borchard, P. Cahalan, and S. Cauffman. Gyrotrons for magnetic fusion applications at 110 GHz and 170 GHz. *EPJ Web of Conferences*, 32:04007, 2012.
- [41] S. Cauffman, M. Blank, P. Borchard, and K. Felch. Testing of megawatt-class gyrotrons. In *Plasma Sciences (ICOPS) held with 2014 IEEE International Conference on High-Power Particle Beams (BEAMS), 2014 IEEE 41st International Conference on*, pages 1–1, May 2014.
- [42] T. Rzesnicki, G. Gantenbein, J. Jelonnek, J. Jin, I. Pagonakis, B. Piosczyk, A. Samartsev, A. Schlaich, and M. Thumm. 2 MW, 170 GHz coaxial-cavity short-pulse gyrotron - Single stage depressed collector operation. In *39th International Conference on Infrared, Millimeter, and Terahertz waves (IRMMW-THz)*, pages 1–2, Sept 2014.
- [43] Litvak, A.G., Denisov, G.G., Myasnikov, V.E., Tai, E.M., Sokolov, E.V., and Ilin, V.I. Recent development results in russia of megawatt power gyrotrons for plasma fusion installations. *EPJ Web of Conferences*, 32:04003, 2012.
- [44] S. Cauffman, M. Blank, P. Borchard, and K. Felch. First tests of a 117.5 GHz 1.8 Megawatt gyrotron for plasma heating and current drive. In *IEEE International Vacuum Electronics Conference*, pages 29–30, April 2014.
- [45] S. Alberti, F. Braunmueller, J. Genoud, J.-P. Hogge, T. Tran, M. Tran, K. Avramidis, I. Pagonakis, J. Jin, S. Illy, G. Gantenbein, J. Jelonnek, and F. Cismondi. Dual-frequency, 126/84 GHz, 1 MW gyrotron for the upgrade of the TCV EC-system. In *Infrared, Millimeter, and Terahertz waves (IRMMW-THz), 2015 40th International Conference on*, pages 1–2, Aug 2015.
- [46] Y. Tatematsu, Y. Yamaguchi, R. Ichioka, M. Kotera, T. Saito, and T. Idehara. Development of the Multifrequency Gyrotron FU CW GV with Gaussian Beam Output. *Journal Of Infrared Millimeter And Terahertz Waves*, 36(8):697–708, Aug 2015.
- [47] G. Gantenbein, A. Samartsev, G. Aiello, G. Dammertz, J. Jelonnek, M. Losert, A. Schlaich, T. A. Scherer, D. Strauss, M. Thumm, and D. Wagner. First Operation of a Step-Frequency Tunable 1-MW Gyrotron With a Diamond Brewster Angle Output Window. *IEEE Transactions On Electron Devices*, 61(6):1806–1811, Jun 2014.
- [48] I. I. Antakov, E. V. Zasytkin, and E. V. Sokolov. Electron tuning of frequency in gyrotrons. *International Journal of Infrared and Millimeter Waves*, 14(5):1001–1015, 1993.
- [49] G. Nusinovich. Analysis of the self-modulation instability of gyrotron radiation. *Radio-physics and Quantum Electronics*, 28(10):926–932, 1985.

BIBLIOGRAPHY

- [50] N. S. Ginzburg, G. S. Nusinovich, and N. A. Zavolsky. Theory of nonstationary processes in gyrotrons with low Q-resonators. *International Journal of Electronics*, 61(6):881–894, Dec 1986.
- [51] A. Lin, Z. Yang, and K. Chu. Particle simulation of a high-power gyrotron oscillator. *IEEE Transactions on Plasma Science*, 16(2):129–134, Apr 1988.
- [52] T. H. Chang, S. H. Chen, L. R. Barnett, and K. R. Chu. Characterization of Stationary and Nonstationary Behavior in Gyrotron Oscillators. *Physical Review Letters*, 87(6):064802, Jul 2001.
- [53] C. T. Fan, T. H. Chang, K. F. Pao, K. R. Chu, and S. H. Chen. Stable, high efficiency gyrotron backward-wave oscillator. *Physics Of Plasmas*, 14(9), Sep 2007.
- [54] S. Alberti, J.-P. Ansermet, K. Avramides, D. Fasel, J.-P. Hogge, S. Kern, C. Lievin, Y. Liu, A. Macor, I. Pagonakis, M. Silva, M. Tran, T. Tran, and D. Wagner. Design of a frequency-tunable gyrotron for DNP-enhanced NMR spectroscopy. In *Infrared, Millimeter, and Terahertz Waves, 2009. IRMMW-THz 2009. 34th International Conference on*, pages 1–2, sept. 2009.
- [55] S. Alberti, J.-P. Ansermet, K. A. Avramides, F. Braunmueller, P. Cuanillon, J. Dubray, D. Fasel, J.-P. Hogge, A. Macor, E. de Rijk, M. da Silva, M. Q. Tran, T. M. Tran, and Q. Vuillemin. Experimental study from linear to chaotic regimes on a terahertz-frequency gyrotron oscillator. *Physics of Plasmas*, 19(12):123102, 2012.
- [56] Y. Rozier, F. Legrand, C. Lievin, J.-C. Racamier, R. Marchesin, S. Alberti, F. Braunmueller, J.-P. Hogge, M. da Silva, M. Q. Tran, T. M. Tran, and A. Macor. Manufacturing of a 263 GHz continuously tunable gyrotron. In *14th International Vacuum Electronics Conference (IVEC)*. IEEE, May 2013.
- [57] A. I. Smirnov, T. I. Smirnova, R. L. MacArthur, J. A. Good, and R. Hall. Cryogen-free superconducting magnet system for multifrequency electron paramagnetic resonance up to 12.1 T. *Review of Scientific Instruments*, 77(3):035108, 2006.
- [58] S. N. Vlasov and I. M. Orlova. Quasioptical transformer which transforms the waves in a waveguide having a circular cross section into a highly directional wave beam. *Radio-physics and Quantum Electronics*, 17(1):115–119, 1974.
- [59] B. G. Danly and R. J. Temkin. Generalized nonlinear harmonic gyrotron theory. *Physics of Fluids*, 29(2):561–567, 1986.
- [60] M. I. Airila and O. Dumbrajs. Stochastic processes in gyrotrons. *Nuclear Fusion*, 43(11):1446–1453, Nov 2003.
- [61] M. Thumm. Effective Cavity Length of Gyrotrons. *Journal of Infrared, Millimeter, and Terahertz Waves*, 35(12):1011–1017, 2014.
- [62] T.-M. Tran, D. R. Whaley, S. Merazzi, and R. Gruber. Daphne, a 2D axisymmetric electron gun simulation code. In *6th Joint EPS-APS International Conference on Physics Computing, EPS (European Physical Society), Petit-Lancy*, page 492., 1994.

- [63] V. Bratman, M. Moiseev, M. Petelin, and R. Érm. Theory of gyrotrons with a nonfixed structure of the high-frequency field. *Radiophysics and Quantum Electronics*, 16(4):474–480, 1973.
- [64] M. Airila. *Chaos in High-Power High-Frequency Gyrotrons*. PhD thesis, Helsinki University of Technology, February 2004.
- [65] A. V. Bieren, A. Macor, E. D. Rijk, and J.-P. Ansermet. Innovative Microwave Transmission Line For DNP-NMR Experiment. In *4th International DNP Symposium*, 2013.
- [66] E. de Rijk, A. Macor, J.-P. Hogge, S. Alberti, and J.-P. Ansermet. Note: Stacked rings for terahertz wave-guiding. *Review of Scientific Instruments*, 82(6), 2011.
- [67] T. Idehara, A. Kuleshov, K. Ueda, and E. Khutoryan. Power-Stabilization of High Frequency Gyrotrons Using a Double PID Feedback Control for Applications to High Power THz Spectroscopy. *Journal of Infrared, Millimeter, and Terahertz Waves*, 35(2):159–168, 2014.
- [68] I. Ogawa, T. Idehara, M. Ui, S. Mitsudo, and W. F orster. Stabilization and modulation of the output power of submillimeter wave gyrotron. *Fusion Engineering and Design*, 53(1–4):571–576, 2001.
- [69] S. K. Jawla. *Phase Retrieval and Gaussian Beam Mode Decomposition of Gyrotron Beams*. PhD thesis, École Polytechnique Fédérale de Lausanne (EPFL): Sciences de Bases - Physique, 2010.
- [70] J.-P. Hogge, F. Braunmueller, S. Alberti, J. Genoud, T. Tran, Q. Vuillemin, M. Tran, J.-P. Ansermet, P. Cuanillon, A. Macor, E. de Rijk, and P. Saraiva. Detailed characterization of a frequency-tunable 260GHz gyrotron oscillator planned for DNP/NMR spectroscopy. In *38th International Conference on Infrared, Millimeter, and Terahertz Waves (IRMMW-THz)*, 2013, pages 1–2, 2013.
- [71] S. Alberti, F. Braunmueller, T. M. Tran, J.-P. Hogge, J. Genoud, and M. Q. Tran. High-Power THz-Waves using gyrotrons: new physics results (Invited paper). *International Journal of Terahertz Science and Technology*, 7(1):23–38, 2014.
- [72] C. Schlatter. *Turbulent ion heating in TCV tokamak plasmas*. PhD thesis, École Polytechnique Fédérale de Lausanne (EPFL): Sciences de Bases - Physique, Lausanne, 2009.
- [73] W. B. Herrmannsfeldt. Electron trajectory program. SLAC Report 226, Stanford University, 1979.
- [74] J. Pagonakis and J. Vomvoridis. The self-consistent 3D trajectory electrostatic code ARIADNE for gyrotron beam tunnel simulation. In *Infrared and Millimeter Waves, 2004 and 12th International Conference on Terahertz Electronics, 2004. Conference Digest of the 2004 Joint 29th International Conference on*, pages 657–658, Sept 2004.
- [75] E. Borie. Computations of radio-frequency behaviour. In C. Edgecombe, editor, *Gyrotron Oscillators*, chapter 3, pages 45–86. Taylor & Francis Ltd, London, 1993.

BIBLIOGRAPHY

- [76] K. R. Chu, H. Y. Chen, C. L. Hung, T. H. Chang, L. R. Barnett, S. H. Chen, T. T. Yang, and D. J. Dialetis. Theory and experiment of ultrahigh-gain gyrotron traveling wave amplifier. *IEEE Transactions on Plasma Science*, 27(2):391–404, Apr 1999. International Workshop on CRMs and Gyrotrons, Ma ale Hachamisha, Israel, May 18-21, 1998.
- [77] D. E. Muller. A Method for Solving Algebraic Equations Using an Automatic Computer. *Mathematical Tables and Other Aids to Computation*, 10(56):pp. 208–215, 1956.
- [78] T. Weiland. Computing in accelerator design and operation. In *Proc. Europhysics Conf., Lecture Notes in Physics*, volume 215, page 21, Sept. 1983.
- [79] B. Goplen, L. Ludeking, D. Smithe, and W. G. User configurable MAGIC code for electromagnetic PIC calculations. *Computational Physics Communications*, 27:54, 1995.
- [80] A. Stock, J. Neudorfer, M. Riedlinger, G. Pirrung, G. Gassner, R. Schneider, S. Roller, and C.-D. Munz. Three-Dimensional Numerical Simulation of a 30-GHz Gyrotron Resonator With an Explicit High-Order Discontinuous-Galerkin-Based Parallel Particle-In-Cell Method. *IEEE Transactions On Plasma Science*, 40(7, 2):1860–1870, Jul 2012.
- [81] M. Lin, D. Smithe, W. Guss, and R. Temkin. Hot test of gyrotron cavity interaction using a 3D CFDTD PIC method. In *Vacuum Electronics Conference, IEEE International*, pages 87–88, April 2014.
- [82] T. M. Tran, G. Jost, K. Appert, S. Alberti, and M. Pedrozzi. Particle-in-cell (PIC) simulations of beam instabilities in gyrotrons. *Physics of Plasmas*, 4(8):3043–3048, 1997.
- [83] V. Y. Zaslavsky, N. S. Ginzburg, M. Y. Glyavin, I. V. Zheleznov, and I. V. Zotova. Three-dimensional particle-in-cell modeling of terahertz gyrotrons with cylindrical and planar configurations of the interaction space. *Physics Of Plasmas*, 20(4), Apr 2013.
- [84] N. Ginzburg, N. Zaitsev, E. Ilyakov, I. Kulagin, and R. Rozental. Self-modulated generation observed in a delayed feedback relativistic microwave gyrotron. *Technical Physics Letters*, 28(5):395–398, 2002.
- [85] A. Kumar, N. Kumar, U. Singh, H. Khatun, V. Vyas, and A. Sinha. Design of interaction cavity of a 170-GHz, 1-MW gyrotron for {ECRH} application. *Vacuum*, 86(2):184 – 188, 2011.
- [86] K. A. Avramidis, Z. C. Ioannidis, S. Kern, A. Samartsev, I. G. Pagonakis, I. G. Tigelis, and J. Jelonnek. A comparative study on the modeling of dynamic after-cavity interaction in gyrotrons. *Physics of Plasmas*, 22(5):-, 2015.
- [87] T. Antonsen, A. A. Mondelli, B. Levush, J. Verboncoeur, and C. Birdsall. Advances in modeling and simulation of vacuum electronic devices. *Proceedings of the IEEE*, 87(5):804–839, May 1999.
- [88] A. W. Fliflet, M. E. Read, K. R. Chu, and R. Seeley. A Self-consistent Field-theory For Gyrotron Oscillators - Application To A Low Q Gyromonotron. *International Journal of Electronics*, 53(6):505–521, 1982.

-
- [89] S. Kern. *Numerische Simulation der Gyrotron-Wechselwirkung in koaxialen Resonatoren*. PhD thesis, Universität Karlsruhe, 1996.
- [90] A. R. Choudhury. *Investigations of After Cavity Interaction in Gyrotrons Including the Effect of Non-uniform Magnetic Field*. PhD thesis, Karlsruher Institut fuer Technologie (KIT), Fakultät fuer Elektrotechnik und Informationstechnik, June 2013.
- [91] K. A. Avramides, I. G. Pagonakis, C. T. Iatrou, and V. J. L. EURIDICE: A code-package for gyrotron interaction simulations and cavity design. In *Proceedings of the EC-17: 17th Joint Workshop on Electron Cyclotron Emission and Electron Cyclotron Resonance Heating*, 2012.
- [92] M. Botton, T. M. Antonsen, B. Levush, K. T. Nguyen, and A. N. VIVlasov. MAGY: A time-dependent code for simulation of slow and fast microwave sources. *IEEE Transactions On Plasma Science*, 26(3):882–892, Jun 1998. International Workshop On High Power Microwave (HPM) Generation And Pulse Shortening, Edinburgh, Scotland, Jun 10-12, 1997.
- [93] N. Ginzburg, N. Zavol'skii, G. Nusinovich, and A. Sergeev. Self-oscillation in uhf generators with diffraction radiation output. *Radiophysics and Quantum Electronics*, 29(1):89–97, 1986.
- [94] S. Alberti, A. Arnold, E. Borie, G. Dammertz, V. Erckmann, P. Garin, E. Giguet, S. Illy, G. L. Cloarec, Y. L. Goff, R. Magne, G. Michel, B. Piosczyk, C. Tran, M. Tran, M. Thumm, and D. Wagner. European high-power CW gyrotron development for ECRH systems. *Fusion Engineering and Design*, 53(1–4):387 – 397, 2001.
- [95] A. P. Fokin, M. Y. Glyavin, and G. S. Nusinovich. Effect of ion compensation of the beam space charge on gyrotron operation. *Physics of Plasmas*, 22(4):–, 2015.
- [96] C. A. Balanis. *Advanced Engineering Electromagnetics*. John Wiley & Sons, 1989.
- [97] M. Abramowitz and I. A. Stegun. *Handbook of mathematical functions: with formulas, graphs, and mathematical tables*. Dover Publications, Inc., 1964.
- [98] S. Alberti, T. Tran, S. Brunner, F. Braunmueller, J. Genoud, J.-P. Hogge, and M. Tran. Generalized Radiation Boundary Conditions in Gyrotron Oscillator Modeling. *Journal of Infrared, Millimeter, and Terahertz Waves*, 36(11):1043–1058, 2015.
- [99] F. Braunmueller, T. M. Tran, S. Alberti, J.-P. Hogge, and M. Q. Tran. Moment-based, self-consistent linear analysis of gyrotron oscillators. *Physics of Plasmas*, 21(4):–, 2014.
- [100] T. Tran and J. Wurtele. Free-electron laser simulation techniques. *Physics Reports*, 195(1):1 – 21, 1990.
- [101] C. K. Birdsall and A. B. Langdon. *Plasma Physics via Computer Simulation, Series in Plasma Physics*. CRC Press, 2004.
- [102] F. Braunmueller. Report: Parallelization of the TWANG-Code With MPI. Technical report, EPFL - CRPP, 2012.

BIBLIOGRAPHY

- [103] S. Alberti, F. Braunmueller, T. M. Tran, J. Genoud, J.-P. Hogge, M. Q. Tran, and J.-P. Ansermet. Nanosecond Pulses in a THz Gyrotron Oscillator Operating in a Mode-Locked Self-Consistent Q-Switch Regime. *Physical Review Letters*, 111:205101, Nov 2013.
- [104] F. Braunmueller, J. Genoud, S. Alberti, T. M. Tran, J.-P. Hogge, Q. Vuillemin, and M. Q. Tran. Experiment-theory comparison of non-stationary and chaotic regimes in gyrotrons. In *38th International Conference on Infrared, Millimeter, and Terahertz Waves (IRMMW-THz), 2013*, pages 1–2, 2013.
- [105] K. A. Avramides, Z. C. Ioannidis, A. Samartsev, A. R. Choudhury, S. Alberti, and I. G. Tigelis. Simulations of Dynamic After-Cavity Interaction in Gyrotrons. In *9th International Workshop Strong Microwaves and Terahertz Waves: Sources and Applications*, 2014.
- [106] R. A. Choudhury, S. Kern, and M. Thumm. Study of Dynamic After Cavity Interaction in Gyrotrons; Part I: Adiabatic Approximation. *IEEE Transactions on Electron Devices*, 62(1):184–191, Jan 2015.
- [107] R. A. Choudhury, D. D’Andrea, and M. Thumm. Study of Dynamic After Cavity Interaction in Gyrotrons; Part II: Influence of a Nonuniform Magnetic Field. *IEEE Transactions on Electron Devices*, 62(1):192–199, Jan 2015.
- [108] A. Schlaich. *Time-dependent spectrum analysis of high power gyrotrons*. PhD thesis, Karlsruhe Institut fuer Technologie (KIT), Institut fuer Hochleistungsimpuls- und Mikrowellentechnik, 2015.
- [109] A. Schlaich, A. R. Choudhury, G. Gantenbein, S. Illy, S. Kern, C. Lievin, A. Samartsev, and M. Thumm. Examination of parasitic after-cavity oscillations in the W7-X series gyrotron SN4R. In *Infrared, Millimeter and Terahertz Waves (IRMMW-THz), 2011 36th International Conference on*, pages 1–2, Oct 2011.
- [110] F. Braunmueller, T. M. Tran, Q. Vuillemin, S. Alberti, J. Genoud, J.-P. Hogge, and M. Q. Tran. TWANG-PIC, a novel gyro-averaged one-dimensional particle-in-cell code for interpretation of gyrotron experiments. *Physics of Plasmas*, 22(6):–, 2015.
- [111] F. Braunmueller, T. Tran, Q. Vuillemin, S. Alberti, J. Genoud, J.-P. Hogge, and M. Tran. TWANG-PIC, a monomode gyro-averaged PIC code for gyrotron simulations. In *39th International Conference on Infrared, Millimeter, and Terahertz waves (IRMMW-THz), 2014*, pages 1–2, Sept 2014.
- [112] F. Braunmueller, S. Alberti, T. Tran, J. Genoud, Q. Vuillemin, J.-P. Hogge, and M. Tran. Evaluation of experimentally measured non-stationary oscillation in gyrotrons using adequate simulation methods. In *40th International Conference on Infrared, Millimeter and Terahertz waves (IRMMW-THz), Hong Kong*, pages 1–2, Sept 2015.
- [113] A. Samartsev, G. Gantenbein, A. Malygin, and M. Thumm. Multimode numerical code for simulation of gyrotron interaction with inclusion of particle-in-cell method. In *4th European Asian Pulsed Power Conference 2012 and 19th Int. Conf. on High-Power Particle Beams 2012, Karlsruhe, Germany*, 2012.

-
- [114] J. Jelonnek. *Untersuchung des Lastverhaltens von Gyrotrons*. PhD thesis, Technische Universität Hamburg-Harburg, 2000.
- [115] N. S. Ginzburg, A. S. Sergeev, and I. V. Zotova. Time-domain self-consistent theory of frequency-locking regimes in gyrotrons with low-Q resonators. *Physics of Plasmas*, 22(3):033101, 2015.
- [116] I. V. Zotova, N. S. Ginzburg, A. V. Sergeev, and I. V. Zheleznov. Non-stationary self-consistent model of gyro-devices operating under action of external signal. In *Strong Microwave Conference, Nijni-Novgorod*, 2014.
- [117] O. Dumbrajs and H. Kalis. Nonstationary oscillations in gyrotrons revisited. *Physics of Plasmas*, 22(5):053113, 2015.
- [118] Q. Vuillemin. Particle In Cell simulation program for gyrotrons - Master thesis. Master's thesis, École Polytechnique Fédérale de Lausanne (EPFL): Sciences de Bases - Physique, 2013.
- [119] T. Tran, S. Brunner, S. Alberti, F. Braunmueller, J. Genoud, J.-P. Hogge, and M. Tran. Generalized non-reflecting radiation boundary conditions: Numerical implementation. In *39th International Conference on Infrared, Millimeter, and Terahertz waves (IRMMW-THz)*, 2014, pages 1–2, Sept 2014.
- [120] B. B. Godfrey. Numerical Cherenkov instabilities in electromagnetic particle codes. *Journal of Computational Physics*, 15(4):504–521, 1974.
- [121] R. Courant, K. Friedrichs, and H. Lewy. On the partial difference equations of mathematical physics. *IBM journal of Research and Development*, 11(2):215–234, 1967.
- [122] K. A. Avramidis. Investigations and advanced concepts on gyrotron interaction modeling and simulations. *Physics of Plasmas*, 22(12), 2015.
- [123] J. L. Hirshfield and V. L. Granatstein. Electron-Cyclotron Maser - Historical Survey. *IEEE Transactions on Microwave Theory And Techniques*, 25(6):522–527, 1977.
- [124] K. E. Kreischer and R. J. Temkin. Linear-theory of An Electron-cyclotron Maser Operating At the Fundamental. *International Journal of Infrared and Millimeter Waves*, 1(2):195–223, 1980.
- [125] J. Yu, T. M. Antonsen, and G. S. Nusinovich. Excitation of Backward Waves in Beam Tunnels of High-Power Gyrotrons. *IEEE Transactions on Plasma Science*, 38(6, Part 1, SI):1193–1199, Jun 2010.
- [126] S. H. Kao, C. Chiu, and K. R. Chu. A study of sub-terahertz and terahertz gyrotron oscillators. *Physics of Plasmas*, 19, 2012.
- [127] T. H. Chang, K. F. Pao, S. H. Chen, and K. R. Chu. Self-Consistent Effects on the Starting Current of Gyrotron Oscillators. *International Journal of Infrared and Millimeter Waves*, 24(9):1415–1420, 2003.

BIBLIOGRAPHY

- [128] S. Chen and L. Chen. Linear and nonlinear behaviors of gyrotron backward wave oscillators. *Physics of Plasmas*, 19, 2012.
- [129] G. S. Nusinovich, R. Pu, O. V. Sinitsyn, J. Yu, T. M. Antonsen, and V. L. Granatstein. Self-Excitation of a Tapered Gyrotron Oscillator. *IEEE Transactions on Plasma Science*, 38(6):1200–1207, 2010.
- [130] M. Yeddulla, G. S. Nusinovich, and T. M. Antonsen. Start currents in an overmoded gyrotron. *Physics of Plasmas*, 10(11):4513–4520, Nov 2003.
- [131] G. S. Nusinovich. Linear-theory of a gyrotron with weakly tapered external magnetic field. *International Journal of Electronics*, 64(1):127–135, Jan 1988.
- [132] H. Saito, T. M. Tran, K. E. Kreischer, and R. J. Temkin. Analytical Treatment of Linearized Self-Consistent Theory of a Gyromonotron with a Non-Fixed Structure. *International Journal of Electronics*, 61(6):895–903, Dec 1986.
- [133] E. Borie and B. Jodicke. Comments on the linear-theory of the gyrotron. *IEEE Transactions on Plasma Science*, 16(2):116–121, Apr 1988.
- [134] S. Y. Park, V. L. Granatstein, and R. K. Parker. A linear-theory and design study for a gyrotron backward-wave oscillator. *International Journal of Electronics*, 57(6):1109–1123, 1984.
- [135] C. S. Kou. Starting oscillation conditions for gyrotron backward-wave oscillators. *Physics of Plasmas*, 1(9):3093–3099, Sep 1994.
- [136] A. H. McCurdy. Self-consistency In the Quasi-linear Theory of Electron-cyclotron Masers. *International Journal of Electronics*, 72(5-6):861–872, May 1992.
- [137] I. G. Chelis, K. A. Avramidis, and J. L. Vomvoridis. Simulation of parasitic gyrotron interaction in beam tunnels. In *Infrared, Millimeter, and Terahertz Waves (IRMMW-THz), 2013 38th International Conference on*, pages 1–2, 2013.
- [138] M. K. Alaria, S. K. Ghosh, Y. Choyal, A. K. Sinha, and P. K. Jain. Design and Simulation of Lossy Interaction Structure for Ka-Band Gyro-TWT. *IEEE Transactions on Plasma Science*, 41(8):2264–2268, 2013.
- [139] L. Thorndahl, S. Alberti, J.-P. Hogge, F. Li, and T. Tran. Comparative study of dielectric loaded structures for suppressing gyro-BWO instabilities in gyrotron beam-ducts (BD) using HFSS. In *Infrared, Millimeter and Terahertz Waves (IRMMW-THz), 2011 36th International Conference on*, pages 1–3, 2011.
- [140] G. Gantenbein, G. Dammertz, J. Flamm, S. Illy, S. Kern, G. Latsas, B. Piosczyk, T. Rzesnicki, A. Samartsev, A. Schlaich, M. Thumm, and I. Tigelis. Experimental Investigations and Analysis of Parasitic RF Oscillations in High-Power Gyrotrons. *IEEE Transactions on Plasma Science*, 38(6, 1, SI):1168–1177, Jun 2010.

- [141] A. Schlaich, J. Flamm, G. Gantenbein, S. Kern, G. Latsas, T. Rzesnicki, A. Samartsev, M. Thumm, and I. Tigelis. Investigations on parasitic oscillations in megawatt gyrotrons. In *IEEE International Vacuum Electronics Conference (IVEC)*, pages 33–34, 2010.
- [142] V. Bratman. The starting regime for an MCR-monotron with a cavity having a low diffraction Q. *Radiophysics and Quantum Electronics*, 17(10):1181–1187, 1974.
- [143] A. K. Ganguly, G. S. Park, and C. M. Armstrong. Linear-analysis Of Backward-wave Oscillations In Azimuthally Varying Transverse Electric (TE) Modes. *Physics Of Fluids B-Plasma Physics*, 5(5):1639–1646, May 1993.
- [144] F. Braunmueller, T. Tran, S. Alberti, J. Genoud, J.-P. Hogge, Q. Vuillemin, and M. Tran. Self-consistent, time-dependent gyrotron linear analysis in nonhomogeneous RF-structures. In *38th International Conference on Infrared, Millimeter, and Terahertz Waves (IRMMW-THz), Mainz*, pages 1–2, 2013.
- [145] J. Genoud. Self-consistent linear analysis of a gyrotron oscillator: spectral approach - Master thesis. Master's thesis, École Polytechnique Fédérale de Lausanne (EPFL): Sciences de Bases - Physique, 2014.
- [146] J. Genoud, T. M. Tran, S. Alberti, F. Braunmueller, J.-P. Hogge, M. Q. Tran, W. C. Guss, and R. J. Temkin. Novel linear analysis for a gyrotron oscillator based on a spectral approach. *submitted to Physics of Plasmas*, 2016.
- [147] D. E. Hoff, B. J. Albert, E. P. Saliba, F. J. Scott, E. J. Choi, M. Mardini, and A. B. Barnes. Frequency swept microwaves for hyperfine decoupling and time domain dynamic nuclear polarization. *Solid State Nuclear Magnetic Resonance*, pages –, 2015.
- [148] S. H. Chen, K. R. Chu, and T. H. Chang. Saturated Behavior of the Gyrotron Backward-Wave Oscillator. *Physical Review Letters*, 85:2633–2636, Sep 2000.
- [149] A. B. Barnes, E. A. Nanni, J. Herzfeld, R. G. Griffin, and R. J. Temkin. A 250 GHz gyrotron with a 3 GHz tuning bandwidth for dynamic nuclear polarization. *Journal of Magnetic Resonance*, 221:147 – 153, 2012.
- [150] A. C. Torrezan, S. tae Han, I. Mastovsky, M. A. Shapiro, J. R. Sirigiri, R. J. Temkin, E. B. Barnes, and R. G. Griffin. Continuous-Wave Operation of a Frequency-Tunable 460-GHz Second-Harmonic Gyrotron for Enhanced Nuclear Magnetic Resonance. *IEEE Transactions On Plasma Science*, 38:1150 ff, 2010.
- [151] S. Jawla, Q. Ni, A. Barnes, W. Guss, E. Daviso, J. Herzfeld, R. Griffin, and R. Temkin. Continuously Tunable 250 GHz Gyrotron with a Double Disk Window for DNP-NMR Spectroscopy. *Journal of Infrared, Millimeter, and Terahertz Waves*, 34(1):42–52, 2013.
- [152] T. Idehara, K. Kosuga, L. Agusu, R. Ikeda, I. Ogawa, and T. Saito. Continuously Frequency Tunable High Power Sub-THz Radiation Source Gyrotron FU CW VI for 600 MHz DNP-NMR Spectroscopy. *Journal of Infrared, Millimeter Terahz Waves*, 31, 2010.

BIBLIOGRAPHY

- [153] T. Idehara, E. Khutoryan, Y. Tatematsu, Y. Yamaguchi, A. Kuleshov, O. Dumbrajs, Y. Matsuki, and T. Fujiwara. High-Speed Frequency Modulation of a 460-GHz Gyrotron for Enhancement of 700-MHz DNP-NMR Spectroscopy. *Journal of Infrared, Millimeter, and Terahertz Waves*, pages 1–11, 2015.
- [154] T. Idehara, S. Mitsudo, S. Saito, I. Ogawa, and S. Okajima. Accurate frequency measurement of a submillimeter wave gyrotron output using a far-infrared laser as a reference. *Review of Scientific Instruments*, 74(5):2860–2862, 2003.
- [155] T. H. Chang, C. T. Fan, K. F. Pao, K. R. Chu, and S. H. Chen. Stability and tunability of the gyrotron backward-wave oscillator. *Applied Physics Letters*, 90(19), May 2007.
- [156] C. Marchewka, P. Larsen, S. Bhattacharjee, J. Booske, S. Sengele, N. Ryskin, and V. Titov. Generation of chaotic radiation in a driven traveling wave tube amplifier with time-delayed feedback. *Physics of Plasmas*, 13(1), Jan 2006.
- [157] R. M. Rozental, N. I. Zaitsev, I. S. Kulagin, E. V. Ilyakov, N. S. Ginzburg, and I. N. A. Nonstationary Processes in an X-Band Relativistic Gyrotron With Delayed Feedback. *IEEE Transactions on Plasma Science*, 32(2):418–421, April 2004.
- [158] G. S. Nusinovich, A. N. Vlasov, and T. M. Antonsen. Nonstationary Phenomena in Tapered Gyro-Backward-Wave Oscillators. *Physical Review Letters*, 87:218301, Oct 2001.
- [159] S. H. Chen, T. H. Chang, K. F. Pao, C. T. Fan, and K. R. Chu. Linear and Time-Dependent Behavior of the Gyrotron Backward-Wave Oscillator. *Physical Review Letter*, 89:268303, Dec 2002.
- [160] E. V. Blokhina, S. P. Kuznetsov, and A. G. Rozhnev. High-dimensional chaos in a gyrotron. *Ieee Transactions On Electron Devices*, 54(2):188–193, Feb 2007.
- [161] M. I. Airila and P. Kall. Effect of reflections on nonstationary gyrotron oscillations. *IEEE Transactions On Microwave Theory And Techniques*, 52(2):522–528, Feb 2004.
- [162] A. Grudiev and K. Schunemann. Nonstationary behavior of a gyrotron in the presence of reflections. *International Journal of Infrared and Millimeter Waves*, 24(4):429–449, Apr 2003.
- [163] A. Grudiev, J. Jelonnek, and K. Schunemann. Time-domain analysis of reflections influence on gyrotron operation. *Physics of Plasmas*, 8(6):2963–2973, 2001.
- [164] R. Rozental, N. Ginzburg, and A. Sergeev. Tuning of the self-modulation period in a relativistic BWO with strong reflections. *Radiophysics and Quantum Electronics*, 50(12):942–945, 2007.
- [165] R. L. Devaney. *An Introduction to Chaotic Dynamical Systems (2nd ed.)*. Westview Press, 2003.
- [166] K. Tomita. Chaotic response of nonlinear oscillators. *Physics Reports*, 86(3):113 – 167, 1982.

- [167] Z. E. Musielak and D. E. Musielak. High-dimensional chaos in dissipative and driven dynamical systems. *International Journal Of Bifurcation And Chaos*, 19(9):2823–2869, Sep 2009.
- [168] E. Blokhina and A. Rozhnev. Chaos and hyperchaos in a gyrotron. *Radiophysics and Quantum Electronics*, 49(10):799–810, 2006.
- [169] T. Chang, K. Pao, C. Fan, and S. Chen. Nonstationary and chaotic behavior of the electron cyclotron maser. In *Conference Digest of the 2004 Joint 29th International Conference on Infrared and Millimeter Waves, 2004 and 12th International Conference on Terahertz Electronics, 2004.*, pages 633 – 634, sept.-1 oct. 2004.
- [170] N. Ginzburg, N. Zaitsev, E. Ilyakov, I. Kulagin, Y. Novozhilova, R. Rozental, and A. Sergeev. Chaotic generation in a megawatt backward-wave tube. *Technical Physics*, 46(11):1420–1427, 2001.
- [171] T. V. Dmitrieva and N. M. Ryskin. Complex dynamics of a distributed parametric oscillator. *Journal Of Experimental And Theoretical Physics*, 93(6):1314–1322, 2001.
- [172] M. J. Feigenbaum. The onset spectrum of turbulence. *Physics Letters A*, 74(6):375 – 378, 1979.
- [173] Y. Pomeau and P. Manneville. Intermittent transition to turbulence in dissipative dynamical systems. *Communications in Mathematical Physics*, 74(2):189–197, 1980.
- [174] P. S. Linsay. Period Doubling and Chaotic Behavior in a Driven Anharmonic Oscillator. *Physical Review Letters*, 47:1349–1352, Nov 1981.
- [175] T. Braun, J. A. Lisboa, R. E. Francke, and J. A. C. Gallas. Observation of deterministic chaos in electrical discharges in gases. *Physical Review Letters*, 59:613–616, Aug 1987.
- [176] H. Lamela, G. Carpintero, and F. Mancebo. Period tripling and chaos in the dynamic behavior of directly modulated diode lasers. *Quantum Electronics, IEEE Journal of*, 34(10):1797–1801, Oct 1998.
- [177] N. M. Ryskin and V. N. Titov. Nonlinear dynamics of the backward-wave oscillator. *Journal of Communications Technology and Electronics*, 45(1):S46–S52, 2000.
- [178] H. D. I. . Abarbanel, R. Brown, J. J. Sidorowich, and L. S. Tsimring. The Analysis of observed chaotic data in physical systems. *Review of Modern Physics*, 65(4):1331–1392, Oct 1993.
- [179] J. Genoud. Analyse des phénomènes chaotiques dans les gyrotrons - Rapport Travaux Pratiques IV. Master's thesis, École Polytechnique Fédérale de Lausanne (EPFL): Sciences de Bases - Physique, 2013.
- [180] M. T. Rosenstein, J. J. Collins, and C. J. De Luca. A practical method for calculating largest lyapunov exponents from small data sets. *Physica D-Nonlinear Phenomena*, 65(1-2):117–134, May 1993.

BIBLIOGRAPHY

- [181] T. Buzug and G. Pfister. Comparison of algorithms calculating optimal embedding parameters for delay time coordinates. *Physica D: Nonlinear Phenomena*, 58:127 – 137, 1992.
- [182] T. Buzug and G. Pfister. Optimal delay time and embedding dimension for delay-time coordinates by analysis of the global static and local dynamical behavior of strange attractors. *Physical Review A*, 45:7073–7084, May 1992.
- [183] E. Blokhina, S. Kuznetsov, and A. Rozhnev. High-dimensional chaotic attractors in a gyrotron with nonfixed field structure. *Technical Physics Letters*, 32(4):364–368, 2006.
- [184] E. Blokhina and A. Rozhnev. Complex dynamics of gyrotron with non-fixed structure. In *Vacuum Electronics, 2003 4th IEEE International Conference on*, pages 168 – 169, may 2003.
- [185] A. H. McCurdy. Nonlinear theory of large-signal mode locking in a gyrotron oscillator. *Applied Physics Letters*, 66(14):1845–1847, 1995.
- [186] G. G. Denisov, S. V. Kuzikov, and A. V. Savilov. Q-switching in the electron backward-wave oscillator. *Physics of Plasmas*, 18(10):–, 2011.
- [187] I. V. Bandurkin and A. V. Savilov. Super-radiant effects in electron oscillators with near-cutoff operating waves. *Physics of Plasmas*, 22(6):–, 2015.
- [188] B. Levush, T. M. Antonsen, A. Bromborsky, W. R. Lou, and Y. Carmel. Theory Of Relativistic Backward-wave Oscillators With End Reflections. *IEEE Transactions On Plasma Science*, 20(3):263–280, Jun 1992.
- [189] S.-H. Chen and L. Chen. Nonstationary oscillation of gyrotron backward wave oscillators with cylindrical interaction structure. *Physics of Plasmas*, 20(12):–, 2013.
- [190] S. Sabchevski and T. Idehara. A Numerical Study on Finite-Bandwidth Resonances of High-Order Axial Modes (HOAM) in a Gyrotron Cavity. *Journal of Infrared, Millimeter, and Terahertz Waves*, 36(7):628–653, 2015.
- [191] K. F. Pao, T. H. Chang, C. T. Fan, S. H. Chen, C. F. Yu, and K. R. Chu. Dynamics of Mode Competition in the Gyrotron Backward-Wave Oscillator. *Physical Review Letters*, 95:185101, Oct 2005.
- [192] K. Sakamoto, A. Kasugai, K. Takahashi, R. Minami, N. Kobayashi, and K. Kajiwara. Achievement of robust high-efficiency 1 MW oscillation in the hard-self-excitation region by a 170GHz continuous-wave gyrotron. *Nature Physics*, 3(6):411–414, Jun 2007.
- [193] S. H. Chen, K. F. Pao, T. H. Chang, C. T. Fan, and K. R. Chu. Study of axial modes in the gyrotron backward-wave oscillator. In *27th International Conference On Infrared And Millimeter Waves, Conference Digest*, pages 333–334, Sep 2002.
- [194] T.-M. Tran, F. Braunmueller, and S. Alberti. Gyrotron Equations. Internal Report v0.8, École Polytechnique Fédérale de Lausanne (EPFL): Sciences de Bases - Physique, August 2013.

- [195] W. H. Press. *Numerical recipes 3rd edition: The art of scientific computing*. Cambridge university press, 2007.
- [196] P. Muggli. *Etude d'un gyrotron a cavité cylindrique: influence des réflexions de puissance et de l'oscillation d'un mode propageant*. PhD thesis, École Polytechnique Fédérale de Lausanne (EPFL): Sciences de Bases - Physique, Lausanne, 1991.
- [197] S. Alberti, T. Tran, K. Avramides, F. Li, and J. P. Hogge. Gyrotron parasitic-effects studies using the time-dependent self-consistent monomode code TWANG. In *Infrared, Millimeter and Terahertz Waves (IRMMW-THz), 2011 36th International Conference on*, pages 1–2, 2011.

Publications and Conferences

Journal publications as first author

- F. Braunmueller et al., "Moment-based, self-consistent linear analysis of gyrotron oscillators"
Physics of Plasmas, 21(4), 2014.
- F. Braunmueller et al., "TWANG-PIC, a novel gyro-averaged one-dimensional particle-in-cell code for interpretation of gyrotron experiments"
Physics of Plasmas, 22(6), 2015.

Journal publications as co-author

- S. Alberti, F. Braunmueller, T. M. Tran, J. Genoud, J.-P. Hogge, M. Q. Tran, and J.-P. Ansermet.
"Nanosecond Pulses in a THz Gyrotron Oscillator Operating in a Mode-Locked Self-Consistent Q-Switch Regime".
Physical Review Letters, 111, Nov 2013.
- S. Alberti, F. Braunmueller, T.M. Tran, J.-P. Hogge, J. Genoud, and M. Q. Tran.
"High-Power THz-Waves using gyrotrons: new physics results" (Invited paper).
International Journal of Terahertz Science and Technology, 7(1), 23–38, 2014.
- D. Yoon, M. Soundararajan, P. Cuanillon, F. Braunmueller, S. Alberti, and J.-P. Ansermet.,
"Dynamic nuclear polarization by frequency modulation of a tunable gyrotron of 260 GHz".
Journal of Magnetic Resonance, 262, 62–67, 2016.
- S. Alberti, J.-P. Ansermet, K. A. Avramides, F. Braunmueller, P. Cuanillon, J. Dubray, D. Fasel, J.-P. Hogge, A. Macor, E. de Rijk, M. da Silva, M. Q. Tran, T. M. Tran, and Q. Vuillemin,
"Experimental study from linear to chaotic regimes on a terahertz-frequency gyrotron oscillator".
Physics of Plasmas, 19(12), 2012.
- S. Alberti, T. Tran, S. Brunner, F. Braunmueller, J. Genoud, J.-P. Hogge, and M. Tran.
"Generalized Radiation Boundary Conditions in Gyrotron Oscillator Modeling".
Journal of Infrared, Millimeter, and Terahertz waves, 36(11), 2015.

- J. Genoud, T. M. Tran, S. Alberti, F. Braunmueller, J.-P. Hogge, M. Q. Tran, W. C. Guss, and R. J. Temkin.
"Novel linear analysis for a gyrotron oscillator based on a spectral approach".
submitted to Physics of Plasmas, 2016.

Conference contributions

- Presentation: "Evaluation of experimentally measured non-stationary oscillation in gyrotrons using adequate simulation methods", F. Braunmueller et al.
40th International Conference on Infrared, Millimeter and Terahertz waves (IRMMW-THz), Hong Kong (China), Sept 2015.
- Presentation: "TWANG-PIC, a monomode gyro-averaged PIC code for gyrotron simulations", F. Braunmueller et al.
39th International Conference on Infrared, Millimeter, and Terahertz waves (IRMMW-THz), Tucson (USA), Sept 2014.
- Presentation: "Experiment-theory comparison of non-stationary and chaotic regimes in gyrotrons", F. Braunmueller et al.
38th International Conference on Infrared, Millimeter, and Terahertz waves (IRMMW-THz), Mainz (Germany), Sept 2013.
- Poster: "Self-consistent, time-dependent gyrotron linear analysis in non-homogeneous RF-structures", F. Braunmueller et al.
38th International Conference on Infrared, Millimeter, and Terahertz Waves (IRMMWTHz), Mainz (Germany), Sept 2013.
- Presentation: "Characterization of an Electron Cyclotron Maser for enhanced Nuclear Magnetic Resonance Spectroscopy", F. Braunmueller et al. Swiss Physical Society Annual Meeting' in Fribourg, June 30-July 2, 2014

Falk Braunmueller

E-mail: falkesb@gmx.de
Phone Number: 0041 774 580190

Home Address: Avenue de Riant-Mont 23
1004 Lausanne
Switzerland

Date of birth: 20th August 1984
Nationality: German



Education

École Polytechnique Fédérale de Lausanne (EPFL, Switzerland)

- 02.2012 - now **Doctoral student** at the Centre de Recherches en Physique des Plasmas (CRPP) in the field of microwave sources (gyrotrons)
- 4 conference contributions at International Conference on Infrared, Millimeter Waves and Terahertz (3 oral, 1 poster)
 - Courses on plasma physics and programming (12 ECTS-points + courses without grading, post-degree courses and 1 master course)
 - Tutoring groups of bachelor students in General Physics courses
 - Organizer of seminar series for doctoral students, 2013-2015

Max-Planck-Institut für Plasmaphysik (IPP) in Greifswald (Germany)

- 09.2010 - 09.2011 **Master Thesis in Experimental Plasma Physics** at VINETA experiment
Writing of the "Diplomarbeit" (equivalent to Master thesis)
- Topic "Fluctuation diagnostics for the measurement of dynamic magnetic fields in plasmas"
 - Design, construction and use of an array of magnetic probes used to measure the current profile of Alfvén waves
 - Thesis as part of the studies at Heidelberg University, Grade: 1,7 ("very good")
03. – 05.2010 Internship at the IPP Greifswald in the VINETA group (microwave interferometry)

Ruprecht-Karls-Universität, Heidelberg (Germany)

- 2005 - 2011 **"Diplom" studies** at Heidelberg University (equivalent to Master studies) in Physics
- 05.2009 - 07.2010 Final oral exams on Experimental Physics, Theoretical Physics, Mathematical Statistics and Atomic & Molecular Physics
Overall grade: 1,5 ("very good")
- 08.2007 - 02.2008 Erasmus semester at the **Uppsala Universitet (Sweden)**, with courses in Physics, Swedish and Meteorology
- 04.2007 "Vordiplom" (2 years university degree) in Physics with Mathematics and IT

Journal Publications (most relevant)

- 05.2015 "TWANG-PIC, a novel gyro-averaged 1D particle-in-cell code for interpretation of gyrotron experiments"
Braunmueller, F.; Tran, T.M.; Vuillemin, V.; Alberti, S.; Genoud, J.; Hogge, J.-P. and Tran, M.Q.
Physics of Plasmas
- 04.2014 "Moment-based, self-consistent linear analysis of gyrotron oscillators"
Braunmueller, F.; Tran, T. M.; Alberti, S.; Hogge, J.-P. and Tran, M. Q.
Physics of Plasmas

11.2013 "Nanosecond Pulses in a THz Gyrotron Oscillator Operating in a Mode-Locked Self-Consistent Q-Switch Regime"
Alberti, S.; Braunmueller, F.; Tran, T. M.; Genoud, J.; Hogge, J.-P.; Tran, M. Q. and Ansermet, J.-P.
Physical Review Letters

Special Skills

Languages

German Native speaker
English Fluent (9 years education at school, 5 years of everyday use)
French Fluent (2 courses, superior level "Oberstufe" at Heidelberg University, 4 years of everyday use)
• certified European level C1
Swedish Basic (1 course at VHS Heidelberg, 2 courses at Uppsala Universitet (SWE))

Methods and techniques

Handling of high-tech RF-equipment
Feedback-control techniques
Planning, setup and execution of experiments
Advanced data analysis techniques
Setup and execution of numerical simulation studies

IT skills

Very good expertise in MATLAB, LaTeX, Microsoft Word and PowerPoint.
Good skills in Fortran
Basic skills of Labview and C++

Work experience

09.2004 - 06.2005 **Paramedic Assistant** during "Zivildienst" (civil service as military service replacement), "Deutsches Rotes Kreuz Heilbronn"

Other work experiences

2002 - 2009 Private tutoring in Mathematics, Physics and English
2008 and 2009 Landscaping and gardening, "Gärtnerei Fleck Heidelberg"
2006 and 2007 Bartender in a beer garden, "Schwanengarten Neckarsteinach"
2005 and 2008 Office occupations, metal processing and packing, "Schunk GmbH Lauffen"
2002 - 2004 Bike mechanic, "Zweirad und Zubehör Botenheim"
Holidays '01 – '04 Working for heating construction, gardening, electrician and plastics processing

Miscellaneous

Sports Climbing, Football, Running (Lausanne Marathon 2014), Rowing, Snowboarding, Cross-country skiing
Others Travelling, Hiking, Cinema, Literature

